JOURNAL AerospaceLab

ONERA
THE FRENCH AEROSPACE LAB

Issue 13
September 2017

DOI: 10.12762/2017.AL13

Design and Validation of Aerospace Control Systems

ISSN: 2107-6596

Jean-Marc BIANNIC
(ONERA)
Research Director

Clément ROOS
(ONERA)
Senior Scientist

DOI: 10.12762/2017.AL13-00

Design and Validation of Aerospace Control Systems: an Overview of Methods & Tools

Since their early development in the 1970's with the introduction of fly-by-wire technology, control systems have considerably evolved. Thanks to powerful on-board computers whose capacities have undergone an exponential growth over the past thirty years, together with the development of enhanced sensors and actuators, the complexity of aerospace control systems is almost no longer bounded today. This is true at least from a technological viewpoint. Control engineers should, however, keep in mind that there are many risks in developing unnecessarily complex systems whose validation will become a real issue. In this world, where technological constraints have been considerably relaxed and where autonomous systems have become a universal Holy Grail, a good balance must be found between the design and validation phases in the development of control systems. Some complexity is inevitable during the design phase to cope with that of the plant itself, as well as with the required level of autonomy. However, complexity must be controlled, so that the validation phase remains as quick and cheap as possible.

In this general context of rapidly growing complexity, the development of efficient control design and analysis tools has become a critical issue. Here again, the exponential growth in computing capacity has played a key role and contributed to a rapid development of many fields in control theory. As a result, if one focuses at least on the linear control framework and its numerous extensions (such as robust control theory, parameter-varying control and adaptive control, to cite a few), a high level of maturity is now reached.

However, the gap between theory and practice remains to be filled. This is the main focus of this thirteenth issue of Aerospace Lab, which is dedicated to the most recent techniques for the design and validation of Aerospace Control Systems, with a particular emphasis on Matlab-oriented tools and toolboxes together with realistic applications. This issue is also strongly connected to the SMAC (Systems Modeling Analysis & Control) toolbox developed by ONERA.

Advanced design and analysis tools

The constantly growing "complexification" of aerospace control systems reinforces the need for advanced but user- friendly design and analysis tools. Within the control community, both in academic and industrial worlds, Mathworks™ with its MATLAB/SIMULINK™ product is the undisputed world-leader in this field. It provides a flexible and powerful object-oriented environment for control system design and analysis, using both Mathworks-provided1[1] and external toolboxes. Among those, this special issue of the Aerospace Lab journal, through various aerospace applications, will focus on the following:

- **SMAC toolbox**: http://w3.onera.fr/smac

  This toolbox developed by ONERA includes several modeling, analysis and control libraries, which are illustrated in various contributions of the present issue [2, 5, 7, 10]. The core of

[1] Such as the Control and Robust Control toolboxes.

this toolbox is the Linear Fractional Representation (LFR) object, which enables a wide class of uncertain systems to be captured in a unified framework perfectly well suited to many design and robustness analysis techniques. Among the nine libraries that are currently available with the SMAC toolbox, four are of particular interest in this issue:

- **SMAC/GSS**: this library interfaced with Simulink, based on the gss object (generalized state-space), is dedicated to LFT modeling, reduction and interconnections.
- **SMAC/SMART**: this library, devoted to linear time-invariant (LTI) robustness analysis, implements a collection of efficient tools to compute accurate robustness margins for complex systems involving numerous states and uncertainties.
- **SMAC/IQCFD**: this library, based on the Integral Quadratic Constraints (IQC) theory can be viewed as an extension of SMART to systems including sector nonlinearities. The computational burden is then higher, but a specific implementation makes this tool quite attractive for large order systems.
- **SMAC/SAW**: this library implements two complementary techniques for design and analysis of anti- windup systems, in order to better understand and then alleviate the effects of saturations in control systems. Thanks to its Simulink interface, this tool is quite user-friendly.

- **LPVtools**: http://www.aem.umn.edu/SeilerControl/software.shtml

  This toolbox, developed by the University of Minneapolis, is dedicated to the class of Linear Parameter Varying (LPV) systems that frequently appear in aerospace applications. Note that LPV systems can always be represented in the aforementioned LFR format. Thus, strong connections and complementarity exist between LPVtools, which is illustrated in [6] and the SMAC toolbox.

- **R-ROMULOC**: http://projects.laas.fr/OLOCEP/romuloc/

  This toolbox, mainly developed by LAAS-CNRS in collaboration with the IEIIT-CNR (Politecnico di Torino, Italy) and at the Institute for Control Science (Moscow, Russia) is intended to gather multiple theoretical results obtained recently in Robust Control and Randomized Methods. The aim is to have some simple functions for manipulating uncertain systems and building LMI optimization problems related to robust multi-objective control problems. Both deterministic and probabilistic methods are considered, as illustrated in [4].

- **SATAW-Tool**: http://homepages.laas.fr/queinnec/sataw-tool.html

  This toolbox (SATuration AWare Tool), developed by I. Queinnec and S. Tarbouriech at the LAAS-CNRS, implements various theoretical results regarding the presence of saturation elements in the control loop, for both analysis and control design operations. Note that strong connections exist between these tools and the SAW Library from the SMAC toolbox, as shown in [7].

A brief summary

This thirteenth issue of the Aerospace Lab journal is composed of ten original papers, with a good balance between design and analysis oriented contributions.

The first paper [1] presents an overview of structured H_∞ control theory and a non-smooth optimization-based approach to solve this difficult non-convex problem. The proposed algorithm has been implemented in the hinfstruct and systune routines provided with the MathWorks Robust Control Toolbox. Various possible extensions are discussed in the paper, such as multi-model design. This is further illustrated in the following two papers [2, 3] dedicated to nonlinear and gain-scheduled control applications, respectively. Challenging applications of structured H_∞ control to future European launchers are also described in [8]. An alternative design approach is then proposed in this special issue, with a contribution describing the application of mixed randomized and robust control tools [4]. The main interest of such a strategy is to relax part of the conservatism induced by fully deterministic methods. In short, the main idea is to avoid low-performance controllers that are unnecessarily robust against unlikely situations. The last design-oriented contribution focuses on the impact of saturations in control systems with an application to anti-PIO (pilot-induced-oscillation) systems [7]. Various anti-windup design algorithms available with SATAW-Tool and SMAC/SAW are proposed and evaluated.

As mentioned above, a significant part of this issue is also dedicated to recent analysis tools taking into account various aspects of the closed-loop systems to be analyzed, such as:

- **Nonlinear elements**: this can be treated by IQC analysis [5, 10]. The main drawback of this approach is the computational load, which has thus deserved specific attention in the proposed algorithms, which are described and illustrated with realistic examples.

- **Parameter-varying elements**: based on the LPV framework, an original approach is detailed in [6] to compute robustness margins for linear parameter-varying systems. One of the potential applications of the proposed algorithm is the stability analysis of systems with fast time-varying dynamics, such as launchers, for example.

The above tools are very useful to “pre-validate” control systems and usually provide constructive information for further improving control laws. Their application is usually restricted to simplified versions of the closed-loop plant. Optimization and oriented simulation-based approaches are therefore required for further validation of complex systems. This aspect is discussed in the last paper [9], in the context of a flexible launcher ■

References

[1] P. APKARIAN, D. NOLL - *The H_∞ Control Problem is Solved*. Aerospace Lab Issue No. 13.

[2] J.-M. BIANNIC, C. ROOS, J. LESPRIER - *Nonlinear Structured H_∞ Controllers for Parameter Dependent Uncertain Systems with Application to Aircraft Landing.* Aerospace Lab Issue No. 13.

[3] F. SEVE, S. THEODOULIS, P. WERNERT, M. ZASADZINKI, M. BOUTAYEB - *Gain-Scheduled H_∞ Loop-Shaping Autopilot Design for Spin-Stabilized Canard-Guided Projectiles*. Aerospace Lab Issue No. 13.

[4] M. CHAMANBAZ, F. DABBENE, D. PEAUCELLE, C. PITTET, R. TEMPO - *Randomized and Robust Methods for Uncertain Systems Using R-ROMULOC, with Applications to DEMETER Satellite Benchmark.* Aerospace Lab Issue No. 13.

[5] F. DEMOURANT - *Stability Analysis by a New Algorithmic Approach Based on Integral Quadratic Constraints: Application to an Aircraft Benchmark*. Aerospace Lab Issue No. 13.

[6] A.-K. SCHUG, P. SEILER, H. PFIFER - *Robustness Margins for Linear Parameter Varying Systems*. Aerospace Lab Issue No. 13.

[7] I. QUEINNEC, S. TARBOURIECH, J.-M. BIANNIC, C. PRIEUR - *Anti-Windup Algorithms for Pilot-Induced-Oscillations Alleviation*. Aerospace Lab Issue #13.

[8] M. GANET-SCHOELLER, J. DESMARIAUX, C. COMBIER - *Structured Control for Future European Launchers*. Aerospace Lab Issue No. 13.

[9] A. KAMATH, P. P. MENON, M. GANET, G. MAURICE, S. BENNANI - *Surrogate Assisted Computation of Parametric Safety Margin of a Flexible Launcher.* Aerospace Lab Issue No. 13.

[10] P. VUILLEMIN, F. DEMOURANT, C. POUSSOT-VASSAL - *Stability Analysis of a Set of Uncertain Large Scale Dynamic Models with Saturations*. Aerospace Lab Issue No. 13.

P. Apkarian
(ONERA)

D. Noll
(Institut de Mathématiques de Toulouse, Université Paul Sabatier)

E-mail: pierre.apkarian@onera.fr

DOI: 10.12762/2017.AL13-01

The H_∞ Control Problem is Solved

The H_∞ control problem was posed by G. Zames in 1981 [1], and various attempts to address it had been made over the years. Ultimately, in 2006, the authors presented their solution, which is based on a tailored non-smooth optimization technique [2]. In this treatise we present the rationale of H_∞ control, give a brief history, and recall the milestones reached before our 2006 solution. We clarify why our novel approach is welcomed in the high-tech and aerospace industry. Recent MATLAB functions, `hinfstruct` and `systune`, based on work by Apkarian, Noll and Gahinet (The MathWorks) are available in the Robust Control Toolbox, since R2010b and R2012b respectively.

What has Rosetta got to do with H_∞-control?

The *Rosetta space probe* developed by the European Space Agency was launched on March 2, 2004 with an Ariane-5 launcher, and its lander module *Philae* was successfully placed on the comet 67P/Churyumov-Gerasimenko by November 12, 2014. What is less known is that in 2011 an unexpected off-pointing of the satellite was detected. In-depth on-ground analysis revealed a loss of efficiency in one of the thrusters. It then became evident that the successful accomplishment of the mission hinged on re-designing the controllers. New sophisticated attitude controllers were synthesized by Airbus Defense and Space in March 2014, using the multi-model features of a novel controller synthesis technique called `hinfstruct`. These new controllers were uploaded in May 2014, just before engaging the final maneuver to get closer to the comet 67P/Churyumov-Gerasimenko [35]. The novel control design tool that was behind this had been pioneered by the authors [2] between 2004 and 2006. It became available to control engineers between 2006 and 2010 via the MATLAB functions `hinfstruct` and `systune`. The mathematical principle underlying these tools is the H_∞-rationale, which we will explain in this treatise.

We mention that a change of paradigm in control engineering is currently underway, where our novel structured H_∞-control design technique is being adopted by leading aerospace industries. For instance, Dassault and ONERA [36] use the H_∞-technique in tandem with the MORE software [37] to test new strategies for anti-vibration control of civil aircraft. Design of new atmospheric flight pilots for the Ariane launcher is being investigated by Airbus Safran Launchers, CNES and ONERA. Other applications include control of flexible satellites by Thales Alenia Space and ADS, inertial line of sight stabilization by SAGEM [34], the design of structured estimators for microsatellites by CNES [33], motor torque control in haptics by the CEA LIST robotics [32], and the list could be continued.

A mathematical principle, the H_∞-paradigm, has found its way into control engineering practice. We investigate its rationale, and gauge the potential of the new method for the high-tech industry.

The H_∞ control problem

The H_∞-problem was framed by G. Zames in two plenary talks at the IEEE CDC in 1976 and the Allerton Conference in 1979, and was posed formally in his 1981 paper [1]. However, the origins of the H_∞-problem are much older and date back to the 1960s, when Zames discovered the small gain theorem [4]. After more than 30 years, the H_∞-problem was "solved" by P. Apkarian and D. Noll in 2006 [2] in a sense that is defined hereafter. Note a related, though very different, technique of stochastic nature has been developed in [3].

In this section we introduce the H_∞-control problem formally, discuss its rationale, and present the context leading to our 2006 solution.

Some history

In their seminal 1989 paper [5], Doyle, Glover, Khargonekar and Francis show that the H_∞ problem requires the solution of two algebraic Riccati equations (AREs). Doyle [6] discusses how this

milestone is reached and mentions an earlier 1984 solution. In 1994, P. Gahinet and P. Apkarian give a solution [7] of the H_∞ problem by reducing it to a linear matrix inequality (LMI), the 1995 solution. How can a problem be solved several times? What do we mean when we say that we solved the problem in 2006 [2], when the 1984, 1989, and 1995 solutions existed already?

Formal statement of the problem

The H_∞ control problem can be stated as follows. Given a real rational transfer matrix $P(s)$, called the *plant*, and a space $\mathcal{K}$ of real rational transfer matrices $K(s)$, called the *controller space*, characterize and compute an optimal solution $K^* \in \mathcal{K}$ to the following optimization program

$$\begin{array}{ll} \text{minimize} & \| T_{w\to z}(P,K) \|_\infty \\ \text{subject to} & K \text{ stabilizes } P \text{ internally} \\ & K \in \mathcal{K} \end{array} \qquad (1)$$

Here, the objective function is the H_∞-norm of the closed-loop performance channel $T_{w\to z}(P,K)$, see Figure 1. As we shall see, the choice of the controller space $\mathcal{K}$ in (1) is the key to a proper understanding of the problem.

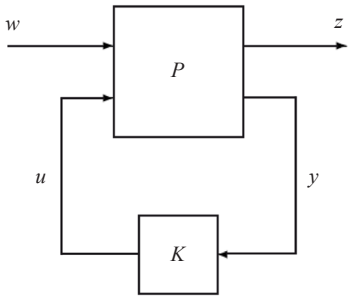

Figure 1 – Standard closed-loop LFT model

Let us recall the notions used to formulate (1). The plant $P(s)$ has a state-space representation of the form

$$P:\begin{cases} \dot{x} = Ax + B_1 w + B_2 u \\ z = C_1 x + D_{11} w + D_{12} u \\ y = C_2 x + D_{21} w + D_{22} u \end{cases} \qquad P(s):\left[\begin{array}{c|cc} A & B_1 & B_2 \\ \hline C_1 & D_{11} & D_{12} \\ C_2 & D_{21} & D_{22} \end{array}\right] \qquad (2)$$

where $x \in \mathbb{R}^{n_p}$ is the state, $u \in \mathbb{R}^{n_u}$ the control, $y \in \mathbb{R}^{n_y}$ the measured output, $w \in \mathbb{R}^{n_w}$ the exogenous input, and $z \in \mathbb{R}^{n_z}$ the regulated output. Similarly, $K(s)$ has the state-space representation

$$K:\begin{cases} \dot{x}_K = A_K x_K + B_K y \\ u = C_K x_K + D_K y \end{cases} \qquad K(s):\left[\begin{array}{c|c} A_K & B_K \\ \hline C_K & D_K \end{array}\right] \qquad (3)$$

where $x_K \in \mathbb{R}^k$ is the state of K. As soon as $D_{22} = 0$, the closed-loop transfer channel $T_{w\to z}(P,K)$ in (1) has the state-space representation

$$T_{w\to z}(P,K):\left[\begin{array}{cc} A(K) & B(K) \\ C(K) & D(K) \end{array}\right] \qquad (4)$$

where

$$A(K)=\begin{bmatrix} A+B_2D_KC_2 & B_2C_K \\ B_KC_2 & A_K \end{bmatrix}, B(K)=\begin{bmatrix} B_1+B_2D_KD_{12} \\ B_KD_{21} \end{bmatrix}, C(K)=\text{etc.} \qquad (5)$$

and where the state dimension is now $n_p + k$. Finally, for a stable real rational transfer function $T(s)$, the H_∞-norm in (1) is defined as

$$\|T\|_\infty = \max_{\omega\in\mathbb{R}} \bar{\sigma}\big(T(j\omega)\big) \qquad (6)$$

where $\bar{\sigma}(M)$ is the maximum singular value of a complex matrix M.

With these notations, we can now give the first explanation. The 1984, 1989 and 1995 solutions of the H_∞ problem (1) are all obtained within the space $\mathcal{K}_{full}$ of full-order controllers

$$\mathcal{K}_{full} = \{K : K \text{ has form (3) with size}(A_K) = \text{size}(A)\}$$

Observe that in $\mathcal{K}_{full}$ *all* entries in A_K, B_K, C_K, D_K are free variables. Altogether, there are $N := n_p^2 + n_p(n_y + n_u) + n_y n_u$ degrees of freedom and we have

$$\mathcal{K}_{full} \cong \mathbb{R}^N$$

In particular, $\mathcal{K}_{full}$ is the largest controller space that we could use in (1)[1]. Finding a solution within $\mathcal{K}_{full}$ is therefore easier. In particular, with $\mathcal{K}_{full}$ as the controller space, (1) is convex, as shown in [7]. When *smaller* and more practical controller spaces $\mathcal{K}$ are chosen, Problem (1) is much harder to solve. Our 2006 solution addresses these difficult cases.

Solutions of the H_∞-control problem in the 1980s and 1990s refer to the full-order case, which is essentially convex.

The rationale

After closing the loop in the feedback scheme (1) we may consider the closed-loop system as a linear operator $T_{w\to z}(P,K)$ mapping input w to output z. If K stabilizes P internally, that is, if $T_{w\to z}(P,K)$ in (5) is stable, then $T_{w\to z}(P,K)$ maps $w \in L^2$ into $z \in L^2$. The H_∞-norm (6) is then nothing else but the L^2-L^2-operator norm, that is,

$$\|T\|_\infty = \sup_{w\neq 0} \frac{\|Tw\|_2}{\|w\|_2} = \sup_{w\neq 0} \frac{\|z\|_2}{\|w\|_2}$$

In other words, for a closed-loop channel $w \to z$ the norm squared $\gamma^2 = \|T_{w\to z}(P,K)\|_\infty^2$ is the factor by which the energy of the input signal is amplified in the output. Input w with energy $\|w\|_2^2$ will produce output z with energy $\|z\|_2^2$ no greater than $\gamma^2 \cdot \|w\|_2^2$, as long as controller K is used. The optimization program (1) strives to find the controller $K^* \in \mathcal{K}$ for which this amplification factor γ is smallest.

In a closed loop with controller K, the input w with energy $\|w\|_2^2$ creates output z with energy $\|z\|_2^2 \le \gamma^2 \|w\|_2^2$, where $\gamma = \|T_{w\to z}(P,K)\|_\infty$. The same relation holds for power signals $w \to z$, i.e., power is amplified by no more than γ^2.

[1] Using even larger state dimensions does not lead to anything new.

This can obviously be very useful. All that we have to do is to find communication channels $w \to z$, where the smallness of answer z to question w tells us something meaningful about the system.

We now give the typical context of *loopshaping*, where this idea is used. The standard control scheme (see Figure 2) features the open-loop system G, the controller K, the measured output y, the control signal u, and the tracking error e. Red signals are inputs, n_s = sensor noise, d = disturbance or process noise, and r = reference signal for y, sometimes called a command. The blue signals are specifically chosen outputs, $\tilde{e} = W_e e$, $\tilde{u} = W_u u$, $\tilde{y} = W_y y$.

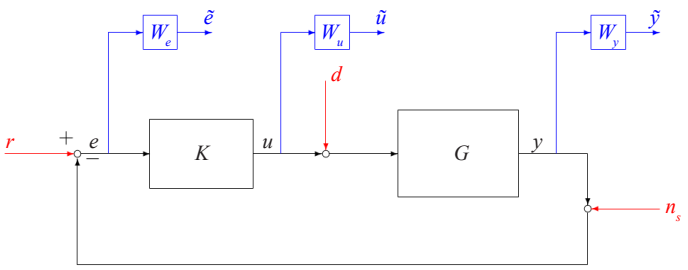

Figure 2 – Standard control scheme

This is a special case of Figure 1, where $w = (r, d, n_s)$ is the input, $z = (\tilde{e}, \tilde{u}, \tilde{y})$ is the output, and where plant G regroups G and the filters W_e, W_u, W_y. The filters may be dynamic, which adds new states to the plant P.

What are useful transfer functions from red to blue? For instance, the transfer from reference r to tracking error e

$$T_{r\to e}(K) = (I + GK)^{-1}$$

is a typical performance channel, because it describes how fast the system follows the reference r. Since one typically wants to track only in the low frequency range, W_e is a low-pass filter. Now, the smallness of the norm

$$\left\| T_{r\to\tilde{e}}(K) \right\|_\infty = \left\| W_e (I + GK)^{-1} \right\|_\infty$$

means that the low frequency component $\tilde{e}$ of the tracking error e becomes small as a result of optimization, so y follows the reference input r in low frequency.

Next consider a typical robustness channel. For instance, the influence of sensor noise n_s on the control signal u. Noise is typically of high frequency, but that should not lead to high frequency components in u, as this bears the risk, for example, of actuator fatigue. Therefore, W_u is typically a high-pass filter and $\tilde{u}$ are high frequency components of u. We find

$$T_{n_s\to\tilde{u}}(K) = -W_u (I + KG)^{-1} K$$

and $\left\| T_{n_s\to\tilde{u}}(K) \right\|_\infty$ puts a cost on high frequency components in u. If program (1) is successful, it will furnish an optimal $K^* \in \mathcal{K}$ that makes this cost as small as possible, thereby building robustness to sensor noise into the system.

To conclude, we can see that, depending on the specific application, there will be several performance and robustness channels. In its basic form, (1) requires fixing a single connection $w \to z$, but in Section 5 we will show how to solve a multi-objective problem with several H_∞-channels.

Setting up the performance channel $w \to z$ in (1) could be interpreted as putting a cost on undesirable behavior of the closed-loop system.

Controller structures

The reason why the H_∞ theory of the 1980s failed to take hold in practice is quickly explained. Controllers computed via algebraic Riccati equations are full order, or *unstructured*. However, for various reasons, practitioners prefer simple controllers like PIDs, or control architectures combining PIDs with filters, and such controllers are *structured*.

The discrepancy between H_∞ theory and control engineering practice is highlighted, for example, by PID control. Until 2010 PID controllers had to be tuned instead of optimized, because software for H_∞-PID control was not available.

During the 1990s and early 2000s a new approach to controller design based on linear matrix inequalities (LMIs) was developed. Unfortunately, LMIs have essentially the same shortcomings as AREs: H_∞ controllers computed via LMIs are still unstructured. The situation only started to improve when, in the late 1990s, the authors pioneered the investigation of feedback controller synthesis via bilinear matrix inequalities (BMIs). While the LMI euphoria was still in full progress, we recognized that what was needed were algorithms that would allow structured controllers to be synthesized. Here is the formal definition of structure (see [2]).

Definition 1
A controller K of the form (3) *is called* structured *if the state-space matrices A_K, B_K, C_K, D_K depend smoothly on a design parameter vector κ varying in some parameter space $\mathbb{R}^n$, or in a constrained subset of $\mathbb{R}^n$.*

In other words, a controller structure $K(\cdot)$, or $K(\kappa)$, consists of four smooth mappings $A_K(\cdot): \mathbb{R}^n \to \mathbb{R}^{k\times k}$, $B_K(\cdot): \mathbb{R}^n \to \mathbb{R}^{k\times n_y}$, $C_K(\cdot): \mathbb{R}^n \to \mathbb{R}^{n_u\times k}$, and $D_K(\cdot): \mathbb{R}^n \to \mathbb{R}^{n_u\times n_y}$.

It is convenient to indicate the presence of structure in K by the notation $K(\kappa)$, where κ denotes the free parameters. In the MATLAB functions `hinfstruct` or `systune` one refers to κ as the vector of tunable parameters.

Three basic examples with structure

The structure concept is best explained by examples. The transfer function of a realizable PID controller is of the form

$$K(s) = k_p + \frac{k_i}{s} + \frac{k_d s}{1 + T_f s} = d_K + \frac{r_i}{s} + \frac{r_d}{s + \tau}, \qquad (7)$$

where $d_K = k_p + k_d / T_f$, $\tau = 1/T_f$, $r_i = k_i$, $r_d = -k_d T_f^2$. Realizable PIDs may therefore be represented in state-space form

$$K_{pid}(\kappa): \begin{bmatrix} 0 & 0 & r_i \\ 0 & -\tau & r_d \\ 1 & 1 & d_K \end{bmatrix} \tag{8}$$

where $\kappa = (r_i, r_d, d_K, \tau) \in \mathbb{R}^4$ is tunable. As we can see,

$$A_K(\kappa) = \begin{bmatrix} 0 & 0 \\ 0 & -\tau \end{bmatrix}, B_K(\kappa) = \begin{bmatrix} r_i \\ r_d \end{bmatrix}, C_K(\kappa) = [1\,1], D_K(\kappa) = d_K$$

If we use the PID structure (8) within the H_∞ framework (1), we compute an H_∞ PID controller, that is, a PID controller that minimizes the closed-loop H_∞-norm among all internally stabilizing PID controllers:

$$\left\| T_{w\to z}\left(P, K_{pid}^*\right) \right\|_\infty \le \left\| T_{w\to z}\left(P, K_{pid}\right) \right\|_\infty$$

The controller space for this structure is

$$\mathcal{K}_{pid} = \left\{ K_{pid}(\kappa) : \text{as in (8)}, \kappa = (r_i, r_d, d_K, \tau) \in \mathbb{R}^4 \right\}$$

The fact that PID is a structure in the sense of Def. 1 means that PIDs may now be optimized instead of tuned.

A second classical controller structure, related to the fundamental work of Kalman in the 1960s, is the observer-based controller, which in state-space has the form:

$$K_{obs}(\kappa): \left[\begin{array}{c|c} A + B_2 K_c + K_f C_2 & -K_f \\ \hline K_c & 0 \end{array}\right] \tag{9}$$

Here, the vector of tunable parameters κ regroups the elements of the Kalman gain matrix K_f and the state-feedback control matrix K_c. That is, $\kappa = \left(vec\left(K_f\right), vec\left(K_c\right)\right)$. Since the plant P has n_p states, n_y outputs and n_u inputs, κ is of dimension $n_p\left(n_y + n_u\right)$, *i.e.*, $n = n_p\left(n_y + n_u\right) < N$, which indicates that the controller is structured, even though $k = n_p$. In fact, formally the structure of observer-based controllers is defined as

$$\mathcal{K}_{obs} = \left\{ K_{obs}(\kappa) : as\ in\ (9),\ \kappa = \left(vec\left(K_f\right), vec\left(K_c\right)\right) \in \mathbb{R}^{n_p(n_y+n_u)} \right\}$$

Now, if we use (9) within the framework of (1), we are computing an observer-based H_∞-controller. However, do not observer-based controllers K_{obs} belong to the realm of H_2-control? This is H_∞ control!

Are we mixing things? Yes we are, but for good reasons! If we are attached to the observer-structure, and at the same time appreciate the robustness of H_∞-control, then we should by all means mix things. The result will be a controller $K_{obs}(\kappa^*)$, where K_c^* gives us two gain matrices K_c^* and K_f^*, neither of which is by itself optimal in any sense[2]. In particular, there are no algebraic Riccati equations for K_f^* or K_c^*. Nonetheless, taken together, they are optimal in the sense that

$$\left\| T_{w\to z}\left(P, K_{obs}(\kappa^*)\right) \right\|_\infty \le \left\| T_{w\to z}\left(P, K_{obs}(\kappa)\right) \right\|_\infty$$

[2] The principle of separation of observation and control is no longer valid.

for any other observer-based controller $K_{obs}(\kappa)$ that stabilizes P internally. In particular, observer-based controllers based on AREs would appear on the right hand side, and hence are sub-optimal.

A third basic controller structure are reduced order controllers. More precisely, the order of K is fixed as $k < n_p$. This is the simplest example of a structure, namely

$$\mathcal{K}_k = \left\{ K : K \text{ as in (3) with size}\left(A_K\right) = k \times k \right\}$$

Here, the vector of tunable elements is $\kappa = \left(vec\left(A_K\right), vec\left(B_K\right), vec\left(C_K\right), vec\left(D_K\right)\right)$ of dimension $n = k^2 + k(n_y + n_u) + n_y n_u$. This is a structure in the spirit of our definition, because it uses fewer degrees of freedom than the full order controller, which has $N = n_p^2 + n_p(n_y + n_u) + n_y n_u$ free places.

Why is it reasonable to call $\mathcal{K}_k$ a structure as soon as $k < n_p$? The reason is that computing reduced fixed-order optimal H_∞-controllers is substantially more complicated than computing the full-order H_∞ controller. In lieu of two coupled Riccati equations, $K^* \in \mathcal{K}_k$ requires four coupled Riccati equations, [8], and the numerical procedures proposed in the 1990s are clearly demanding. In the realm of matrix inequalities the H_∞-problem for reduced-order controllers has also been well-studied. One obtains an LMI in tandem with a rank constraint, a non-convex problem that is equivalent to a BMI.

Controllers with structure arise naturally. That is why the authors pioneered the investigation of structured H_∞-synthesis in the 1990s.

The solution of the H_∞-control problem

A problem that was left open for 30 years may be expected to be difficult. The difficulty in the H_∞-control problems is due to the fact that it is non-convex, and that the objective in (1) is non-smooth. Moreover, there is a third difficulty, which is related to stability in closed-loop.

Non-smooth optimization

Assuming that $K(\kappa)$ is structured with parameter $\kappa \in \mathbb{R}^n$, we write the closed-loop transfer channel $w \to z$ in (4) as

$$T_{w\to z}\left(P, K(\kappa)\right): \left[\begin{array}{c|c} A\left(K(\kappa)\right) & B\left(K(\kappa)\right) \\ \hline C\left(K(\kappa)\right) & D\left(K(\kappa)\right) \end{array}\right]$$

Then, the H_∞-objective function in (1) becomes

$$\begin{aligned} f(\kappa) &:= \left\| T_{w\to z}\left(P, K(\kappa)\right) \right\|_\infty \\ &= \max_{\omega\in\mathbb{R}} \bar{\sigma}\left(C\left(K(\kappa)\right)\left(j\omega I - A\left(K(\kappa)\right)\right)^{-1} B\left(K(\kappa)\right) + D\left(K(\kappa)\right) \right) \end{aligned} \tag{10}$$

a non-smooth, non-convex function, which in addition is not defined everywhere. Its domain $D_f = \left\{ \kappa \in \mathbb{R}^n : f(\kappa) < \infty \right\}$ contains the internally stabilizing set

$$\begin{aligned} D_s &= \left\{ \kappa \in \mathbb{R}^n : K(\kappa) \text{stabilizes } P \text{internally} \right\} \\ &= \left\{ \kappa \in \mathbb{R}^n : A\left(K(\kappa)\right) \text{ stable} \right\} \end{aligned} \tag{11}$$

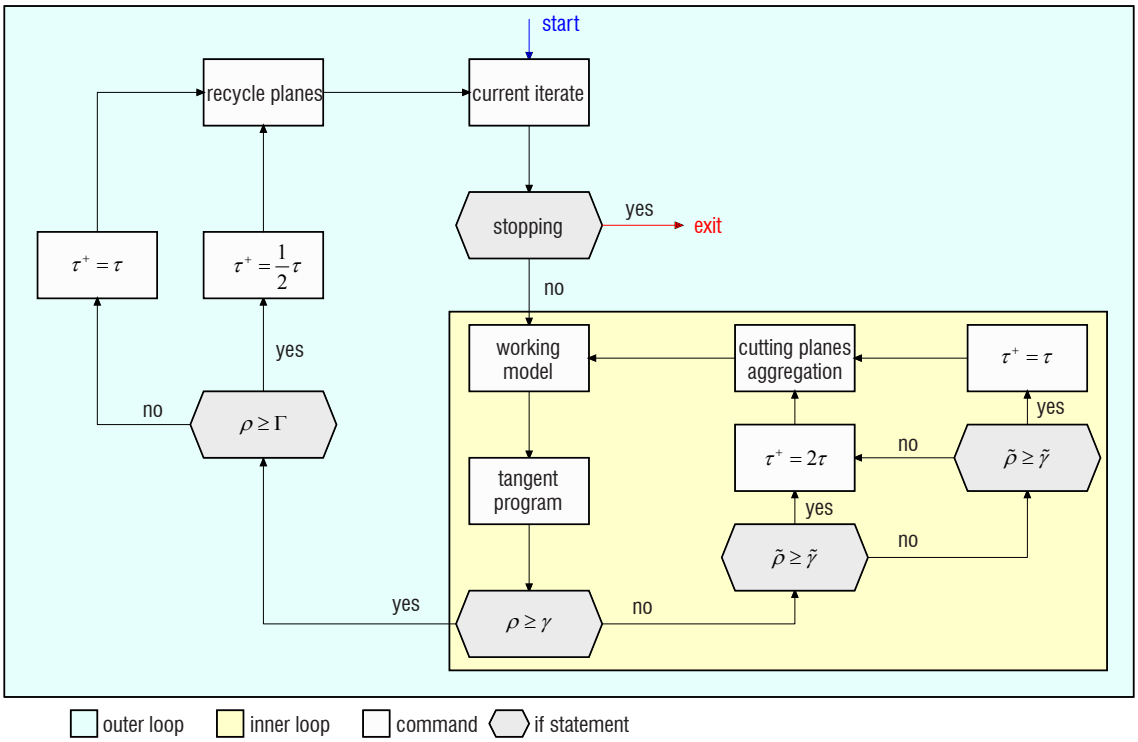

Figure 3 – Flowchart of the proximity control algorithm

The first major step toward the solution of the H_∞ control problem in the seminal paper [2] was to characterize and compute the Clarke subdifferential of the function f. This allowed necessary optimality conditions to be formulated, and thereby enabled locally optimal solutions of (1) to be characterized. These conditions are of primal-dual type, which means that they are expressed in terms of primal variables κ and dual variables X, Y. The latter correspond to the Lyapunov variables used in the ARE and LMI solutions.

The classical solution of the H_∞-problem within $\mathcal{K}_{full}$ using AREs or LMIs for two Lyapunov matrix variables X, Y has the following particularity. The Lyapunov matrices X, Y can be interpreted as the dual variables of our own more general approach, while the primal variable, $K = (A_K, B_K, C_K, D_K)$, can be eliminated. Only in this very specific case is the problem convex in (X, Y).

The second major challenge was to find algorithmic tools to compute solutions of the structured H_∞-problem (1). The objective being non-convex and non-smooth, we had to develop new optimization methods and to prove their convergence. This was started in [2], and continued in [10, 11, 12, 14, 15, 16]. We invented non-convex bundle methods. The bundle technique originated in the 1980s and is the most successful approach to deal with *convex* non-smooth problems in Lagrangian relaxation or stochastic control. We succeeded in extending this to non-convex functions, which represents a major breakthrough.

Stabilization

As we stressed before, the objective $f(\kappa)$ in (1), respectively (10), is only defined on the set

$$D_s = \{\kappa \in \mathbb{R}^n : A(K(\kappa)) \text{is stable}\}$$

from (11). Our optimization method therefore not only has to *iterate* within this set, we first have to *find* a feasible parameter $\kappa \in D_s$. Surprisingly, this is already the first difficulty.

Note that we have to answer the following yes-or-no question:

$$\text{Does there exist } \kappa \text{ such that } A(K(\kappa)) \text{ is stable ?} \qquad (12)$$

Or in our previous notation: Given a controller space $\mathcal{K}$

$$\text{Does there exist } K \in \mathcal{K} \text{ such that } A(K) \text{ is stable ?} \qquad (13)$$

We want an algorithm that computes such a $K \in \mathcal{K}$ if the answer to (13) is "yes", and provides a certificate of non-existence if the answer is "no". Also, we would like these answers reasonably fast, for example, in polynomial time.

How is this related to Kalman's classical theory of stabilizability, detectability, controllability and observability? Stabilizability of (A, B) means that we can stabilize by state feedback. And detectability of (A, C) means that we can add an observer. Therefore, if (A, B) is stabilizable and (A, C) is detectable, then the answer to Question (12) is "yes" for the class $\mathcal{K}_{obs}$ of observer-based controllers. Since stabilizability of (A, B) and detectability of (A, C) are conditions that can be checked by linear algebra (in polynomial time), we can say that (12) is conveniently decided for the class of observer-based controllers $\mathcal{K}_{obs}$ and for any larger class $\mathcal{K} \supset \mathcal{K}_{obs}$.

However, and this is the bad part of the message, for practically important controller structures $K(\kappa)$ the decision (12) is NP-complete. Blondel and Tsitsiklis [17] prove NP-completeness for the classes $\mathcal{K}_k$ of reduced-order controllers, $k < n_p$, including the class $\mathcal{K}_{stat}$ of static controllers, and for the class $\mathcal{K}_{dec}$ of decentralized controllers. It is also known that the decision is hard for PID control. For short, the

most important classes in practice lead already to a difficult problem when it comes to mere stabilization.

Deciding whether a stabilizing controller $K(\kappa)$ with a given structure exists is in general NP-complete.

What does this mean in practice? Complexity theory usually produces pessimistic results. The situation is by no means hopeless. Practical systems are designed to be stabilizable, so as a rule there is a good chance of finding a stabilizing structured controller $K \in \mathcal{K}$ if there is one. What we expect to be hard, is a certificate of non-existence when no such controller exists, because this requires an exhaustive search. Complexity also tells us that we cannot expect a linear algebra procedure as in Kalman's classical theory, at least not one with polynomial complexity. We also know that for most classes $\mathcal{K}$ Problem (12) is decidable, but in exponential time. This follows, for instance, as soon as the problem can be transformed into a polynomial decision problem, to which the Tarski-Seidenberg procedure can, at least in principle, be applied.

Local versus global optimization

The fact that program (1) is non-convex for practical controller structures $\mathcal{K}$ creates a dilemma. Should we go for a globally optimal solution, or should we be modest and be content with locally optimal solutions? In our approach, we have opted for the local approach, since it is more realistic. This does not mean that we advise against the use of global optimization techniques. Such techniques might prove successful for small to medium size problems.

There is, however, one specific global approach on which we wish to comment, because it has contributed substantially to the field of mathematical poppycock. We are speaking about the so-called sums-of-squares (SOS) approach, which is still rumored to be suited for control problems like (1). We now argue that this is a red herring.

For most controller structures $\mathcal{K}$ it is possible to transform program (1) into a bilinear matrix inequality (BMI) using the bounded real lemma. Typically, the BMI is of the form

$$min\left\{c^{\mathrm{T}}x : B(x) \preceq 0\right\} \tag{14}$$

where x now stands for the triple (κ, X, Y) featuring controller gains κ and Lyapunov variables X, Y as unknowns with possibly additional slack variables γ, etc. The SOS approach interprets (14) as a system of polynomial inequalities and uses the sums-of-squares approximation of positive polynomials to creates a hierarchy of LMI problems

$$min\left\{c^{\mathrm{T}}x : L_i(x) \preceq 0\right\} \tag{15}$$

with the property that the solution of (15) converges to the solution of (14). It may even happen that convergence is *finite*, meaning that there exists $i = i(B)$ such that the solution of $min\left\{c^{\mathrm{T}}x : L_{i(B)} \preceq 0\right\}$ solves $min\left\{c^{\mathrm{T}}x : B \preceq 0\right\}$ globally. The way in which this hierarchy is constructed has been much inspired on the idea of a cutting plane proof for a linear integer feasibility problem $Ax \le b,\ x \in \mathbb{Z}^n$.

Let us for simplicity assume that convergence is indeed finite. Then we might be able, it seems, to write down an explicit linear matrix equality

$$min\left\{c^{\mathrm{T}}x : L_{i(B)}(x) \preceq 0\right\} \tag{16}$$

which when solved gives a *globally optimal solution* of (1). (Strictly speaking, we might not be able to write down (16) directly, but rather only to reach it eventually by climbing up in the hierarchy until we get to $i(B)$. This would, of course, spoil the whole idea. However, let us assume, as is often claimed in the SOS community, that we *can* write down (16) explicitly!

Doesn't this sound nice? After all, we have been told since the early 1990s that LMIs can be solved efficiently in quasi-polynomial time. Therefore, all that we have to do is to solve (16) quickly and obtain the global minimum of (14), and respectively of (1).

Of course, this is all rubbish. We *know* that solving Problem (1) globally is NP-complete. The SOS algorithm is even provably exponential. The size of $L_{i(B)} \preceq 0$ grows therefore exponentially in the data size (B). In fact, these problems explode extremely fast. We will need exponential space even to write down $L_{i(B)} \preceq 0$. For sizable plants we might not even be able to *store* the problem on the computer, let alone solve it. The fact that LMIs are solved in polynomial time is pointless, because we are speaking about a problem of *polynomial (exponential)* size.

However, could not something similar be said about *every* global method? Are we too severe when we call SOS a red herring? Indeed, the problem being NP-complete, *every* global method is bound to be exponential. The point is that SOS is a particularly ungainly global method, because it commits two errors, which other global methods may avoid.

The first error is that it transforms (1) to a BMI. This adds a large number of additional variables X, Y, which can be avoided, for example, by our non-smooth approach. We have demonstrated abundantly since the late 1990s that the presence of Lyapunov variables leads to serious ill-conditioning. To wit:

The power oscillation damping control problem, which we solved in [18] using non-smooth optimization, has a system with 90 states, 3 performance connections, 1 input, 1 output, and a controller of reduced order 8. Therefore $\dim(\kappa) = 81$. Transformed to a BMI, it requires additional $3 \cdot \frac{90 \cdot 91}{2} = 12285$ Lyapunov variables. For the SOS approach this is just the bottom line $i = 1$, where the LMI hierarchy starts. The LMI $L_{i(B)} \preceq 0$ will be of size exponential(12366).

The second error in the SOS approach is that it only seeks global minima. That is, it will *not* find local minima of (1) on its way toward the global. This is infelicitous, because local minima are very helpful. They may allow bounds to be improved in branch-and-bound methods, and they give good practical solutions as a rule. The fact that SOS does not use this information (e.g., to infer where it is in the hierarchy $L_i \preceq 0$) is by itself already suspicious.

The H_2/H_∞-problem is also solved

It became already apparent in the 1-DOF scheme (2) that the L^2-L^2, respectively power-to-power, operator norm is not the only possible measure of smallness in a channel $w \to z$. Consider, for instance, the transfer $T_{n_s \to \tilde{u}}$ from sensor noise n_s to the high frequency part $\tilde{u} = W_u u$ of the control law u. If we model n_s as white noise, then

it makes sense to gauge $n_s \to \tilde{u}$ by the operator norm from white noise at the input toward power at the output. This is the H_2-norm. For a stable transfer operator $G(s)$ the H_2-norm is given as

$$\|G\|_2 = \left(\frac{1}{2}\pi \int_0^\infty \mathrm{Tr}\left(G(j\omega)G^H(j\omega)\right)d\omega\right)^{1/2}$$

which makes it an Euclidean norm in the space of stable transfer matrices. Unlike the H_∞-norm, the H_2-norm is *not* an operator norm in the traditional sense. It becomes one as soon as stochastic signals are considered.

$\|w\|$	$\|z\|$	operator norm $\|T_{w\to z}\|$
energy	energy	H_∞
power	power	H_∞
white noise	power	H_2
Sobolev $W^{\infty,\infty}$	L^∞	worst case response norm
L^∞	L^∞	peak gain
past excitation	system ring	Hankel

In the 1-DOF scheme (2) we might decide to use two different norms. We might assess the tracking error $r \to \tilde{e}$ in the H_∞-norm, and the influence of sensor noise on the control $n_s \to \tilde{u}$ by the H_2-norm. Then, we obtain a mixed H_∞ / H_2-control problem

$$\begin{aligned} &\text{minimize} && \left\|T_{r\to\tilde{e}}(P,K)\right\|_\infty \\ &\text{subject to} && \left\|T_{n_s\to\tilde{u}}(P,K)\right\|_2 \le \gamma_2 \\ & && K \text{ stabilizes } P \text{ internally} \\ & && K = K(\kappa) \text{ has a fixed structure} \end{aligned} \tag{17}$$

where γ_2 is some threshold limiting the power of $\tilde{u}$ in response to white noise in the input n_s. We may introduce the following more abstract setting. Consider a plant in state-space form

$$P: \quad \begin{bmatrix} \dot{x} \\ z_\infty \\ z_2 \\ y \end{bmatrix} = \left[\begin{array}{c|ccc} A & B_\infty & B_2 & B \\ \hline C_\infty & D_\infty & 0 & D_{\infty u} \\ C_2 & 0 & 0 & D_{2u} \\ C & D_{y\infty} & D_{y2} & 0 \end{array}\right] \begin{bmatrix} x \\ w_\infty \\ w_2 \\ u \end{bmatrix} \tag{18}$$

where $x \in \mathbb{R}^{n_x}$ is the state, $u \in \mathbb{R}^{n_u}$ the control, $y \in \mathbb{R}^{n_y}$ the output, and where $w_\infty \to z_\infty$ is the H_∞, $w_2 \to z_2$ the H_2 performance channel. Then the mixed H_2 / H_∞-synthesis problem is the optimization program

$$\begin{aligned} &\text{minimize} && \left\|T_{w_2\to z_2}(P,K)\right\|_2 \\ &\text{subject to} && \left\|T_{w_\infty\to z_\infty}(P,K)\right\|_\infty \le \gamma_\infty \\ & && K \text{ stabilizes } P \text{ internally} \\ & && K \in \mathcal{K} \end{aligned} \tag{19}$$

where $\mathcal{K}$ is a structured controller space as before, and γ_∞ is a suitable threshold, now for the H_∞-norm in the constraint. Notice that the H_2 / H_∞- and H_∞ / H_2-problems are equivalent under suitable choices of γ_2 and γ_∞.

The mixed $K(\kappa)$-synthesis problem with structured controllers $K(\kappa)$ is a natural extension of H_∞-control. This problem also has a long history. It was posed for the first time by Haddad and Bernstein [19] and by Doyle, Zhou, Bodenheimer [20] in 1989. We solved this problem in 2008 in [21].

Naturally, one may immediately think about other multi-objective extensions of (1). For instance, combining the H_∞-norm with time-domain constraints like in IFT(Iterative Feedback Tuning), or H_∞ / H_∞-control. For the first theme, we refer the reader to our solution presented in [22, 23], while H_∞ / H_∞-control will be addressed in the next section.

The H_∞ / H_∞-control problem and other variants

The H_∞ / H_∞-problem can be seen as a special case of (1). Suppose that we have two plants P_1 and P_2 with performance channels $w_i \to z_i$, $i = 1, 2$. Assume that the outputs y_i and inputs u_i into P_i have the same dimension, *i.e.*, $dim(y_1) = dim(y_2)$ and $dim(u_1) = dim(u_2)$. Then, we can connect the same controller $u_i = K(\kappa)y_i$ to both plants simultaneously. That is, we may solve a program of the form

$$\begin{aligned} &\text{minimize} && \left\|T_{w_1\to z_1}(P_1,K)\right\|_\infty \\ &\text{subject to} && \left\|T_{w_2\to z_2}(P_2,K)\right\|_\infty \le \gamma_2 \\ & && K \text{ stabilizes } P_1 \text{ and } P_2 \\ & && K = K(\kappa) \text{ is structured} \end{aligned} \tag{20}$$

It turns out that we may transform (20) favorably into a program of the form

$$\begin{aligned} &\text{minimize} && max\left\{\left\|T_{w_1\to z_1}(P_1,K(\kappa))\right\|_\infty, \beta\left\|T_{w_2\to z_2}(P_2,K(\kappa))\right\|_\infty\right\} \\ &\text{subject to} && K(\kappa) \text{ stabilizes } P_1 \text{ and } P_2 \end{aligned} \tag{21}$$

which is sometimes called a multidisk problem [10]. For suitable choices of γ_2 and β these two programs are equivalent. However, since the maximum of two H_∞-norms is again an H_∞-norm of an augmented plant, we can solve (21) directly via (1) with a new specific structure, which consists in repeating $K(\kappa)$, as illustrated in Figure 4.

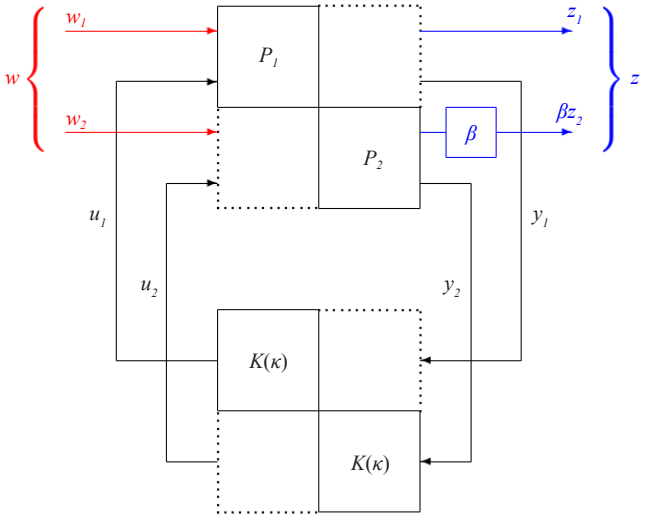

Figure 4 – Illustration of the multidisk problem

and the only connection between the two diagonal parts is the fact that the diagonal block of K is repeated. The objective of (21) is then the channel $w=(w_1,w_2)\to z=(z_1,\beta z_2)$ of the augmented plant. We may now have to update β in order to solve the problem of Figure 4 for a specific γ_2.

Multi-model H_∞-synthesis

Controlling several plants via the same structured controller is one of the most fundamental properties of `hinfstruct` and `systune`. The theoretical basis and implementation of this option has been given in the paper Apkarian and Noll [10] in 2006. The problem setting is as follows. Given N plants $P_1,\ldots,P_N$

$$P_i(s):\left[\begin{array}{c|cc} A_i & B_{1i} & B_{2i} \\ \hline C_{1i} & D_{11i} & D_{12i} \\ C_{2i} & D_{21i} & D_{22i} \end{array}\right], i=1,\ldots,N \qquad (22)$$

with identical dimensions of control inputs, that is, $dim(u_1)=\ldots=dim(u_N)$ and also identical dimensions of the measured outputs, *i.e.*, $dim(y_1)=\ldots=dim(y_N)$, we connect the same controller $K(s)$ to these N plants simultaneously. This controller may, in addition, be structured

$$u_i(s)=K(\kappa,s)\,y_i(s), i=1,\ldots,N$$

where κ represents the tunable elements in K. The multi-objective or multidisk H_∞-control problem can now take on several forms, all familiar in multi-objective optimization. For instance, we could consider:

$$\begin{array}{ll} \text{find} & \kappa\in\mathbb{R}^n \\ \text{such that} & \left\|\mathcal{F}_l(P_i,K(\kappa))\right\|_\infty \le \gamma_i, i=1,\ldots,N \\ & K(\kappa) \text{ stabilizes } P_i \text{ internally}, i=1,\ldots,N. \end{array} \qquad (23)$$

A related form of the multi-objective approach is

$$\begin{array}{ll} \text{minimize} & \left\|\mathcal{F}_l(P_1,K(\kappa))\right\|_\infty \\ \text{such that} & \left\|\mathcal{F}_l(P_i,K(\kappa))\right\|_\infty \le \gamma_i, i=2,\ldots,N \\ & K(\kappa) \text{ stabilizes } P_i \text{ internally}, i=1,\ldots,N. \end{array} \qquad (24)$$

and the following third form is known as the multidisk approach used in Apkarian and Noll [10]:

$$\min_{\kappa\in\mathbb{R}^n}\ \max_{i=1,\ldots,N}\ \alpha_i\left\|\mathcal{F}_l(P_i,K(\kappa))\right\|_\infty \qquad (25)$$

where the $\alpha_i>0$ are appropriate weights. We shall in the sequel discuss several examples to understand this approach in practical situations.

Reliable and fault-tolerant control

Reliable or fault-tolerant control is an application of multi-model H_∞-control. The first occurrence of this approach in the literature where an optimization program of the form (22) is applied is Simões *et al.* [26]. In that reference, control of an F-16 aircraft in nominal mode along with 6 failure modes is discussed. These are the failure of left or right stabilizer, failure of left or right aileron, 75% impairment of the stabilizers, and unspecific failure in one of the redundant controllers. Since in each of the 7 modes one needs to ensure satisfactory performance of the system, 3 performance channels are proposed, leading to a total of 21 scenarios, *i.e.*, $N=21$ in (22).

Simultaneous stabilization is NP-complete even in the case of 3 systems and a full order (unstructured) controller. Not surprisingly, simultaneous H_∞-control will therefore fail every now and then. The functions `hinfstruct` and `systune` just offer good practical chances of solving such problems.

System reduction via non-smooth programming

An idea already put forward in our paper [2] is H_∞-system reduction. Consider a stable system

$$G=\left[\begin{array}{c|c} A & B \\ \hline C & D \end{array}\right]$$

with size $(A)=n\times n$. Suppose that n is large and that we want to compute a reduced stable system

$$G_{red}=\left[\begin{array}{c|c} A_{red} & B_{red} \\ \hline C_{red} & D_{red} \end{array}\right]$$

of smaller state dimension size $(A_{red})=k\ll n$ that represents G as accurately as possible. The model matching error is $e=(G-G_{red})w$, and after adding a suitable filter W_e (see Figure 5) we might want to have $w\to z$ small in a suitable norm.

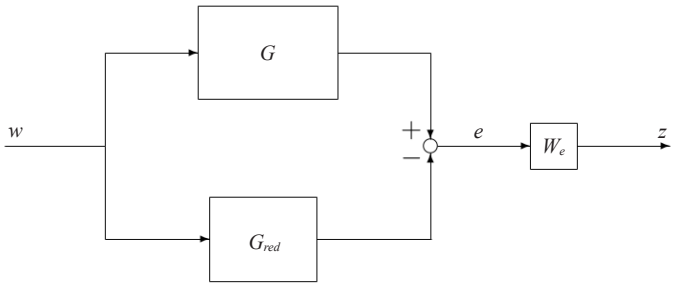

Figure 5 – Illustration of the model reduction problem

The Hankel norm reduction method minimizes $\left\|W_e(G-G_{red})\right\|_H$ in the Hankel norm $\|.\|_H$, the advantage being that the solution can be obtained by linear algebra. A more natural norm would be the H_∞-norm, but the classical balanced reduction method gives only upper bounds of $\left\|W_e(G-G_{red})\right\|_\infty$.

However, we can solve the H_∞-norm reduction problem directly as a special case of (1). In the case $z=e$ without filter we can pass to the standard form by considering the plant

$$P:\left[\begin{array}{c|cc} A & B & 0 \\ \hline C & D & -I \\ 0 & I & 0 \end{array}\right]=\left[\begin{array}{c|cc} A & B_1 & B_2 \\ \hline C_1 & D_{11} & D_{12} \\ C_2 & D_{21} & 0 \end{array}\right] \qquad (26)$$

then G_{red} is the controller, which is of fixed reduced-order.

Note that structured H_∞-filtering is a further application of our non-smooth optimization techniques. A program structure similar to system reduction is obtained in that case.

Optimizing plant and controller simultaneously

In many practical situations it may be advantageous to choose not only the controller, but also certain parameters of the open-loop system in such a way that the entire controlled system behaves optimally in closed loop. Current practice does *not* work this way! What is usually done is that the open-loop system is designed first, and then a feedback controller is computed[3]. However, why not optimize both simultaneously, *i.e.*, plant and controller together? Well, there is now a method that allows this to be done. We illustrate it by means of a simple example.

Consider the second-order spring model with stiffness k, friction f, and mass m

$$P_1:\begin{cases}\dot{x}_1 &= & x_2 \\ \dot{x}_2 &= -\frac{k}{m}x_1 & -\frac{f}{m}x_2 & +\frac{1}{m}w+\frac{1}{m}u \\ y &= x_1 \\ z &= x_1\end{cases}$$

where w is a disturbance, u is the control, x_1 is the position, and x_2 is the velocity. We measure the position, $y = x_1$, and the position is also the coordinate that we wish to control, hence $z = x_1$. We need a SISO controller $u(s) = K(s)y(s)$ to control the system.

Now, suppose that we also wish to optimize the stiffness k and friction f so that the closed loop system is optimal in the channel $w \to z$. Suppose that we have bounds $\underline{k} \le k \le \overline{k}$ and $\underline{f} \le f \le \overline{f}$ between which we can choose the parameters. And at the same time we want to optimize $K = K(\kappa)$, which can as usual be structured, $\kappa \in \mathbb{R}^n$. Mathematically, this problem can be written as

$$\begin{array}{ll}\text{minimize} & \left\| T_{w\to z}\left(P(k,f),K(\kappa)\right)\right\|_\infty \\ \text{subject to} & K(\kappa)\ \text{closed-loop stabilizing} \\ & \underline{k} \le k \le \overline{k}, \underline{f} \le f \le \overline{f} \\ & (k,f,\kappa) \in \mathbb{R}^{n+2}\end{array} \qquad (27)$$

Naturally, the non-smooth algorithms in [2] or [14] are versatile and can include such simple bounds easily. They just need expressions for subgradients of the objective with respect to all unknowns (k,f,κ). The question is how this non-standard option is put to work using our non-smooth optimization techniques. The idea is to shuffle all unknown parameters into an augmented structured controller $\widetilde{K}(k,f,\kappa)$, and to connect it to an artificial plant $\widetilde{P}$. The new formulation for (27) is then

$$\begin{array}{ll}\text{minimize} & \left\| T_{w\to z}\left(\widetilde{P},\widetilde{K}(k,f,\kappa)\right)\right\|_\infty \\ \text{subject to} & \widetilde{K}(k,f,\kappa)\ \text{closed-loop stabilizing for}\ \widetilde{P} \\ & \underline{k} \le k \le \overline{k}, \underline{f} \le f \le \overline{f} \\ & (k,f,\kappa) \in \mathbb{R}^{n+2}\end{array} \qquad (28)$$

Note that the routines `hinfstruct` and `systune` automatize this operation so that it remains hidden from the user.

Nonstandard use of H_∞/H_∞-synthesis

The standard way to use multiple H_∞ criteria is certainly in H_∞-loop-shaping, and the documentation of `hinfstruct` makes this a strong point. However, there are some less obvious ideas in which one can use a program of the form (20). Two heuristics for parametric robust control, which we proposed in [24] and [25], can indeed be solved via `hinfstruct` and `systune`.

Control of nonlinear systems with structured H_∞-synthesis

In this section, we discuss a somewhat unexpected application of structured H_∞-synthesis in the control of nonlinear systems. The class of systems that we have in mind are of the form

$$P(y):\begin{array}{rcl}\dot{x} &= A(y)x &+ B_1(y)w &+ B_2(y)u \\ z &= C_1(y)x &+ D_{11}(y)w &+ D_{12}(y)u \\ y &= C_2(y)x &+ D_{21}(y)w &+ D_{22}(y)u\end{array} \qquad (29)$$

where the system matrices depend smoothly on the measured output y. It appears therefore natural to devise a controller of the form

$$K(y):\begin{array}{rcl}\dot{x}_K &= A_K(y)x_K + B_K(y)y \\ u &= C_K(y)x_K + D_K(y)y\end{array} \qquad (30)$$

which uses the same measurement y available in real time. A natural idea, going back to [29], is to consider y as a time-varying external parameter p and pre-compute $K(p)$ for $P(p)$ for a large set $p \in \Pi$ of possible parameter values. In flight control, for instance, Π is the *flight envelope*, $p = (h,V) \in \mathbb{R}^2$, indexed by altitude h and ground speed V, or sometimes by Mach number and dynamic pressure.

We now propose the following control strategy. In a first step, we pre-compute the optimal H_∞ controller $K^*(p)$ for every $p \in \Pi$ using Program (1):

$$\begin{array}{ll}\text{minimize} & \| T_{w\to z}\left(P(p),K\right)\|_\infty \\ \text{subject to} & K\ \text{stabilizes}\ P(p)\ \text{internally} \\ & K \in \mathcal{K}\end{array} \qquad (31)$$

The solution $K^*(p)$ of (31) has the structure $\mathcal{K}$. In the terminology of [29], this is the best way to control the system $P(p)$ frozen at $p(t) = y(t)$ instantaneously. In other words, at instant t, we apply the control law $K^*(y(t))$ based on the real-time measurement $y(t)$.

If we could do real-time structured H_∞-synthesis, then controller $K^*(y(t))$ would be computed and applied instantaneously at time t using (31) *and the measurement $y(t)$ available at instant t. As long as this is impossible, we may pre-compute $K^*(p)$ for a large set of possible parameter values $p \in \Pi$, and as soon as $y(t)$ becomes available at time t, look $K^*(y(t))$ up in the table $\{K^*(p) : p \in \Pi\}$, and apply it instantaneously.*

There are two limitations to this ideal approach. Firstly, the ideal table $\{K^*(p) : p \in \Pi\}$ may be too large. And secondly, the behavior of $K^*(p)$ as a function of p may be quite irregular. In fact, it was the latter effect that had stopped this idea in the past[4]. With structured

[3] For instance, in optimal sensor or actuator location the usual line is to optimize P alone, for instance, by maximizing the degree of controllability of P. Instead, one should include K from scratch.

[4] When ARE solvers were used to compute H_∞-controllers, the idea of embedding such a solver into the system obviously came to mind. This failed not due to lack of CPU, but due to the highly irregular behavior of $p \mapsto K^*_{full}(p)$.

control laws $K(\kappa)$ the situation is substantially improved, because one uses fewer degrees of freedom in κ.

What we have tested in [30] is a compromise between optimality of $K^*(p)$ in the sense of Program (31), the necessity to avoid irregular behavior of the curves $p \mapsto K^*(p)$, and the storage requirement of such a law. We use the following definition. A controller parameterization $p \mapsto K(p)$ of the given structure $\mathcal{K}$ is *admissible* for the control of $P(y)$ if the following holds: $K(p)$ stabilizes $P(p)$ internally for every $p \in \Pi$, and

$$\left\| T_{w\to z}\left(P(p), K(p)\right)\right\|_\infty \le (1+\alpha)\left\| T_{w\to z}\left(P(p), K^*(p)\right)\right\|_\infty \quad (32)$$

for every $p \in \Pi$, where α is some fixed threshold, say $\alpha = 0.1\%$. We now seek a parameterization $K(p)$ that is close to the ideal H_∞-parameterization $K^*(p)$ in the sense that (32) is respected, but otherwise is easy to store (to embed) and shows as regular a behavior as possible. Note that (32) allows $K(p)$ to lag behind $K^*(p)$ in performance by no more than $\alpha\%$. Also, observe that this approach is heuristic in so far as internal stability at every $p \in \Pi$ does not guarantee stability of the parameter-varying system as a whole.

Parametric robust H_∞-control

The design of feedback controllers that are robust in the presence of system uncertainty is a recurrent problem in control engineering, from which designers rarely escape due to the inevitable mismatch between a physical system and its mathematical model. It is generally agreed that one should account for the uncertainty already at the modeling stage. In the following, we briefly comment on two such forms of uncertainty: real uncertain parameters Δ_p in the model equations, and complex dynamic uncertainty Δ_d.

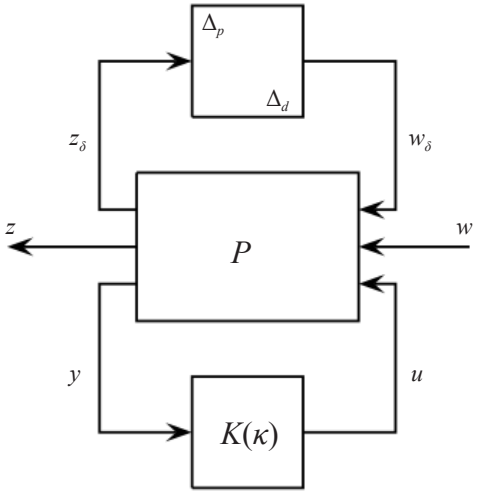

Figure 6 – Illustration of the robust control design problem

Within the H_∞-framework, this *mixed parametric control problem* can be cast as a semi-infinite minmax optimization problem of the form

$$\min_{\kappa\in\mathbb{R}^n} \max_{\Delta\in\mathbf{\Delta}} \left\| T_{w\to z}(\Delta, \kappa)\right\|_\infty \quad (33)$$

where optimization is over a structured control law $K(\kappa)$, as before, but where now in contrast with (25) an infinity of plants, $P(\Delta)$, indexed over a set $\Delta := (\Delta_p, \Delta_d) \in \mathbf{\Delta}$ of mixed uncertain scenarios, has to be controlled *simultaneously*. This problem is therefore considerably more complex than the nominal H_∞-problem (1). Parametric mixed control has been on the control engineering agenda since the late 1970s and 1980s, but no satisfactory solution had been presented until recently. In two recent contributions [9, 38] we have developed a satisfactory mathematically sound solution to this problem, which in parts is already seized by The MathWorks in its 2015b version of the Robust Control Toolbox ■

References

[1] G. ZAMES - *Feedback and Optimal Sensitivity: Model Reference Transformations, Multiplicative Seminorms, and Approximate Inverses*. IEEE Transactions on Automatic Control, vol. AC-26, p. 301-320, 1981.

[2] P. APKARIAN, D. NOLL - *Non-Smooth H_∞-Synthesis*. IEEE Transactions on Automatic Control, vol. 51, no. 1, p. 229-244, 2006.

[3] J. V. BURKE, D. HENRION, A. S. LEWIS, M. L. OVERTON - *HIFOO – A Matlab Package for Fixed-Order Controller Design and H_∞ Optimization*. 5th IFAC Symposium on Robust Control Design, Toulouse, France, July 2006.

[4] G. ZAMES - *On the Input-Output Stability of Nonlinear Time-Varying Feedback Systems, Part I and II*. IEEE Transactions on Automatic Control, vol. AC-11, p. 228 and 465, 1966.

[5] J.C. DOYLE, K. GLOVER, P. P. KHARGONEKAR, B. A. FRANCIS - *State-Space Solutions to Standards H_2 and H_∞ Control Problems*. IEEE Transactions on Automatic Control, vol. AC-34, no. 8, p. 831-847, 1989.

[6] J. C. DOYLE - *Robust and Optimal Control*. Proceedings of the 35th Conference on Decision and Control, Kobe, Japan, Conference Proceedings, p. 1595- 1598, 1996.

[7] P. GAHINET, P. APKARIAN - *A Linear Matrix Inequality Approach to H_∞ Control*. International Journal of Robust and Nonlinear Control, 4:421-448, 1994.

[8] D.C. HYLAND, D.S. BERNSTEIN - *The Optimal Projection Equations for Fixed-Order Dynamic Compensation*. IEEE Trans. Autom. Control, vol. AC-29, no. 11, p. 1034-1037, 1984.

[9] P. APKARIAN, M. N. DAO, D. NOLL - *Parametric Robust Structured Control Design*. IEEE Transactions on Automatic Control, vol. 60, issue 7, p. 1857-1869, 2015.

[10] P. APKARIAN, D. NOLL - *Non-Smooth Optimization for Multidisk H_∞ Synthesis*. European Journal of Control, vol. 12, no. 3, p. 229-244, 2006.

[11] P. APKARIAN, D. NOLL - *Non-Smooth Optimization for Multiband Frequency Domain Control Design*. Automatica, vol. 43, no. 4, p. 724-731, 2007.

[12] P. APKARIAN, D. NOLL, O. PROT - *A Trust Region Spectral Bundle Method for Non-Convex Eigenvalue Optimization*. SIAM Journal on Optimization, vol. 19, no. 1, p. 281-306, 2008.

[13] P. APKARIAN, D. NOLL, L. RAVANBOD - *Branch and Bound Algorithm with Applications to Robust Stability*. Journal of Global Optimization, published electronically march 2016. DOI 10.1007/s10898-016-0424-6.

[14] D. NOLL, O. PROT, A. RONDEPIERRE - *A Proximity Control Algorithm to Minimize Non-Smooth and Non-Convex Functions*. Pacific Journal of Optimization, vol. 4, no. 3, pp. 569-602, 2008.

[15] P. APKARIAN, D. NOLL, O. PROT - *A Proximity Control Algorithm to Minimize Non-Smooth and Non-Convex Semi-Infinite Maximum Eigenvalue Functions*. Journal of Convex Analysis, vol. 16, no. 3 & 4, p. 641-666, 2009.

[16] D. NOLL - *Cutting Plane Oracles to Minimize Non-Smooth and Non-Convex Functions*. Journal of Set-Valued and Variational Analysis, vol. 18, no. 3-4, p. 531-568, 2010.

[17] V. D. BLONDEL, J. N. TSITSIKLIS - *NP-Hardness of Some Linear Control Design Problems*. SIAM J. of Control and Opt., 35:6, p. 2118-2127, 1997.

[18] P. APKARIAN, A. SIMOES, D. NOLL - *A Non-Smooth Progress Function Algorithm for Frequency Shaping Control Design*. IET Control Theory & Applications, vol. 2, no. 4, pp. 323 - 336, 2008.

[19] W. M. HADDAD, D. S. BERNSTEIN - *LQG Control with a H_∞ Performance Bound: A Riccati Equation Approach*. IEEE Trans. Aut. Control, AC-34(3):293-305, 1989.

[20] J. C. DOYLE, K. ZHOU, B. BODENHEIMER - *Optimal Control with Mixed H_2 and H_∞ Performance Objectives*. Proceedings of the American Control Conference, vol.3, p. 2065-2070, 1989.

[21] P. APKARIAN, D. NOLL, A. RONDEPIERRE - *Mixed H_2 / H_∞ Control via Nonsmooth Optimization*. SIAM Journal on Control and Optimization, vol. 47, no. 3, p. 1516-1546, 2008.

[22] P. APKARIAN, L. RAVANBOD, D. NOLL - *Time Domain Constrained Structured H_∞ Synthesis*. International Journal of Robust and Nonlinear Control, vol. 21, no. 2, p. 197-217, 2011.

[23] P. APKARIAN, D. NOLL, A. SIMÕES - *Time Domain Control Design: A Non-Smooth Approach*. IEEE Transactions on Control Systems Technology, vol. 17, no. 6, p. 1439-1445, 2009.

[24] L. RAVANBOD, D. NOLL, P. APKARIAN - *Robustness via Structured H_∞ / H_∞-Synthesis*. International Journal of Control, vol. 84, issue 5, 2011, p. 851-866, 2011.

[25] P. APKARIAN - *Non-Smooth μ-Synthesis*. International Journal of Robust and Nonlinear Control, vol. 21(8), p. 1493-1508, 2011.

[26] P. APKARIAN, A. SIMÕES, D. NOLL - *Non-Smooth Multi-Objective Synthesis with Applications*. Control Engineering Practice, 17(11):2009,1338-1348.

[27] L. RAVANBOD, D. NOLL - *Gain-Scheduled Autopilot for an Aircraft*. 7th IFAC Symposium on Robust Control Design, 2012 Aalborg. Conference Proceedings, 2011.

[28] M. GABARROU, D. ALAZARD, D. NOLL - *Structured Flight Control Law Design Using Non-Smooth Optimization*. 18th IFAC Symposium on Automatic Control in Aerospace (ACA 2010), Nara, Japan, September 6-10, 2010.

[29] J. S. SHAMMA, M. ATHANS - *Analysis of Gain Scheduled Control for Nonlinear Plants*. IEEE Transactions on Automatic Control, vol. 35, no. 4, p. 898-907, 1990.

[30] L. RAVANBOD, D. NOLL - *Gain-Scheduled PID for Imbalance Compensation of a Magnetic Bearing*. 8th International Conference on Informatics, Automation and Robotics (ICINCO 2011), Noordwijkerhout, The Netherlands, Conference Proceedings, p. 330-337, July 2011.

[31] S. SKOGESTAD, I. POSTLETHWAITE - *Multivariable Feedback Control*. Wiley, 2005.

[32] N. ABROUG, B. MORINIERE - *Enhancing Motor Torque Control by Implementing H_∞ Controller and Compensating Electronics Nonlinearities*. IEEE 23rd International Symposium on Industrial Electronics, p. 111-116, 2014.

[33] C. PITTET, P. PRIEUR - *Structured Accelero-Stellar Estimator for Microscope Drag-Free Mission*. Advances in Aerospace Guidance, Navigation and Control, p. 591-604, 2015.

[34] S. HIRWA, P. FEYEL, G. DUC, G. SANDOU - *Reduced-Order Controllers for Line of Sight Stabilization*. 7th IFAC Symposium on Robust Control Design, vol. 45, no. 13, p. 103-108, 2012.

[35] A. FALCOZ, P. CHRISTELLE, S. BENNANI, A. GUIGNARD, B. FRAPARD - *Systematic Design Methods of Robust and Structured Controllers for Satellites*. CEAS Space Journal, vol. 7, no. 3, p. 319-334; 2015.

[36] C. MEYER, J. PRODIGUE, G. BROUX, O. CANTINAUD, C. POUSSOT-VASSAL - *Ground Test for Vibration Control Demonstrator*. International Conference on Motion and Vibration Control (MOVIC'16), 2016.

[37] C. POUSSOT-VASSAL, P. VUILLEMIN - *Introduction to MORE: A MOdel REduction Toolbox.* IEEE Multi-Conference on Systems and Control, p. 776-781, 2012.

[38] R. S. DE AGUIAR, P. APKARIAN, D.NOLL - *Structured Robust Control against Mixed Uncertainty.* Submitted.

AUTHORS

Pierre Apkarian received the Ph.D. degree in control engineering from the *Ecole Nationale Supérieure de l'Aéronautique et de l'Espace* (ENSAE), France, in 1988. He was qualified as a Professor from University of Toulouse (France) in both control engineering and applied mathematics in 1999 and 2001, respectively. Since 1988, he has been a Research Scientist at ONERA (*Office National d'Etudes et de Recherches Aérospatiales*) and an Associate Professor at the University of Toulouse. Pierre Apkarian has served as an associate editor for the IEEE Transactions on Automatic Control. His research interests include robust and gain-scheduling control theory through LMI methods or optimization-based techniques. More recently, his research has focused on the development of specialized non-smooth programming techniques for control system design. He is co-author of the `hinfstruct` and `systune` software in MATLAB's Robust Control Toolbox.

Dominikus Noll received his Ph.D. and habilitation in 1983 and 1989 from *Universität Stuttgart* (Germany). Since 1995 he is a professor of applied mathematics at the University of Toulouse (France), and a distinguished professor of mathematics since 2009. Dr. Noll has held visiting positions at Uppsala University, Dalhousie University, the University of Waterloo, Simon Fraser University, and the University of British Columbia. Dr. Noll's current research interests include nonlinear optimization, optimal control, projection-based iterative schemes, and robust feedback control design. He is co-inventor of the synthesis tools `hinfstruct` and `systune`. Dr. Noll is Associate Editor of the Journal of Convex Analysis.

J.-M. Biannic, C. Roos, J. Lesprier
(ONERA)

E-mail: jean-marc.biannic@onera.fr

DOI: 10.12762/2017.AL13-02

Nonlinear Structured H_∞ Controllers for Parameter-Dependent Uncertain Systems with Application to Aircraft Landing

A new design methodology inspired by dynamic inversion techniques is proposed in this paper. It combines partially linearizing inner-loops with structured and robust outer-loops, which are designed using a non-smooth multi-model H_∞ optimization approach. The proposed methodology also includes a robustness analysis scheme providing worst-case configurations, which are then used to enrich the bank of design models and thus iteratively improve the robustness properties of the designed outer-loops. Our approach is successfully tested on a realistic nonlinear aircraft control problem subject to large parametric variations and uncertainties.

Introduction

Robust feedback linearization techniques [10] have proved their efficiency in many aerospace applications, especially to control highly maneuverable aircraft or UAVs in large operating domains [25, 2, 20, 21, 11, 4]. Interestingly, such techniques do not only permit a large class of nonlinear systems to be linearized and decoupled, but also make it possible to adapt the control laws to the operating point. Thus, they become a competitive alternative to standard gain-scheduling techniques, which often entail many adjustments, or to LPV control design strategies, which require high fidelity LPV models [15]. However, standard dynamic inversion methods are often criticized for their lack of robustness and the need for an accurate model. This drawback is generally bypassed via robust linear outer-loops [6], which still require difficult and possibly time-consuming robustness evaluation *a posteriori* [18, 19]. Severe problems are also likely to occur when the actuator dynamics and limitations prevent an exact cancellation of the nonlinear terms. As emphasized in [12], it is therefore essential to take these dynamics into account in the design process. As observed in [8], one of the main reasons why standard dynamic inversion schemes exhibit poor robustness properties is due to the fact that the linearizing inner-loops are designed to convert the nonlinear system into a generic Brunovsky's form. Following an intuitive path, it is then proposed in [8] to design the inner-loops so that, for given operating conditions, the nonlinear system will converge to its Jacobian linearization. Hence, the design of the linear robust outer-loops is no longer based on a generic model, but now explicitly depends on the linearized dynamics of the initial plant. A similar path, consisting of promoting interactions between inner and outer loops, is followed in this paper. More precisely, as in [8] a feedback linearization step is applied so that, in some enlarged neighborhood of given trim conditions, the nonlinear plant behaves like its linearization. In a second step, a robust linear outer-loop is designed. The originality of our approach lies in the particular structure of our H_∞-based outer controller, which uses a nonlinear input as a key input to further enlarge the operating domain of the nonlinear closed-loop system. Various uncertainties are also taken into account in our procedure by a μ-based robustness analysis phase, during which worst-case configurations are identified and then used in an iterative multi-objective and multi-model H_∞ design process. It should be pointed out here that the resolution of such highly non-convex optimization problems has considerably improved in the past few years with recent advances in non-smooth H_∞ optimization algorithms [3, 9]. Indeed, the latter now make it possible to fix the order of the H_∞ controller as well as its structure and to consider multi-channel objectives and multiple models simultaneously, in order to increase the robustness margins. Such algorithms will then be a key ingredient in our proposed methodology.

The paper is organized as follows. A thorough description of the proposed methodology with its three main steps is first given. An application to a realistic landing aircraft control problem is then detailed. More precisely, we focus on the longitudinal part and give many details on how the method is applied. Then we briefly deal with the lateral part of the control problem, before presenting the global landing application on the full nonlinear aircraft model using the designed controller. Finally, we conclude the paper.

Description of the methodology

Robust Nonlinear Compensation Technique

Consider a continuous-time parameter-dependent nonlinear input-affine system described as follows

$$\begin{cases} \dot{\xi}(t) &= f\left(\xi(t),\theta_p(t)\right)+G\left(\xi(t),\theta_p(t)\right)u(t) \\ u(t) &= L_A\left(u_c(t)\right) \end{cases} \quad (1)$$

where $\xi(t)\in\mathbb{R}^n$ denotes the physical states evolving in the admissible operating domain $\mathcal{X}\subset\mathbb{R}^n$. The realized control inputs $u(t)\in\mathbb{R}^m$ are derived from the commanded inputs $u_c(t)\in\mathbb{R}^m$ via linear time-invariant actuators – denoted by $L_A(.)$ – with unitary static gains. The nonlinearities and parametric variations of the system are captured by $f(.,.)\in\mathbb{R}^n$ and $G(.,.)\in\mathbb{R}^{n\times m}$, which both nonlinearly depend not only on the state vector but also on a set of parameters $\theta_p(t)\in\Theta\subset\mathbb{R}^r$.

Notation 1
Let us denote $\left(\bar{\xi},\bar{\theta}_p,\bar{u}\right)\in\mathbb{R}^n\times\mathbb{R}^r\times\mathbb{R}^m$ *an equilibrium point for system (1), thus satisfying:*

$$f\left(\bar{\xi},\bar{\theta}_p\right)+G\left(\bar{\xi},\bar{\theta}_p\right)\bar{u}=\bar{f}+\bar{G}\bar{u}=0 \quad (2)$$

and rewrite $f\left(\xi(t),\theta_p(t)\right)$ as follows:

$$f\left(\xi(t),\theta_p(t)\right)=\bar{f}+Ax(t)+\Delta_f(t) \quad (3)$$

where:

$$A=\left.\frac{\partial f}{\partial\xi}\right|_{\bar{\xi},\bar{\theta}_p} \quad \text{and} \quad x(t)=\xi(t)-\bar{\xi}(t) \quad (4)$$

and where $\Delta_f(t)$ denotes the deviation between the nonlinear function $f(.,.)$ and its linear approximation.

Assumption 1
There exists a constant matrix $B\in\mathbb{R}^{n\times m}$ *such that, for all* $\left(\xi(t),\theta_p(t)\right)\in\mathcal{X}\times\Theta$, *a* ***nonsingular*** *matrix* $\Lambda\in\mathbb{R}^{m\times m}$ *and a residual error matrix* $\Delta_G\in\mathbb{R}^{n\times m}$ *can be found such that:*

$$G\left(\xi(t),\theta_p(t)\right)=B\Lambda+\Delta_G \quad (5)$$

$$\forall\upsilon(t)\in\mathbb{R}^m,\ L_A\left(\Lambda^{-1}\upsilon(t)\right)\approx\Lambda^{-1}L_A\left(\upsilon(t)\right) \quad (6)$$

The square matrix Λ typically represents the control input efficiency. When considering aerospace systems evolving in standard operating domains, the above non-singularity assumption – connected to the notion of controllability – is not restrictive. Moreover, the variations of this diagonal-dominant matrix are mainly induced by slowly-varying terms, such as the dynamic pressure. This observation justifies the commutative property (6) between Λ^{-1} and the fast dynamics $L_A(.)$ of the actuators. Yet, a possible relaxation of (6) is introduced next.

Given any two signals $v(t)\in\mathbb{R}^m$ and $\zeta(t)\in\mathbb{R}^m$, let us now define the intermediate, input linearizing, control law

$$u_c(t)=\Lambda\left(\xi(t),\theta_p(t)\right)^{-1}\left(v(t)-\zeta(t)\right)+\bar{u} \quad (7)$$

Combining equations (7) and (1), one readily obtains with the above notation in mind:

$$\dot{x}=Ax+BL_A(v)+w_f+w_u \quad (8)$$

where:

$$w_f=\Delta_f-BL_A(\zeta) \quad (9)$$

$$w_u=(G-\bar{G})\bar{u}+\Delta_G\Lambda^{-1}L_A(v-\zeta) \quad (10)$$

As is clear from Equation (8), where parametric-dependence and time-dependence have been omitted to alleviate notation, the parameter-dependent nonlinear system (1) has been reduced to a linear model with a new control input v and two measured perturbations w_f and w_u. As is usual in dynamic inversion schemes, w_f can be partly canceled by an optimal choice of the auxiliary input signal $\zeta(t)$:

$$\hat{\zeta}(t)=Arg\min_{\zeta(t)\in\mathbb{R}^m}\left\|\Delta_f(t)-BL_A\left(\zeta(t)\right)\right\| \quad (11)$$

Remark 1
In the special case of square systems with idealized actuators (i.e., $L_A(u(t))=u(t)$*), one easily obtains* $w_f=0$ *with* $\hat{\zeta}(t)=B^{-1}\Delta_f(t)$.

Let us denote by $w=w_f+w_u$ the vector of remaining input perturbations, which cannot be canceled, and assume that the latter is available for feedback, via estimation, at least on a limited bandwidth. The following structure for the linear outer-loop may thus be considered:

$$v=K(s)\begin{pmatrix}\hat{w}\\ w_c\\ y\end{pmatrix} \quad (12)$$

where $\hat{w}$, w_c and y denote respectively the estimation of w, the target on the variables z to be tracked and the measurement signal. Without any significant loss of generality in most applications, both $y(t)=Cx(t)\in\mathbb{R}^p$ and $z(t)=Lx(t)\in\mathbb{R}^q$ are assumed to depend linearly on the state vector. The output feedback gain $K(s)$ in (12) is to be designed so as to satisfy the following requirements:

- good tracking properties, by minimizing the error between z and the reference signal $z_r=R(s)w_c$, where the LTI model $R(s)$ describes the nominal reference closed-loop dynamics,
- a reasonable control activity, which is indirectly obtained by limiting v to avoid control input saturations,
- good rejection of the perturbations $w=w_u+w_f$ that could not be entirely removed by the linearizing inner loop to enlarge the operating domain.

Denoting by $\Sigma_A(s)$ the transfer matrix associated to the linear operator $L_A(.)$ and by $\Sigma(s)$ the linearized plant interconnection:

$$\Sigma(s)=\begin{bmatrix}L\\ C\end{bmatrix}(sI-A)^{-1}\begin{bmatrix}I & B\end{bmatrix} \quad (13)$$

the above outer-loop design issue can be recast into a linear framework as a multi-objective H_∞ minimization problem. More precisely,

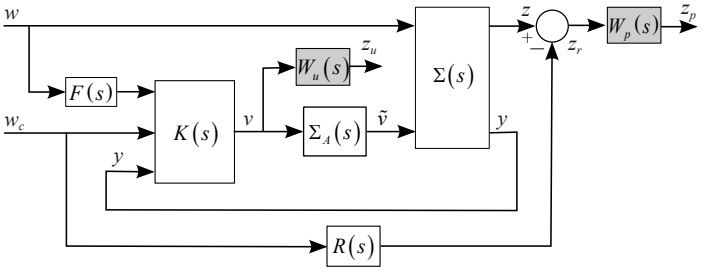

Figure 1 – H_∞ design-oriented scheme.

considering the linear interconnection of Figure 1, it is proposed to compute $K(s)$ as follows:

$$\hat{K}(s) = \underset{K(s)\in\mathcal{K}}{argmin} \left\| \mathcal{T}_{w_c \to z_p}(s) \right\|_\infty \tag{14}$$

with:

$$\begin{cases} \left\| \mathcal{T}_{w_c \to z_u}(s) \right\|_\infty \le \gamma_u \\ \left\| \mathcal{T}_{w \to z_p}(s) \right\|_\infty \le \gamma_r \end{cases} \tag{15}$$

The H_∞-norm minimization considered in (14) corresponds to the nominal tracking requirement. As is standard in H_∞ design approaches, a weighting function – typically a low-pass filter – $W_p(s)$ is introduced to specify the frequency domain where the tracking performance should be more efficient. Next, the second and third requirements are respectively taken into account by the additional two constraints in (15). The first one involves a high-pass weighting function $W_u(s)$ to minimize the control activity in the high-frequency domain. Finally, note the presence of a low-pass function denoted by $F(s)$, which can be viewed as an approximation of the estimation process ($\hat{w} \approx F(s)w$).

Problem (14)-(15) is a difficult non-convex and non-smooth optimization problem. However, it is now efficiently solved thanks to recent advances in non-smooth optimization techniques [3, 9]. Moreover, the structure of the controller as well as its order can also be fixed *a priori*, which makes the implementation easier. Last but not least, multiple models can be considered simultaneously during the design procedure. This flexibility will be used below to improve the robustness properties of our proposed design scheme.

Preliminary LTI Robustness Analysis

After an initial controller has been obtained as the solution of the above multi-objective design problem, closer attention is now paid to the validity of a few approximations that were made and their potential impact on the closed-loop behavior. More precisely, it is shown here how LTI robustness analysis tools (such as μ or skew-f bounds) can be used to detect potential difficulties induced by three main sources of uncertainties.

Plant uncertainties

When combining Equations (7) and (1) to obtain (8), it is assumed that both f and G are well known. However, in practice, uncertainties δ are always present so that Equation (8) is now written as:

$$\dot{x} = A(\delta)x + B(\delta)L_A(v) + w \tag{16}$$

where $\delta = \left[\delta_1 \dots \delta_l\right]^T \in \mathbb{R}^l$. Assuming that both A and B rationally depend on δ, it is then possible through an LFT modeling approach [14] to rewrite $\Sigma(s)$ as the following Linear Fractional Representation (LFR), as depicted in Figure 2:

$$\Sigma(s) = \mathcal{F}_u\left(M(s), \Delta_M\right) \tag{17}$$

where $\mathcal{F}_u(.)$ denotes the upper Linear Fractional Transformation (LFT), $M(s)$ is an LTI system and:

$$\Delta_M \in \Delta_M = \left\{ diag\left(\delta_1 I_{k_1}, \dots, \delta_l I_{k_l}\right), \delta_i \in \mathbb{R} \right\} \tag{18}$$

Actuator uncertainties

In Assumption 1, the commutative property (6) might not be valid in all cases. Following [5], it is then proposed to relax it as follows.

Assumption 2

There exist a nonlinear bounded operator $\Gamma(.)$ *and a positive bound* $k_\Gamma \in \mathbb{R}^+$ *such that* $\forall \upsilon(t) \in \mathbb{R}^m$*:*

$$L_A\left(\Lambda^{-1}\upsilon(t)\right) = \Lambda^{-1}L_A\left(\upsilon(t)\right) + \Gamma\left(\upsilon(t)\right) \tag{19}$$

$$\left\| \Gamma\left(\upsilon(t)\right) \right\| \le k_\Gamma \left\| \upsilon(t) \right\| \tag{20}$$

It results from Assumption 2 that the linear model $\Sigma_A(s)$ in Figure 1 should now be replaced by the nonlinear uncertain version $\Sigma_A(s) + \Gamma(.)$, as illustrated in Figure 2.

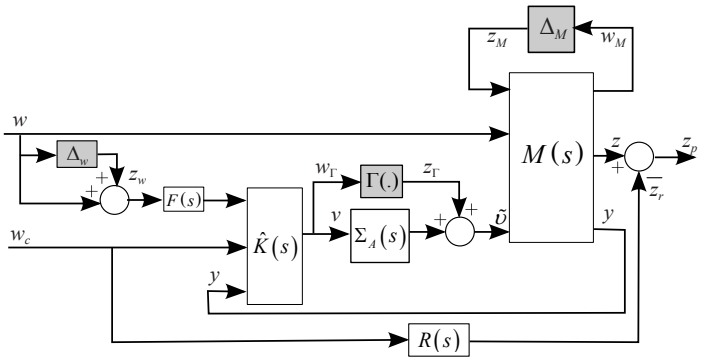

Figure 2 – Closed-loop scheme for LTI stability analysis.

Estimation uncertainties

Finally, one should notice that only an estimated $\hat{w}$ of the nonlinear input perturbations w is available to the outer-loop controller $\hat{K}(s)$. While this estimation process has been taken into account in the design phase through the approximation $\hat{w} \approx F(s)w$, it might be too optimistic in practice. A diagonal perturbation block Δ_w will then be considered to introduce some multiplicative uncertainties on the signal so that $\hat{w}$ is now transformed into $\left(I + \Delta_w\right)\hat{w}$. This is also visualized in the robustness analysis diagram in Figure 2.

As is usual in any standard LFT modeling process, the three uncertain blocks that have been described above are normalized, merged into a single block-diagonal operator $\Delta = diag\left(\Delta_M, \Gamma(.), \Delta_w\right)$ and pulled out to generate an augmented linear model $P(s)$. These operations are summarized in Figure 3. The APRICOT Library from the Matlab

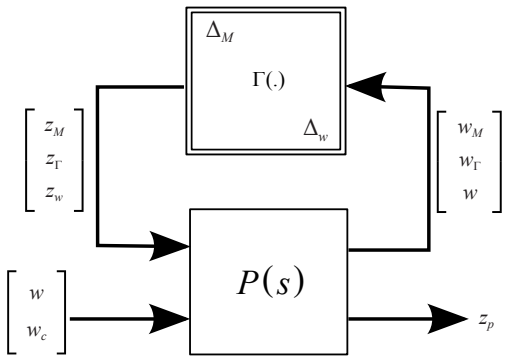

Figure 3 – LFT of the system for LTI robustness analysis.

Toolbox SMAC [22] can be used to generate such an LFT, from a set of LTI models.

Temporarily assuming that Δ is a time-invariant operator, μ or skew-μ analysis can be used to quantify, respectively, the stability and performance properties of the uncertain closed-loop depicted in Figure 3. Using the SMART Library from the Matlab Toolbox SMAC [22] allows bounds on the structured singular value [24] to be computed. Since Δ has been normalized, the system is said to be robustly stable to LTI perturbations if the μ upper-bound verifies $\overline{\mu} < 1$. Otherwise, a destabilizing worst-case perturbation Δ^* might exist such that $\overline{\sigma}(\Delta^*) < 1$.

Multi-model Design

Using the above robustness analysis results, two main ways exist to improve the initial controller $\hat{K}(s)$. Since it was designed within the H_∞ framework, a natural way consists in using a μ-synthesis approach. While this strategy, already implemented in MATLAB™ [26], works well in the case of complex-valued uncertainties, numerical difficulties are often reported with real-valued uncertain parameters. Moreover, results might be quite conservative in that case. For these reasons, the alternative path, consisting of a multi-model design approach, will be preferred next. First considered in [1], this intuitive approach leads to non-convex optimization problems. However, as has been already pointed out, it has regained interest recently thanks to the flexibility of non-smooth H_∞ optimization algorithms. The latter indeed offer new perspectives in this direction, since multiple models can be considered simultaneously. From this observation, a simple iterative algorithm can be proposed. Starting from a single-model design, the principle consists of analysis & multi-model design iterations. During the analysis step, worst-case configurations (associated with Δ^*) are isolated, in order to enrich the bank of models to be considered in the next design step. This is summarized below.

Algorithm 1
Robust multi-model design

1. Define a nominal configuration model $\Sigma_0(s)$ using the input linearizing inner-loop control law (7), leading to (8).

2. Set $i = 0$ and solve (14)-(15) to compute an initial controller $\hat{K}_0(s)$.

3. Perform LFT modeling & robustness analysis pursuant to previous Subsection. Extract a destabilizing perturbation Δ_i^*. If $\overline{\sigma}(\Delta_i^*) < 1$, then go to Step 4, otherwise go to Step 5.

4. Enrich the bank of models with Δ_i^*, set $i \leftarrow i+1$, compute $\hat{K}_i(s)$ via multi-model H_∞ design and return to Step 3.

5. Perform a final robustness analysis with μ upper-bound evaluation.

Remark 2
Unlike μ-synthesis based approaches, the above algorithm implements necessary conditions for robust stability with respect to LTI perturbations, which become sufficient if the μ upper-bound in Step 1) is less than 1.

Towards a Global Robustness Analysis

In the simplified robustness analysis approach of page 3, the nonlinear input signal w is considered as an external perturbation. Yet, considering Equations (8) and (9), it is clear that w may depend on x and θ_p in a quite complicated way. Consequently, robustness analysis becomes tricky in the most general case. Fortunately, with a good knowledge of the studied process, reasonably simpler approximations can be obtained in practice, such as:

$$w = H(\theta_p)x + W(x) \tag{21}$$

with the following assumptions:

- $H(.)$ is assumed to depend rationally on θ_p, and can thus be rewritten as an LFT.
- the nonlinear operator $W(x)$ satisfies Lipschitz conditions.

Hence, the LFT $F_u(P(s),\Delta)$ of Figure 3 – further denoted $F_u(\tilde{P}(s),\tilde{\Delta})$ – is modified to include additional blocks in $\tilde{\Delta}$ so that w will no longer appear as an external perturbation:

$$\tilde{\Delta} = diag\left(\Delta_M, \Gamma(.), \Delta_w, W(.), \Theta_p\right) \tag{22}$$

The extended uncertain operator $\tilde{\Delta}$ now clearly contains uncertainties Δ_M, Δ_w and time-varying parameters Θ_p as well as memoryless nonlinearities $\Gamma(.)$ and $W(.)$. Robustness analysis then must be performed with more general tools based, for example, on the IQC framework [16].

Application to longitudinal aircraft control design

The above robust nonlinear compensation framework is now applied to a longitudinal aircraft control problem. Note that the lateral motion is not yet considered, assuming a steady flat-wing aircraft with no sideslip. Lateral controller design will be described while global simulations with both combined motions will be presented.

Nonlinear Longitudinal Aircraft Model

The longitudinal motion of a civil aircraft can be described by the following 4-state model [7]:

$$\begin{cases} m\dot{V} &= -\overline{q}S\hat{C}_D(\alpha) - mg\sin\gamma + F\cos\alpha \\ mV\dot{\gamma} &= \overline{q}S\hat{C}_L(\alpha,q,V,\delta_e) - mg\cos\gamma + F\sin\alpha \\ J\dot{q} &= \overline{q}SL\hat{C}_m(\alpha,q,V,\delta_e) + z_e F \\ \dot{\theta} &= q \end{cases} \tag{23}$$

where V is the airspeed, γ is the flight path angle, q is the pitch rate, θ is the pitch angle, $\bar{q} = \frac{1}{2}\rho V^2$ is the dynamic pressure, J is the longitudinal inertia, m is the mass, S is the reference surface, L is the reference length (often taken as the half span), ρ is the air density, α is the angle of attack ($\alpha = \theta - \gamma$), F is the engine thrust on the longitudinal axis and z_e is the vertical shift between the position of the center of gravity and the thrust application point. The drag, lift and pitching coefficients $\hat{C}_D$, $\hat{C}_L$ and $\hat{C}_m$ can be expressed as follows:

$$\begin{aligned} \hat{C}_D(\alpha) &= C_{D0} + C_{D\alpha}\alpha + C_{D\alpha 2}\alpha^2 \\ \hat{C}_L(\alpha,q,V,\delta_e) &= \underbrace{C_{L0} + C_{L\alpha}\alpha + C_{Lq}\frac{q}{V}}_{\tilde{C}_L} + C_{L\delta_e}\delta_e \\ \hat{C}_m(\alpha,q,V,\delta_e) &= \underbrace{C_{m0} + C_{m\alpha}\alpha + C_{mq}L\frac{q}{V}}_{\tilde{C}_m} + C_{m\delta_e}\delta_e \end{aligned} \quad (24)$$

where δ_e is the elevator deflection angle and the C_{xy} are fixed aerodynamic coefficients, whose values can be obtained from the benchmark library of the SMAC Toolbox[1] and do not depend on the Mach number. Here $\xi = [V\ \gamma\ q\ \theta]^T$, $u = [F\ \delta_e]^T$ and $\theta_p = [m\ x_{cg}\ V_0]^T$, where x_{cg} is the center of gravity position and V_0 is the initial airspeed. The operating domain for a landing application is such that $V \in [60\ 90] m/s$, $m \in [123\ 180] tons$ and $x_{cg} \in [15\ 41]\%$, defining the admissible set Θ. F and δ_e follow the first-order actuator dynamics $\Sigma_A(s)$:

$$\Sigma_A(s) = \begin{pmatrix} \frac{1}{2s+1} & 0 \\ 0 & \frac{1}{0.07s+1} \end{pmatrix} \quad (25)$$

Remark 3

Using first-order models for the actuators is common practice in the aeronautical industry, and it is sufficiently representative here. However, rate limitations are neglected, but it would be possible to add an anti-windup controller to take them into account.

The aerodynamic coefficients can have up to 30% of multiplicative uncertainties. Using the notation of (1) and applying (5) from Assumption 1, (23) is rewritten the same way with:

$$f = \begin{pmatrix} \frac{-\bar{q}SC_D}{m} - g\sin\gamma \\ \frac{\bar{q}S\tilde{C}_L}{mV} - \frac{g}{V}\cos\gamma \\ \frac{\bar{q}SL}{J}\tilde{C}_m \\ q \end{pmatrix} \qquad B = \begin{pmatrix} 1 & 0 & 0 & 0 \\ 0 & 0 & 1 & 0 \end{pmatrix}^T$$

$$\Lambda = \begin{pmatrix} \frac{\cos\alpha}{m} & 0 \\ \frac{z_e}{J} & \frac{\bar{q}SL}{J}C_{m_{\delta_e}} \end{pmatrix} \qquad \Delta_G = \begin{pmatrix} 0 & 0 \\ \frac{\sin\alpha}{mV} & \frac{\bar{q}S}{mV}C_{L_{\delta_e}} \\ 0 & 0 \\ 0 & 0 \end{pmatrix}$$

Remark 4

Given the operating domain of the system, Λ is non-singular. Furthermore, Λ is slowly varying, since its dynamics mainly come from the dynamic pressure $\bar{q}$. These two conditions verify Assumption 1.

[1] http://w3.onera.fr/smac/

Remark 5

The choice of B was made based on the maximum control efficiency. Indeed, as is clear from (23), the thrust input F mainly affects the airspeed V, and the elevator deflection δ_e has a large impact on the pitch rate q.

The goal is to track the airspeed V and the flight path angle γ, and the state is assumed to be fully available to the controller, yielding $C = I$. The reference model $R(s)$ for the airspeed (1st order dynamics) and the flight path angle (3rd order dynamics) is given by:

$$R(s) = \begin{pmatrix} \frac{1}{6.5s+1} & 0 \\ 0 & \frac{0.35^2}{(2s+1)(s^2+2*0.7*0.35s+0.35^2)} \end{pmatrix} \quad (26)$$

Nonlinear Compensation Technique

Using the previous notation it is now possible to apply the method described in page 2. First applying the control input (7) leads to the linearized system (8). $\hat{\zeta}$ is chosen so that w_f only preserves the nonlinear terms on the flight path angle dynamics γ, canceling the nonlinear dynamics on V_a and q. The nominal configuration $\bar{\theta}_p$ is set for a mass of 150 tons, a center of gravity position at 21%, an initial airspeed of 70 m/s and an altitude of 300 m (landing configuration). This configuration is "central" in terms of the system pole location, ensuring that the other configurations are covered as much as possible when designing the robust controller. Choosing a worst-case configuration could also be a possibility, but the nominal performance is highly degraded in this case and the "opposite" worst-case configurations may be harder to control. According to the specifications of the robust nonlinear compensation technique; the frequency weightings $W_p(s)$ and $W_u(s)$ are chosen respectively as low-pass and high-pass filters:

$$W_p(s) = \begin{pmatrix} \frac{s/2+0.15}{s+1.5\times10^{-4}} & 0 \\ 0 & \frac{s/20+0.40}{s+4\times10^{-4}} \end{pmatrix} \quad (27)$$

$$W_u(s) = \begin{pmatrix} \frac{s+2}{0.001s+20} & 0 \\ 0 & \frac{s+0.2}{0.001s+2} \end{pmatrix} \quad (28)$$

The filter $F(s)$ is such that:

$$F(s) = \begin{pmatrix} \frac{0.1}{2s+1} & 0 & 0 & 0 \\ 0 & \frac{1}{2s+1} & 0 & 0 \\ 0 & 0 & \frac{0.1}{2s+1} & 0 \\ 0 & 0 & 0 & 0 \end{pmatrix} \quad (29)$$

The second term in (29) on the diagonal is higher than the others, since it is not compensated by the input signal $\hat{\zeta}$ (which only compensates for the first and the third nonlinear terms). This enables the controller to focus more on this one than on the others. The last term is 0 since the last equation in (23) does not contain any nonlinear terms.

A third-order controller is chosen, since it offers a good compromise between the achievable performance and a preferable low-order controller for easier implementation. Solving the multi-objective H_∞ minimization problem (14)-(15) with the routine hinfstruct of the Robust Control Toolbox for Matlab [3] yields an H_∞-norm of $\gamma_\infty = 0.9653$ after a few iterations, thus insuring that the frequency-domain

specifications are fulfilled. Nonlinear simulations are performed with the obtained initial controller $\hat{K}_0(s)$, and the corresponding results are depicted in Figure 4 and Figure 5.

In Figure 4, the aircraft responses to a 3 degree step demand on the flight path angle γ are visualized for various configurations of mass $\in \{120,150,180\}$ tons, initial airspeed $V \in \{60,70,80\}$ m/s, and center-of-gravity locations $x_{cg} \in \{15,20,40\}$%.

Similarly, the responses to a 3 m/s variation step demand on the longitudinal airspeed V are shown in Figure 5. In both cases, the dashed red plots correspond to the reference signals to be tracked.

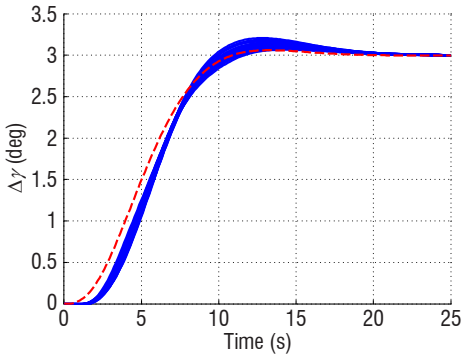

(a) Flight path angle vs. time

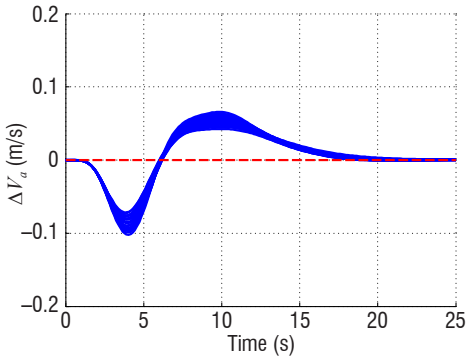

(b) Airspeed vs. time

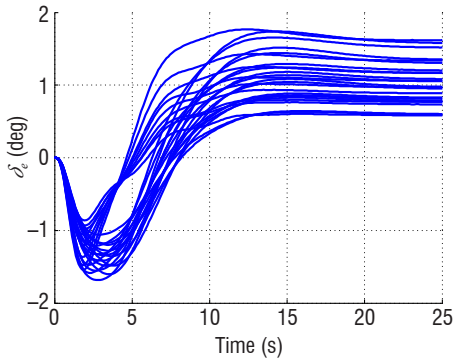

(c) Elevator deflection vs. time

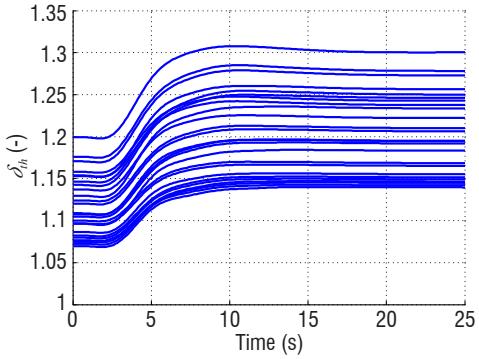

(d) Thrust factor vs. time

Figure 4 – Nonlinear Simulations with a 3° step on γ, for different initial aircraft configurations and no aerodynamic coefficient uncertainties, with the initial controller $\hat{K}_0(s)$.

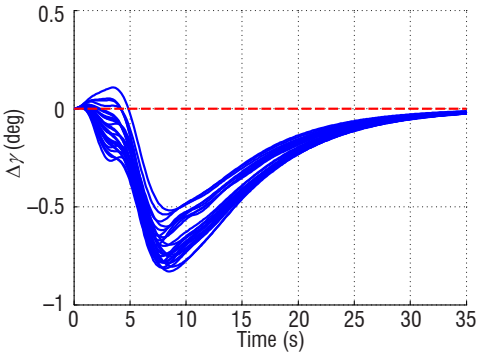

(a) Flight path angle vs. time

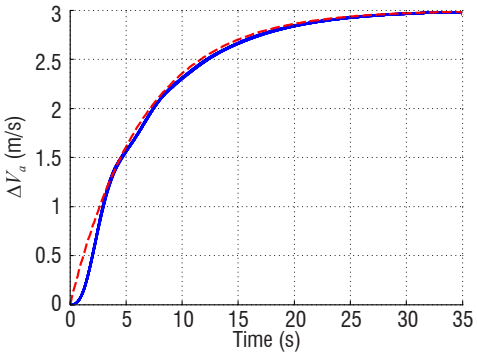

(b) Airspeed vs. time

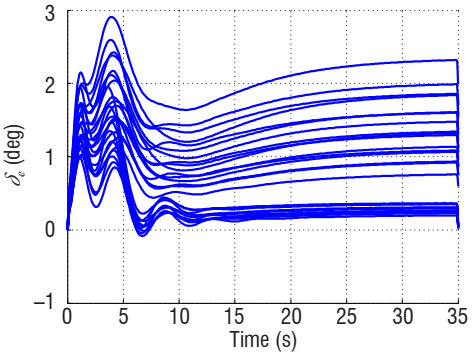

(c) Elevator deflection vs. time

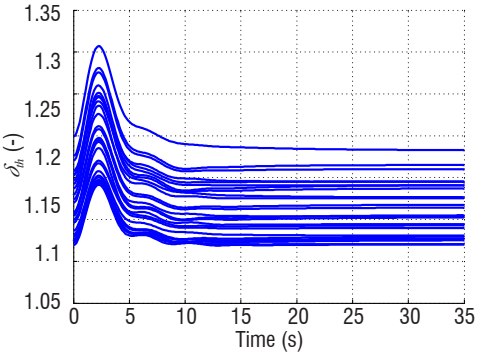

(d) Thrust factor vs. time

Figure 5 – Nonlinear Simulations with a 3 m/s step on V, for different initial aircraft configurations and no aerodynamic coefficient uncertainties, with the initial controller $\hat{K}_0(s)$.

Both simulations prove the effectiveness of the robust nonlinear compensation scheme with regard to performance and robustness properties. The flight domain is indeed very large thanks to the nonlinear compensation part of the controller being aimed at maintaining as much as possible the nominal performance. The controller manages to follow the reference models quite well, while also ensuring a good decoupling. Note however that no uncertainties in the aerodynamic coefficients have been considered yet. These will have significant impact on the performance and stability of the system, as will be shown in the next section dealing with robust stability analysis.

Robustness analysis and multi-model design

The above controller $\hat{K}_0(s)$ has been designed to cope with a large operating domain under nominal conditions. The uncertain operators represented by "gray boxes" in Figure 2 have thus not been considered yet. The objective of this section is twofold. First, the effects of the aforementioned uncertainties are studied within the LTI frameworks with the help of μ-analysis tools. Next, the identified worst cases are used in a multi-model design strategy detailed in Algorithm 1 to improve the robustness properties of the initial controller.

LTI modeling and μ-analysis

LFT modeling is a key step in our robustness analysis process. Starting from the set of nonlinear equations (23), parametric uncertainties are first introduced in the aerodynamic coefficients:

$$C_D = \left(1+\delta_{C_D}\right)\hat{C}_D$$

$$C_L = \left(1+\delta_{C_L}\right)\hat{C}_L$$

$$C_m = \left(1+\delta_{C_m}\right)\hat{C}_m$$

and variations are also introduced in the airspeed V, mass m and center of gravity location: $V = V_0 + \delta_V$, $m = m_0 + \delta_m$, $x_{cg} = x_{cg_0} + \delta_{x_{cg}}$. Next, the equations are linearized so that a bank of parameter-dependent linear models, as described in (16), is obtained. From this continuous set, a low-order LFT model $\mathcal{F}_u\left(M(s),\Delta_M\right)$ (see Eq. (17)) is rather easily obtained with the help of the most recent algorithms implemented in the APRICOT Library of the SMAC Toolbox [23]. These algorithms, using orthogonal least square techniques, are based on low-order polynomial interpolation methods. For this application the size of the Δ_M-block is kept reasonably low:

$$\Delta_M = \mathrm{diag}\left(\delta_V I_6, \delta_{C_D} I_2, \delta_{C_L} I_3, \delta_{C_m} I_2, \delta_m I_1, \delta_{x_{cg}} I_1\right) \in \mathbb{R}^{15\times 15}$$

As a result, the size of the global Δ-block including $\Gamma(.)$ and Δ_w (see Figure 3) verifies:

$$\Delta = \mathrm{diag}\left(\Delta_M, \Delta_w, \Delta_\Gamma\right) \in \mathbb{R}^{20\times 20}$$

A normalization step is finally applied so that variations of Δ in the unit ball induce 30% uncertainties in the aerodynamic coefficients, and 30% variations in Δ_w and Δ_Γ. Note that this last step is easily achieved with the LFT modeling library available in the SMAC Toolbox. Based on this normalized LFT object, both upper and lower bounds of the structured singular value μ are evaluated with the SMART Library of the SMAC Toolbox. With the nominal controller $\hat{K}_0(s)$, a lower-bound $\underline{\mu}_\Delta > 1$ is found together with its corresponding worst-case configuration Δ_1^* such that $\bar{\sigma}\left(\Delta_1^*\right) = \underline{\mu}_\Delta^{-1} < 1$.

Multi-model design

Following step 4 of Algorithm 1, Δ_1^* is used to initialize our multi-model design procedure. Note that this case corresponds to a retracted position of the center of gravity, maximum weight and high values of the aerodynamic coefficient uncertainties. After 5 more iterations, a new controller $\hat{K}(s)$ is obtained that significantly improves the worst-case configuration. For this controller one indeed obtains $\underline{\mu}_\Delta < 1$. However, using standard algorithms, the upper-bound $\bar{\mu}_\Delta$ remains above 1, which does not make it possible to conclude on stability. Refined versions of the algorithm using branch-and-bound techniques [17], now available in the SMART Library, are then used, which greatly improves the accuracy of the upper-bound. One eventually obtains $\bar{\mu}_\Delta < 1$, as is summarized in Table 1.

Controller	Lower-bound $\underline{\mu}_\Delta$	Upper-bound $\bar{\mu}_\Delta$
Nominal – DG-scaling	1.4610	1.5110
Multi-model – DG-scaling	0.8957	1.0780
Multi-model – branch-and-bound	0.8999	0.9449

Table 1 – Values of the μ-bounds for the nominal and multi-model controllers. The computations for the multi-model controller are made using the initial DG-scaling method and the improved branch-and-bound algorithm.

Time-domain evaluation

To conclude this section, a few nonlinear simulations are performed with the above multi-model based controller. The flight path angle (γ) and airspeed (V) step demands are first applied for various aircraft configurations without uncertainties. The results, to be compared with those obtained with the nominal controller, are displayed in Figures 6 and 7.

As expected, the decoupling is a bit degraded and the responses are slightly slower but major improvements will be shown in the presence of uncertainties.

Let us now introduce 25% uncertainties in the aerodynamic coefficients (not 30%, so that the nominal controller is not completely unstable). The aircraft responses to a step demand on γ are visualized in Figure 8. The left subplot (Figure 8a) reveals poor robustness properties of the nominal controller, while significant improvements are clearly observed on the right subplot (Figure 8b) with the multi-model controller. This clearly demonstrates the efficiency of the proposed methodology.

Application to lateral aircraft control design

Now that the method has been successfully applied on the longitudinal part of the aircraft, the lateral part will be dealt with using the exact same strategy as explained below.

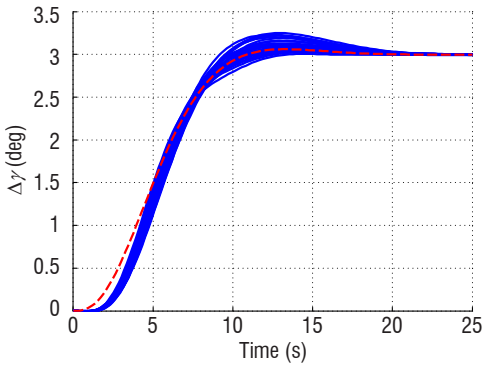

(a) Flight path angle vs. time

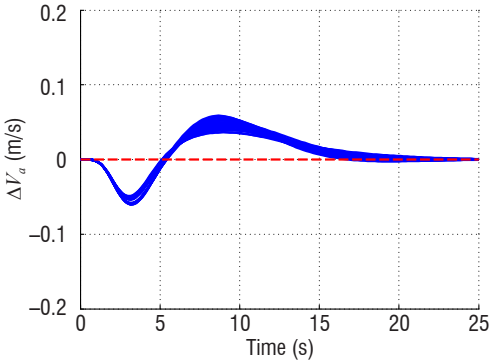

(b) Airspeed vs. time

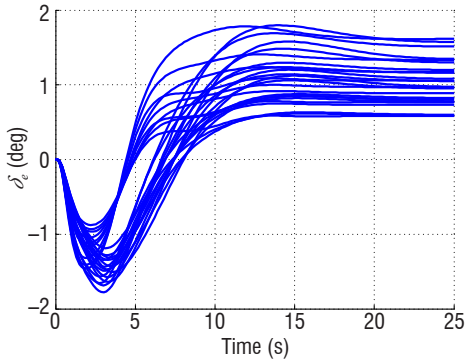

(c) Elevator deflection vs. time

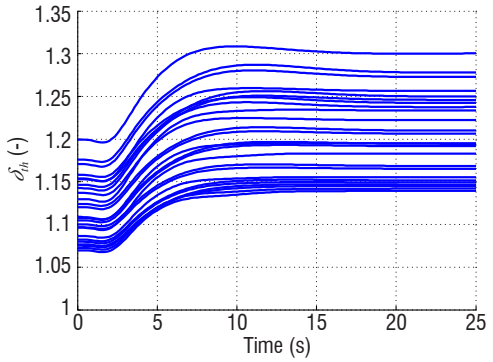

(d) Thrust factor vs. time

Figure 6 – Nonlinear Simulations with a 3° step on γ, for different initial aircraft configurations and no aerodynamic coefficient uncertainties, with the multi-model controller $\hat{K}(s)$.

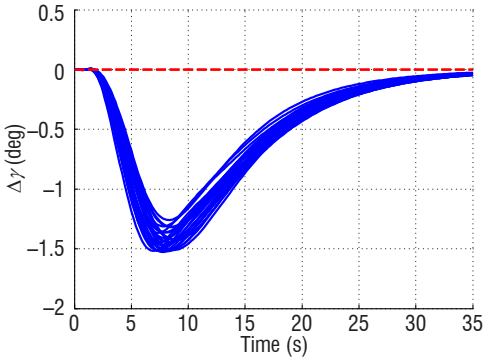

(a) Flight path angle vs. time

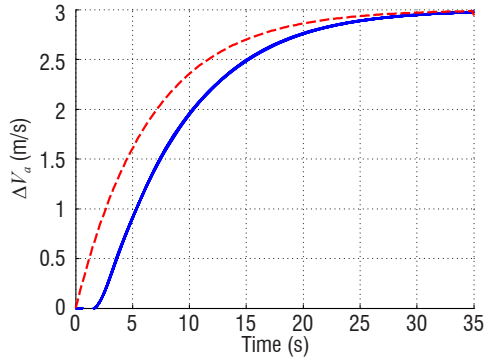

(b) Airspeed vs. time

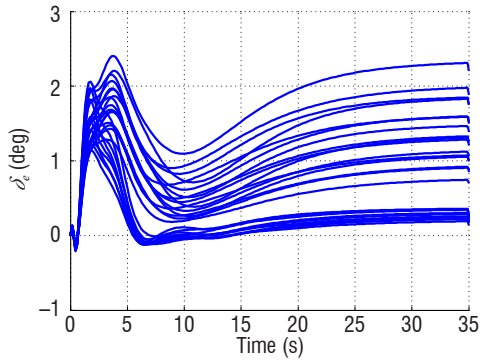

(c) Elevator deflection vs. time

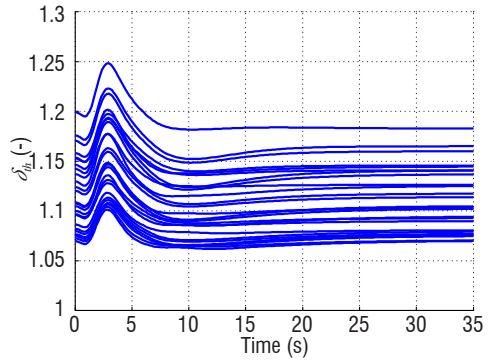

(d) Thrust factor vs. time

Figure 7 – Nonlinear Simulations with a 3 m/s step on V, for different initial aircraft configurations and no aerodynamic coefficient uncertainties, with the multi-model controller $\hat{K}(s)$.

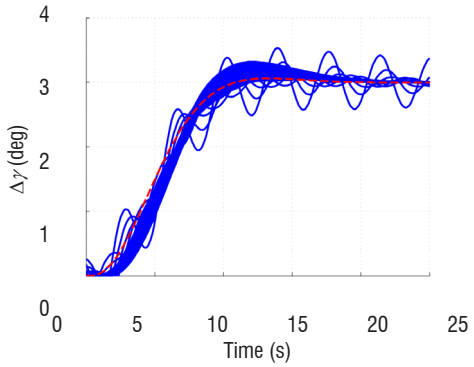

(a) γ step responses for the nominal controller

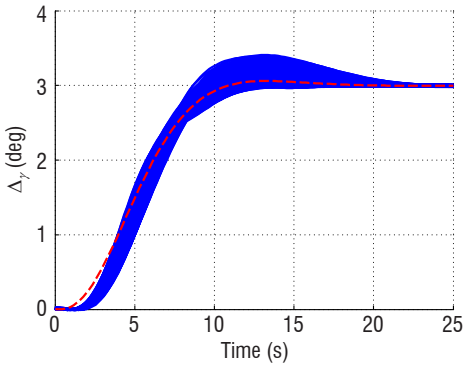

(b) γ step responses for the multi-model controller.

Figure 8 – Comparison between the nominal controller $\hat{K}_0(s)$ (a) and the multi-model controller $\hat{K}(s)$ (b) for all admissible configurations with ±25% of uncertainties: γ step responses versus time.

Nonlinear Lateral Aircraft Model

The lateral motion of a civil aircraft can be described by the following 4-state model [7]:

$$\begin{cases} mV\dot{\beta} &= mV\left(p\sin\alpha - r\cos\alpha\right) + mg\left(\sin\theta\cos\alpha\sin\beta \right. \\ &\quad + \cos\theta\sin\phi\cos\beta - \cos\theta\sin\alpha\cos\phi\sin\beta \\ &\quad \left. + \bar{q}S\hat{C}_Y - F\sin\beta\cos\alpha \right. \\ \dot{\phi} &= p + \tan\theta\left(q\sin\phi + r\cos\phi\right) \\ I_{zz}\dot{r} &= \bar{q}SL\hat{C}_n + \left(I_{xx} - I_{yy}\right)pq \\ I_{xx}\dot{p} &= \bar{q}SL\hat{C}_l + \left(I_{yy} - I_{zz}\right)rq \end{cases} \tag{30}$$

where β and ϕ are, respectively, the sideslip and roll angles, p and r are the roll and yaw rates, and I_{xx} and I_{zz} are the inertias along the x-body and z-body axes. The side force, roll and yaw coefficients $\hat{C}_Y$, $\hat{C}_l$ and $\hat{C}_n$ are expressed as follows:

$$\begin{aligned} \hat{C}_Y &= \underbrace{C_{Y_\beta}\beta}_{\tilde{C}_Y} + C_{Y_r}\delta_r \\ \hat{C}_l &= \underbrace{C_{l_\beta}\beta + \frac{L}{V}\left(C_{l_p}p + \left(C_{l_{r_0}} + C_{l_{r_\alpha}}\alpha\right)r\right)}_{\tilde{C}_l} + C_{l_{\delta_a}}\delta_a + C_{l_{\delta_r}}\delta_r \\ \hat{C}_n &= \underbrace{(C_{n_{\beta_0}} + C_{n_{\delta_\alpha}})\beta + \frac{L}{V}\left(C_{n_r}r + (C_{n_{p0}} + C_{n_{p\alpha}}\alpha)p\right)}_{\tilde{C}_n} \\ &\quad + C_{n_{\delta_a}}\delta_a + C_{n_{\delta_r}}\delta_r \end{aligned} \tag{31}$$

where δ_a and δ_r are the aileron and rudder deflection angles, and the C_{xy} are aerodynamic coefficients specific to the given aircraft. Using similar notations to those used in the longitudinal case, let us define: $\xi = [\beta\ \phi\ r\ p]^T$, $u = [\delta_a\ \delta_r]^T$ and $\theta_p = [m\ x_{cg}\ V_0]^T$. δ_a and δ_r follow the first-order actuator dynamics $\Sigma_A(s)$:

$$\Sigma_A(s) = \begin{pmatrix} \frac{1}{0.06s+1} & 0 \\ 0 & \frac{1}{0.2s+1} \end{pmatrix} \tag{32}$$

Using the notation of (1) and applying (5) from Assumption 1, (23) is rewritten in the same way with:

$$\Lambda = \begin{pmatrix} \frac{\bar{q}SL}{I_{zz}}C_{n_{\delta_a}} & \frac{\bar{q}SL}{I_{zz}}C_{n_{\delta_r}} \\ \frac{\bar{q}SL}{I_{xx}}C_{l_{\delta_a}} & \frac{\bar{q}SL}{I_{xx}}C_{l_{\delta_r}} \end{pmatrix}$$

$$\Delta_G = \begin{pmatrix} 0 & \frac{\bar{q}S}{mV}C_{Y_r} \\ 0 & 0 \\ 0 & 0 \\ 0 & 0 \end{pmatrix}$$

$$f = \begin{pmatrix} p\sin\alpha - r\cos\alpha + \frac{g}{V}(\sin\theta\cos\alpha\sin\beta + \cos\theta\sin\phi\cos\beta - \cos\theta\sin\alpha\cos\phi\sin\beta) + \frac{\bar{q}S}{mV}\tilde{C}_Y - \frac{F}{V}\sin\beta\cos\alpha \\ p + \tan\theta\left(q\sin\phi + r\cos\phi\right) \\ \frac{\bar{q}SL}{I_{zz}}\tilde{C}_n + \frac{I_{xx} - I_{yy}}{I_{zz}}pq \\ \frac{\bar{q}SL}{I_{xx}}\tilde{C}_l + \frac{I_{yy} - I_{zz}}{I_{xx}}rq \end{pmatrix}$$

$$B = \begin{pmatrix} 0 & 0 & 1 & 0 \\ 0 & 0 & 0 & 1 \end{pmatrix}^T$$

The goal is to track the roll and sideslip angles ϕ and β, respectively. The reference model $R(s)$ is given by:

$$R(s)=\begin{pmatrix} \frac{1}{\frac{s^2}{0.80^2}+\frac{2*0.75}{0.80}s+1} & 0 \\ 0 & \frac{1}{\frac{s^2}{0.75^2}+\frac{2*0.75}{0.75}s+1} \end{pmatrix} \quad (33)$$

Remark 6

Note that some longitudinal state variables are present in the lateral dynamics equations. For the computation of the lateral controller it will be assumed that these variables maintain a predefined equilibrium. The simulations will be performed on the full model with the previous satisfactory longitudinal controller, in order to maintain the longitudinal equilibrium despite the lateral motion.

Lateral Controller Design

The same method as for the computation of the longitudinal controller is used here (some details will be omitted). The nominal configuration $\overline{\theta}_p$ is the same as before. For the lateral case, the frequency weightings used for the H_∞-design procedure $W_p(s)$ and $W_u(s)$ are chosen respectively as:

$$W_p(s)=\begin{pmatrix} \frac{s/5+2.5}{s+2.5\times10^{-3}} & 0 \\ 0 & \frac{s/5+1}{s+1\times10^{-3}} \end{pmatrix} \quad (34)$$

$$W_u(s)=\begin{pmatrix} \frac{s+2}{0.001s+20} & 0 \\ 0 & \frac{s+0.5}{0.001s+5} \end{pmatrix} \quad (35)$$

The filter $F(s)$ is such that: (see the explanations for the choice of (29) for a better understanding)

$$F(s)=\begin{pmatrix} \frac{1}{s+1} & 0 & 0 & 0 \\ 0 & \frac{1}{s+1} & 0 & 0 \\ 0 & 0 & \frac{0.02}{s+1} & 0 \\ 0 & 0 & 0 & \frac{0.02}{s+1} \end{pmatrix} \quad (36)$$

For the same reasons as for the longitudinal controller, a second-order controller is chosen. Solving the multi-objective H_∞ minimization problem (14)-(15) with the routine hinfstruct of the Robust Control Toolbox for Matlab [3] yields a H_∞-norm $\gamma_\infty = 1.03$ after a few iterations. The stability of the closed-loop system with the initial "nominal" controller $\hat{K}_0(s)$ is checked. Using the same strategy as for the longitudinal case, an LFT is computed yielding a "Δ-block" of dimension 24 x 24. Then, both the upper and the lower bounds of the structured singular value μ are evaluated yielding $\mu_\Delta \in [1.007\ 1.118]$ which does not prove stability. Following Algorithm 1, after 3 iterations, the final controller $\hat{K}(s)$ greatly improves the worst-case stability since now $\mu_\Delta \in [0.7948\ 0.8845]$ which proves stability with respect to LTI uncertainties. Note that, unlike the longitudinal case, no branch-and-bound techniques were needed here to reduce the gap between the lower and upper bounds.

Simulations were run for various initial configurations (different values of θ_p) and with $\pm 30\%$ uncertainties on the lateral aerodynamic coefficients (729 runs were executed). As expected, the lateral multi-model controller performs very well as shown in Figures 9

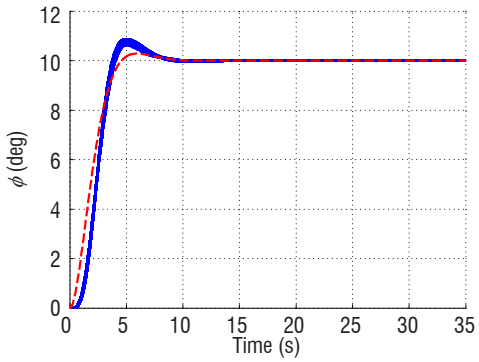

(a) Roll angle vs. time

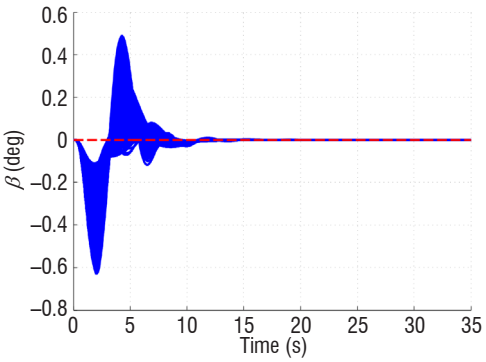

(b) Sideslip angle vs. time

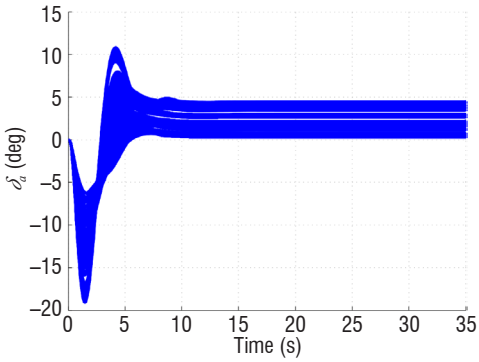

(c) Ailerons deflection vs. time

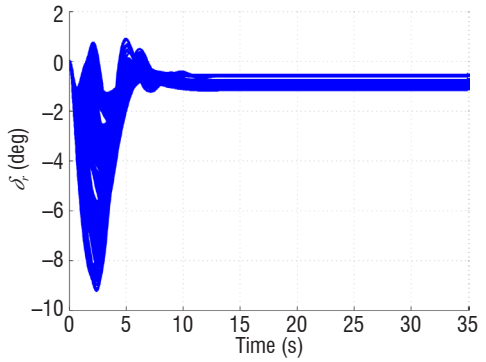

(d) Rudder deflection vs. time

Figure 9 – Nonlinear Simulations with a 10 deg step on ϕ, for various initial aircraft configurations and $\pm 30\%$ aerodynamic coefficient uncertainties, with the lateral multi-model controller 10.

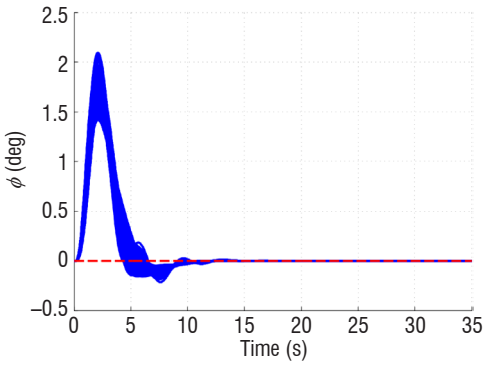

(a) Roll angle vs. time

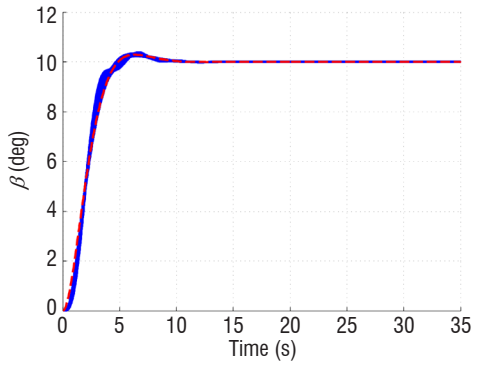

(b) Sideslip angle vs. time

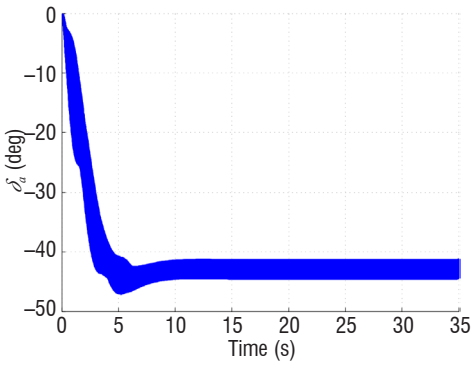

(c) Ailerons deflection vs. time

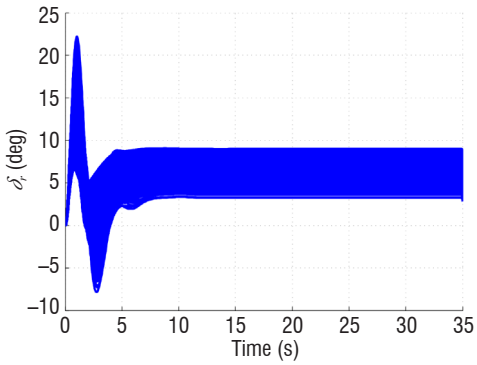

(d) Rudder deflection vs. time

Figure 10 – Nonlinear Simulations with a 10 deg step on β, for various initial aircraft configurations and ±30% aerodynamic coefficient uncertainties, with the lateral multi-model controller $\hat{K}(s)$.

and 10, where respectively the references of the roll and sideslip angles ϕ and β (red dashed line) are well tracked with reasonable control inputs δ_a and δ_r. Furthermore, no sign of even slight instability is present and the decoupling is greatly ensured.

Global application: aircraft landing

Finally, the longitudinal and lateral controllers are tested on a realistic landing application. The Instrument Landing System (ILS) allows the aircraft to operate and automatically land despite difficult weather conditions (e.g., restricted visibility). It is composed of ground-based signal transmitters and on-board receiving equipment. The ground-based equipment, located at the edges of the runway, comprises localizer and glide path radio transmitters and some marker beacons. On board, the receivers allow the emitted radio signals to be processed.

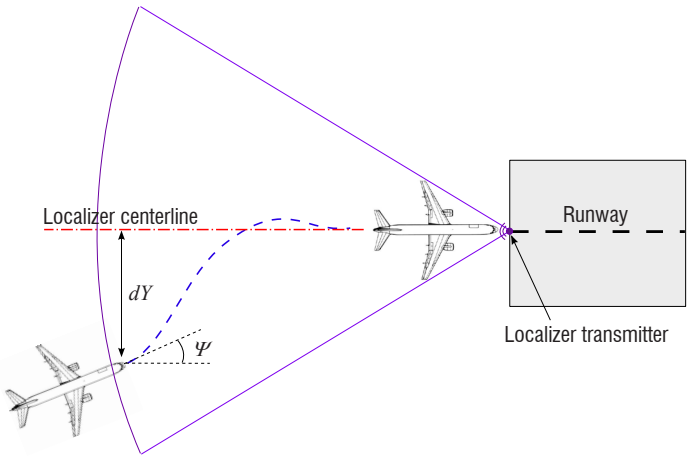

Figure 11 – The localizer beam system for aircraft lateral deviation adjustment.

The glide and localizer signals are the ones of interest for performing an automatic landing. They both allow the position of the aircraft relative to the ideal trajectory for landing to be known. Thus, a guidance control law can be designed so that the aircraft trajectory follows the centerline of the runway with a nominal descent path angle of $\gamma_{nom} = -3$ degrees. The lateral deviation is given by the localizer beam, while the longitudinal deviation is given by the glide beam. Figures 11 and 12 present the principles. Further details on autoland can be found in [13].

The aim is thus to track the glide and localizer signals and to perform the landing, via the addition of simple guidance outer loops which provide necessary inputs orders to the controller. The aircraft must hit the ground with a vertical speed $V_z = [2-3]$ ft/s not further than 500 meters after the runway threshold. Furthermore, if a lateral wind is blowing the aircraft must be able to have a final azimuth angle Ψ of 0° without being out of the axis of the runway during the process.

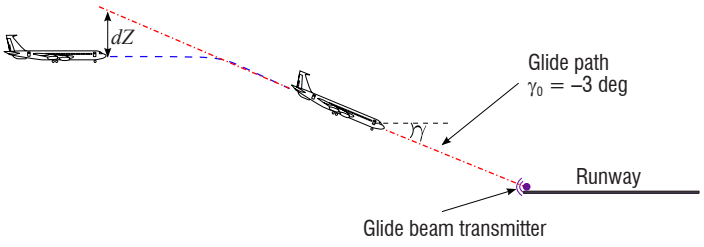

Figure 12 – The glide beam system for aircraft longitudinal deviation adjustment.

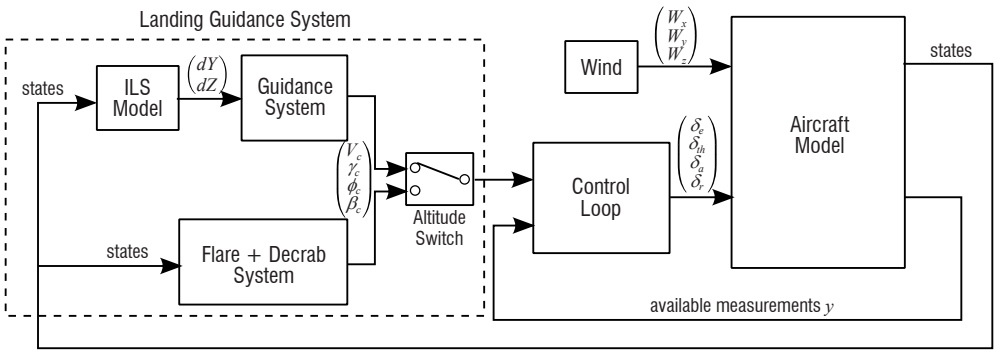

Figure 13 – Guidance and control for landing scheme.

These challenging goals will be verified by running many simulations on the full nonlinear model with, as before, model uncertainties, different initial conditions and wind.

Guidance system

Thanks to an ILS model block the vertical and lateral shifts dZ and dY respectively between the actual position of the aircraft and the glide and localizer signals are recovered. PID controllers, which have as inputs dZ and dY, have been designed to provide the longitudinal and lateral controllers with the necessary values of γ_c and ϕ_c to cancel these shifts. The design is not detailed in the paper, since it really consists of classical design techniques (linearization of the plant from dZ and dY to the controller inputs γ_c and ϕ_c, and PID design from frequency domain specifications). The nominal airspeed will be kept constant ($V = 70$ m/s). The general principle of the landing guidance + control system is given in Figure 13. Note that the flare + decrab control system block will be described in the following subsection.

Flare and decrab phases

Just before landing, thanks to the ILS guidance detailed above, the aircraft should fly with a fixed airspeed of –3° m/s, a flight path angle of –3° and be aligned with the runway. The objective of the flare control system, usually activated at 50 ft (15 m) above ground consists in generating an appropriate slope angle γ_c to be tracked so that the vertical speed at touchdown approaches 2.5 ft/s (0.75 m/s) and the aircraft hits the ground 400 m after the runway threshold. In order to do so, a corresponding trajectory $h(x)$ is determined using some geometric considerations and γ_c is given in real time using the following relation:

$$\dot{h}\left(x(t)\right) = \frac{dh(x)}{dx} V_{gr}(t) = -V(t)\sin\left(\gamma_c(t)\right)$$

(where V_{gr} is the ground speed). The procedure is shown in Figure 14.

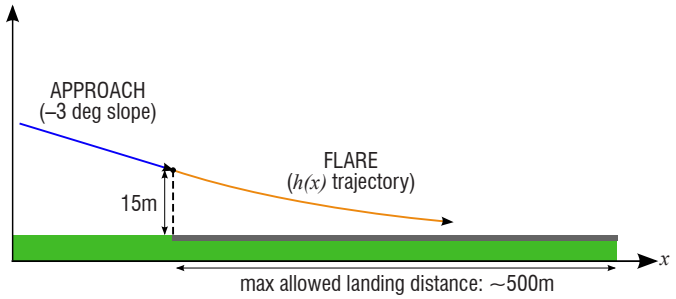

Figure 14 – Trajectory scheme for the flare procedure.

The decrab or align phase, usually activated at 30 ft above the runway, is aimed at setting the azimuth angle Ψ to zero (relative to the azimuth angle of the runway) so that the fuselage is aligned with the runway axis at touchdown. This phase is essential in case of cross wind. It is realized by a PID controller that delivers the appropriate sideslip angle β_c to be tracked as a function of Ψ.

Results

Complete landing simulations, including the flare and decrab phases, are successfully run for different initial conditions with regard to mass, center of gravity position, uncertainties and initial flight path angles. These are shown in Figure 15. Two lateral wind gusts are generated at 35 sec and 55 sec. Arriving above the runway, the azimuth angle is brought back to 0° using the rudder inputs (see Figure 15d). One can check that during this procedure the aircraft does not shift out of the runway when landing (see Figure 15a), and that the wings stay in an horizontal position (Figure 15c). Finally, after having properly recovered the glide reference slope, the flare procedure allows the aircraft to land at around 400 m after the threshold (Figure 15b), while bringing the flight path angle to the proper value allowing the vertical air speed (Figure 15e) to be kept within.

Table 2 summarizes the landing minimum, maximum and mean values for the final azimuth angles ψ, vertical speeds V_z, pitch angles θ, pitch rates X_l and landing distances X_l obtained for every simulation, in order to check whether the landing requirements are met. The main difficult variable to control was the pitch rate q which is not positive but still near 0 deg/s. The other values are within an acceptable range with regard to the mean value and also the standard deviation is not higher than the limits, which shows that the whole method (controller synthesis, guidance laws and flare+decrab laws) is clearly robust to uncertainties and allows a proper landing to be performed under many flight conditions. There are a few extreme condition cases (especially for a maximum amount of uncertainties) for which the objectives are slightly exceeded, but this is not critical (the aircraft still lands safely).

Parameters	min	max	mean	standard deviation	objectives
Azimuth angle Ψ (deg)	–1.06	0.59	0.01	0.32	0±1
Vertical speed V_z (ft/s)	0.88	4.46	2.33	0.82	2.5±1
Pitch angle θ (deg)	–2.81	13.01	3.95	4.19	>0
Pitch rate q (deg/s)	–0.73	0.25	–0.25	0.26	>0
Landing distance X_l (m)	190	567	393	115	$0 < X_l < 500$

Table 2 – Final minimum/maximum/mean values for the relevant landing parameters considering all of the simulations.

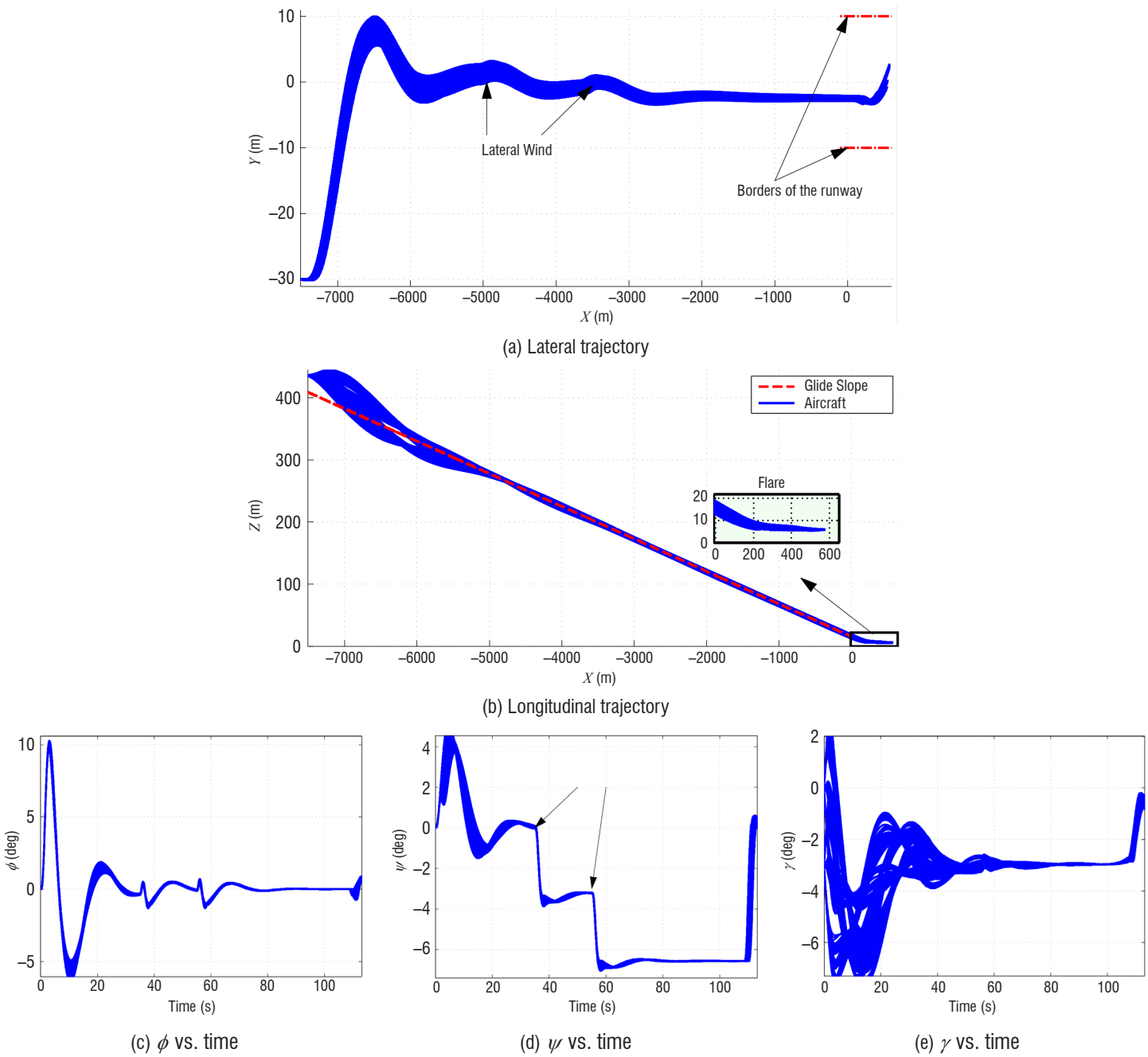

(a) Lateral trajectory

(b) Longitudinal trajectory

(c) ϕ vs. time

(d) ψ vs. time

(e) γ vs. time

Figure 15 – Complete landing simulations in the presence of lateral wind, for various initial aircraft configurations.

Conclusion

Inspired by dynamic inversion techniques, an original methodology is proposed in this paper to design nonlinear controllers over possibly large flight envelopes. The procedure combines a partial feedback linearization of the plant with a fixed-structure multi-model H_∞ design technique. Our methodology also includes a preliminary μ-based validation phase, during which worst-case models are obtained and then used to enrich the set of design models. Finally, a global nonlinear robustness analysis strategy is briefly sketched and the paper concludes with a detailed application of the methodology to a realistic aircraft landing problem. Future work will be devoted to further improvements of the design strategy and its application to a small autonomous aircraft, including flight tests ■

References

[1] J. ACKERMANN - *Multi-Model Approaches to Robust Control System Design*. Uncertainty and Control. Vol. 70 of Lecture Notes in Control and Information Sciences. Springer Berlin Heidelberg, p. 108-130, 1985.

[2] R. ADAMS, S. BANDA - *Robust Flight Control Design Using Dynamic Inversion and Structured Singular Value Synthesis.* IEEE Transactions on Control Systems Technology 1 (2), p. 80-92, 1993.

[3] P. APKARIAN, D. NOLL - *Non-Smooth H_∞ Synthesis*. IEEE Transactions on Automatic Control 51 (1), p. 71-86, 2006.

[4] J.-M. BIANNIC, L. BURLION, H. DE PLINVAL - *Robust Control Design Over Large Flight Envelopes: A Promising Approach for Aerial Robotics*. Issue 8 of the AerospaceLab Journal. http://www.aerospacelab-journal.org/aerial-robotics, 2014.

[5] J.-M. BIANNIC, L. BURLION, S. TARBOURIECH, G. GARCIA - *On Dynamic Inversion with Rate Limitations*. Proceedings of the American Control Conference. Montreal, QC, p. 191-196, 2012.

[6] Z. BING-YU, M. BLAISE - *Robustness Analysis of Dynamic Inversion Control Laws Applied to Nonlinear Aircraft Pitch-Axis Models*. Nonlinear Analysis Theory, Methods and applications 32 (4), p. 501-532, 1998.

[7] J.-L. BOIFFIER - *The Dynamics of Flight: The Equations*. Dynamics of Flight Series. Wiley, 1998.

[8] A. FRANCO, H. BOURLÈS, E. D. PIERI, H. GUILLARD - *Robust Nonlinear Control Associating Robust Feedback Linearization and H_∞ Control*. IEEE Transactions on Automatic Control 51 (7), p. 1200-1207, 2006.

[9] S. GUMUSSOY, M. OVERTON - *Fixed-Order H_∞ Controller Design via HIFOO, a Specialized Non-Smooth Optimization Package*. Proceedings of the American Control Conference. Seattle, USA, p. 2750-2754, 2008.

[10] A. ISIDORI - *Nonlinear Control Systems.* Vol. 1 of Communications and Control Engineering. Springer, 1995.

[11] M. KARA MOHAMED, A. LANZON - *Design and Control of Novel Tri-Rotor UAV.* Proceedings of the 2012 UKACC International Conference on Control. Cardiff, Wales, p. 304-309, 2012.

[12] M. KARA MOHAMED, A. LANZON - *Effect of Unmodelled Actuator Dynamics on Feedback Linearized Systems and a Two Stage Feedback Linearization Method*. Proceedings of the 52nd IEEE Conference on Decision and Control. Florence, Italy, p. 841-846, 2013.

[13] G. LOOYE, H.-D. JOOS - *Design of Autoland Controller Functions with Multi-Objective Optimization*. Journal of Guidance, Control and Dynamics 29 (2), p. 475-484, 2006.

[14] J.-F. MAGNI - *Linear Fractional Representation Toolbox for Use with Matlab.* Tech. rep., ONERA, report and software available at http://w3.onera.fr/smac/, 2006.

[15] A. MARCOS, G. BALAS - *Development of Linear-Parameter-Varying Models for Aircraft*. Journal of Guidance, Control and Dynamics 27 (2), p. 218-228, 2004.

[16] A. MEGRETSKI, A. RANTZER - *System Analysis via Integral Quadratic Constraints*. IEEE Transactions on Automatic Control 42 (6), p. 819-830, 1997.

[17] M. NEWLIN, P. YOUNG - *Mixed μ Problems and Branch and Bound Techniques*. International Journal of Robust and Nonlinear Control 7 (2), p. 145-164, February 1997.

[18] C. PAPAGEORGIOU, K. GLOVER -*Robustness Analysis of Nonlinear Dynamic Inversion Control Laws with Application to Flight Control.* Proceedings of the 43rd IEEE Conference on Decision and Control. Vol. 4. Nassau, The Bahamas, p. 3485-3490, 2004.

[19] C. PAPAGEORGIOU, K. GLOVER - *Robustness Analysis of Nonlinear Flight Controllers.* Journal of Guidance, Control and Dynamics 28 (4), p. 639-648, 2005.

[20] J. REINER, G. BALAS, W. GARRARD - *Robust Dynamic Inversion for Control of Highly Maneuverable Aircraft*. Journal of Guidance, Control and Dynamics 18 (1), p. 18-24, 1995.

[21] J. REINER, G. BALAS, W. GARRARD - *Flight Control Design Using Robust Dynamic Inversion and Time-Scale Separation.* Automatica 32 (11), p. 1493-1504, 1996.

[22] C. ROOS - *Systems Modeling, Analysis and Control (SMAC) Toolbox: An Insight into the Robustness Analysis Library.* Proceedings of the IEEE Multiconference on Systems and Control. Hyderabad, India, p. 176-181, 2013.

[23] C. Roos, G. Hardier, J.-M. Biannic - *Polynomial and Rational Approximation with the APRICOT Library of the SMAC Toolbox*. Proceedings of the IEEE Multiconference on Systems and Control. Antibes, France, 2014.

[24] C. ROOS, F. LESCHER, J.-M. BIANNIC, C. DOLL, G. FERRERES - *A Set of μ-Analysis Based Tools to Evaluate the Robustness Properties of High-Dimensional Uncertain Systems*. Proceedings of the IEEE Multiconference on Systems and Control. Denver, CO, USA, p. 644-649, 2011.

[25] S. A. SNELL, F. DALE, L. WILLIAM GARRARD - *Nonlinear Inversion Flight Control for a Supermaneuverable Aircraft.* Journal of Guidance, Control, and Dynamics 15 (4), p. 976-984, 1992.

[26] The MathWorks, Inc., 2014. *Robust Control Toolbox for Use with MATLAB.* Release 2014a. Natick, Massachusetts, United States., http://www.mathworks.com/help/robust/mu-synthesis.html.

Jean-Marc Biannic graduated from SUPAERO Engineering School in 1992 and received the PhD degree in Robust Control Theory with the highest honors in 1996 from SUPAERO as well. He joined ONERA as a research scientist in 1997 and received the HDR degree (French habilitation as PhD supervisor) from Paul Sabatier's University of Toulouse in 2010. Jean-Marc Biannic has supervised 6 PhD students. He is the author or co-author of 20 journal papers, beyond 50 conference papers, many book chapters, teaching documents, a tutorial book on multivariable control and Matlab toolboxes. He received in 2011 the second research distinction grade(MR2) from ONERA and the "ERE" distinction from ISAE (Aeronautics and Space Institute) thanks to which he is recognized as a full-professor in PhD committees. Jean-Marc Biannic has participated to several European projects and Garteur Groups (on PIO and nonlinear control). From 2012 to 2016, he has led a research project involving 10 research scientists for the development of the SMAC toolbox (w3.onera.fr/smac) for systems modeling, analysis and control.

Jérémy Lesprier is currently working as a professional engineer in the Attitude and Orbit Control Systems Development & Studies Department at Airbus Defence and Space, Toulouse, France. He graduated from the French engineering school *Arts et Métiers* ParisTech with a double degree in Aerospace Engineering at KTH (Stockholm, Sweden) in 2012. He received his Ph.D degree in automatic control from the University of Toulouse in 2015, for his work on robust control laws design, robustness analysis, and modeling for aerospace applications.

Clément Roos graduated from ISAE-SUPAERO in 2004 and holds a PhD in Automatic Control. He joined ONERA as a research scientist in 2007. He takes part in industrial projects with Airbus, Dassault and Safran. He is or was also involved in several European projects such as GARTEUR-AG17, COFCLUO, CLEANSKY, ERA and VISION. His research interests focus on aircraft modeling, robustness analysis and control laws validation, as well as robust and nonlinear control. He is the author or co-author of several papers, book chapters, teaching documents and Matlab tools implemented in the Systems Modeling, Analysis and Control toolbox.

Gain-Scheduled $\mathcal{H}_\infty$ Loop-Shaping Autopilot Design for Spin-Stabilized Canard-Guided Projectiles

F. Sève, S. Theodoulis, P. Wernert
(French-German Research Institute of Saint-Louis (ISL), Department of Guidance Navigation and Control, Saint-Louis (FR))

M. Zasadzinski, M. Boutayeb
(Research Center for Automatic Control of Nancy (CRAN), University of Lorraine, UMR 7039, CNRS, Cosnes-et-Romain (FR))

E-mail: Florian.Seve@isl.eu

DOI: 10.12762/2017.AL13-03

This article is dedicated to the design of a complete guidance & control system for the roll/pitch/yaw-channels of a 155 mm dual-spin projectile equipped with nose-mounted trajectory correction canards. The projectile airframe parameter-dependent nonlinear model including aerodynamic and actuator/sensor uncertainty descriptions is given and the subsequently computed linearized models necessary for autopilot design are presented. The pitch/yaw-channel dynamics linearized system is useful for highlighting important properties specific to these dynamics, in particular in relation with the parameter vector dimension and the sensor position. The computation of a linear structured controller for the nose roll-axis and of a gain-scheduled structured compensator for the airframe pitch/yaw-axes, using an $\mathcal{H}_\infty$ loop-shaping design approach, is detailed with the assessment of the obtained performance and robustness properties. Finally, various guided flight nonlinear 7DoF simulation results are exposed for the purpose of evaluating over the projectile flight envelope the effectiveness of the proposed guidance & control scheme.

Introduction

Destroying a target on a battlefield with an artillery unit traditionally requires several ballistic rounds to be fired due to the lack of accuracy of such weapons. Significant ballistic impact point miss distances can originate from incorrect launch initial conditions (muzzle velocity and gun barrel pointing and azimuth) or wind perturbations. However, the multiplication of the number of firings causes potential unwanted collateral damage, pushes the mission costs higher, and can lead to an excessive engagement time and logistical issues that render the artillery crew vulnerable to enemy counter fire. The interest of industrial and academic communities in developing projectile trajectory correction mechanisms has grown over the last forty years, in order to improve the ballistic shell terminal accuracy and subsequently to overcome the aforementioned drawbacks.

An attractive approach consists in equipping a projectile with aerodynamic control surfaces, despite their fragile mechanical structure, which can be rotating or reciprocating nose-mounted canards, tail fins, or both [24, 31, 10, 26, 12, 9, 33, 13, 34]. Those possess the advantage of creating efforts that are quite easily modeled and the generated control is a continuous-time signal. In addition, these trajectory control mechanisms are very similar to the well-mastered ones mounted on traditional missiles [35, 29, 36, 3, 25, 37, 7]. The projectile concept studied here results from retrofitting an existing unguided 155 mm ballistic *spin-stabilized* shell with a roll-decoupled nose equipped with two pairs of rotating canards, hence leading to a so-called *dual-spin* control configuration. The latter is also, here, of a *Skid-To-Turn* (STT) type, *i.e.*, the projectile trajectory correction is performed thanks to maneuvers in the pitch and yaw planes using the two pairs of canards, while the nose is maintained at a fixed angular position. The previous guided spin-stabilized projectile concept, which is dynamically stabilized thanks to its high body roll rate [21, 6], is attractive for maintaining low development and production costs. However, spin-stabilization, which causes a strong coupling between the highly nonlinear pitch/yaw-channel dynamics, makes the design of a truly multivariable nose-embedded guidance & control (G&C) function necessary in order to devise a smart weapon, which is more challenging than for classical missiles with decoupled pitch and yaw axes.

The flight G&C system, which must retain a quite simple structure, easy to tune and implement while delivering high-performance over a large operating domain, has to handle additional constraints, such as

the use of low-cost, small and gun-hardened actuators and sensors with limited performance, which are also inevitably integrated in the projectile nose and not at the center of mass (CM), as is usually done in the literature regarding guided projectiles. Considering this severe practical position restriction constitutes a major novelty with respect to the previous works of [33, 34]. In addition, sensor measurement noise and aerodynamic and component uncertainty, along with external disturbances, must be taken into account.

The linearization-based divide-and-conquer gain-scheduling control approach [19, 27] coupled with the linear robust control theory tools [41, 30] have proven their value in computing efficient autopilots for aerospace applications. Hence, the parameter-dependent nonlinear system dynamics are first linearized around an equilibrium manifold covering the operating domain [20]. The set of designed linear controllers is then smoothly interpolated to yield a gain-scheduled controller, in order to operate at any nonlinear system operating point. However, the previous local control design technique lacks global stability and performance property guarantee, hence necessitating a multitude of nonlinear simulations to be performed for validation. With regard to the design of guidance module, proportional navigation (PN) algorithms are traditionally used in the case of missiles.

This paper is aimed at extending and improving the works of [33, 34] concerning autopilot design for guided ammunition. A nonlinear model for the complete projectile dynamics is first presented, based on a more generic aerodynamic force and moment description, in addition to the aforementioned critical sensor position constraint. Distinct linearized models for the nose roll and for the complete projectile pitch/yaw dynamics are then computed to design, using an $\mathcal{H}_\infty$ loop-shaping design procedure [22, 23] offering an alternative to the standard robust control technique used in [34], separate two-degree-of-freedom (2DoF) fixed structure and reduced order autopilots. Indeed, the regulated roll-channel dynamics must respond faster than the controlled pitch/yaw ones in the STT control configuration employed.

A single robust linear controller is sufficient for the purpose of controlling the nose roll-channel throughout the projectile flight envelope, whereas a gain-scheduling control strategy is developed for the parameter-highly varying pitch/yaw dynamics. A robust stability analysis is then proposed for both linear controller designs using various robustness tools, such as μ-analysis [41, 30]. Finally, the effectiveness of the obtained PN guidance & gain-scheduled control system to intercept a ballistic impact point is assessed through extensive nonlinear simulations.

This paper is organized as follows. The first part addresses the development of the projectile nonlinear and linearized models. The second part presents the autopilot designs and robustness analyses for both the nose roll-channel and the complete projectile pitch/yaw-channels. The third part addresses PN guidance. Finally, the fourth part details nonlinear simulation results for the STT guided projectile.

Airframe Modeling

Canard-Guided Projectile Concept

The studied dual-spin STT canard-guided projectile concept is given in Fig. 1 with several of the flight mechanics state and control variables used in the nonlinear mathematical model representing its behavior. The rapidly spinning aft part incorporates the explosive charge, whereas the forward part embeds two servomotors deflecting the steering canards and a coaxial servomotor used for decoupling and controlling the nose roll-axis dynamics. The forward part also integrates a three-axis IMU assisted by a GPS module, along with the necessary guidance and control processors.

Nonlinear Parameter-Dependent Dynamics & Kinematics

The 7DoF nonlinear model for a canard-guided dual-spin projectile is composed of translational & attitude *dynamic* equations. The first ones describe the linear motion of the projectile CM B with respect to the Earth inertial frame E, whereas the second ones represent the rotational movements of the forward "f" and aft "a" projectile parts $\mathrm{B_f}$, $\mathrm{B_a}$ with respect to the inertial frame. Those dynamic equations, which are expressed in a coordinate system (CS) related to a non-rolling frame $\mathrm{B'}$, are defined as:

$$\begin{bmatrix} \dot{u} \\ \dot{v} \\ \dot{w} \end{bmatrix} = \left(\frac{1}{m}\right)\begin{bmatrix} X \\ Y \\ Z \end{bmatrix} - \begin{bmatrix} 0 & -r & q \\ r & 0 & r\tan\theta \\ -q & -r\tan\theta & 0 \end{bmatrix}\begin{bmatrix} u \\ v \\ w \end{bmatrix} \tag{1a}$$

$$\begin{bmatrix} \dot{p}_\mathrm{f} \\ \dot{p}_\mathrm{a} \\ \dot{q} \\ \dot{r} \end{bmatrix} = \begin{bmatrix} 0 \\ 0 \\ -\left(I_{\mathrm{xa}} I_\mathrm{t}^{-1} p_\mathrm{a} + r\tan\theta\right) r \\ \left(I_{\mathrm{xa}} I_\mathrm{t}^{-1} p_\mathrm{a} + r\tan\theta\right) q \end{bmatrix} + \left[\begin{array}{c|ccc} I_{\mathrm{xf}}^{-1} & 0 & 0 & 0 \\ \hline 0 & I_{\mathrm{xa}}^{-1} & 0 & 0 \\ 0 & 0 & I_\mathrm{t}^{-1} & 0 \\ 0 & 0 & 0 & I_\mathrm{t}^{-1} \end{array}\right]\begin{bmatrix} L_\mathrm{f} \\ L_\mathrm{a} \\ M \\ N \end{bmatrix} \tag{1b}$$

The nonlinear model comprises additional translational & attitude *kinematic* equations symbolizing a change from the inertial CS to the non-rolling frame CS that is applied to the linear and angular velocities of both projectile parts:

$$\begin{bmatrix} \dot{x}_\mathrm{e} \\ \dot{y}_\mathrm{e} \\ \dot{z}_\mathrm{e} \end{bmatrix} = \begin{bmatrix} \cos\psi\cos\theta & -\sin\psi & \cos\psi\sin\theta \\ \sin\psi\cos\theta & \cos\psi & \sin\psi\sin\theta \\ -\sin\theta & 0 & \cos\theta \end{bmatrix}\begin{bmatrix} u \\ v \\ w \end{bmatrix} \tag{2a}$$

$$\begin{bmatrix} \dot{\phi}_\mathrm{f} \\ \dot{\phi}_\mathrm{a} \\ \dot{\theta} \\ \dot{\psi} \end{bmatrix} = \begin{bmatrix} 1 & 0 & 0 & \tan\theta \\ 0 & 1 & 0 & \tan\theta \\ 0 & 0 & 1 & 0 \\ 0 & 0 & 0 & \sec\theta \end{bmatrix}\begin{bmatrix} p_\mathrm{f} \\ p_\mathrm{a} \\ q \\ r \end{bmatrix} \tag{2b}$$

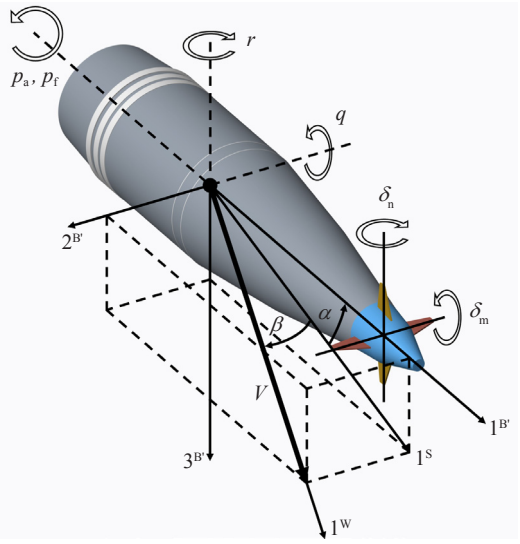

Figure 1 – 155 mm canard-guided dual-spin projectile concept

The system dynamic state variables in Eqs. (1), (2) are the projectile CM linear $[u\ \ v\ \ w]^{\mathrm{T}} = [\boldsymbol{v}_{\mathrm{B}}^{\mathrm{E}}]^{\mathrm{B}'}$ velocities and the forward and aft part angular $[p_{\mathrm{f}}\ \ p_{\mathrm{a}}\ \ q\ \ r]^{\mathrm{T}} = [\boldsymbol{\omega}^{\mathrm{B_{fa}E}}]^{\mathrm{B}'}$ rates. The system kinematic states are the CM linear $[x_{\mathrm{e}}\ \ y_{\mathrm{e}}\ \ z_{\mathrm{e}}]^{\mathrm{T}} = [\boldsymbol{s}_{\mathrm{BE}}]^{\mathrm{E}}$ positions and the body and nose angular $[\phi_{\mathrm{f}}\ \ \phi_{\mathrm{a}}\ \ \theta\ \ \psi]^{\mathrm{T}} = \boldsymbol{e}^{\mathrm{B_{fa}E}}$ orientations. The external forces X, Y, Z are composed of gravitational (g) and aerodynamic contributions [drag/lift forces being mainly applied to the projectile body (dl), canards (c) and Magnus (m)] and are given by:

$$\begin{bmatrix} X \\ Y \\ Z \end{bmatrix} = \begin{bmatrix} X_{\mathrm{dl}} \\ Y_{\mathrm{dl}} \\ Z_{\mathrm{dl}} \end{bmatrix} + \begin{bmatrix} X_{\mathrm{c}} \\ Y_{\mathrm{c}} \\ Z_{\mathrm{c}} \end{bmatrix} + \begin{bmatrix} X_{\mathrm{m}} \\ Y_{\mathrm{m}} \\ Z_{\mathrm{m}} \end{bmatrix} + \begin{bmatrix} X_{\mathrm{g}} \\ Y_{\mathrm{g}} \\ Z_{\mathrm{g}} \end{bmatrix}$$
$$= \bar{q}S \left(\begin{bmatrix} -C_{\mathrm{A0}}(\mathcal{M},\alpha,\beta) \\ C_{\mathrm{Y0}}(\mathcal{M},\beta) \\ -C_{\mathrm{N0}}(\mathcal{M},\alpha) \end{bmatrix} + \begin{bmatrix} 0 \\ C_{\mathrm{Y}\delta}(\mathcal{M})(\delta_{\mathrm{z}} - \beta) \\ -C_{\mathrm{N}\delta}(\mathcal{M})(\delta_{\mathrm{y}} + \alpha) \end{bmatrix} \right. \tag{3}$$
$$\left. + \left(\frac{p_{\mathrm{a}} d}{V}\right) \begin{bmatrix} 0 \\ C_{\mathrm{Y}p}(\mathcal{M},\alpha,\beta) \\ -C_{\mathrm{N}p}(\mathcal{M},\alpha,\beta) \end{bmatrix} \right) + mg \begin{bmatrix} -\sin\theta \\ 0 \\ \cos\theta \end{bmatrix}$$

The external moments consist of similar aerodynamic components, along with additional aerodynamic damping (d) and mechanical control/friction (cf) terms:

$$\begin{bmatrix} L_{\mathrm{f}} \\ L_{\mathrm{a}} \\ M \\ N \end{bmatrix} = \begin{bmatrix} L_{\mathrm{f,dl}} \\ L_{\mathrm{a,dl}} \\ M_{\mathrm{dl}} \\ N_{\mathrm{dl}} \end{bmatrix} + \begin{bmatrix} L_{\mathrm{f,c}} \\ L_{\mathrm{a,c}} \\ M_{\mathrm{c}} \\ N_{\mathrm{c}} \end{bmatrix} + \begin{bmatrix} L_{\mathrm{f,m}} \\ L_{\mathrm{a,m}} \\ M_{\mathrm{m}} \\ N_{\mathrm{m}} \end{bmatrix} + \begin{bmatrix} L_{\mathrm{f,d}} \\ L_{\mathrm{a,d}} \\ M_{\mathrm{d}} \\ N_{\mathrm{d}} \end{bmatrix} + \begin{bmatrix} L_{\mathrm{f,cf}} \\ L_{\mathrm{a,cf}} \\ M_{\mathrm{cf}} \\ N_{\mathrm{cf}} \end{bmatrix}$$
$$= \bar{q}Sd \left(\begin{bmatrix} 0 \\ 0 \\ C_{\mathrm{m0}}(\mathcal{M},\alpha) \\ C_{\mathrm{n0}}(\mathcal{M},\beta) \end{bmatrix} + \begin{bmatrix} 0 \\ 0 \\ C_{\mathrm{m}\delta}(\mathcal{M})(\delta_{\mathrm{z}} + \alpha) \\ C_{\mathrm{n}\delta}(\mathcal{M})(\delta_{\mathrm{y}} - \beta) \end{bmatrix} \right. \tag{4}$$
$$\left. + \left(\frac{p_{\mathrm{a}} d}{V}\right) \begin{bmatrix} 0 \\ 0 \\ C_{\mathrm{m}p}(\mathcal{M},\alpha,\beta) \\ C_{\mathrm{n}p}(\mathcal{M},\alpha,\beta) \end{bmatrix} + \left(\frac{d}{V}\right) \begin{bmatrix} 0 \\ C_{lp}(\mathcal{M}) p_{\mathrm{a}} \\ C_{mq}(\mathcal{M}) q \\ C_{nr}(\mathcal{M}) r \end{bmatrix} \right) + \begin{bmatrix} L_{\mathrm{co}} + L_{\mathrm{f-a}} \\ -L_{\mathrm{f-a}} \\ 0 \\ 0 \end{bmatrix}$$

The coaxial motor torque is denoted by L_{co}, whereas the friction moment $L_{\mathrm{f-a}}$ created between the forward and aft parts is defined as:

$$L_{\mathrm{f-a}} = \bar{q}Sd\, C_{\mathrm{A0}}(\mathcal{M},\alpha,\beta_{\mathrm{F}}) \cdot \mathrm{sign}(p_{\mathrm{a}} - p_{\mathrm{f}}) \left(K_{\mathrm{s}} + K_{\mathrm{v}} |p_{\mathrm{a}} - p_{\mathrm{f}}|\right) \tag{5}$$

The variables $\delta_{\mathrm{z}}, \delta_{\mathrm{y}}$ are the system virtual normal and lateral control signals, which depend on the actual canard pair deflections $\delta_{\mathrm{m}}, \delta_{\mathrm{n}}$ and on the nose roll angular position ϕ_{f} as:

$$\begin{bmatrix} \delta_{\mathrm{z}} \\ \delta_{\mathrm{y}} \end{bmatrix} = \begin{bmatrix} \cos\phi_{\mathrm{f}} & -\sin\phi_{\mathrm{f}} \\ \sin\phi_{\mathrm{f}} & \cos\phi_{\mathrm{f}} \end{bmatrix} \begin{bmatrix} \delta_{\mathrm{m}} \\ \delta_{\mathrm{n}} \end{bmatrix} = \mathbf{T}(\phi_{\mathrm{f}}) \begin{bmatrix} \delta_{\mathrm{m}} \\ \delta_{\mathrm{n}} \end{bmatrix} \tag{6}$$

The elements $C_{\mathrm{A0}}, C_{\mathrm{Y0}}, C_{\mathrm{N0}}$ represent the drag/lift-induced, $C_{\mathrm{Y}\delta}, C_{\mathrm{N}\delta}$ the canard, and $C_{\mathrm{Y}p}, C_{\mathrm{N}p}$ the Magnus force aerodynamic coefficients, whereas the elements $C_{\mathrm{m0}}, C_{\mathrm{n0}}$ symbolize the drag/lift-induced, $C_{\mathrm{m}\delta}, C_{\mathrm{n}\delta}$ the canard, $C_{\mathrm{m}p}, C_{\mathrm{n}p}$ the Magnus, and C_{lp}, C_{mq}, C_{nr} the damping moment aerodynamic coefficients. Due to imperfect wind-tunnel measurements and computational fluid dynamics simulation results, those aerodynamic coefficients (and their partial derivatives used below in the linearized model) take uncertain values with variations around the nominal values of up to 5% for C_{A0}, 10% for $C_{\mathrm{Y0}}, C_{\mathrm{N0}}, C_{\mathrm{m0}}, C_{\mathrm{n0}}, C_{\mathrm{Y}\delta}, C_{\mathrm{N}\delta}$ and $C_{\mathrm{m}\delta}, C_{\mathrm{n}\delta}$, 20% for C_{lp}, and 30% for $C_{\mathrm{Y}p}, C_{\mathrm{N}p}, C_{\mathrm{m}p}, C_{\mathrm{n}p}$ and C_{mq}, C_{nr}. All of the aerodynamic coefficients are tabulated in a highly nonlinear manner as a function of the Mach number $\mathcal{M} = V/a$, and of the aerodynamic angles of attack (AoA) α and sideslip (AoS) β for some of them. The airframe velocity V and the angles α, β given in Fig. 1 are defined as follows under a no-wind assumption [40]:

$$V = \sqrt{u^2 + v^2 + w^2} \tag{7a}$$

$$\alpha = \arctan\left(\frac{w}{u}\right) \tag{7b}$$

$$\beta = \arcsin\left(\frac{v}{V}\right) = \arctan\left(\frac{v}{\sqrt{u^2 + w^2}}\right) \tag{7c}$$

The preceding force and moment dynamic equations (1) also depend on the altitude-dependent $(h = |z_{\mathrm{e}}|)$ gravitational acceleration $g(h)$, on the projectile mass m and on the roll-axis projectile forward and aft part moments of inertia $I_{\mathrm{xf}}, I_{\mathrm{xa}}$, along with the transversal moment of inertia I_{t}. Finally, the forces and moments (3)-(5) are parameterized by the reference area S, caliber d, and static and viscous friction coefficients $K_{\mathrm{s}}, K_{\mathrm{v}}$, and they vary with the dynamic pressure $\bar{q} = \frac{1}{2}\rho V^2$, where $\rho = \rho(h)$ and $a = a(h)$ are the altitude-dependent air density and speed of sound.

As is generally done in the literature [8, 5], the complete aforementioned translational nonlinear dynamic equations include the linear velocities (u, v, w) as state variables, which are however less suited for pitch/yaw-channel autopilot design than the wind-frame W variables (V, α, β). Equivalent (under a no-wind assumption) nonlinear translational dynamic equations using the states (V, α, β) are hence preferred, and those are obtained by first differentiating Eqs. (7) with respect to time:

$$\dot{V} = \frac{u\dot{u} + v\dot{v} + w\dot{w}}{V} \tag{8.a}$$

$$\dot{\alpha} = \frac{u\dot{w} - w\dot{u}}{u^2 + w^2} \tag{8.b}$$

$$\dot{\beta} = \frac{-uv\dot{u} + (u^2 + w^2)\dot{v} - vw\dot{w}}{V^2\sqrt{u^2 + w^2}} \tag{8.c}$$

The projectile linear velocities, which are obtained as follows by inverting Eqs. (7):

$$u = V\cos\alpha\cos\beta \tag{9.a}$$

$$v = V\sin\beta \tag{9.b}$$

$$w = V\sin\alpha\cos\beta \tag{9.c}$$

are then inserted into the wind-frame variable dynamics equations (8) along with the expressions of $(\dot{u},\dot{v},\dot{w})$ given in Eq. (1a), in order to provide the equivalent nonlinear translational state dynamics:

$$\begin{bmatrix}\dot{V}\\ \dot{\alpha}\\ \dot{\beta}\end{bmatrix}=\begin{bmatrix}0\\ q+r\left(\cos\alpha\tan\theta-\sin\alpha\right)\tan\beta\\ -r\left(\cos\alpha+\sin\alpha\tan\theta\right)\end{bmatrix}+\left(\frac{1}{mV}\right)\begin{bmatrix}V\cos\alpha\cos\beta & V\sin\beta & V\sin\alpha\cos\beta\\ -\sin\alpha/\cos\beta & 0 & \cos\alpha/\cos\beta\\ -\cos\alpha\sin\beta & \cos\beta & -\sin\alpha\sin\beta\end{bmatrix}\begin{bmatrix}X\\ Y\\ Z\end{bmatrix} \tag{10}$$

Equivalent nonlinear translational kinematics can be derived by inserting Eqs. (9) into Eq. (2a).

The projectile nonlinear state dynamics & kinematics mathematical model in (V,α,β) is then complemented with nonlinear output dynamics & kinematics equations providing the signals measured at a longitudinal distance $x_{\text{IMU}}>0$ from the projectile CM. The output Euler angles are directly the nose state angular positions $[\phi_{\text{f}}\ \ \theta\ \ \psi]^{\text{T}}=\boldsymbol{e}^{\text{B}_{\text{f}}\text{E}}$, whereas the load factors $[n_{\text{x,f}}\ \ n_{\text{y,f}}\ \ n_{\text{z,f}}]^{\text{T}}=[\boldsymbol{n}^{\text{B}_{\text{f}}\text{E}}]^{\text{B}_{\text{f}}}$ and the angular rates $[p_{\text{f,f}}\ \ q_{\text{f}}\ \ r_{\text{f}}]^{\text{T}}=[\boldsymbol{\omega}^{\text{B}_{\text{f}}\text{E}}]^{\text{B}_{\text{f}}}$, which are obtained in the nose frame B_{f} CS from the accelerometer and gyrometer measurements, respectively, are given as follows, together with the nose GPS inertial positions $[x_{\text{f}}\ \ y_{\text{f}}\ \ z_{\text{f}}]^{\text{T}}=[\boldsymbol{s}_{\text{B}_{\text{f}}\text{E}}]^{\text{E}}$:

$$\begin{bmatrix}n_{\text{x,f}}\\ n_{\text{y,f}}\\ n_{\text{z,f}}\end{bmatrix}=\begin{bmatrix}1 & 0 & 0\\ 0 & \cos\phi_{\text{f}} & \sin\phi_{\text{f}}\\ 0 & -\sin\phi_{\text{f}} & \cos\phi_{\text{f}}\end{bmatrix}\left\{\begin{bmatrix}n_{\text{CM,x}}\\ n_{\text{CM,y}}\\ n_{\text{CM,z}}\end{bmatrix}+\left(\frac{x_{\text{IMU}}}{g}\right)\begin{bmatrix}-\left(q^2+r^2\right)\\ p_{\text{f}}q+\dot{r}\\ p_{\text{f}}r-\dot{q}\end{bmatrix}\right\} \tag{11a}$$

$$\begin{bmatrix}p_{\text{f,f}}\\ q_{\text{f}}\\ r_{\text{f}}\end{bmatrix}=\begin{bmatrix}1 & 0 & 0\\ 0 & \cos\phi_{\text{f}} & \sin\phi_{\text{f}}\\ 0 & -\sin\phi_{\text{f}} & \cos\phi_{\text{f}}\end{bmatrix}\begin{bmatrix}p_{\text{f}}\\ q\\ r\end{bmatrix} \tag{11b}$$

$$\begin{bmatrix}x_{\text{f}}\\ y_{\text{f}}\\ z_{\text{f}}\end{bmatrix}=\begin{bmatrix}x_{\text{e}}\\ y_{\text{e}}\\ z_{\text{e}}\end{bmatrix}+x_{\text{IMU}}\begin{bmatrix}\cos\psi\cos\theta\\ \sin\psi\cos\theta\\ -\sin\theta\end{bmatrix} \tag{11c}$$

where the load factors $[n_{\text{CM,x}}\ \ n_{\text{CM,y}}\ \ n_{\text{CM,z}}]^{\text{T}}=[\boldsymbol{n}^{\text{BE}}]^{\text{B}'}$ at the projectile CM and expressed in the non-rolling frame CS are equal to the specific forces divided by the projectile weight.

Linearized Dynamics

Roll-Channel

The nose roll angular position and velocity state dynamics given in Eqs. (1b), (2b) are first augmented with the coaxial DC servomotor current i linear dynamics, and the result is rearranged into the following linear parameter-dependent form:

$$\mathcal{S}_{\text{R}}^{\lambda}(\boldsymbol{\lambda}_{\text{R}}):\ \begin{bmatrix}\dot{\phi}_{\text{f}}\\ \dot{p}_{\text{f}}\\ \dot{i}\end{bmatrix}=\begin{bmatrix}0 & 1 & 0\\ 0 & -K_{\text{a}}(\boldsymbol{\lambda}_{\text{R}})K_{\text{v}} & I_{\text{xf}}^{-1}K_{\text{m}}\\ 0 & -K_{\text{b}}L^{-1} & -RL^{-1}\end{bmatrix}\begin{bmatrix}\phi_{\text{f}}\\ p_{\text{f}}\\ i\end{bmatrix}+\begin{bmatrix}d_{\phi}\\ d_{p}\\ d_{i}\end{bmatrix}+\begin{bmatrix}0\\ 0\\ L^{-1}\end{bmatrix}V_{\text{e}},\quad \boldsymbol{\lambda}_{\text{R}}\in\boldsymbol{\Gamma}_{\text{R}}^{\lambda} \tag{12}$$

with:

$$K_{\text{a}}(\boldsymbol{\lambda}_{\text{R}})=\left(\frac{\bar{q}Sd}{I_{\text{xf}}}\right)C_{\text{A0}}(\mathcal{M},\alpha,\beta) \tag{13}$$

and the time-varying parameter vector $\boldsymbol{\lambda}_{\text{R}}=[V\ \ \alpha\ \ \beta\ \ h]^{\text{T}}$ capturing the dependence of the system dynamics on the projectile operating condition, and taking its values inside an operating domain $\boldsymbol{\Gamma}_{\text{R}}^{\lambda}\subset\mathbb{R}^4$. The system inputs are the control applied voltage V_{e} with a saturation level $V_{\text{e,sat}}=\pm 60\ \text{V}$ and the time-varying external disturbances d_{ϕ},d_{p},d_{i} defined as:

$$\boldsymbol{d}=\begin{bmatrix}d_{\phi}\\ d_{p}\\ d_{i}\end{bmatrix}=\begin{bmatrix}r\tan\theta\\ K_{\text{a}}(\boldsymbol{\lambda}_{\text{R}})\left[\text{sign}\left(p_{\text{a}}-p_{\text{f}}\right)K_{\text{s}}+K_{\text{v}}p_{\text{a}}\right]\\ K_{\text{b}}L^{-1}p_{\text{a}}\end{bmatrix} \tag{14}$$

The electromotive force constant K_{b}, the motor inductance L, resistance R, and torque constant K_{m} verifying $L_{\text{co}}=K_{\text{m}}i$, along with the viscous friction coefficient K_{v} are taken as real uncertain parameters with errors of 15% for $L,R,K_{\text{b}},K_{\text{m}}$ and of 40% for K_{v}.

Finally, the projectile flight-condition dependence of the model $\mathcal{S}_{\text{R}}^{\lambda}(\boldsymbol{\lambda}_{\text{R}})$ is transformed into an uncertainty on the aerodynamic element $K_{\text{a}}(\boldsymbol{\lambda}_{\text{R}})$ corresponding to its variations over $\boldsymbol{\Gamma}_{\text{R}}^{\lambda}$, and to the errors on the axial force aerodynamic coefficient C_{A0}. This practice leads to defining a new unique uncertain linear (not parameter-dependent) model $\Sigma_{\text{R}}^{\lambda}$ used for nose roll-channel autopilot design, with the nose angular position and rate being the feedback signals.

Pitch/Yaw-Channels

The STT projectile trajectory correction feedback system, which acts on the nonlinear pitch/yaw axis dynamics represented by the α,q and β,r state dynamic equations in Eqs. (10), (1b), uses the canard deflections $\boldsymbol{\delta}=[\delta_{\text{m}}\ \ \delta_{\text{n}}]^{\text{T}}$ as the control inputs, the normal/lateral load factors $\boldsymbol{n}_{\text{zy,f}}=[n_{\text{z,f}}\ \ n_{\text{y,f}}]^{\text{T}}$ as the tracking outputs, and the pitch/yaw angular rates $\boldsymbol{\omega}_{qr,\text{f}}=[q_{\text{f}}\ \ r_{\text{f}}]^{\text{T}}$ as additional measured outputs. The state and output pitch/yaw dynamics are directly influenced by the airframe airspeed V, the projectile nose and body rates $p_{\text{f}},p_{\text{a}}$ and some of the kinematic states. Actually, the normal inertial position z_{e} enters the aerodynamic coefficient and dynamic pressure expressions, the pitch angle θ influence is due to the flight mechanics equation structure, and the nose roll angle ϕ_{f} is used in the virtual control and measured output expressions. A parameter vector $\boldsymbol{\sigma}_{\text{PY}}=[V\ \ p_{\text{f}}\ \ p_{\text{a}}\ \ h\ \ \phi_{\text{f}}\ \ \theta]^{\text{T}}$ is then defined, takes its values from a set $\boldsymbol{\Gamma}_{\text{PY}}^{\sigma}\subset\mathbb{R}^6$ and is considered as a relatively slowly-varying external input to the pitch/yaw dynamics.

In the context of a linearization-based, divide-and-conquer gain-scheduling control strategy, the computation of a pitch/yaw dynamics linearized model needs to calculate a set of equilibrium points for any admissible fixed value of the parameter vector $\boldsymbol{\sigma}_{\text{PY}}$ by imposing $\dot{\alpha}=\dot{\beta}=\dot{q}=\dot{r}=0$. The result is an underdetermined system of four nonlinear algebraic equations with the six unknown states α,β,q,r and controls $\delta_{\text{m}},\delta_{\text{n}}$. A solution for making the problem solvable is to define an *extended* trimming vector $\boldsymbol{\rho}_{\text{PY}}=[V\ \alpha\ \beta\ p_{\text{f}}\ \ p_{\text{a}}\ h\ \phi_{\text{f}}\ \theta]^{\text{T}}\in\boldsymbol{\Gamma}_{\text{PY}}^{\rho}\subset\mathbb{R}^8$ by imposing the aerodynamic angles α,β. An efficient home-made trimming analytical procedure that is specifically developed for spin-stabilized projectiles with strongly coupled pitch/yaw-axes dynamics can be found in [33].

The linearized model, whose state-space matrix elements are functions of the trimming vector $\boldsymbol{\rho}_{\mathrm{PY}}$, and which possesses a q-LPV form due to the trimming vector dependence on the system states α, β, is expressed in the following generic form:

$$\mathcal{S}^{\rho}_{\mathrm{PY}}\left(\boldsymbol{\rho}_{\mathrm{PY}}\right): \left[\begin{array}{c} \dot{\boldsymbol{x}}_{\mathrm{PY},\varepsilon}(t) \\ \boldsymbol{y}_{\mathrm{PY},\varepsilon}(t) \end{array}\right] = \left[\begin{array}{c|c} \mathbf{A}\left(\boldsymbol{\rho}_{\mathrm{PY}}\right) & \mathbf{B}\left(\boldsymbol{\rho}_{\mathrm{PY}}\right) \\ \hline \mathbf{C}\left(\boldsymbol{\rho}_{\mathrm{PY}}\right) & \mathbf{D}\left(\boldsymbol{\rho}_{\mathrm{PY}}\right) \end{array}\right] \left[\begin{array}{c} \boldsymbol{x}_{\mathrm{PY},\varepsilon}(t) \\ \boldsymbol{u}_{\mathrm{PY},\varepsilon}(t) \end{array}\right], \quad \forall \boldsymbol{\rho}_{\mathrm{PY}} \in \boldsymbol{\Gamma}^{\rho}_{\mathrm{PY}},\ t \in \mathbb{R}^{+} \tag{15}$$

with the state $\boldsymbol{x}_{\mathrm{PY},\varepsilon}(t) = \boldsymbol{x}_{\mathrm{PY}}(t) - \boldsymbol{x}_{\mathrm{PY}}[\boldsymbol{\rho}_{\mathrm{PY}}(t)] = [\alpha_{\varepsilon}\ q_{\varepsilon}\ \beta_{\varepsilon}\ r_{\varepsilon}]^{\mathrm{T}}$, the control $\boldsymbol{u}_{\mathrm{PY},\varepsilon}(t) = \boldsymbol{u}_{\mathrm{PY}}(t) - \boldsymbol{u}_{\mathrm{PY}}[\boldsymbol{\rho}_{\mathrm{PY}}(t)] = [\delta_{\mathrm{m},\varepsilon}\ \delta_{\mathrm{n}_z\varepsilon}]^{\mathrm{T}}$ and the output $\boldsymbol{y}_{\mathrm{PY},\varepsilon}(t) = \boldsymbol{y}_{\mathrm{PY}}(t) - \boldsymbol{y}_{\mathrm{PY}}[\boldsymbol{\rho}_{\mathrm{PY}}(t)] = [n_{z,\varepsilon}\ n_{y,\varepsilon}\ q_{\varepsilon}\ r_{\varepsilon}]^{\mathrm{T}}$ deviation vectors. The state-space matrices $\mathbf{A}(\boldsymbol{\rho}_{\mathrm{PY}})$, $\mathbf{B}(\boldsymbol{\rho}_{\mathrm{PY}})$, $\mathbf{C}(\boldsymbol{\rho}_{\mathrm{PY}})$ and $\mathbf{D}(\boldsymbol{\rho}_{\mathrm{PY}})$ are given below by Eqs. (16a)-(16d), in which the matrix $\overline{\mathbf{T}}(\phi_{\mathrm{f}})$ is the transpose of $\mathbf{T}(\phi_{\mathrm{f}})$ defined in Eq. (6). Similar expressions for the force $Z_{\alpha\alpha}, Z_{\alpha\beta}, Z_{\beta\alpha}, Z_{\beta\beta}$ and the moment $M_{q\alpha}, M_{qq}, M_{q\beta}, M_{qr}, M_{q\delta_z}$, $M_{r\alpha}, M_{rq}, M_{r\beta}, M_{rr}, M_{r\delta_y}$ elements of Eqs. (16a)-(16d) and for the load factor elements $N_{n_z\alpha}, N_{n_z\beta}, N_{n_y\alpha}, N_{n_y\beta}, N_{n_z\delta_z}, N_{n_y\delta_y}$ of Eqs. (16c), (16d) can be found in detail in [34].

As shown in [33], the stability matrix of the q-LPV model given in Eq. (16a) is very useful for highlighting the important pitch/yaw-axes dynamics cross-coupling of spin-stabilized projectiles, which is caused by their high body roll rate p_{a}. Hence, the design of a separate autopilot for each axis, as for missiles, is to be undoubtedly avoided since the resulting closed-loop system would experience poor performance and even instability.

The pitch/yaw-dynamics q-LPV model finds also four important applications in addition to autopilot design, which are only summarized here for brevity. The first application concerns a pitch/yaw-axis internal dynamics analysis [33], from which the two precession and nutation modes that are specific to spin-stabilized bodies as stated by the classical aeroballistic theory [6, 21], are clearly identified. The second application addresses the investigation of open-loop local stability properties and shows that a spin-stabilized projectile, which should be unstable statically by referring to non-spinning missile stability theory [36, 16], is however maintained stable dynamically thanks to the sufficiently high body roll rate [33].

The third application demonstrates, through a sensitivity analysis, that retaining only the airframe airspeed and altitude in a reduced dimension, slowly-varying and fully-measurable trimming vector $\boldsymbol{\lambda}_{\mathrm{PY}} = [V\ \ h]^{\mathrm{T}} \in \boldsymbol{\Gamma}^{\lambda}_{\mathrm{PY}} \subset \boldsymbol{\Gamma}^{\rho}_{\mathrm{PY}}$ is sufficient to maintain a good local approximation of the nonlinear dynamics with a resulting simplified q-LPV model $\mathcal{S}^{\lambda}_{\mathrm{PY}}(\boldsymbol{\lambda}_{\mathrm{PY}})$ parameterized by $\boldsymbol{\lambda}_{\mathrm{PY}}$. This practice leads to significantly attenuating the computational burden, thanks to a reduction in the number of controllers to be designed now for a trimming envelope $\boldsymbol{\Gamma}^{\lambda}_{\mathrm{PY}}$ of a dimension of 2 only, instead of 8 initially. In addition, the gain-scheduling control design method is more easily adapted for any value of the reduced two-dimension trimming vector, and the complexity of the implemented controller interpolation law is reduced. However, this practice introduces additional uncertainty on the trimming operating point, making the design of an autopilot even more challenging.

Finally, the fourth application shows the influence of the accelerometer position on the pitch/yaw load factor output nonlinear dynamics, and the necessity of considering the actual position for designing the best possible autopilot [28]. The actual position of the nose-embedded accelerometers is critical and needs a specific treatment due to low-frequency non-minimum phase (NMP) transmission zeros in the I/O SISO load factor-related transfer functions of the linearized model, which are close to the autopilot desired bandwidth [2, 15].

The projectile simplified q-LPV model $\mathcal{S}^{\lambda}_{\mathrm{PY}}(\boldsymbol{\lambda}_{\mathrm{PY}})$ is now augmented for autopilot design by uncertain 2nd order linear models for the canard

$$\mathbf{A} = \left[\begin{array}{cc|cc} Z_{\alpha\alpha} & 1 & Z_{\alpha\beta} & \tan\beta(\cos\alpha\tan\theta - \sin\alpha) \\ M_{q\alpha} & M_{qq} & M_{q\beta} & M_{qr} \\ \hline Z_{\beta\alpha} & 0 & Z_{\beta\beta} & -(\sin\alpha\tan\theta + \cos\alpha) \\ M_{r\alpha} & M_{rq} & M_{r\beta} & M_{rr} \end{array}\right] \tag{16a}$$

$$\mathbf{B} = \left[\begin{array}{c|c} -\left(\dfrac{\bar{q}S}{mV}\right)\left(\dfrac{\cos\alpha}{\cos\beta}\right)C_{\mathrm{N}\delta} & 0 \\ M_{q\delta_z} & 0 \\ \hline \left(\dfrac{\bar{q}S}{mV}\right)\sin\alpha\sin\beta\ C_{\mathrm{N}\delta} & \left(\dfrac{\bar{q}S}{mV}\right)\cos\beta\ C_{\mathrm{Y}\delta} \\ 0 & M_{r\delta_y} \end{array}\right] \cdot \mathbf{T}(\phi_{\mathrm{f}}) \tag{16b}$$

$$\mathbf{C} = \left[\overline{\mathbf{T}}(\phi_{\mathrm{f}}) \middle| \mathbb{O}_2\right] \cdot \left[\begin{array}{cc|cc} N_{n_z\alpha} - \left(\dfrac{x_{\mathrm{IMU}}}{g}\right)M_{q\alpha} & -\left(\dfrac{x_{\mathrm{IMU}}}{g}\right)M_{qq} & N_{n_z\beta} - \left(\dfrac{x_{\mathrm{IMU}}}{g}\right)M_{q\beta} & \left(\dfrac{x_{\mathrm{IMU}}}{g}\right)(p_{\mathrm{f}} - M_{qr}) \\ N_{n_y\alpha} + \left(\dfrac{x_{\mathrm{IMU}}}{g}\right)M_{r\alpha} & \left(\dfrac{x_{\mathrm{IMU}}}{g}\right)(p_{\mathrm{f}} + M_{rq}) & N_{n_y\beta} + \left(\dfrac{x_{\mathrm{IMU}}}{g}\right)M_{r\beta} & \left(\dfrac{x_{\mathrm{IMU}}}{g}\right)M_{rr} \end{array}\right] \tag{16c}$$

$$\mathbf{D} = \left[\overline{\mathbf{T}}(\phi_{\mathrm{f}}) \middle| \mathbb{O}_2\right] \cdot \left[\begin{array}{c|c} N_{n_z\delta_z} - \left(\dfrac{x_{\mathrm{IMU}}}{g}\right)M_{q\delta_z} & 0 \\ 0 & N_{n_z\delta_z} + \left(\dfrac{x_{\mathrm{IMU}}}{g}\right)M_{r\delta_y} \end{array}\right] \cdot \mathbf{T}(\phi_{\mathrm{f}}) \tag{16d}$$

actuators, accelerometers and gyrometers, with additional amplitude and rate saturation levels $\delta_{sat} = \pm 30°$ and $\dot{\delta}_{sat} = \pm 100°/s$ for the actuators. Uncertainty represents here unstructured high-frequency neglected dynamics [30].

Autopilot Design

The same $\mathcal{H}_\infty$ loop-shaping controller design approach [22, 23] detailed in the following section is applied for designing a robust structured controller, first for the nose roll-channel angular position dynamics, and second for the more complex projectile pitch/yaw-channel dynamics linearized at any equilibrium fixed operating point. The pitch/yaw-channel gain-scheduled controller is also described.

$\mathcal{H}_\infty$ Loop-Shaping Controller Design Methodology

The $\mathcal{H}_\infty$ loop-shaping controller design method comprises two main distinct steps, named as *open-loop shaping* and *robust stabilization*. As seen in Fig. 2, the first step consists in attaining a desired level of closed-loop performance by shaping over frequency, using pre- and post-filters $\mathbf{W}_1(s), \mathbf{W}_2(s)$ for the initial open-loop system $\mathbf{G}_K(s)$, the singular values of the open-loop system $\mathbf{G}_S(s) = \mathbf{W}_2(s)\,\mathbf{G}_K(s)\,\mathbf{W}_1(s)$. Typically, high gains at low frequencies and low gains at high frequencies are desirable for reference tracking/disturbance rejection and for noise attenuation, respectively, with no excessive roll-off ($\simeq 20$ dB/dec) at intermediate frequencies around the crossover frequency.

The second step is dedicated to robustness optimization by calculating an $\mathcal{H}_\infty$ controller $\mathbf{K}_\infty(s)$ robustly stabilizing $\mathbf{G}_S(s)$ with respect to unstructured normalized coprime factor (NCF) uncertainties. The maximal stability margin ε_{max} potentially reached can be calculated exactly and before robust controller computation. This margin indicates the success of loop-shaping: an $\varepsilon_{max} \ll 1$ means an incompatibility between performance and robustness specifications and the pre- and post-filters must be adapted; an $\varepsilon_{max} \gtrsim 0.3$ is satisfactory. A good value for ε_{max} also indicates that the open-loop shaped plant singular values should not be degraded too much by the robust controller. Finally, the global implemented controller is obtained as $\mathbf{K}(s) = \mathbf{W}_1(s)\,\mathbf{K}_\infty(s)\,\mathbf{W}_2(s)$.

The previous design technique is an alternative to standard $\mathcal{H}_\infty$ closed-loop shaping methods [41, 30], since the performance and robustness requirements are treated separately. It also tends to produce more robust controllers, since for robustness optimization those minimize implicitly the $\mathcal{H}_\infty$-norm of a set of four closed-loop sensitivity functions with each of them being associated with a specific uncertainty type.

Open-Loop Shaping

The definition of an open-loop shaped plant $\mathbf{G}_S(s)$ is here facilitated using the results of a first mixed-sensitivity $\mathcal{H}_\infty$ controller synthesis [17, 41, 30] incorporating a model-matching constraint [14] whose design setup is given in Fig. 3. In the linearized-based gain-scheduling control context for pitch/yaw dynamics autopilot design, this technique is relatively easy to adapt automatically to the synthesis point. In addition, since the same fixed control structure can be imposed for any operating condition using the $\mathcal{H}_\infty$ non-smooth optimization techniques proposed in [1], similar performance properties can be obtained over the whole projectile trimming envelope. Interpolation and implementation of the designed local controllers are also simplified.

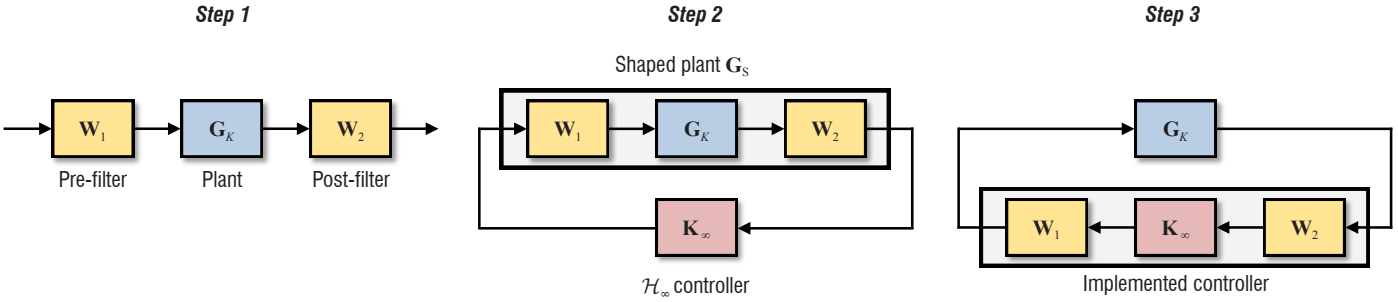

Figure 2 – The $\mathcal{H}_\infty$ loop-shaping controller design procedure

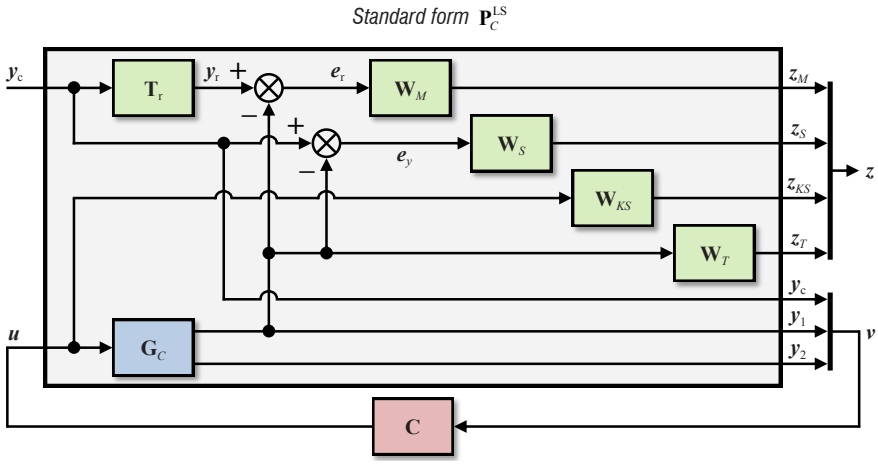

Figure 3 – Mixed-sensitivity $\mathcal{H}_\infty$ controller synthesis block diagram for open-loop shaping

The $\mathcal{H}_\infty$ synthesis problem of Fig. 3 consists in computing a controller $\mathbf{C}(s)$ with output $\boldsymbol{u}(s)$ and inputs $\boldsymbol{v}(s)=[\boldsymbol{y}_c(s)\ \ \boldsymbol{y}_1(s)\ \ \boldsymbol{y}_2(s)]^T$ containing a reference signal $\boldsymbol{y}_c(s)$, a tracking output $\boldsymbol{y}_1(s)$ and an additional measured output $\boldsymbol{y}_2(s)$, in order to maintain nominal (no uncertainty) internal stability and to guarantee that the closed-loop transfer function from the exogenous input $\boldsymbol{w}(s)=\boldsymbol{y}_c(s)$ to the performance outputs $\boldsymbol{z}(s)=[\boldsymbol{z}_S(s)\ \ \boldsymbol{z}_{KS}(s)\ \ \boldsymbol{z}_T(s)\ \ \boldsymbol{z}_M(s)]^T$ satisfies the following standard condition, given a performance index $\gamma>0$ to be minimized [41, 30]:

$$\left\|\mathbf{T}_{zw}^{\mathrm{LS}}(s)\right\|_\infty=\left\|\mathcal{F}_l\left[\mathbf{P}_C^{\mathrm{LS}}(s),\mathbf{C}(s)\right]\right\|_\infty=\left\|\begin{bmatrix}\mathbf{W}_M(s)\mathbf{M}(s)\\ \mathbf{W}_S(s)\mathbf{S}(s)\\ \mathbf{W}_{KS}(s)\mathbf{KS}(s)\\ \mathbf{W}_T(s)\mathbf{T}(s)\end{bmatrix}\right\|_\infty<\gamma \quad (17)$$

where the augmented nominal open-loop standard form $\mathbf{P}_C^{\mathrm{LS}}(s)$ is the interface between, on the one hand, the exogenous inputs and the controller outputs and, on the other hand, the performance outputs and controller inputs. The latter system comprises the nominal open-loop plant $\mathbf{G}_C(s)$ and a target closed-loop model $\mathbf{T}_r(s)$ used for model matching. It also contains the weighting filters $\mathbf{W}_M(s),\mathbf{W}_S(s),\mathbf{W}_{KS}(s)$ and $\mathbf{W}_T(s)$ which are used for shaping over frequency, in accordance with the desired closed-loop time and frequency objectives, the singular values of the closed-loop transfer functions related to the model-matching error $\boldsymbol{e}_r(s)=\boldsymbol{y}_r(s)-\boldsymbol{y}_1(s)$ (model-matching sensitivity $\mathbf{M}(s)$), tracking error $\boldsymbol{e}_y(s)=\boldsymbol{y}_c(s)-\boldsymbol{y}_1(s)$ (sensitivity $\mathbf{S}(s)$), control input $\boldsymbol{u}(s)$ (control sensitivity $\mathbf{KS}(s)$), and tracking output $\boldsymbol{y}_1(s)$ (complementary sensitivity $\mathbf{T}(s)$), respectively.

If the sensitivity functions meet the design requirements, an open-loop shaped plant $\mathbf{G}_S(s)=\mathbf{W}_2(s)\,\mathbf{G}_K(s)\,\mathbf{W}_1(s)$ is obtained by opening the closed-loop system $\mathbf{T}_{y_1w}^{\mathrm{LS}}(s)$. The latter, which results from connecting the designed controller $\mathbf{C}(s)$ to the plant $\mathbf{G}_C(s)$ to be controlled, is the closed-loop transfer function between the exogenous reference $\boldsymbol{w}(s)=\boldsymbol{y}_c(s)$ and the tracking output $\boldsymbol{y}_1(s)$ of the block diagram in Fig. 3.

The closed-loop system $\mathbf{T}_{y_1w}^{\mathrm{LS}}(s)$ is here broken at the level of the tracking error $\boldsymbol{e}_y(s)$. The initial open-loop system $\mathbf{G}_K(s)$ contains the plant to be controlled $\mathbf{G}_C(s)$, along with elements of the controller $\mathbf{C}(s)$, whereas the pre- and post-filters $\mathbf{W}_1(s),\mathbf{W}_2(s)$ only comprise controller elements. In addition, the point where the closed-loop system is broken corresponds to the point where the $\mathcal{H}_\infty$ controller $\mathbf{K}_\infty(s)$ is subsequently included.

2DoF $\mathcal{H}_\infty$ NLCF Robust Stabilization

The open-loop shaped plant $\mathbf{G}_S(s)$ is factored as:

$$\mathbf{G}_S(s)=\mathbf{M}_S^{-1}(s)\,\mathbf{N}_S(s),\ \text{with}\ \ \mathbf{M}_S(s)\in\mathbb{R}\mathcal{H}_\infty,\mathbf{N}_S(s)\in\mathbb{R}\mathcal{H}_\infty \quad (18)$$

where $\mathbf{M}_S(s),\mathbf{N}_S(s)$ are stable normalized left coprime factors (NLCF). A family $\mathcal{G}_{S,\Delta}$ of perturbed open-loop shaped plants $\mathbf{G}_{S,\Delta}(s)$ defined about the nominal open-loop shaped plant $\mathbf{G}_S(s)$ and reflecting the modeling uncertainty is given by:

$$\mathcal{G}_{S,\Delta}=\left\{\begin{array}{l}\mathbf{G}_{S,\Delta}(s)=\left[\mathbf{M}_S(s)+\boldsymbol{\Delta}_M(s)\right]^{-1}\left[\mathbf{N}_S(s)+\boldsymbol{\Delta}_N(s)\right]:\\ \left\|\left[\boldsymbol{\Delta}_N(s),-\boldsymbol{\Delta}_M(s)\right]\right\|_\infty<\varepsilon\end{array}\right\} \quad (19)$$

where the stable unknown unstructured perturbations $\boldsymbol{\Delta}_M(s),\boldsymbol{\Delta}_N(s)$ represent the uncertainty. The objective of $\mathcal{H}_\infty$ NLCF robust stabilization is to calculate a controller $\mathbf{K}_\infty(s)$ stabilizing both the nominal $\mathbf{G}_S(s)$ and any perturbed $\mathbf{G}_{S,\Delta}(s)$ open-loop shaped plants, and also verifying the following robustness condition with $\gamma>0$ minimized:

$$\left\|\begin{bmatrix}\mathbf{K}_\infty(s)\\ \mathbb{I}\end{bmatrix}\left\{\mathbb{I}-\mathbf{G}_S(s)\mathbf{K}_\infty(s)\right\}^{-1}\mathbf{M}_S^{-1}(s)\right\|_\infty=\gamma\le\varepsilon^{-1} \quad (20)$$

The stability margin $1/\gamma$ obtained with the controller $\mathbf{K}_\infty(s)$ is upper bounded by the maximum achievable stability margin $\varepsilon_{\max}=1/\gamma_{\min}$, which is calculated exactly as a function of the NLCF $\mathbf{M}_S(s),\mathbf{N}_S(s)$ as follows:

$$\varepsilon_{\max}=\sqrt{1-\left\|\left[\mathbf{N}_S(s),\mathbf{M}_S(s)\right]\right\|_H^2}>0 \quad (21)$$

where $\|\cdot\|_H$ denotes the Hankel norm.

In this work, robust stabilization with an $\mathcal{H}_\infty$ controller $\mathbf{K}_\infty(s)$ leads to significantly degrading the closed-loop system time-domain performance properties initially obtained with a good open-loop shaping. A solution is to devise a 2DoF controller for the set $\mathcal{G}_{S,\Delta}$ of perturbed open-loop shaped plants with input $\boldsymbol{u}_S(s)$ and output $\boldsymbol{y}_S(s)=\boldsymbol{y}_1(s)$ due to the structure chosen above for $\mathbf{G}_S(s)$, generally at the expense of an increase in the stability margin. The 2DoF controller $\mathbf{K}_{f\infty}(s)=[\mathbf{K}_f(s)\ \ \mathbf{K}_\infty(s)]$ here possesses the structure of Fig. 4, comprising a robustifying controller $\mathbf{K}_\infty(s)$ acting on the tracking error $\boldsymbol{e}_y(s)$ and an injection filter $\mathbf{K}_f(s)$ used for recovering the time-domain performance specified by the target system $\mathbf{T}_r(s)$.

A stabilizing structured 2DoF controller $\mathbf{K}_{f\infty}(s)$ is designed, again using the algorithms of [1], to minimize the $\mathcal{H}_\infty$-norm of the closed-loop system from the exogenous reference $\boldsymbol{y}_c(s)$ and disturbance $\boldsymbol{d}_{NM}(s)=\boldsymbol{d}_N(s)+\boldsymbol{d}_M(s)$ inputs symbolizing the NLCF uncertainty to the performance outputs $\boldsymbol{z}_N(s),\boldsymbol{z}_M(s),\boldsymbol{z}_r(s)$, where $\boldsymbol{z}_r(s)$ is the model-matching error: $\left\|\mathbf{T}_{zw}^{\mathrm{RS2}}(s)\right\|_\infty\le\gamma$ with $\gamma>0$. The parameter η permits the designer to adapt the weighted reference signal $\boldsymbol{y}_{c,\eta}(s)=\eta\cdot\boldsymbol{y}_c(s)$, in order to place more or less emphasis on model-matching at the expense of robustness.

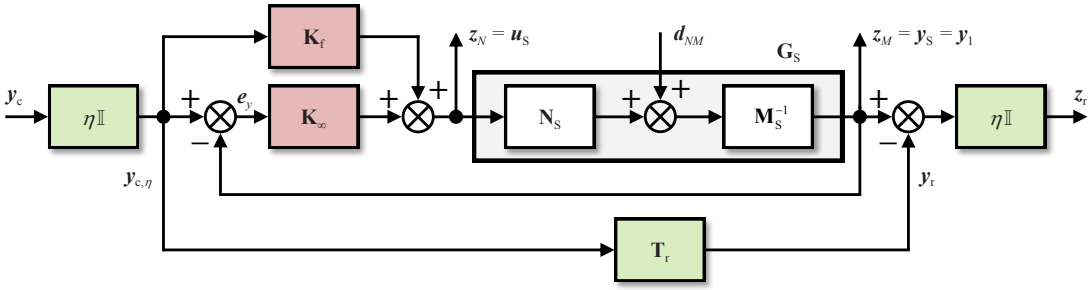

Figure 4 – 2DoF $\mathcal{H}_\infty$ robustifying controller synthesis block diagram

Robust stability is guaranteed if the closed-loop system $\mathrm{T}^{\mathrm{RS2}}_{z_{NM}d_{NM}}(s)$ from the disturbance input $\boldsymbol{d}_{NM}(s)$ to the performance output $\boldsymbol{z}_{NM}(s)=[z_N(s)\ \ \boldsymbol{z}_M(s)]^{\mathrm{T}}$ satisfies the following condition:

$$\left\|\mathrm{T}^{\mathrm{RS2}}_{z_{NM}d_{NM}}(s)\right\|_{\infty}=\gamma^{\star}\leq\varepsilon^{-1},\quad\text{with}\ \ \gamma>\gamma^{\star}>0 \tag{22}$$

where $\gamma^{\star}$ is the obtained stability margin.

Roll-Channel Autopilot

The complete nose roll-channel autopilot structure illustrated in Fig. 5 is composed of two cascaded loops. The internal fast loop contains the *rate controller* $K_p(s)$ that is used for reducing the nose rate $p_{\mathrm{f,f}}(t)$ following the reference signal $p_{\mathrm{f,c}}(t)$, during the ballistic flight subphase ($t_{\mathrm{start}}\leq t<t_{\mathrm{switch}}$). The preceding rate loop also aids the outer slow loop containing the *position controller* $\mathbf{K}_{\phi}(s)$ to ensure tracking of the reference position $\phi_{\mathrm{f,c}}(t)$ during the guided phase ($t_{\mathrm{switch}}\leq t\leq t_{\mathrm{impact}}$). The two controllers are designed separately, with the rate controller obtained first and the position one subsequently computed using the compensated internal rate control loop.

The design of a SISO PID rate controller $K_p(s)$ using the classical loop-shaping approach [30] is not detailed here for brevity purposes. This controller is sufficient to provide good performance properties in terms of robustness, as well as reference tracking and disturbance rejection, as shown from the nonlinear simulation results given at the end of the paper. A position controller $\mathbf{K}_{\phi}(s)$, which must satisfy critical and stringent performance and robustness specifications, is calculated by applying the particular $\mathcal{H}_{\infty}$ loop-shaping design technique proposed in the previous Subsection "$\mathcal{H}_{\infty}$ Loop-Shaping Controller Design Methodology".

The uncertain open-loop transfer function $\tilde{\mathbf{G}}_{\mathrm{R}}(s)$ of the uncertain LTI model of Eqs. (12)-(14) can be written as follows:

$$\begin{bmatrix}\dfrac{\phi_{\mathrm{f}}(s)}{p_{\mathrm{f,f}}(s)}\end{bmatrix}=\tilde{\mathbf{G}}_{\mathrm{R}}(s)\begin{bmatrix}\boldsymbol{d}(s)\\ V_{\mathrm{e}}(s)\end{bmatrix}=\left[\tilde{\mathbf{G}}_{\mathrm{R},d}(s)\ \middle|\ \tilde{\mathbf{G}}_{\mathrm{R},u}(s)\right]\begin{bmatrix}\boldsymbol{d}(s)\\ V_{\mathrm{e}}(s)\end{bmatrix} \tag{23}$$

where the control $\tilde{\mathbf{G}}_{\mathrm{R},u}(s)$ and disturbance $\tilde{\mathbf{G}}_{\mathrm{R},d}(s)$ dynamics are expressed as:

$$\left[\tilde{\mathbf{G}}_{\mathrm{R},d}(s)\ \middle|\ \tilde{\mathbf{G}}_{\mathrm{R},u}(s)\right]= \tag{24}$$
$$\left[\begin{array}{ccc|c}\tilde{G}_{\mathrm{R},\phi d_{\phi}}(s) & \tilde{G}_{\mathrm{R},\phi d_p}(s) & \tilde{G}_{\mathrm{R},\phi d_i}(s) & \tilde{G}_{\mathrm{R},\phi u}(s)\\ 0 & \tilde{G}_{\mathrm{R},pd_p}(s) & \tilde{G}_{\mathrm{R},pd_i}(s) & \tilde{G}_{\mathrm{R},pu}(s)\end{array}\right]$$

Only the control dynamics $\tilde{\mathbf{G}}_{\mathrm{R},u}(s)=[\tilde{G}_{\mathrm{R},\phi u}(s)\ \ \tilde{G}_{\mathrm{R},pu(s)}]^{\mathrm{T}}$ are used here to design a nose position controller, since the effects of the disturbances $\boldsymbol{d}(s)$ of Eq. (14) are insignificant.

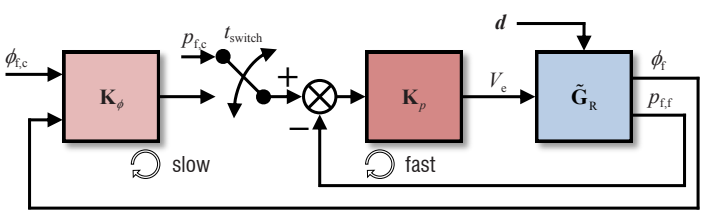

Figure 5 – Complete nose roll-channel autopilot architecture

Open-Loop Shaping

The design of a position controller uses the open-loop system $F_{\mathrm{R},\phi u}(s)$, which is obtained as the series interconnection of the nominal (no uncertainty) control dynamics of the compensated internal loop of Fig. 5 with the nominal position control dynamics $G_{\mathrm{R},\phi u}(s)$ and which is given by:

$$F_{\mathrm{R},\phi u}(s)=\frac{\phi_{\mathrm{f}}(s)}{p_{\mathrm{f,c}}(s)}=G_{\mathrm{R},\phi u}(s)\cdot\frac{K_p(s)}{1+G_{\mathrm{R},pu}(s)K_p(s)} \tag{25}$$

Following the general $\mathcal{H}_{\infty}$ linear controller design setup of Fig. 3, where the open-loop system $G_C(s)=F_{\mathrm{R},\phi u}(s)$ has $u(s)=p_{\mathrm{f,c}}(s)$ as input and $y_1(s)=\phi_{\mathrm{f}}(s)$ as tracking output (no additional output $y_2(s)$). With the reference signal $y_{\mathrm{c}}(s)=\phi_{\mathrm{f,c}}(s)$, the controller inputs are $\boldsymbol{v}(s)=[y_{\mathrm{c}}(s)\ \ y_1(s)]^{\mathrm{T}}=[\phi_{\mathrm{f,c}}(s)\ \ \phi_{\mathrm{f}}(s)]^{\mathrm{T}}$ and the tracking error $e_y(s)=e_{\phi}(s)=\phi_{\mathrm{f,c}}(s)-\phi_{\mathrm{f}}(s)$. The target model $T_{\mathrm{r}}(s)=T_{\phi,\mathrm{r}}(s)$ with input $\phi_{\mathrm{f,c}}(s)$ and output $y_{\mathrm{r}}(s)=\phi_{\mathrm{f,r}}(s)$ is chosen as a second-order filter with a desired natural frequency $\omega_{\phi,\mathrm{r}}=14.5$ rad/s and a damping ratio $\xi_{\phi,\mathrm{r}}=0.79$, giving a settling time $t_{\phi,\mathrm{s}}=0.254$ s for a 2% envelope around steady state. The settling time $t_{\phi,\mathrm{s}}$ is taken as sufficiently large compared to that of the nose-channel internal rate loop and sufficiently small compared to that of the projectile pitch/yaw-channel control loop without leading to saturation of the coaxial motor.

Controller design is here performed by shaping only the closed-loop model-matching, sensitivity and control sensitivity functions using the following model-matching filter $W_M(s)$:

$$W_M(s)=\frac{\frac{1}{k_M}s+\omega_M}{s+\omega_M\varepsilon_M} \tag{26}$$

whose inverse is a high-pass filter, since the model-matching transfer function frequency content is in the shape of a bell centered on the intermediate frequencies (see Fig. 7b). The error between the responses of the target and shaped closed-loop transfer functions is reduced as much as possible at low frequencies in order to ensure a good reference tracking and, at intermediate frequencies, to improve the transient response. The values given to the parameters ε_M and k_M adequately adjust the gain of $W_M^{-1}(s)$ at low and high frequencies, respectively, whereas the critical parameter ω_M, initially set to the target closed-loop system bandwidth $\omega_{\phi,\mathrm{c}}$, is used to adapt the cutoff frequency. The tracking error filter $W_S(s)$ is chosen as:

$$W_S(s)=\frac{s^2+2\xi_{\phi,\mathrm{r}}\omega_{\phi,\mathrm{r}}s+\omega_{\phi,\mathrm{r}}^2}{s^2+2\xi_{\phi,\mathrm{r}}\omega_{\phi,\mathrm{r}}s+\varepsilon_S} \tag{27}$$

whose inverse is equal to the 2nd-order low-pass filter $S_{\phi,\mathrm{r}}(s)=1-T_{\phi,\mathrm{r}}(s)$, in which a small $\varepsilon_S>0$ is added to obtain a stable filter. The weighting $W_S(s)$ is used to adjust the closed-loop system bandwidth, steady-state error and overshoot. The control filter $W_{KS}(s)$ is defined as:

$$W_{KS}(s)=\left(\frac{k_{KS}\varepsilon_{KS}}{\omega_{KS}}\right)\cdot\frac{s+\omega_{KS}}{s+\varepsilon_{KS}} \tag{28}$$

whose inverse is a 1st-order low-pass filter with a static gain k_{KS}^{-1}, a bandwidth ω_{KS} and a high-frequency negative real zero ensured by $\varepsilon_{KS}>0$ and used to obtain a proper and stable weighting $W_{KS}(s)$. The control signal weight limits the control bandwidth at high frequencies by adjusting ω_{KS}, initially fixed to $\omega_{\phi,\mathrm{c}}$, in order to limit the risk of coaxial motor saturations.

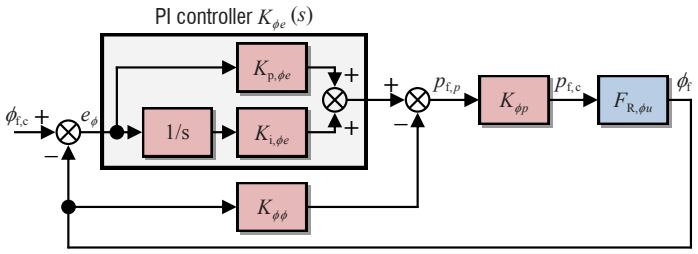

Figure 6 – Structure of the nose position PI-P controller $\mathbf{C}(s)$

Controller synthesis results

The designed reduced-order (RO) controller $\mathbf{C}(s)$ of Fig. 3 possesses the PI-P (proportional-integral & proportional) structure illustrated in detail in Fig. 6. It comprises a tracking error PI servo-controller $K_{\phi e}(s)$, an output feedback regulation proportional gain $K_{\phi\phi}$ and a roll-off/protection 1st-order filter $K_{\phi p}(s)$. The control signal is given by:

$$p_{f,c}(s) = K_{\phi p}(s)\left\{K_{\phi e}(s)\phi_{f,c}(s) - \left[K_{\phi e}(s) + K_{\phi\phi}\right]\phi_f(s)\right\} \quad (29)$$

with:

$$K_{\phi e}(s) = \frac{K_{p,\phi e}\, s + K_{i,\phi e}}{s} \quad (30a)$$

$$K_{\phi p}(s) = \frac{1}{\tau_{\phi p} s + 1} \quad (30b)$$

Figures 7a-7d give the RO and fixed structure controller synthesis results (blue), which are compared to those obtained for the design of a full-order (FO) controller (magenta). The target (red) and shaped (magenta for FO and blue for RO controllers) closed-loop transfer functions possess the desired properties conforming to robust control theory [11, 30]. For the sensitivities $\mathbf{S}(s)$, the small low-frequency gains indicate a very good minimization of the steady-state tracking error and the peak at intermediate frequencies, which remains small, leads to a good robustness with respect to unstructured inverse multiplicative uncertainties. For the model-matching sensitivities $\mathbf{M}(s)$, the small gains, in particular at intermediate frequencies, show a good target model following. For the control sensitivities $\mathbf{KS}(s)$ that present a peak around the desired closed-loop system bandwidth $\omega_{\phi,c}$, those possess a good roll-off from the intermediate frequencies avoiding large controller gains and limiting the control bandwidth, and hence maintaining moderate actuator usage. Finally, for the complementary sensitivities $\mathbf{T}(s)$, the low-frequency gains close to 0 dB also indicate the excellent steady-state tracking error reduction, the absence of a peak at intermediate frequencies denotes robustness with respect to unstructured multiplicative uncertainties, and small high-frequency gains help with measurement noise attenuation.

Open-loop shaped plant

A nominal RO open-loop shaped plant $G_S(s) = W_2 G_K(s)\, W_1(s)$, which is illustrated in Fig. 8, is here defined by breaking the closed-loop system of Fig. 6 at the level of the tracking error $e_\phi(s)$, as

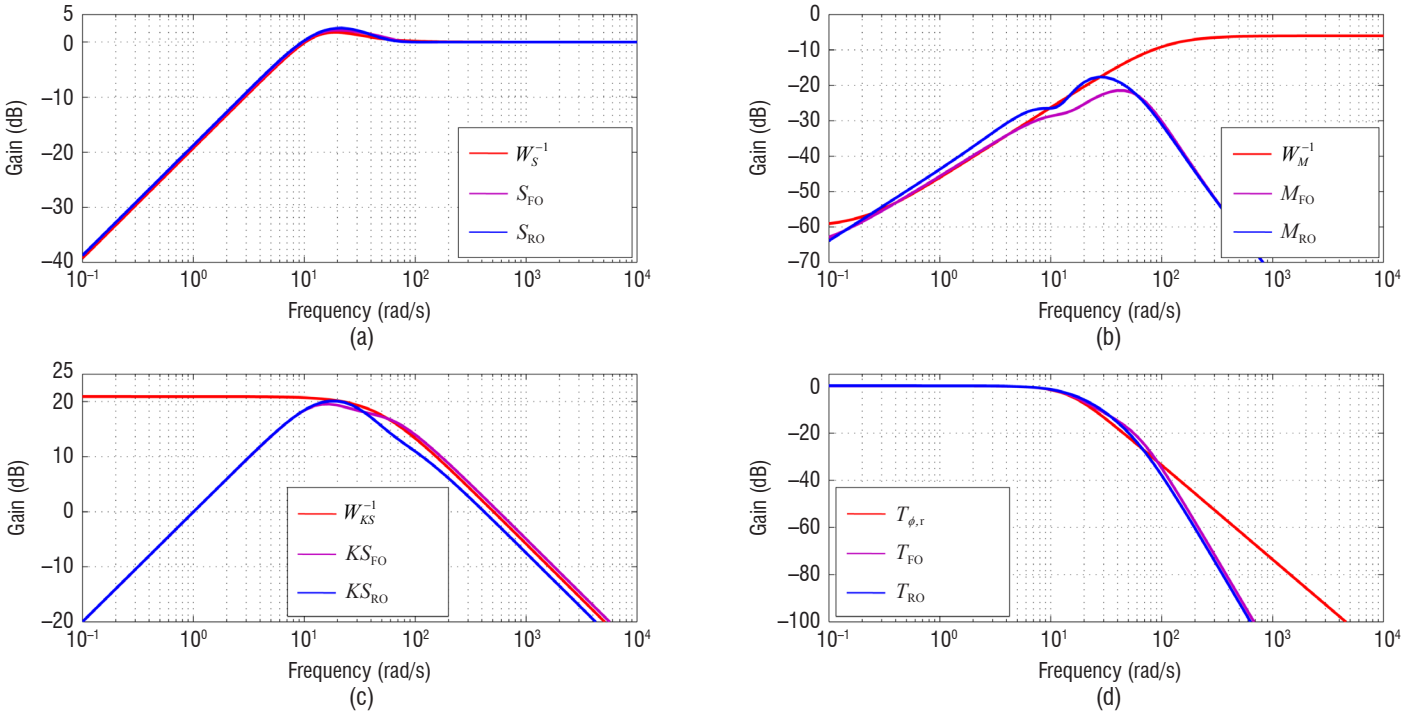

Figure 7 – Frequency responses of the position loop target (red) and shaped (magenta: FO, blue: RO) closed-loop transfer functions related to the: (a) tracking error $e_\phi(s)$, (b) model-matching error $e_r(s)$, (c) control $p_{f,c}(s)$, (d) output $\phi_f(s)$ signals

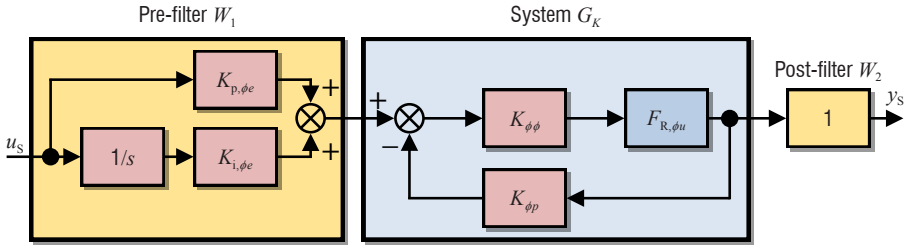

Figure 8 – Open-loop shaped plant $G_S(s) = W_2 G_K(s)\, W_1(s)$ block diagram

explained in Subsection "$\mathcal{H}_\infty$ Loop-Shaping Controller Design Methodology". The gain of $G_{\mathrm{S}}(s)$ (blue), along with that of a similar FO open-loop shaped plant built with the closed-loop system containing the FO controller (magenta), are shown in Fig. 9 and compared to the initial open-loop system $F_{\mathrm{R},\phi u}(s)$ (black). The RO and FO open-loop shaped plants have close gains with desired properties, and possess crossover frequencies larger than that of the open-loop system denoting a faster system response obtained thanks to open-loop shaping. Finally, the very good value $\varepsilon_{\max} = 0.5942$ is achieved for the maximum stability margin associated with $G_{\mathrm{S}}(s)$.

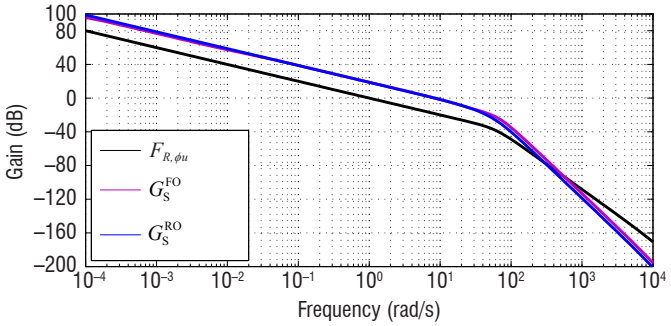

Figure 9 – Gains of the open-loop system $F_{\mathrm{R},\phi u}(s)$ (black), and of the FO (magenta) and RO (blue) open-loop shaped plants $G_{\mathrm{S}}^{\mathrm{FO}}(s)$ and $G_{\mathrm{S}}^{\mathrm{RO}}(s)$

2DoF NLCF $\mathcal{H}_\infty$ Robust Stabilization

A 2DoF fixed structure and reduced order controller $\mathbf{K}_{\phi\mathrm{f}\infty}(s)$, which is calculated for the open-loop shaped plant $G_{\mathrm{S}}(s)$ depicted in Fig. 8 using the linear controller design setup of Fig. 4, here comprises a robustifying gain $K_{\phi\infty}$ and an injection 1st-order lead-lag filter $K_{\phi\mathrm{f}}(s)$ with time constants $\tau_{\phi\mathrm{f}}^{\mathrm{lead}}$ and $\tau_{\phi\mathrm{f}}^{\mathrm{lag}}$ and defined as:

$$K_{\phi\mathrm{f}}(s) = \frac{\tau_{\phi\mathrm{f}}^{\mathrm{lead}}\, s + 1}{\tau_{\phi\mathrm{f}}^{\mathrm{lag}}\, s + 1} \tag{31}$$

The target system $T_{\phi,\mathrm{r}}(s)$ is used again for NLCF $\mathcal{H}_\infty$ robust stabilization, and controller tuning using $\eta = 0.1$ gives the reasonable performance index $\gamma_{\mathrm{RO2}} = 1.8473$. The actually achieved stability margin $\varepsilon_{\mathrm{RO2}} = 1/\gamma_{\mathrm{RO2}}^{\star} = 0.5487$ is excellent and close both to the stability margin $\varepsilon_{\mathrm{FO2}} = 1/\gamma_{\mathrm{FO2}}^{\star} = 0.5933$ obtained with a robustifying FO 2DoF controller and to the very good maximum stability margin $\varepsilon_{\max} = 0.5942$. Consequently, the degradation of the low and high-frequency gains of the initial open-loop shaped plant $G_{\mathrm{S}}(s)$ is very limited.

The complete external nose-channel position 2DoF structured controller $\mathbf{K}_{\phi}(s)$ of Fig. 5 is obtained by combining the PI-P controller $\mathbf{C}(s)$ used for open-loop shaping, along with the 2DoF robustifying RO controller $\mathbf{K}_{\phi\mathrm{f}\infty}(s)$, as illustrated in detail in Fig. 10. A static pre-filter $K_{\phi\mathrm{sc}}$ is added after robust stabilization, in order to ensure a unitary steady-state gain for the closed-loop transfer function between the reference $\phi_{\mathrm{f,c}}(s)$ and the output $\phi_{\mathrm{f}}(s)$ signals, given the integral action in the PI-P controller. This pre-filter is obtained as follows:

$$K_{\phi\mathrm{sc}} = \frac{K_{\phi\infty}}{K_{\phi\infty} + K_{\phi\mathrm{f}}(s)\big|_{s=0}} \tag{32}$$

The control signal $p_{\mathrm{f,c}}(s)$ is given by:

$$\begin{aligned} p_{\mathrm{f,c}}(s) = {} & K_{\phi p}(s) K_{\phi e}(s) \left\{ K_{\phi\mathrm{f}}(s) + K_{\phi\infty} \right\} K_{\phi\mathrm{sc}}\, \phi_{\mathrm{f,c}}(s) \\ & - K_{\phi p}(s) \left\{ K_{\phi e}(s) K_{\phi\infty} + K_{\phi\phi} \right\} \phi_{\mathrm{f}}(s) \end{aligned} \tag{33}$$

The singular value of the complete nose position 2DoF RO controller $\mathbf{K}_{\phi}(s)$ (green) possesses a limited bandwidth with a good roll-off at high frequencies, as shown in Fig. 11. It also remains close to the singular values of the PI-P controller used for open-loop shaping (black), and of a 2DoF controller built with the PI-P and the robustifying 2DoF FO controllers (magenta).

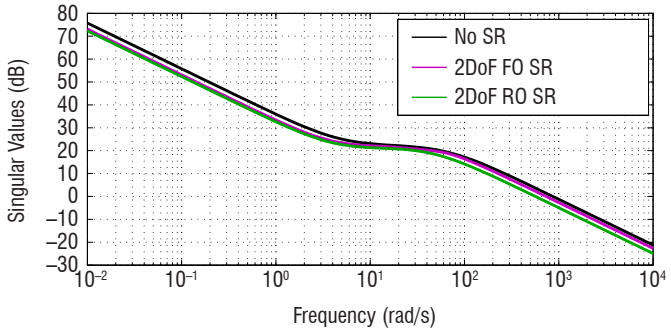

Figure 11 – Singular values of the nose position controllers: without any robustifying 2DoF controller (black), with the robustifying 2DoF FO controller (magenta), and with the robustifying 2DoF RO controller (green)

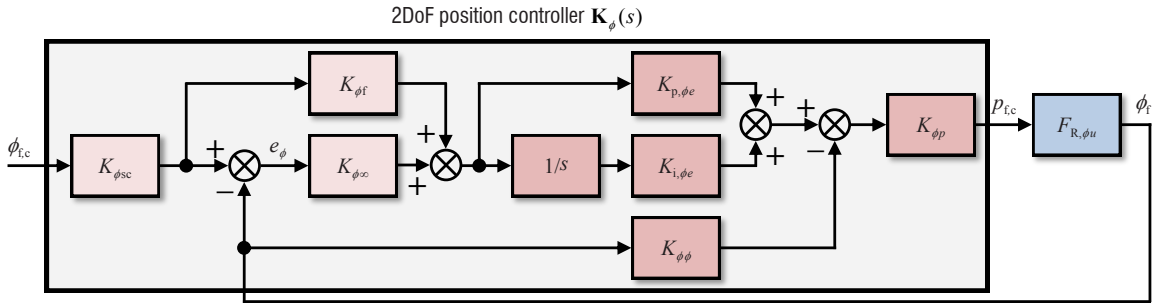

Figure 10 – 2DoF structure of the nose position controller $\mathbf{K}_{\phi}(s)$

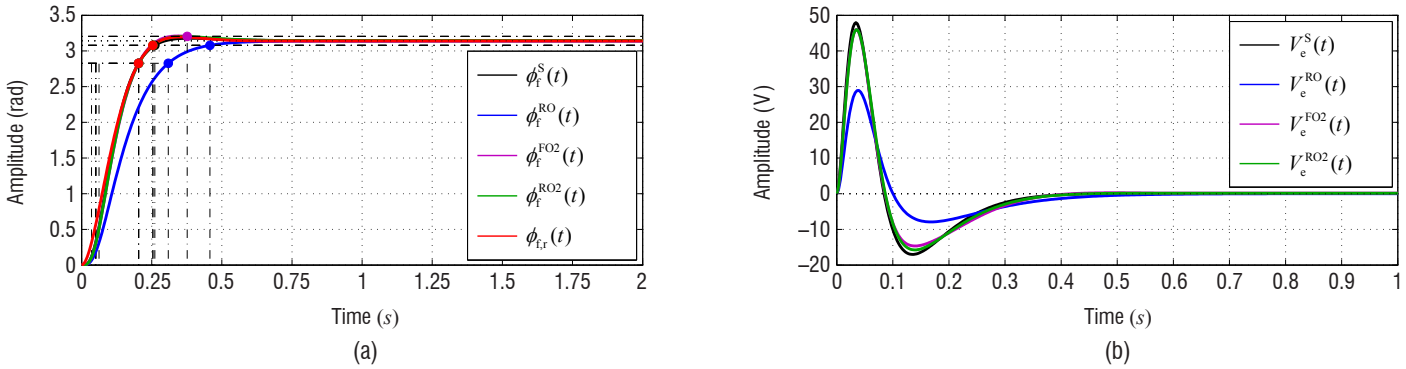

Figure 12 – Closed-loop step responses: (a) roll angle $\phi_{\mathrm{f}}(t)$, (b) actuator input voltage $V_{\mathrm{e}}(t)$

Finally, Figs. 12a, 12b give the step responses for the transfer functions of the complete nose position control loop of Fig. 10, which are related to the output $\phi_{\mathrm{f}}(t)$ and voltage $V_{\mathrm{e}}(t)$ (green), for a step amplitude of π rad corresponding to the maximal value potentially taken by $\phi_{\mathrm{f,c}}(t)$ at the beginning of the projectile flight guided phase. In Fig. 12a, the output-related time response follows very well the target system response (red), contrary to that of a closed-loop system obtained with the open-loop shaped plant $G_{\mathrm{S}}(s)$ and a 1DoF robustifying controller (blue). Hence, the time performance initially obtained for the closed-loop system used for open-loop shaping (black) is perfectly recovered. The use of the robustifying 2DoF FO controller does not give satisfactory performance results. In Fig. 12b, the voltage $V_{\mathrm{e}}(t)$ applied to the coaxial motor remains reasonable.

Robust Stability Analysis

The preceding complete nose position autopilot is tested for robust stability, first with respect to an NLCF uncertainty block $[\boldsymbol{\Delta}_N(s), \boldsymbol{\Delta}_M(s)]$, using the robustness criterion of the $\mathcal{H}_\infty$ loop shaping design procedure. The estimated size $\varepsilon = 0.0627$ of this unstructured uncertainty, which corresponds to the various uncertain parameters considered in the nose-channel dynamics linear model of Eq. (12), verifies $\varepsilon \leq \varepsilon_{\mathrm{RO2}} = 0.5413$ and hence robust stability is guaranteed[1].

Robust stability is also tested by applying the μ-analysis theory tools [41, 30] to the uncertain closed-loop system $\tilde{\mathbf{T}}_{\phi_{\mathrm{f}}\phi_{\mathrm{f,c}}}(s) = \mathcal{F}_{\mathrm{l}}[\tilde{\mathbf{P}}_K(s), \mathbf{K}_\phi(s)]$ associated with the nominal closed-loop model of Fig. 10. The uncertain open-loop augmented plant $\tilde{\mathbf{P}}_K(s)$ enclosing all of the real parametric uncertainties can be written as the u-LFT of a nominal open-loop system $\mathbf{P}_K^{\Delta}(s)$ and of a stable, diagonal, real, normalized parametric perturbation $\boldsymbol{\Delta}$ as:

$$\tilde{\mathbf{P}}_K(s) = \mathcal{F}_{\mathrm{u}}[\mathbf{P}_K^{\Delta}(s), \boldsymbol{\Delta}] \tag{34}$$

with:

$$\boldsymbol{\Delta} = \left\{ \mathrm{diag}\left[\delta_{K_{\mathrm{a}}}\mathbb{I}_1, \delta_{K_{\mathrm{b}}}\mathbb{I}_1, \delta_{K_{\mathrm{m}}}\mathbb{I}_1, \delta_{K_{\mathrm{v}}}\mathbb{I}_1, \delta_L\mathbb{I}_1, \delta_R\mathbb{I}_1 \right] : |\delta_i| \leq 1, \delta_i \in \mathbb{R} \right\} \tag{35}$$

The uncertain closed-loop system $\tilde{\mathbf{T}}_{\phi_{\mathrm{f}}\phi_{\mathrm{f,c}}}(s)$ can hence be obtained as the following *l*-LFT:

$$\begin{aligned} \tilde{\mathbf{T}}_{\phi_{\mathrm{f}}\phi_{\mathrm{f,c}}}(s) &= \mathcal{F}_{\mathrm{u}}\left[\mathbf{N}_K^{\Delta}(s), \boldsymbol{\Delta} \right] \\ &\triangleq \mathbf{N}_K^{\Delta,22}(s) + \mathbf{N}_K^{\Delta,21}(s)\boldsymbol{\Delta}\left[\mathbb{I} - \mathbf{N}_K^{\Delta,11}(s)\boldsymbol{\Delta} \right]^{-1} \mathbf{N}_K^{\Delta,12}(s) \end{aligned} \tag{36}$$

where the nominal system $\mathbf{N}_K^{\Delta}(s)$, internally stabilized by the controller $\mathbf{K}_\phi(s)$, is given by:

$$\mathbf{N}_K^{\Delta}(s) = \mathcal{F}_{\mathrm{l}}\left[\mathbf{P}_K^{\Delta}(s), \mathbf{K}_\phi(s) \right] \tag{37}$$

The only source of instability in the uncertain closed-loop system of Eq. (36) can originate from the feedback term $[\mathbb{I} - \mathbf{N}_K^{\Delta,11}(s)\boldsymbol{\Delta}]^{-1}$ between the stable systems $\mathbf{M}_K^{\Delta}(s) = \mathbf{N}_K^{\Delta,11}(s)$ and $\boldsymbol{\Delta}$. Robust stability (RS) of the uncertain closed-loop system with respect to the uncertainty $\boldsymbol{\Delta}$ is guaranteed if and only if:

$$\mathrm{RS} \Leftrightarrow \mu_{\Delta}\left[\mathbf{M}_K^{\Delta}(j\omega) \right] < 1, \quad \forall \omega \in \mathbb{R}^+ \tag{38}$$

where $\mu_{\Delta}(\cdot)$ is the structured singular value (SSV).

Upper and lower bounds for the SSV are numerically calculated over a frequency grid for the levels of parametric uncertainties presented in Subsection "Roll-Channel" of Part "Airframe Modeling". Given that the upper bound is always smaller than 1, as seen in Fig. 13, RS is confirmed with an important stability margin here.

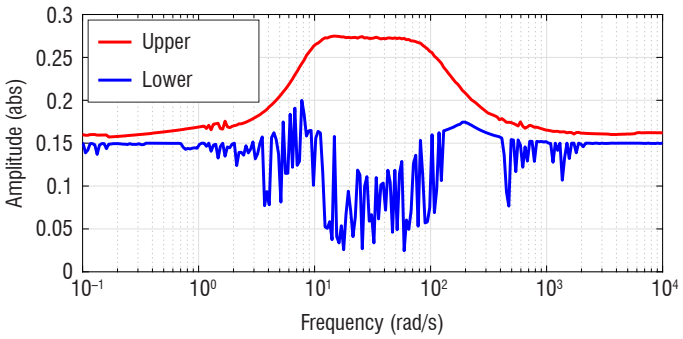

Figure 13 – Upper and lower SSV bounds calculated for the uncertain closed-loop system

[1] It is worth noting that a good robustness to coprime uncertainty to the open-shaped plant $G_{\mathrm{S}}(s)$ of Fig. 8 does not necessarily lead to good robustness margins at the input and outputs of the actual nominal control dynamics plant $\mathbf{G}_{\mathrm{R},u}(s)$ given by Eqs. (23), (24), the latter plant being contained in the system $F_{\mathrm{R},\phi u}(s)$ given by Eq. (25). Satisfactory multi-loop disk gain and phase margins [4] are, however, obtained here at the actual plant input (MDG = ±10.4 dB and MDP = ±56.4°) and outputs (MDG = ±3.7 dB and MDP = ±24.1°).

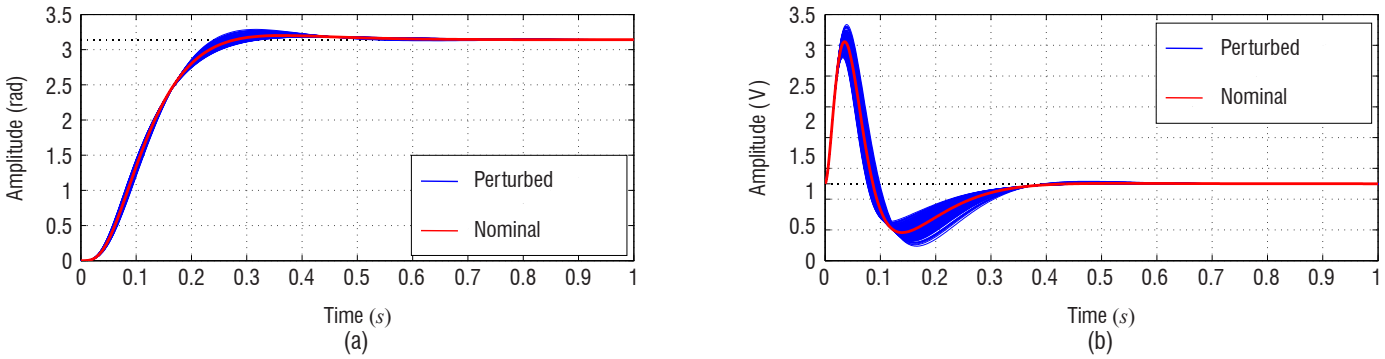

Figure 14 – Uncertain closed-loop system step responses: (a) roll angle, (b) actuator voltage

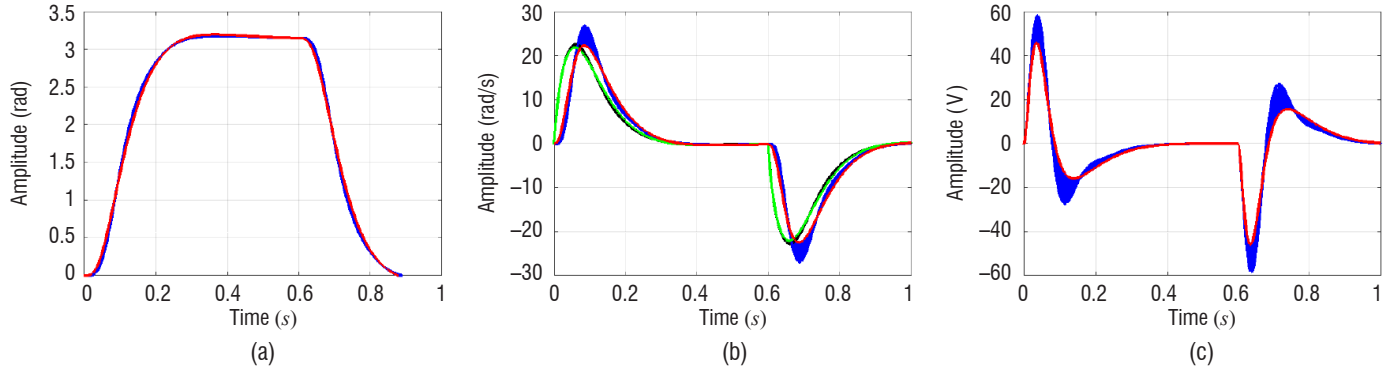

Figure 15 – Closed-loop time responses with transmission delays at actuator input: (a) roll angle (blue: perturbed, red: nominal), (b) reference (black: perturbed, green: nominal) and output (blue: perturbed, red: nominal) roll rates, (c) actuator voltage (blue: perturbed, red: nominal)

Two additional linear simulation results are given in Figs. 14, 15. The first figure depicts nose-channel output angle $\phi_{\mathrm{f}}(t)$ and actuator voltage $V_{\mathrm{e}}(t)$ step responses of 200 uncertain closed-loop system random samples, from which robust stability can be verified again and no excessive input voltage to the coaxial motor is demanded. The second figure shows step responses related to the output roll position and rate $\phi_{\mathrm{f}}(t), p_{\mathrm{f,f}}(t)$, internal loop input roll rate $p_{\mathrm{f,c}}(t)$, and voltage $V_{\mathrm{e}}(t)$, given actuator input transmission delays of up to 9 ms, *i.e.*, around 5 times a rate of 1/600 s with which the control signal could be sampled. Stability is preserved, the degradations appearing on the different time responses remain more or less limited with respect to the nominal case, and there is no actuator saturation. Hence, the nose position control loop can handle realistic delays of up to 3 times the control signal sampling rate [32], *i.e.*, 5 ms.

Pitch/Yaw-Channel Autopilot

Augmented Plant for Controller Synthesis

Autopilot design for the pitch/yaw-channel dynamics linearized at any operating point is based on the open-loop actuator/projectile/sensor dynamics *q*-LPV model described in Subsection "Pitch/Yaw-Channels" of Part "Airframe Modeling". The load factor output measurements are actually provided at the projectile nose, and hence those do not match the necessary feedback signals, which must be available here at the projectile CM, since the nonlinear force dynamic equations are written for this point. The load factor feedback signals are calculated at the CM through a transformation based on an inverse Grubin transformation [40] and using the measured load factor and angular rate outputs. The angular rate measurements remain valid for any point of the projectile. The transformation system $\mathbf{T}^{\rho}_{n\omega}(s,\boldsymbol{\rho}_{\mathrm{PY}})$, which calculates in the non-rolling frame B′ CS at the CM the load factors $\breve{\boldsymbol{n}}_{\mathrm{zy},\varepsilon}(s)=[\breve{n}_{\mathrm{z},\varepsilon}(s)\ \breve{n}_{\mathrm{y},\varepsilon}(s)]^{\mathrm{T}}$ and angular rates $\breve{\boldsymbol{\omega}}_{qr,\varepsilon}(s)=[\breve{q}_{\varepsilon}(s)\ \breve{r}_{\varepsilon}(s)]^{\mathrm{T}}$, from the measurements $\boldsymbol{n}_{\mathrm{zy},\varepsilon,\mathrm{m}}(s)=[n_{\mathrm{z},\varepsilon,\mathrm{m}}(s)\ n_{\mathrm{y},\varepsilon,\mathrm{m}}(s)]^{\mathrm{T}}$ and $\boldsymbol{\omega}_{qr,\varepsilon,\mathrm{m}}(s)=[q_{\varepsilon,\mathrm{m}}(s)\ r_{\varepsilon,\mathrm{m}}(s)]^{\mathrm{T}}$ obtained in the nose frame $\mathrm{B_f}$ CS, is defined as:

$$\begin{aligned}\begin{bmatrix}\breve{n}_{\mathrm{z},\epsilon}(s)\\ \breve{n}_{\mathrm{y},\epsilon}(s)\end{bmatrix}&=\mathbf{T}(\phi_{\mathrm{f}})\mathbf{W}_{\mathrm{b},n}(s,\boldsymbol{\lambda}_{\mathrm{PY}})\begin{bmatrix}n_{\mathrm{z},\epsilon,\mathrm{m}}(s)\\ n_{\mathrm{y},\epsilon,\mathrm{m}}(s)\end{bmatrix}\\&-\left(\frac{x_{\mathrm{IMU}}}{g}\right)p_{\mathrm{f,f}}(s)\mathbf{T}(\phi_{\mathrm{f}})\mathbf{W}_{\mathrm{b},\omega}(s,\boldsymbol{\lambda}_{\mathrm{PY}})\begin{bmatrix}r_{\epsilon,\mathrm{m}}(s)\\ q_{\epsilon,\mathrm{m}}(s)\end{bmatrix}\\&+\left(\frac{x_{\mathrm{IMU}}}{g}\right)\mathbf{W}_{\mathrm{d},\omega}(s,\boldsymbol{\lambda}_{\mathrm{PY}})\overline{\mathbf{T}}(\phi_{\mathrm{f}})\mathbf{W}_{\mathrm{b},\omega}(s,\boldsymbol{\lambda}_{\mathrm{PY}})\begin{bmatrix}q_{\epsilon,\mathrm{m}}(s)\\ r_{\epsilon,\mathrm{m}}(s)\end{bmatrix}\end{aligned}\tag{39a}$$

$$\begin{bmatrix}\breve{q}_{\epsilon}(s)\\ \breve{r}_{\epsilon}(s)\end{bmatrix}=\overline{\mathbf{T}}(\phi_{\mathrm{f}})\mathbf{W}_{\mathrm{b},\omega}(s,\boldsymbol{\lambda}_{\mathrm{PY}})\begin{bmatrix}q_{\epsilon,\mathrm{m}}(s)\\ r_{\epsilon,\mathrm{m}}(s)\end{bmatrix}\tag{39b}$$

with the matrix $\mathbf{T}(\phi_{\mathrm{f}})$ given in Eq. (6). The diagonal parameter-dependent 1st-order approximated derivative filters $\mathbf{W}_{\mathrm{d},\omega}(s,\boldsymbol{\lambda}_{\mathrm{PY}})=\mathrm{diag}[W_{\mathrm{d},\omega}(s,\boldsymbol{\lambda}_{\mathrm{PY}}),-W_{\mathrm{d},\omega}(s,\boldsymbol{\lambda}_{\mathrm{PY}})]$ are applied to the angular rates, and the identical diagonal parameter-dependent 2nd-order low-pass filters $\mathbf{W}_{\mathrm{b},n}(s,\boldsymbol{\lambda}_{\mathrm{PY}})=\mathbf{W}_{\mathrm{b},\omega}(s,\boldsymbol{\lambda}_{\mathrm{PY}})=\mathrm{diag}[W_{\mathrm{b}}(s,\boldsymbol{\lambda}_{\mathrm{PY}}),W_{\mathrm{b}}(s,\boldsymbol{\lambda}_{\mathrm{PY}})]$, which are obtained as the product of two 1st-order systems, are used for measurement noise attenuation. Tuning the parameters of the previous filters is critical due to their significant influence on closed-loop system performance and robust stability.

Finally, controller synthesis following the strategy presented in Subsection "$\mathcal{H}_{\infty}$ Loop-Shaping Controller Design Methodology" is performed with an augmented open-loop uncertain plant $\tilde{\mathbf{G}}_{\mathrm{PY}}(s,\boldsymbol{\lambda}_{\mathrm{PY}})$, which is composed of the simplified *q*-LPV model of the uncertain actuator/projectile/sensor dynamics parameterized by $\boldsymbol{\lambda}_{\mathrm{PY}}=[V\ \ h]^{\mathrm{T}}$, and of a simplified transformation system $\mathbf{T}^{\lambda}_{n\omega}(s,\boldsymbol{\lambda}_{\mathrm{PY}})$ obtained by imposing $(\phi_{\mathrm{f}},p_{\mathrm{f,f}})=(0,0)$ in Eqs. (39). The multivariable plant $\tilde{\mathbf{G}}_{\mathrm{PY}}(s,\boldsymbol{\lambda}_{\mathrm{PY}})$,

having the actuator commands $\boldsymbol{\delta}_{\mathrm{mn},\varepsilon,\mathrm{c}}(s)$ as inputs and the feedback signals $\breve{\boldsymbol{n}}_{\mathrm{zy},\varepsilon}(s), \breve{\boldsymbol{\omega}}_{qr,\varepsilon}(s)$ as outputs, contains zeros in its SISO load factor transfer functions that are potentially NMP as a function of the operating condition. These zeros are, however, sufficiently fast compared to the desired closed-loop bandwidth, contrary to those of the projectile pitch/yaw-channel dynamics (see Subsection "Pitch/Yaw-Channels" of Part "Airframe Modeling").

Open-Loop Shaping

The various systems and signals, appearing in the $\mathcal{H}_\infty$ linear controller design diagram of Fig. 3 used here for defining at any fixed synthesis point $\overline{\boldsymbol{\lambda}}_{\mathrm{PY}}$ a pitch/yaw-channel open-loop shaped plant, are explicitly presented. The system to control $\mathbf{G}_C(s)$ is equal to the augmented plant $\breve{\mathbf{G}}_{\mathrm{PY}}(s,\overline{\boldsymbol{\lambda}}_{\mathrm{PY}}) = [\breve{\mathbf{G}}_{\mathrm{PY},n}(s,\overline{\boldsymbol{\lambda}}_{\mathrm{PY}}), \breve{\mathbf{G}}_{\mathrm{PY},\omega}(s,\overline{\boldsymbol{\lambda}}_{\mathrm{PY}})]^{\mathrm{T}}$ with input $\boldsymbol{u}(s) = \boldsymbol{\delta}_{\mathrm{mn},\varepsilon,\mathrm{c}}(s)$ and outputs $\boldsymbol{y}_1(s) = \breve{\boldsymbol{n}}_{\mathrm{zy},\varepsilon}(s), \boldsymbol{y}_2(s) = \breve{\boldsymbol{\omega}}_{qr,\varepsilon}(s)$. The target model $\mathbf{T}_{\mathrm{r}}(s)$, with input $\boldsymbol{y}_{\mathrm{c}}(s) = \boldsymbol{n}_{\mathrm{zy},\varepsilon,\mathrm{c}}(s) = [n_{\mathrm{z,c}}(s)\ \ n_{\mathrm{y,c}}(s)]^{\mathrm{T}}$ and output $\boldsymbol{y}_{\mathrm{r}}(s) = \boldsymbol{n}_{\mathrm{zy},\varepsilon,\mathrm{r}}(s) = [\boldsymbol{n}_{\mathrm{z,r}}(s)\ \ \boldsymbol{n}_{\mathrm{y,r}}(s)]^{\mathrm{T}}$, is a block-diagonal 2nd-order system $\mathbf{T}_{n,\mathrm{r}}(s) = \mathrm{diag}[T_{n,\mathrm{r}}(s), T_{n,\mathrm{r}}(s)]$ with a natural frequency $\omega_{n,\mathrm{r}} = 4.9\,\mathrm{rad/s}$ and a damping ratio $\xi_{n,\mathrm{r}} = 0.79$ giving a settling time $t_{n,\mathrm{s}} = 0.751\,\mathrm{s}$ for a 2% envelope around steady state. The obtained pitch/yaw-channel closed system response is hence sufficiently fast without saturating the canard actuators, while being sufficiently slow with respect to the nose-channel position control loop response.

The parameter-dependent model-matching $\mathbf{W}_M(s,\overline{\boldsymbol{\lambda}}_{\mathrm{PY}}) = \mathrm{diag}[W_M(s,\overline{\boldsymbol{\lambda}}_{\mathrm{PY}}), W_M(s,\overline{\boldsymbol{\lambda}}_{\mathrm{PY}})]$ and the performance $\mathbf{W}_S(s) = \mathrm{diag}[W_S(s), W_S(s)]$ weights are defined as for nose position autopilot design, whereas the control signal weight $\mathbf{W}_{KS}(s,\overline{\boldsymbol{\lambda}}_{\mathrm{PY}}) = \mathrm{diag}[W_{KS}(s,\overline{\boldsymbol{\lambda}}_{\mathrm{PY}}), W_{KS}(s,\overline{\boldsymbol{\lambda}}_{\mathrm{PY}})]$ is:

$$W_{KS}\left(s,\overline{\boldsymbol{\lambda}}_{\mathrm{PY}}\right) = \left(\frac{s+\omega_{KS}\left(\overline{\boldsymbol{\lambda}}_{\mathrm{PY}}\right)k_{KS}^{1/2}\left(\overline{\boldsymbol{\lambda}}_{\mathrm{PY}}\right)}{\varepsilon_{KS}^{-1/2}s+\omega_{KS}\left(\overline{\boldsymbol{\lambda}}_{\mathrm{PY}}\right)}\right)^2 \tag{40}$$

The inverse of $W_{KS}(s,\overline{\boldsymbol{\lambda}}_{\mathrm{PY}})$ is equal to the product of two identical 1st-order low-pass filters with a steady-state gain $k_{KS}^{-1/2}(\overline{\boldsymbol{\lambda}}_{\mathrm{PY}})$, a bandwidth adjusted with $\omega_{KS}(\overline{\boldsymbol{\lambda}}_{\mathrm{PY}})$, and a high-frequency negative real zero ensured by $\varepsilon_{KS} > 0$ and making the weight proper and stable. For any synthesis point $\overline{\boldsymbol{\lambda}}_{\mathrm{PY}}$, the steady-state gain $k_{KS}^{-1}(\overline{\boldsymbol{\lambda}}_{\mathrm{PY}})$ of $W_{KS}(s,\overline{\boldsymbol{\lambda}}_{\mathrm{PY}})$ is conditioned by the low-frequency minimal singular value of the synthesis system: $k_{KS}(\overline{\boldsymbol{\lambda}}_{\mathrm{PY}}) \simeq \underline{\sigma}[\breve{\mathbf{G}}_{\mathrm{PY}}(0,\overline{\boldsymbol{\lambda}}_{\mathrm{PY}})]$. The frequency $\omega_{KS}(\overline{\boldsymbol{\lambda}}_{\mathrm{PY}})$, which is initially set to the target closed-loop system bandwidth $\omega_{n,\mathrm{r}} = 4.9\,\mathrm{rad/s}$, can be increased for specific operating conditions where a faster control signal is needed, such as, for example, at a low airspeed/high altitude flight point. Finally, the output signal weight $\mathbf{W}_T(s) = \mathrm{diag}[W_T(s), W_T(s)]$ is defined as:

$$W_T\left(s\right) = \frac{s^2+2\xi_{n,\mathrm{r}}\,\omega_{n,\mathrm{r}}s+\omega_{n,\mathrm{r}}^2}{\omega_{n,\mathrm{r}}^2\left(\varepsilon_T^{-1}s+1\right)^2} \tag{41}$$

The filter $W_T(s)$ is the result of inverting the target system and adding two high-frequency negative real poles $\varepsilon_T > 0$ to render it proper and stable. The output signal weight leads to attenuating noise on the feedback output load factors $\breve{\boldsymbol{n}}_{\mathrm{zy},\varepsilon}$ and helps both the performance filter to minimize the steady-state error $\boldsymbol{e}_n(s)$ and the model-matching filter to reduce the difference between the target and shaped closed-loop system at intermediate frequencies.

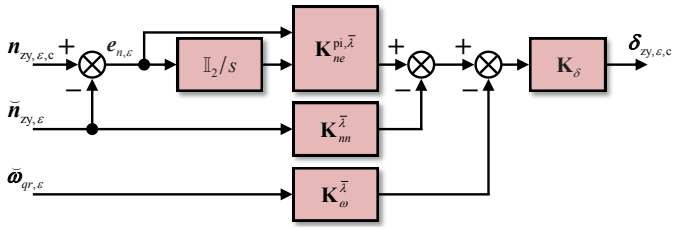

Figure 16 – PI-P-P structure of the pitch/yaw-channel linear controller $\mathbf{C}(s,\overline{\boldsymbol{\lambda}}_{\mathrm{PY}})$

Controller synthesis results

The PI-P-P fixed and RO structure chosen for the controller $\mathbf{C}(s)$ of Fig. 3 comprises four blocks, as shown by Fig. 16: a tracking error PI servo-controller $\mathbf{K}_{ne}(s,\overline{\boldsymbol{\lambda}}_{\mathrm{PY}})$ containing the gain matrix $\mathbf{K}_{ne}^{\mathrm{pi}}(\overline{\boldsymbol{\lambda}}_{\mathrm{PY}})$, two output feedback regulation proportional controllers $\mathbf{K}_{nn}(\overline{\boldsymbol{\lambda}}_{\mathrm{PY}})$ and $\mathbf{K}_{\omega}(\overline{\boldsymbol{\lambda}}_{\mathrm{PY}})$ applied to the output load factors and angular rates, respectively, and finally a block-diagonal roll-off and actuator protection filter $\mathbf{K}_{\delta}(s)$ composed of 1st-order low-pass systems. The control signal $\boldsymbol{\delta}_{\mathrm{zy},\varepsilon,\mathrm{c}}(s)$ is given by:

$$\boldsymbol{\delta}_{\mathrm{zy},\varepsilon,\mathrm{c}}\left(s\right) = \mathbf{K}_{\delta}\left(s\right)\left[\mathbf{K}_{ne}^{\overline{\boldsymbol{\lambda}}}\left(s\right), -\mathbf{K}_{ne}^{\overline{\boldsymbol{\lambda}}}\left(s\right) - \mathbf{K}_{nn}^{\overline{\boldsymbol{\lambda}}}, -\mathbf{K}_{\omega}^{\overline{\boldsymbol{\lambda}}}\right]\begin{bmatrix}\boldsymbol{n}_{\mathrm{zy},\varepsilon,\mathrm{c}}\left(s\right)\\ \breve{\boldsymbol{n}}_{\mathrm{zy},\varepsilon}\left(s\right)\\ \breve{\boldsymbol{\omega}}_{qr,\varepsilon}\left(s\right)\end{bmatrix} \tag{42}$$

where, *i.e.*, $\mathbf{K}_{ne}^{\overline{\boldsymbol{\lambda}}}(s) = \mathbf{K}_{ne}(s,\overline{\boldsymbol{\lambda}}_{\mathrm{PY}})$, and with:

$$\begin{aligned}\mathbf{K}_{ne}\left(s,\overline{\boldsymbol{\lambda}}_{\mathrm{PY}}\right) = &\begin{bmatrix}K_{ne}^{\mathrm{p},11}\left(\overline{\boldsymbol{\lambda}}_{\mathrm{PY}}\right) & K_{ne}^{\mathrm{p},12}\left(\overline{\boldsymbol{\lambda}}_{\mathrm{PY}}\right)\\ K_{ne}^{\mathrm{p},12}\left(\overline{\boldsymbol{\lambda}}_{\mathrm{PY}}\right) & -K_{ne}^{\mathrm{p},11}\left(\overline{\boldsymbol{\lambda}}_{\mathrm{PY}}\right)\end{bmatrix}\\ &+\begin{bmatrix}K_{ne}^{\mathrm{i},11}\left(\overline{\boldsymbol{\lambda}}_{\mathrm{PY}}\right) & K_{ne}^{\mathrm{i},12}\left(\overline{\boldsymbol{\lambda}}_{\mathrm{PY}}\right)\\ K_{ne}^{\mathrm{i},12}\left(\overline{\boldsymbol{\lambda}}_{\mathrm{PY}}\right) & -K_{ne}^{\mathrm{i},11}\left(\overline{\boldsymbol{\lambda}}_{\mathrm{PY}}\right)\end{bmatrix}\begin{bmatrix}1/s & 0\\ 0 & 1/s\end{bmatrix}\end{aligned} \tag{43a}$$

$$\mathbf{K}_{nn}\left(\overline{\boldsymbol{\lambda}}_{\mathrm{PY}}\right) = \begin{bmatrix}K_{nn}^{11}\left(\overline{\boldsymbol{\lambda}}_{\mathrm{PY}}\right) & K_{nn}^{12}\left(\overline{\boldsymbol{\lambda}}_{\mathrm{PY}}\right)\\ K_{nn}^{12}\left(\overline{\boldsymbol{\lambda}}_{\mathrm{PY}}\right) & -K_{nn}^{11}\left(\overline{\boldsymbol{\lambda}}_{\mathrm{PY}}\right)\end{bmatrix} \tag{43b}$$

$$\mathbf{K}_{\omega}\left(\overline{\boldsymbol{\lambda}}_{\mathrm{PY}}\right) = \begin{bmatrix}K_{\omega}^{11}\left(\overline{\boldsymbol{\lambda}}_{\mathrm{PY}}\right) & K_{\omega}^{12}\left(\overline{\boldsymbol{\lambda}}_{\mathrm{PY}}\right)\\ -K_{\omega}^{12}\left(\overline{\boldsymbol{\lambda}}_{\mathrm{PY}}\right) & K_{\omega}^{11}\left(\overline{\boldsymbol{\lambda}}_{\mathrm{PY}}\right)\end{bmatrix} \tag{43c}$$

$$\mathbf{K}_{\delta}\left(s\right) = \begin{bmatrix}\dfrac{1}{\tau_{\delta}s+1} & 0\\ 0 & \dfrac{1}{\tau_{\delta}s+1}\end{bmatrix} \tag{43d}$$

The actual controls $\boldsymbol{\delta}_{\mathrm{mn},\varepsilon,\mathrm{c}}(s)$ sent to the canard actuators are computed from the virtual ones $\boldsymbol{\delta}_{\mathrm{zy},\varepsilon,\mathrm{c}}(s)$ using the matrix $\mathbf{T}(\phi_{\mathrm{f}})$ of Eq. (6). The preceding controller structure, including only gains and simple filters with particular symmetries, permits the designer to significantly reduce interpolation and implementation efforts and costs compared to a FO controller. The eight controller gains are tuned for any synthesis point, whereas the roll-off filter bandwidth remains fixed.

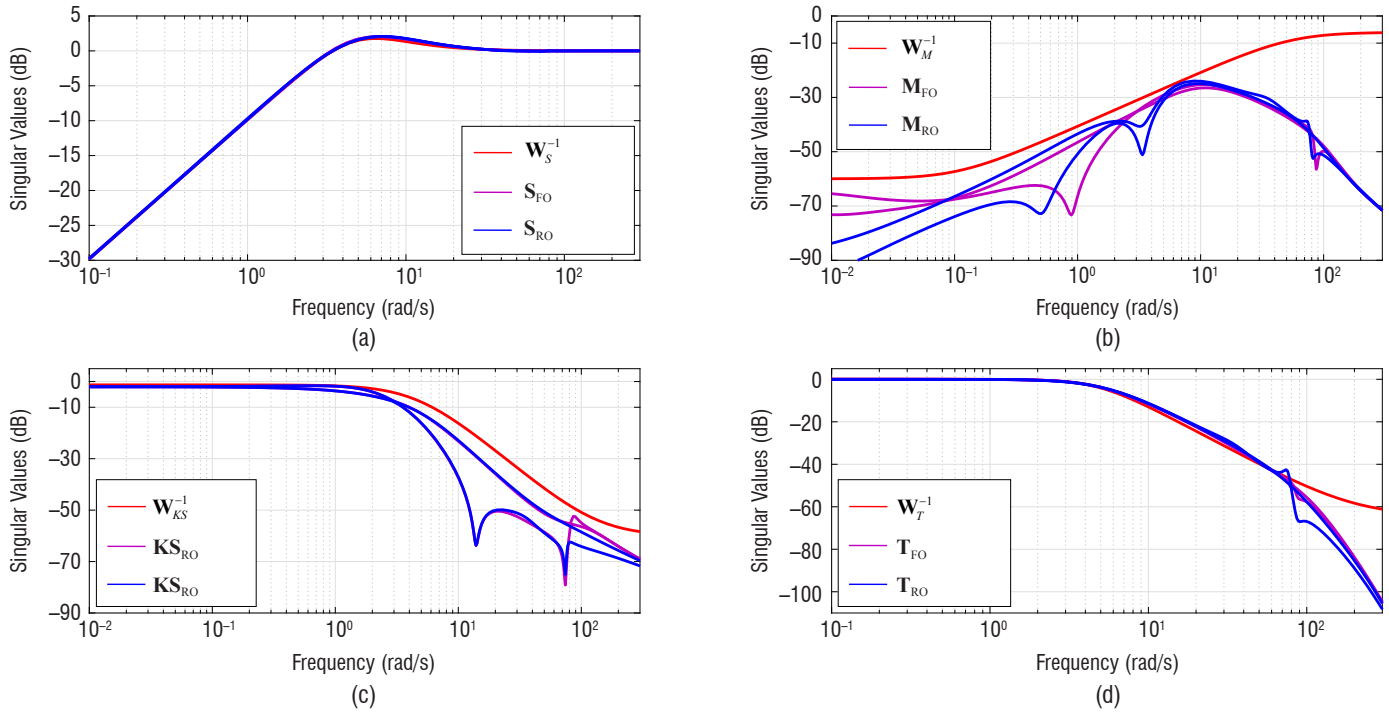

Figure 17 – Frequency responses of the target system (red) and shaped (magenta: FO, blue: RO) closed-loop transfer functions computed at the *critical point* and related to the: (a) tracking error $\boldsymbol{e}_{n,\varepsilon}(s)$, (b) model-matching error $\boldsymbol{e}_{\mathrm{r}}(s)$, (c) control $\boldsymbol{\delta}_{\mathrm{zy},\varepsilon,\mathrm{c}}(s)$, (d) output $\breve{\boldsymbol{n}}_{\mathrm{zy},\varepsilon}(s)$ signals

The RO and fixed-structure controller synthesis frequency results (blue) for a fixed critical low airspeed/high altitude operating point are illustrated in Figs. 17a-17d and compared to the results obtained with a FO controller (magenta). The various shaped closed-loop transfer functions verify the constraints imposed by the weighting filters (red), and hence possess the desired properties as in the case of nose position autopilot design (see Figs. 7a-7d).

Open-loop shaped plant

A nominal RO open-loop shaped plant $\mathbf{G}_{\mathrm{S}}(s)=\mathbf{W}_2\mathbf{G}_K(s)\mathbf{W}_1(s)$ defined by breaking the computed closed-loop system before the tracking error PI servo-controller is shown in Fig. 18. Figure 19 gives the singular values for the RO open-shaped plant (blue), for a FO one that is similarly defined using the previously calculated FO controller (magenta), and for the initial airframe load factor open-loop system $\breve{\mathbf{G}}_{\mathrm{PY},n}(s,\overline{\boldsymbol{\lambda}}_{\mathrm{PY}})$ (black). The RO and FO open-loop shaped plant singular values are close to each other, with desired properties. In addition, open-loop shaping leads to significantly dampening (more than 60 dB) the precession and nutation modes. Finally, the maximum stability margin calculated for the RO $\mathbf{G}_{\mathrm{S}}(s)$ plant is very good, with $\varepsilon_{\max}=0.6131$.

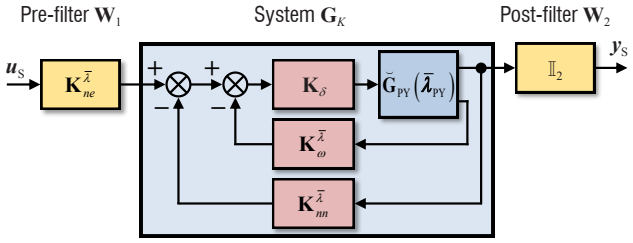

Figure 18 – Nominal open-loop shaped plant $\mathbf{G}_{\mathrm{S}}(s,\overline{\boldsymbol{\lambda}}_{\mathrm{PY}})=\mathbf{W}_2\mathbf{G}_K(s,\overline{\boldsymbol{\lambda}}_{\mathrm{PY}})\mathbf{W}_1(s,\overline{\boldsymbol{\lambda}}_{\mathrm{PY}})$

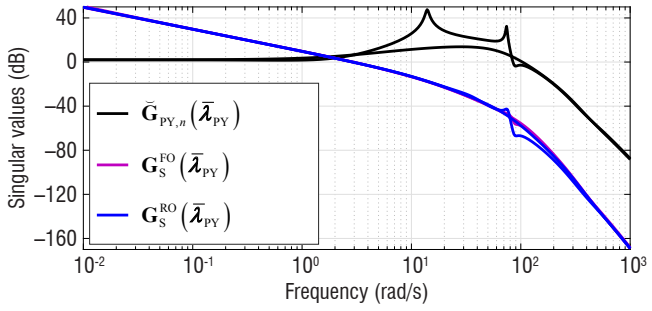

Figure 19 – Singular values of the open-loop load factor system $\breve{\mathbf{G}}_{\mathrm{PY},n}(s,\overline{\boldsymbol{\lambda}}_{\mathrm{PY}})$ (black), and of the FO (magenta) and RO (blue) open-loop shaped plants $\mathbf{G}_{\mathrm{S}}^{\mathrm{FO}}(s,\overline{\boldsymbol{\lambda}}_{\mathrm{PY}})$ and $\mathbf{G}_{\mathrm{S}}^{\mathrm{RO}}(s,\overline{\boldsymbol{\lambda}}_{\mathrm{PY}})$

2DoF NLCF $\mathcal{H}_\infty$ Robust Stabilization

A 2DoF $\mathcal{H}_\infty$ controller $\mathbf{K}_{nf\infty}(s)$ computed with the loop-shape of Fig. 18 using the controller design diagram of Fig. 4 is chosen with the parameter-dependent RO and fixed structure robustifying static part $\mathbf{K}_{n\infty}(\overline{\boldsymbol{\lambda}}_{\mathrm{PY}})=\mathrm{diag}[K_{n\infty}(\overline{\boldsymbol{\lambda}}_{\mathrm{PY}}),K_{n\infty}(\overline{\boldsymbol{\lambda}}_{\mathrm{PY}})]$ and injection dynamic part $\mathbf{K}_{nf}(s,\overline{\boldsymbol{\lambda}}_{\mathrm{PY}})=\mathrm{diag}[K_{nf}(s,\overline{\boldsymbol{\lambda}}_{\mathrm{PY}}),K_{nf}(s,\overline{\boldsymbol{\lambda}}_{\mathrm{PY}})]$. The latter is composed of two identical 1st-order lead-lag systems $K_{nf}(s,\overline{\boldsymbol{\lambda}}_{\mathrm{PY}})$ with a steady-state gain $k_{nf}(\overline{\boldsymbol{\lambda}}_{\mathrm{PY}})$ and time constants $\tau_{nf}^{\mathrm{lead}}(\overline{\boldsymbol{\lambda}}_{\mathrm{PY}}),\tau_{nf}^{\mathrm{lag}}(\overline{\boldsymbol{\lambda}}_{\mathrm{PY}})$:

$$K_{nf}\left(s,\overline{\boldsymbol{\lambda}}_{\mathrm{PY}}\right)=k_{nf}\left(\overline{\boldsymbol{\lambda}}_{\mathrm{PY}}\right)\cdot\frac{\tau_{nf}^{\mathrm{lead}}\left(\overline{\boldsymbol{\lambda}}_{\mathrm{PY}}\right)s+1}{\tau_{nf}^{\mathrm{lag}}\left(\overline{\boldsymbol{\lambda}}_{\mathrm{PY}}\right)s+1} \tag{44}$$

The parameters to be tuned are the controller $\mathbf{K}_{n\infty}(\overline{\boldsymbol{\lambda}}_{\mathrm{PY}})$ and the steady-state gain and time constants of the injection filter $\mathbf{K}_{nf}(s,\overline{\boldsymbol{\lambda}}_{\mathrm{PY}})$. For the same target model $\mathbf{T}_{n,\mathrm{r}}(s)$ as that used for open-loop shaping in the previous Subsection "Open-Loop Shaping" and $\eta=0.1$, controller parameter tuning at the critical low airspeed/high altitude operating point gives the very good performance index $\gamma_{\mathrm{RO2}}=1.7588$. The excellent stability margin $\varepsilon_{\mathrm{RO2}}=1/\gamma_{\mathrm{RO2}}^{\star}=0.5721$ remains close to a stability margin $\varepsilon_{\mathrm{FO2}}=1/\gamma_{\mathrm{FO2}}^{\star}=0.6114$ offered by a robustifying 2DoF FO controller and to the maximum stability margin $\varepsilon_{\max}=0.6131$.

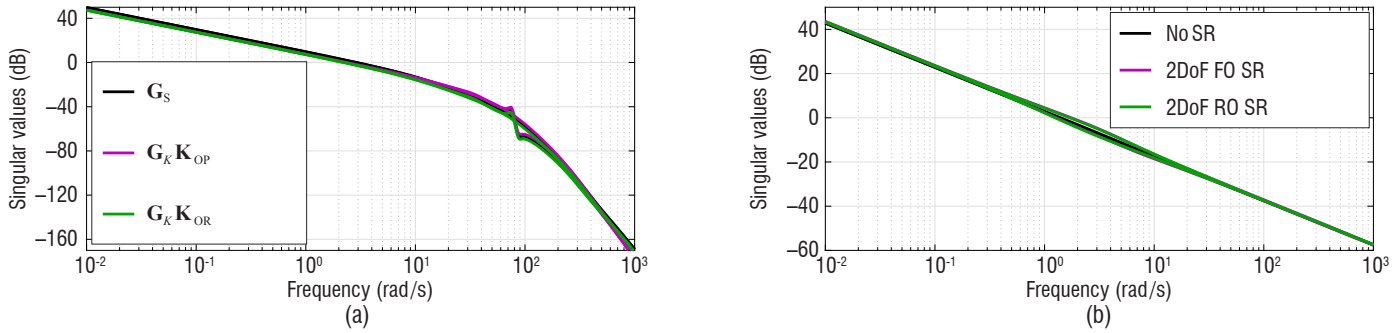

Figure 20 – Singular values of the: (a) desired $\mathbf{G}_S(s)$ (black), actual FO $\mathbf{G}_K\mathbf{K}_{FO}(s)$ (magenta) and actual RO $\mathbf{G}_K\mathbf{K}_{RO}(s)$ (green) loop-shapes; (b) pitch/yaw-channel linear controllers: without any robustifying controller (black), with the robustifying 2DoF FO controller (magenta), and with the robustifying 2DoF RO controller (green)

It can be then noticed, using the RO and FO actual open-loop shaped plants $\mathbf{G}_K\mathbf{K}_{RO}(s,\bar{\boldsymbol{\lambda}}_{PY})$ and $\mathbf{G}_K\mathbf{K}_{FO}(s,\bar{\boldsymbol{\lambda}}_{PY})$[2], which are obtained at system $\mathbf{G}_K(s)$ output and plotted in Fig. 20a, that the degradations at low and high frequencies in the initial open-loop shaped plant due to the $\mathcal{H}_\infty$ controller are very small.

The complete 2DoF RO and fixed structure obtained at any synthesis point for a pitch/yaw-channel linearized dynamics controller is shown in Fig. 21. It particularly comprises a parameter-dependent diagonal static pre-filter $\mathbf{K}_{nsc}(\bar{\boldsymbol{\lambda}}_{PY}) = \text{diag}[K_{nsc}(\bar{\boldsymbol{\lambda}}_{PY}), K_{nsc}(\bar{\boldsymbol{\lambda}}_{PY})]$, which is added after robust stabilization to ensure a unitary steady-state gain for the closed-loop transfer function between the reference $\boldsymbol{n}_{zy,\varepsilon,c}(s)$ and tracking output $\breve{\boldsymbol{n}}_{zy,\varepsilon}(s)$ signals, given the integral action in the PI controller. The expression of the diagonal components $K_{nsc}(\bar{\boldsymbol{\lambda}}_{PY})$ is similar to Eq. (32). The controller fixed structure, which remains simple and easy to interpolate and implement, generates the virtual control signal $\boldsymbol{\delta}_{zy,\varepsilon,c}(s)$ given by Eq. (45), in which, *i.e.*, $\mathbf{K}_\omega^{\bar{\lambda}} = \mathbf{K}_\omega(\bar{\boldsymbol{\lambda}}_{PY})$. The actuator commands $\boldsymbol{\delta}_{mn,\varepsilon,c}(s)$ are computed again using Eq. (6).

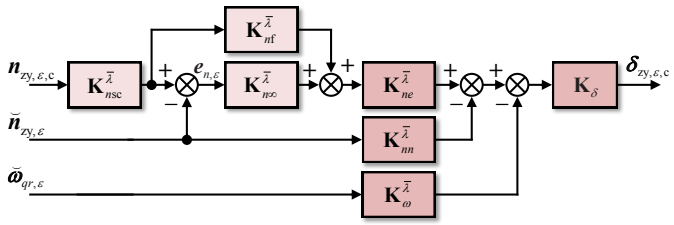

Figure 21 – 2DoF controller for the linearized pitch/yaw-channel dynamics

Figure 20b shows the singular values for the complete RO controller of Fig. 21 (green), for a complete FO controller containing the robustifying 2DoF FO controller instead (magenta), and for the PI-P-P controller of Fig. 16 used for open-loop shaping (black). All of the singular values remain close to each other and hence the good properties of the PI-P-P controller (low-frequency integral action, high-frequency sufficient roll-off, reasonable bandwidth) are well preserved.

Finally, Figs. 22a-22d illustrate the step responses for the transfer functions of the pitch/yaw-channel complete RO linear control loop

$$\boldsymbol{\delta}_{zy,\varepsilon,c}(s) = \mathbf{K}_\delta(s)\left[\mathbf{K}_{ne}^{\bar{\lambda}}(s)\left\{\mathbf{K}_{nf}^{\bar{\lambda}}(s)+\mathbf{K}_{n\infty}^{\bar{\lambda}}\right\}\mathbf{K}_{nsc}^{\bar{\lambda}} \;\middle|\; -\left\{\mathbf{K}_{ne}^{\bar{\lambda}}(s)\mathbf{K}_{n\infty}^{\bar{\lambda}}+\mathbf{K}_{nn}^{\bar{\lambda}}\right\} \quad -\mathbf{K}_{\omega}^{\bar{\lambda}}\right]\begin{bmatrix}\boldsymbol{n}_{zy,\varepsilon,c}(s)\\ \breve{\boldsymbol{n}}_{zy,\varepsilon}(s)\\ \breve{\boldsymbol{\omega}}_{qr,\varepsilon}(s)\end{bmatrix} \tag{45}$$

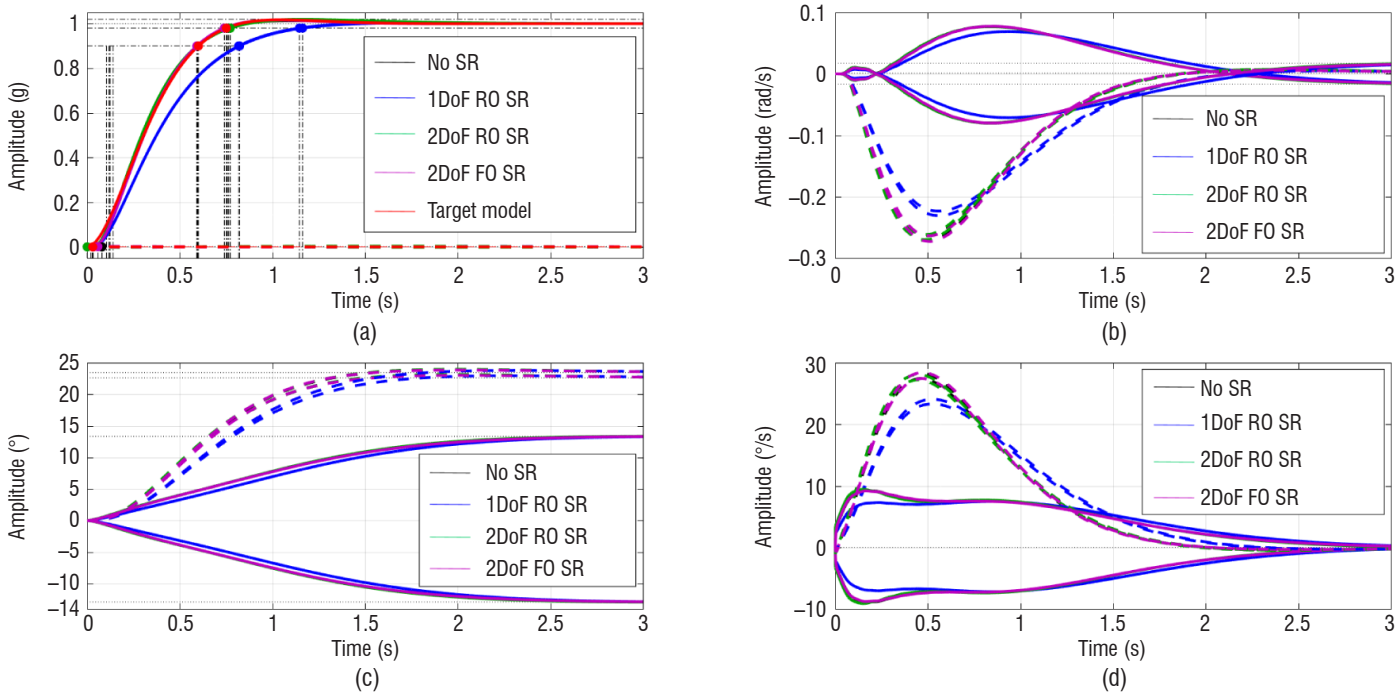

Figure 22 – Closed-loop step responses: (a) normalized load factor $\breve{\boldsymbol{n}}_{zy,\varepsilon}(t)$, (b) angular rate $\breve{\boldsymbol{\omega}}_{qr,\varepsilon}(t)$, (c) control $\boldsymbol{\delta}_{zy,\varepsilon,c}(t)$, (d) control rate $\dot{\boldsymbol{\delta}}_{zy,\varepsilon,c}(t)$ signals (solid: response on the same axis as the reference, dashed: response on the opposite axis to the reference)

[2] RO and FO actual loop-shapes: $\mathbf{G}_K\mathbf{K}_{RO} = \mathbf{G}_K\mathbf{W}_1\mathbf{K}_{n\infty}\mathbf{W}_2$ and $\mathbf{G}_K\mathbf{K}_{FO} = \mathbf{G}_K\mathbf{W}_1\mathbf{K}_{n\infty}^{FO}\mathbf{W}_2$.

that are related to the load factor output $\breve{\boldsymbol{n}}_{\mathrm{zy},\varepsilon}(s)$ (green in Fig. 22a), the angular rate output $\breve{\boldsymbol{\omega}}_{qr,\varepsilon}(s)$ (green in Fig. 22b), the control signal $\boldsymbol{\delta}_{\mathrm{mn,c},\varepsilon}(s)$ (green in Fig. 22c), and the control signal derivative $\dot{\boldsymbol{\delta}}_{\mathrm{mn,c},\varepsilon}(s)$ (green in Fig. 22d). The sufficiently large reference step amplitudes used on the pitch and yaw-axes are coherent with nonlinear simulations. In Fig. 22a, the pitch/yaw-channel load factor-related responses match the target system responses (red), and hence the time performance in terms of reference tracking (solid lines) and load factor output decoupling (dashed lines) obtained before robust stabilization (black) is very well recovered using the 2DoF RO structure for the robustifying controller, as with the robustifying 2DoF FO controller (magenta). The use of a robustifying 1DoF RO controller is clearly not satisfactory (blue). In Fig. 22b, the output angular rates used for feedback remain small and help to enhance closed loop damping. In Figs. 22c and 22d, the control signals behave well without any saturation nor fast variations.

Robust Stability Analysis

The pitch/yaw-channel linear controller of Fig. 21 is tested for robust stability at the critical operating condition with respect to the projectile dynamics aerodynamic parametric uncertainties, as well as the unstructured uncertainties representing neglected dynamics in the actuator and sensor models. As for the nose position autopilot design, robustness is first assessed using the criterion of the $\mathcal{H}_\infty$ loop-shaping design procedure. The estimated size $\varepsilon = 0.3424$ of NLCF perturbations corresponding to all of the aforementioned modeling uncertainties remains smaller than the stability margin $\varepsilon_{\mathrm{RO2}} = 0.5685$, and hence robust stability is guaranteed.

The μ-analysis theory presented in Subsection "Robust Stability Analysis" of the previous Section "Roll-Channel Autopilot" is also applied to the uncertain pitch/yaw-channel linear closed-loop system, in which the aerodynamic parametric uncertainty block $\boldsymbol{\Delta}_{n\omega}$ similar to Eq. (35), along with the unstructured actuator $\boldsymbol{\Delta}_{\delta}(s)$ and sensor $\boldsymbol{\Delta}_{n,\mathrm{m}}(s), \boldsymbol{\Delta}_{\omega,\mathrm{m}}(s)$ perturbation blocks, are regrouped in a single block-diagonal $\boldsymbol{\Delta}(s) = \mathrm{diag}[\boldsymbol{\Delta}_{\delta}(s), \boldsymbol{\Delta}_{n\omega}, \boldsymbol{\Delta}_{n,\mathrm{m}}(s), \boldsymbol{\Delta}_{\omega,\mathrm{m}}(s)] \in \mathbb{R}\mathcal{H}_\infty, \left\|\boldsymbol{\Delta}(s)\right\|_\infty \leq 1$. Figure 23 gives the upper and lower SSV bounds calculated over a frequency grid, which remain smaller than one and thus indicate robust stability with a good stability margin.

Figures 24a-24f present pitch/yaw load factor, actuator angle and rate time responses for 200 uncertain closed-loop system random samples, using pulse signals of constant amplitude for the reference pitch/yaw-channel load factors. Robust stability of the closed-loop system can be verified, and performance in terms of reference tracking and load factor output decoupling is relatively well ensured, with no canard actuator saturation despite the various sources of modeling uncertainty.

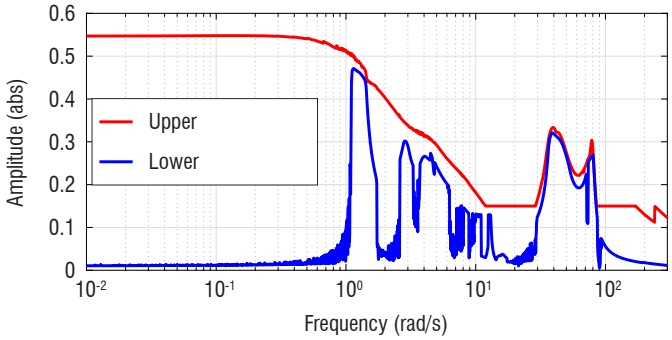

Figure 23 – Upper and lower SSV bounds calculated for the uncertain closed-loop system

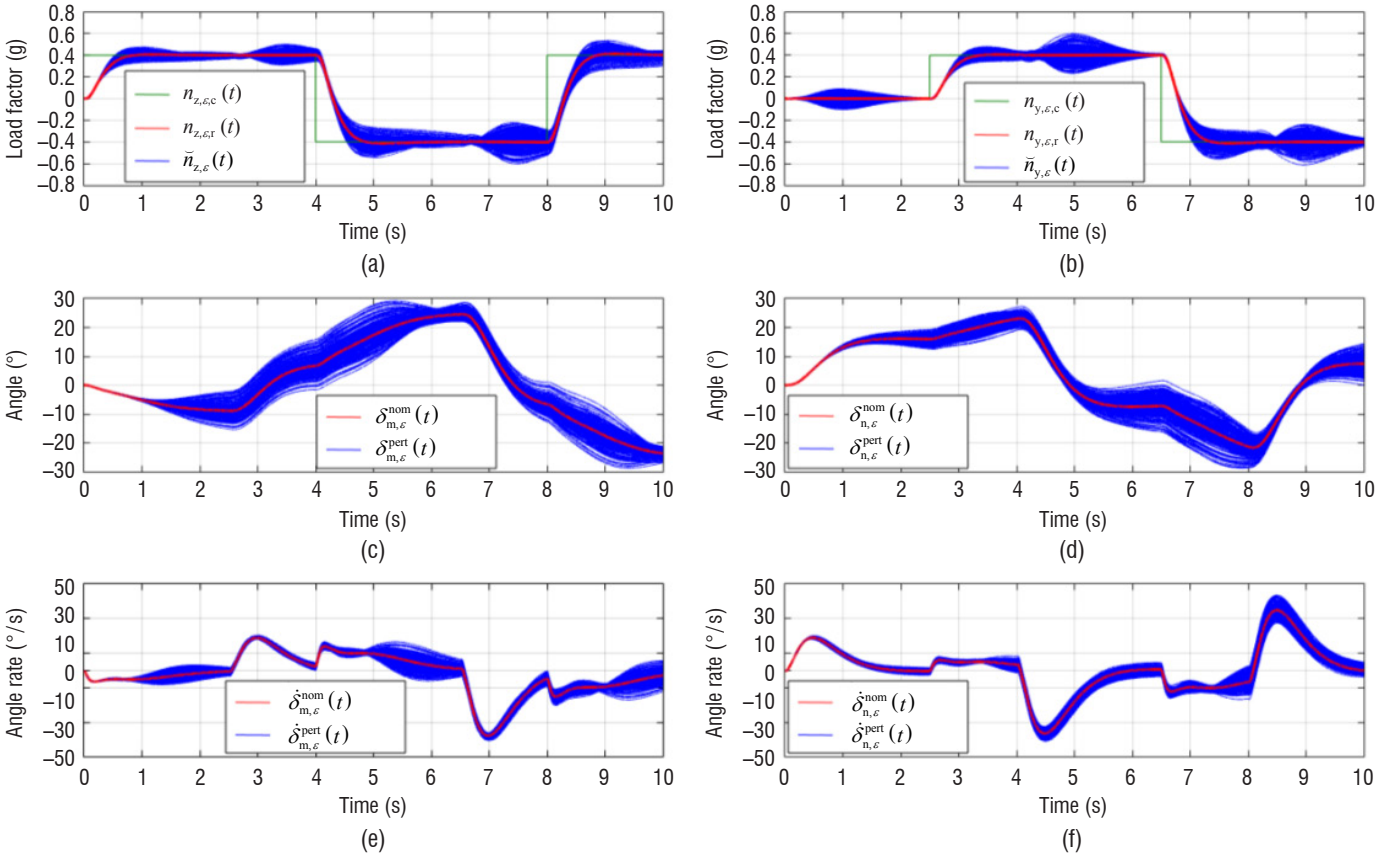

Figure 24 – Uncertain closed-loop simulations: (a) pitch load factor, (b) yaw load factor, (c) pitch actuator angle, (d) yaw actuator angle, (e) pitch actuator angle rate, (f) yaw actuator angle rate

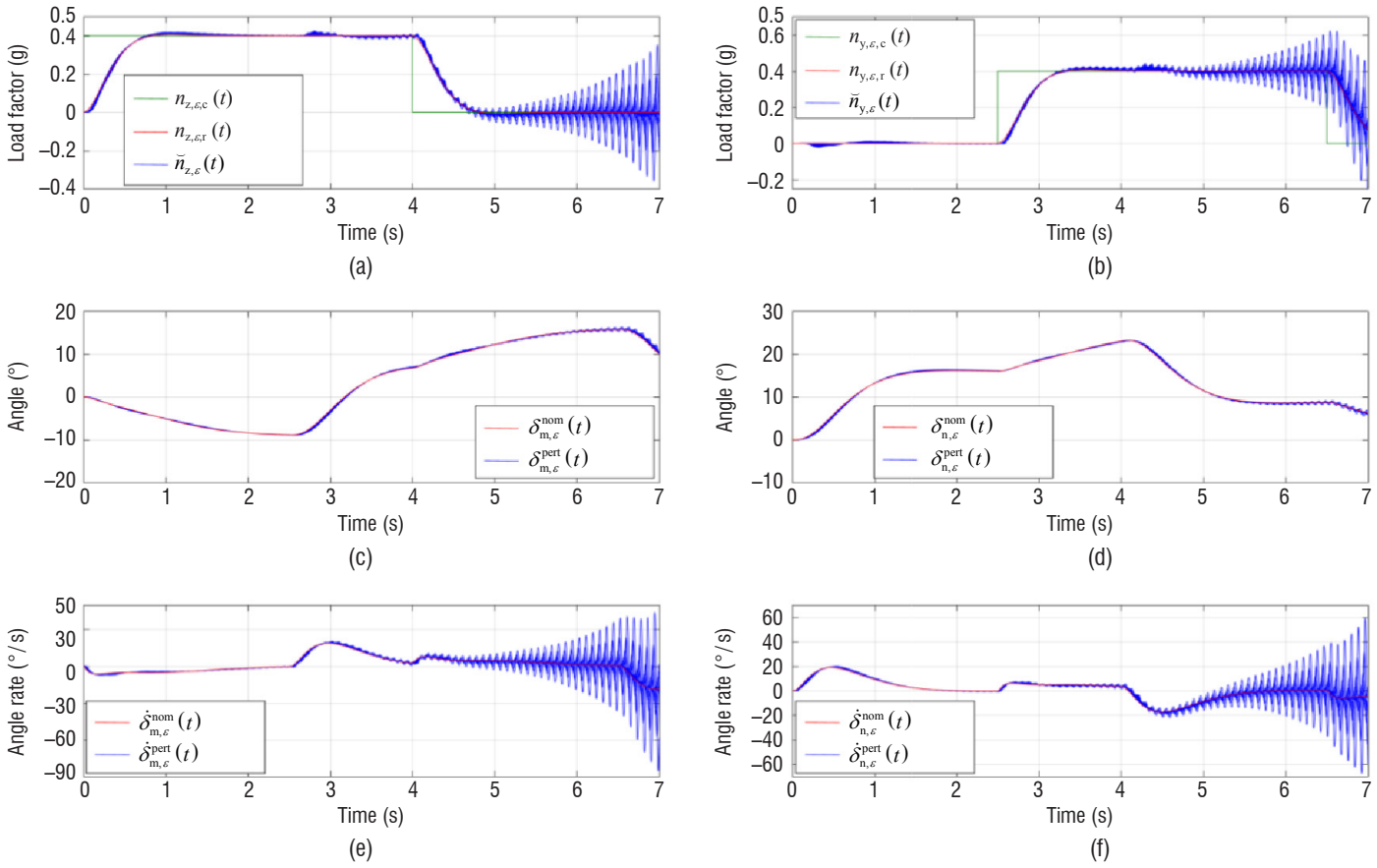

Figure 25 – Closed-loop time responses with transmission delays at actuator inputs: (a) pitch load factor, (b) yaw load factor, (c) pitch actuator angle, (d) yaw actuator angle, (e) pitch actuator angle rate, (f) yaw actuator angle rate

Finally, robust stability of the closed-loop system is verified with respect to transmission delays injected simultaneously at each canard actuator input. For delays of up to 30 ms, *i.e.*, 18 times a rate of 1/600 s with which the control signal could be sampled, Figs. 25a-25f show degradations, on the different time responses considered, which become significant only for the biggest delays. However, for realistic delays of up to 3 times the control signal sampling rate [32], *i.e.*, 5 ms, closed-loop system stability and performance properties are well maintained.

Gain-Scheduled Nonlinear Controller

The development of a gain-scheduled nonlinear controller valid for the entire operating domain $\boldsymbol{\Gamma}_{\mathrm{PY}}^{\lambda}$ of the projectile parameter-dependent pitch/yaw-channel dynamics permits the designer to suitably adapt the control signal level to changes occurring in these dynamics, contrary to a single linear controller, which would be insufficiently robust to ensure desired stability and performance properties for all operating points. Linearly interpolating the eight tuned parameters of a set of controllers, each of which possesses the same structure of Fig. 21 computed by repeating the design procedure of the previous subsections over a grid of equidistant synthesis points covering the trimming envelope $\boldsymbol{\Gamma}_{\mathrm{PY}}^{\lambda}$, produces, for the simplified *q*-LPV model $\mathcal{S}_{\mathrm{PY}}^{\lambda}(\boldsymbol{\lambda}_{\mathrm{PY}})$ of Subsection "Pitch/Yaw-Channels" in Part "Airframe Modeling", a gain-scheduled controller [18]. Implementing directly its structure with the projectile pitch/yaw-channel nonlinear dynamics provides the gain-scheduled *nonlinear* controller of Eq. (46) in which, *i.e.*, $\mathbf{K}_{\omega}^{\lambda} = \mathbf{K}_{\omega}[\boldsymbol{\lambda}_{\mathrm{PY}}(t)]$. The time-dependent scheduling vector $\boldsymbol{\lambda}_{\mathrm{PY}}(t) = [V(t) \;\; h(t)]^{\mathrm{T}}$ is assumed to be measurable as well as slowly-varying for preserving closed-loop system stability. The actuator commands $\boldsymbol{\delta}_{\mathrm{mn,c}}(s)$ are computed again using Eq. (6).

The transformation system $\mathbf{T}_{n\omega}^{\rho}(s, \boldsymbol{\rho}_{\mathrm{PY}})$ of Eqs. (39) is also directly implemented with the nonlinear system dynamics in order to compute for any operating point the necessary feedback signals at the projectile CM, depending on the simultaneously controlled nose angle and rate. The various parameters of the derivative $\mathbf{W}_{\mathrm{d},\omega}(s, \boldsymbol{\lambda}_{\mathrm{PY}})$ and low-pass $\mathbf{W}_{\mathrm{b},n}(s, \boldsymbol{\lambda}_{\mathrm{PY}})$ and $\mathbf{W}_{\mathrm{b},\omega}(s, \boldsymbol{\lambda}_{\mathrm{PY}})$ filters are linearly interpolated using the selected values for the design point grid.

The design of 1886 linear controllers is performed for the same target performance level demanded throughout the entire operating domain. Both the derivative and low-pass filters contained in the transformation system and the model-matching and control signal weighting filters included in the linear controller design setup of Fig. 3 used for open-loop shaping are automatically and smoothly adapted. The PI-P-P controller gain surfaces obtained as a function of the projectile

$$\boldsymbol{\delta}_{\mathrm{zy,c}}(s) = \mathbf{K}_{\delta}(s)\left[\mathbf{K}_{ne}^{\lambda}(s)\left\{\mathbf{K}_{nf}^{\lambda}(s) + \mathbf{K}_{n\infty}^{\lambda}\right\}\mathbf{K}_{\mathrm{nsc}}^{\lambda} \;\middle|\; -\left\{\mathbf{K}_{ne}^{\lambda}(s)\mathbf{K}_{n\infty}^{\lambda} + \mathbf{K}_{nn}^{\lambda}\right\} \;\; -\mathbf{K}_{\omega}^{\lambda}\right]\begin{bmatrix} \boldsymbol{n}_{\mathrm{zy,c}}(s) \\ \breve{\boldsymbol{n}}_{\mathrm{zy}}(s) \\ \breve{\boldsymbol{\omega}}_{qr}(s) \end{bmatrix} \tag{46}$$

airspeed V and altitude h are given in Figs. 26, 27, whereas the values of the different parameters of the pre-filter and of the robustifying 2DoF $\mathcal{H}_\infty$ controller, which remain almost constant over the flight envelope, are not shown for brevity purposes. The reasonable values of the PI-P-P controller gains vary relatively smoothly[3], hence aiding the obtainment of a good continuity of the gain-scheduled control signal during transitions between synthesis operating points, which is desirable for preserving the performance and robustness properties [19, 27].

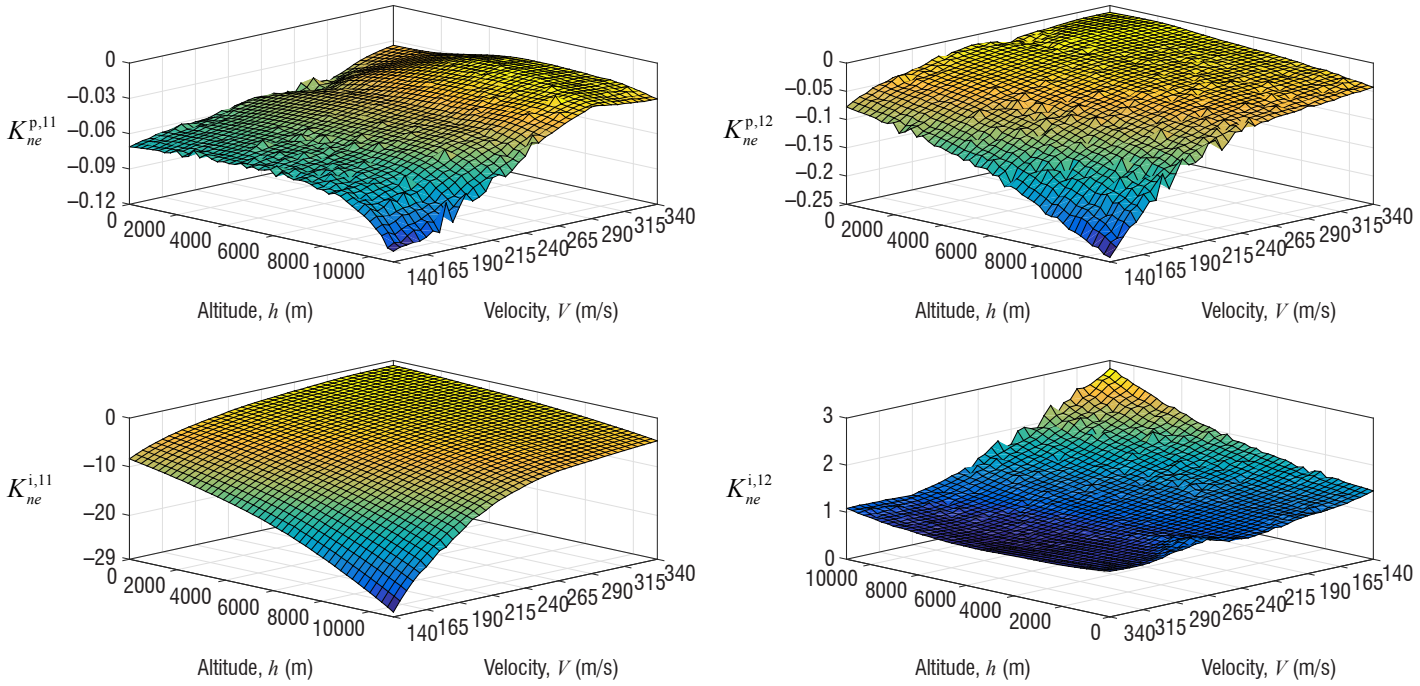

Figure 26 – Gain surfaces as a function of the synthesis point for controller $\mathbf{K}_{ne}(s,\overline{\boldsymbol{\lambda}}_{\mathrm{PY}})$

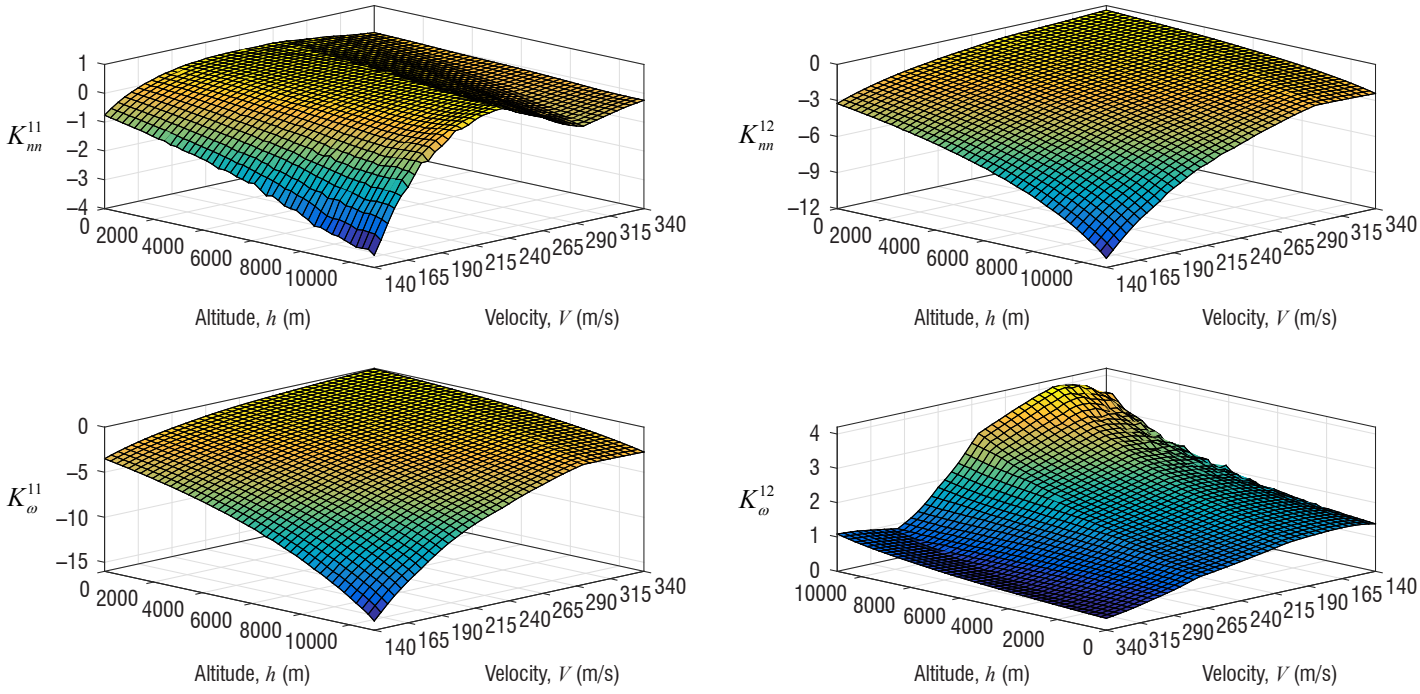

Figure 27 – Gain surfaces as a function of the synthesis point for controllers $\mathbf{K}_{nn}(\overline{\boldsymbol{\lambda}}_{\mathrm{PY}}),\mathbf{K}_{\omega}(\overline{\boldsymbol{\lambda}}_{\mathrm{PY}})$

[3] Whereas the proposed controller design procedure provides gain surfaces which are already relatively smooth, a subsequent smoothing could be applied to the gains in order to obtain smoother variations.

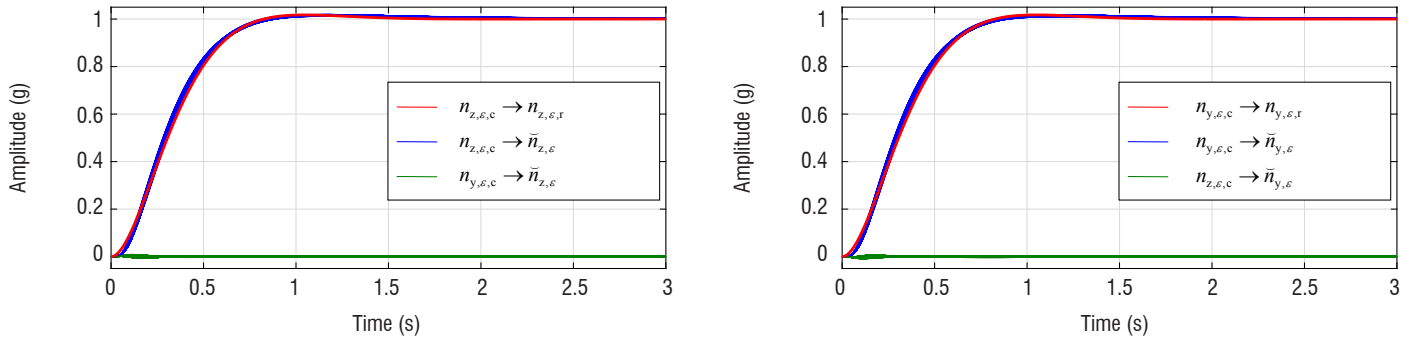

Figure 28 – Closed-loop load factor step responses for all design points: (a) pitch-axis, (b) yaw-axis

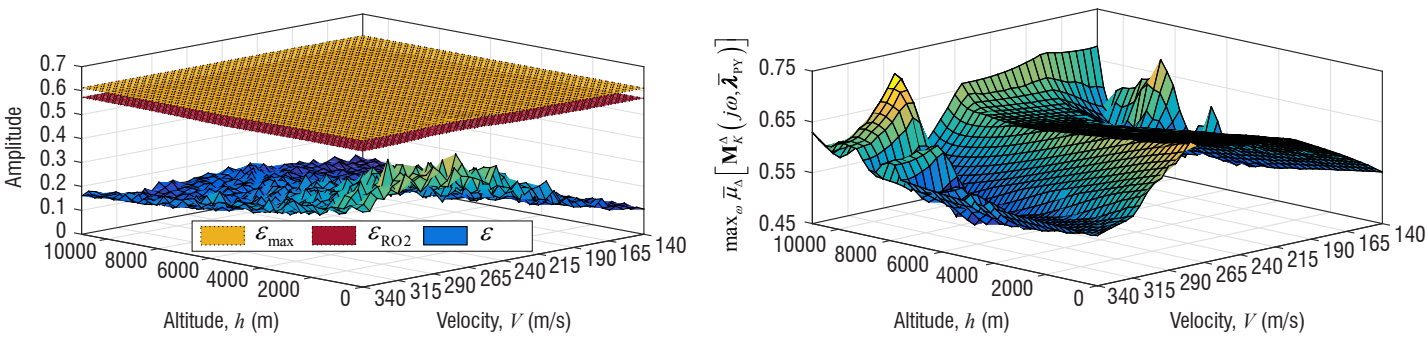

Figure 29 – Robustness results as a function of the synthesis point: (a) maximal $\varepsilon_{\max}(\bar{\boldsymbol{\lambda}}_{PY})$ (yellow) and achieved $\varepsilon_{RO2}(\bar{\boldsymbol{\lambda}}_{PY})$ (red) NLCF stability margins along with uncertainty size $\varepsilon(\bar{\boldsymbol{\lambda}}_{PY})$ (blue), (b) maximal value over frequency of the SSV upper bound

Figures 28a, 28b illustrate for all synthesis points the closed-loop pitch/yaw load factor output-related step responses (blue, green) indicating that the reference tracking and output decoupling local performance objectives specified by the reference dynamics (red) are very well met over the trimming envelope. Figures 29a, 29b indicate that closed-loop system local robust stability is proved at each design point using both the robustness criterion of the $\mathcal{H}_\infty$ loop-shaping design procedure and μ-analysis theory. For the considered modeling uncertainty, the inequalities $\varepsilon(\bar{\boldsymbol{\lambda}}_{PY}) < \varepsilon_{RO2}(\bar{\boldsymbol{\lambda}}_{PY})$ and $\max_{\omega} \bar{\mu}_{\Delta}[\mathbf{M}_K^{\Delta}(j\omega, \bar{\boldsymbol{\lambda}}_{PY})] < 1, \forall \omega \in \mathbb{R}^+$ are verified for any synthesis point $\bar{\boldsymbol{\lambda}}_{PY} \in \boldsymbol{\Gamma}_{PY}^{\lambda}$.

The nonlocal stability and performance properties provided by the gain-scheduled controller are now verified using the simplified q-LPV model $\mathcal{S}_{PY}^{\lambda}(\boldsymbol{\lambda}_{PY})$ proposed in Subsection "Pitch/Yaw-Channels" of Part "Airframe Modeling". The latter is simulated during 28 s along a parameter vector test trajectory $\boldsymbol{\lambda}_{PY}(t)$ covering the flight envelope $\boldsymbol{\Gamma}_{PY}^{\lambda}$, as shown in Fig. 30. The altitude trajectory originates from a ballistic simulation of 28 s between the apogee and the impact point, whereas the airspeed is a chirp sinusoidal signal whose frequency increases from 0.01 Hz to 0.1 Hz at a linear rate with time during 15 s and then at the same rate up to 28 s. The simulation time results obtained with reference pitch/yaw load factors taken as pulse signals of constant amplitude are presented in Figs. 31a-31d. Performance in terms of reference tracking and decoupling is satisfactory and the pitch and yaw actuator angular position and rate signals behave well.

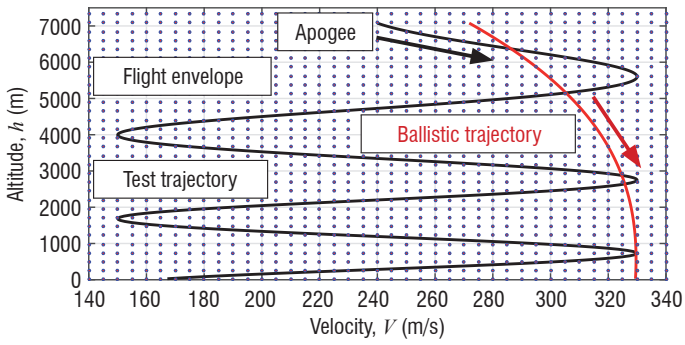

Figure 30 – Evolution of the scheduling vector test trajectory within the projectile flight envelope covered by the equidistant synthesis point grid (black: test trajectory, red: ballistic trajectory)

Proportional Navigation Guidance Algorithm

This part describes the gravity-compensation *pure* proportional navigation (PPN) guidance algorithm, which generates the suitable reference pitch/yaw-channel load factor orders commanded to the autopilot in order to steer with accuracy the projectile to a given target. The load factor commands expressed in the non-rolling frame CS are given by [40]:

$$\left[\boldsymbol{n}_c^{BE}\right]^{B'} = \frac{N\left[\boldsymbol{\omega}^{OE}\right]^{B'} \times \left[\boldsymbol{v}_B^E\right]^{B'} - \left[\mathbf{T}\right]^{B'E}\left[\boldsymbol{g}\right]^E}{\left\|\left[\boldsymbol{g}\right]^E\right\|} \tag{47}$$

The vector $[\boldsymbol{\omega}^{OE}]^{B'}$ is the line of sight O rate of change with respect to the inertial frame E and is defined as:

$$\left[\boldsymbol{\omega}^{OE}\right]^{B'} = \left[\mathbf{T}\right]^{B'E} \frac{\left[\boldsymbol{s}_{TB}\right]^E \times \left[\boldsymbol{v}_{TB}^E\right]^E}{\left\|\left[\boldsymbol{s}_{TB}\right]^E\right\|^2} \tag{48}$$

where the line of sight vector $[\boldsymbol{s}_{TB}]^E = [\boldsymbol{s}_{TE}]^E - [\boldsymbol{s}_{BE}]^E$ is the differential inertial position vector between the projectile CM B and the target

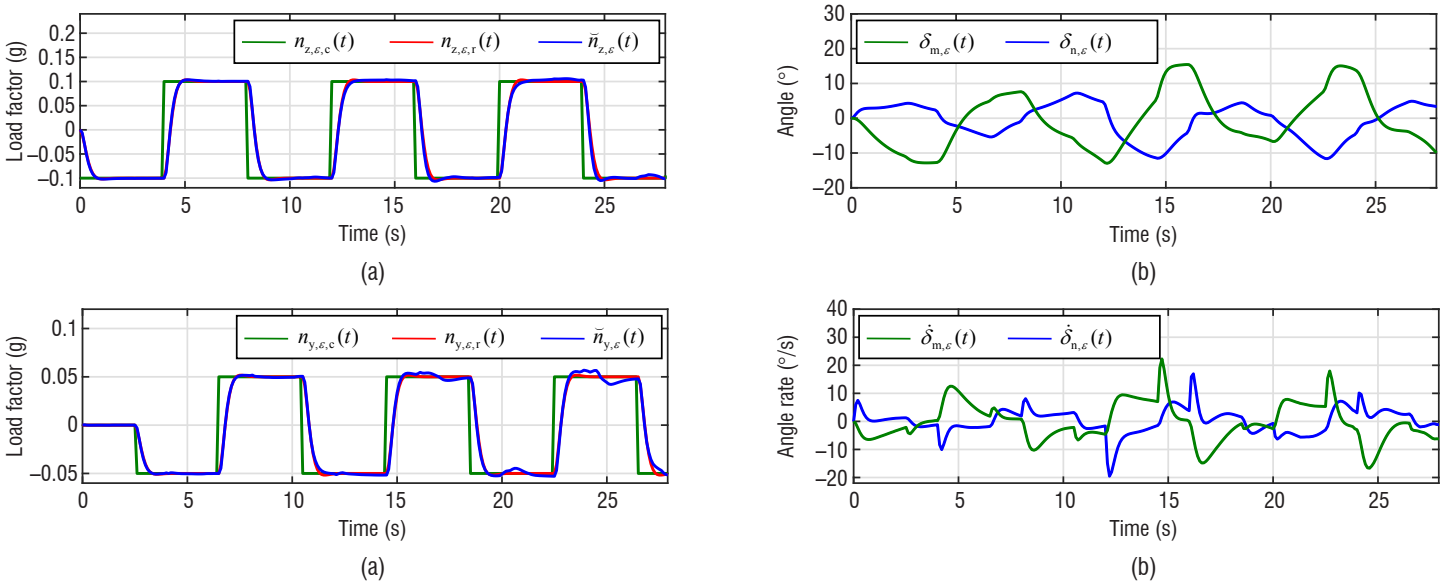

Figure 31 – Closed-loop simulations: (a) pitch load factor, (b) yaw load factor, (c) pitch/yaw actuator angles, (d) pitch/yaw actuator angular rates

CM T positions, which are considered as perfectly known, and the differential velocity vector $[\boldsymbol{v}_{\mathrm{TB}}^{\mathrm{E}}]^{\mathrm{E}} = [\boldsymbol{v}_{\mathrm{T}}^{\mathrm{E}}]^{\mathrm{E}} - [\boldsymbol{v}_{\mathrm{B}}^{\mathrm{E}}]^{\mathrm{E}}$ of the projectile CM B with respect to the target frame T is the difference between the inertial projectile and target velocity vectors.

The PPN constant is here set to $N = 2.5$, since this value leads to reasonable amplitudes for the reference load factors, and to smaller, slower-varying and more homogenous over time amplitudes for the canard actuator control signals. Hence, the risk of actuator saturation is limited, while a very good impact accuracy is maintained.

The gravitational acceleration vector is given by $[\boldsymbol{g}]^{\mathrm{E}} = [0 \;\; 0 \;\; g]^{\mathrm{T}}$ in the inertial CS and it is expressed in the non-rolling frame CS using the transformation matrix $[\mathbf{T}]^{\mathrm{B'E}}$, which is defined as follows as a function of the projectile pitch and yaw Euler angles assumed as perfectly known:

$$[\mathbf{T}]^{\mathrm{B'E}} = \begin{bmatrix} \cos\theta\cos\psi & \cos\theta\sin\psi & -\sin\theta \\ -\sin\psi & \cos\psi & 0 \\ \sin\theta\cos\psi & \sin\theta\sin\psi & \cos\theta \end{bmatrix} \tag{49}$$

There exists an alternative *true* PN (TPN) guidance law [39, 40] which possesses a similar expression to that of the PPN law. The difference comes from the use in Eq. (47) of the differential velocity vector expressed in the non-rolling frame CS $[\boldsymbol{v}_{\mathrm{TB}}^{\mathrm{E}}]^{\mathrm{B'}}$ instead of the projectile CM velocity vector $[\boldsymbol{v}_{\mathrm{B}}^{\mathrm{E}}]^{\mathrm{B'}}$. A PPN guidance law generates a commanded load factor vector that is normal to the inertial velocity vector $[\boldsymbol{v}_{\mathrm{B}}^{\mathrm{E}}]^{\mathrm{E}}$, whereas a TPN guidance law orders a load factor vector normal to the line of sight, *i.e.*, normal to the differential inertial velocity vector $[\boldsymbol{v}_{\mathrm{TB}}^{\mathrm{E}}]^{\mathrm{E}}$. However, both PPN and TPN laws yield identical commanded load factors in the case of a non-maneuvering target.

Nonlinear Simulation Results

This part proves the effectiveness of the guidance & gain-scheduled nonlinear control (G&C) system designed for an STT canard-guided dual-spin projectile, when it is implemented with the complete 7DoF nonlinear model of Part "Airframe Modeling" augmented with the transformation system, throughout various simulation scenarios of a complete guided flight. Such a guided flight here comprises two main phases: the *ballistic* phase (from launch to a few seconds after the projectile trajectory apogee) and the *guided* phase (from the end of the ballistic phase to the projectile impact).

The ballistic phase $(0 \le t < t_{\mathrm{guid}})$, where no guidance function is engaged, starts at projectile launch with a muzzle velocity $V_0 = 803$ m/s, and gun barrel pointing $\theta_0 \simeq 899.9$ mil $= 50.62°$ and azimuth $\psi_0 \simeq +2026.7$ mil $= +114°$ (south-easterly direction). The ballistic phase comprises three subphases: a first *starting* subphase $(0 \le t < t_{\mathrm{start}} = 20\,\mathrm{s})$, a second *nose rate reduction* subphase $(t_{\mathrm{start}} = 20\,\mathrm{s} \le t < t_{\mathrm{switch}} = 40\,\mathrm{s})$, and a third *nose position reset* subphase $(t_{\mathrm{switch}} = 40\,\mathrm{s} \le t < t_{\mathrm{guid}})$. During the first subphase, the nose embedded electronic components (G&C modules, actuators and sensors) are started only a few seconds after launch, in order to avoid their potential degradation caused by the extreme launch accelerations. Large disturbances appearing in different system signals are also sufficiently reduced during this first subphase. During the second subphase, the high roll rate of the nose initially fixed with the projectile body is reduced to zero using the rate autopilot. During the third subphase, the nose angle is reset to $\phi_{\mathrm{f}} = 180°$ by the position autopilot and the steering canards are deployed at $t_{\mathrm{eng}} = 40.5\,\mathrm{s}$.

The guided phase $(t_{\mathrm{guid}} \le t \le t_{\mathrm{impact}})$ starts after the trajectory apogee, when the projectile arrives at less than 10 km from the target. With the projectile maneuvering with an STT mode for trajectory correction, the nose angle is permanently regulated about $\phi_{\mathrm{f}} = 180°$ from t_{guid}. The pitch/yaw-channel PPN guidance function, which is however engaged only as from $t_{\mathrm{guid}} + 3\,\mathrm{s}$ when the large disturbances on the feedback signals due to canard deployment are sufficiently reduced, actively directs the projectile with accuracy towards a ballistic impact point.

Nonlinear simulation results are given in Figs. 32 and 33, considering nominal initial conditions (IC), no wind and no modeling uncertainty. Figures 32a-32f illustrate on the left for the pitch/yaw-channels the tracking load factors and the canard actuator deflection angles and rates, whereas on the right the nose roll-channel controlled angle, the angular rate and the input voltage to the coaxial motor are given. Figures 33a-33b show the aerodynamic angles AoA and AoS and their derivatives with respect to time. During the ballistic phase $(0 \le t \lesssim 49\,\mathrm{s})$, the nose roll rate is correctly reduced to zero from

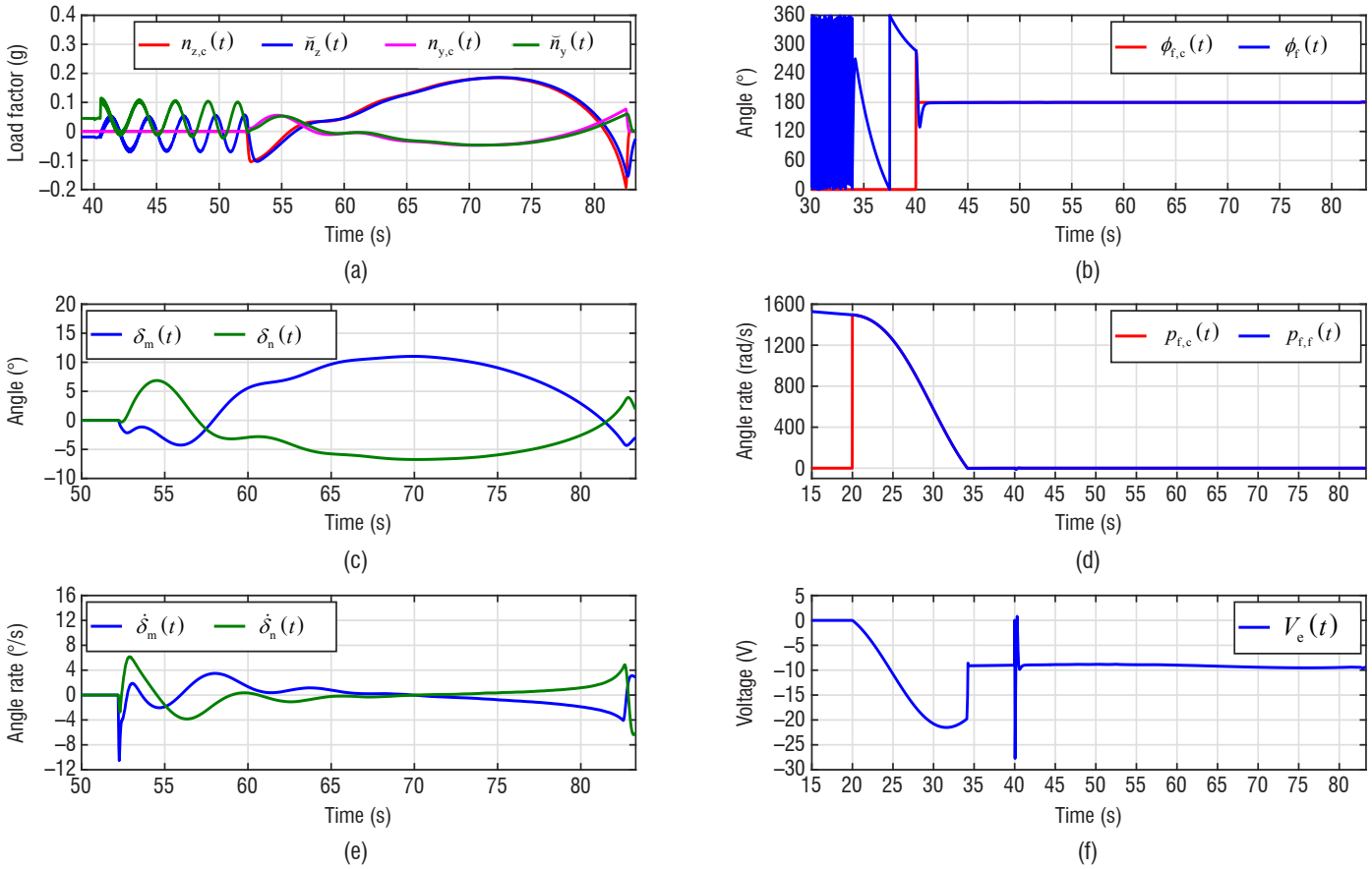

Figure 32 – Nominal scenario: (a) pitch/yaw load factors, (b) nose angle, (c) pitch/yaw actuator angles, (d) nose angle rate, (e) pitch/yaw actuator angle rates, (f) actuator voltage

$t_{start} = 20$ s (Fig. 32d), and the nose angle is then well reset to the position $\phi_f = 180°$ from $t_{switch} = 40$ s (Fig. 32a), despite the disturbances of Eq. (14) appearing in the nose position and rate dynamics. In addition, the voltage applied to the coaxial motor never exceeds the saturation value $V_{e,sat} = 60$ V and behaves almost always smoothly (Fig. 32f), hence aiding in saving energy.

During the guided phase ($49 \text{ s} \lesssim t \lesssim 83$ s), the nose position autopilot keeps on performing well (Figs. 32b, 32f) and does not inject any perceptible lag into the controlled pitch/yaw-channels, for which the commanded load factor tracking starting at $t \simeq 52$ s is excellent even for fast reference load factors sent by the PPN guidance loop at the end of the flight (Fig. 32a). The ballistic impact accuracy for a range of more than 20 km is very good, using here a perfect navigation, as the range and crossrange errors are both smaller than 25 cm.

The STT projectile globally maneuvers more in the vertical plane rather than in the horizontal plane, as shown in Figs. 32c and 32e, where the pitch canard actuator is the most solicited. However, the canard actuator deflection angles and rates remain all the time quite far from the saturation limits $\delta_{sat} = \pm 30°$ and $\dot{\delta}_{sat} = \pm 100°/s$.

The large disturbances caused on the load factor output signals by canard deployment at $t_{eng} = 40.5$ s are well rejected. The gain-scheduled nonlinear controller also provides a very good nonlocal performance, although the aerodynamic angles illustrated in Fig. 33a take values more or less far from the zero values imposed in the trimming vector for computing the set of linear controllers. Hence, the obtained performance is robust with respect to the resulting uncertainty on the trimming vector. In addition, performance is well maintained even though the pitch/yaw-channel dynamics system does not actually operate at equilibrium, as seen from the non-zero values of $\dot{\alpha}, \dot{\beta}$ given in Fig. 33b.

Three additional nonlinear simulation scenarios are finally addressed. The first scenario considers uncertainty on the launch IC's through errors placed on the muzzle velocity V_0 and on the gun barrel pointing θ_0 and azimuth ψ_0. The second scenario studies the capability of the autopilot to reject wind disturbances. The third scenario

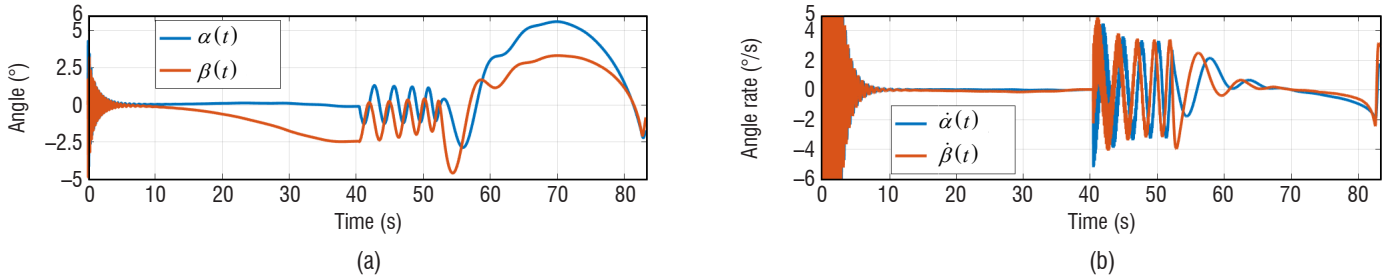

Figure 33 – Nominal closed-loop simulations: (a) AoA and AoS, (b) AoA and AoS time derivatives

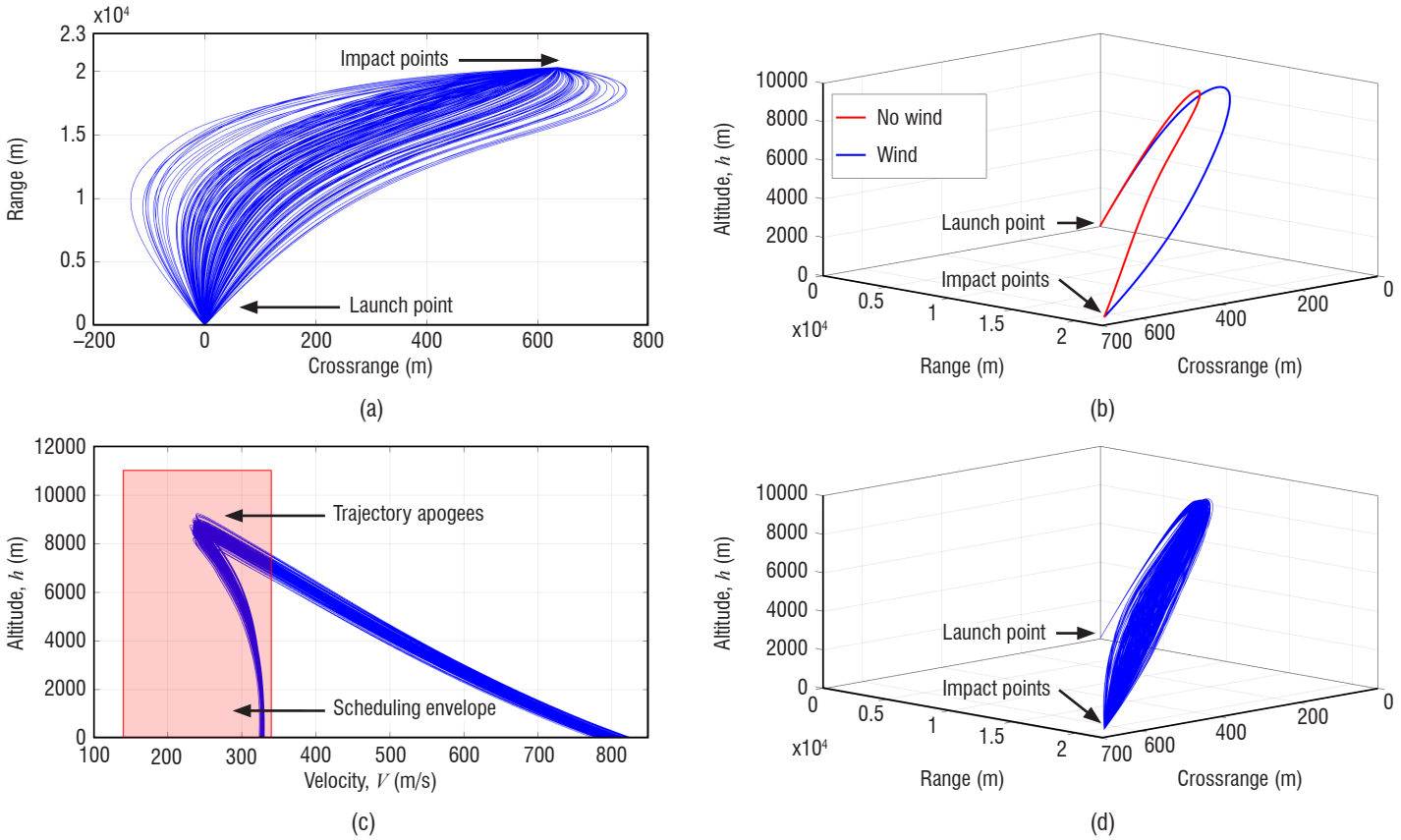

Figure 34 – Nonlinear scenarios: (a) & (c) uncertain IC's, (b) wind disturbances, (d) aerodynamic and component uncertainties

evaluates the robustness to the uncertainty modeled in the projectile aerodynamic coefficients and in the actuator and sensor dynamics (see Part "Airframe Modeling").

Concerning the first scenario, 200 random cases are simulated, in which the variables V, θ, ψ are independent, normally distributed, random numbers with a mean value equal to their nominal values $V_0 = 803$ m/s, $\theta \simeq 899.9$ mil, $\psi_0 \simeq +2026.7$ mil and a standard deviation of 10 m/s for V and of $0.5° \simeq 8.9$ mil for θ,ψ. Figure 34a illustrates the top view of the various projectile trajectories, where it can be seen that the designed G&C system performs well to always direct the projectile to the target with good precision and accuracy. Figure 34c gives the trajectories for the pitch/yaw-channel controller scheduling vector $\boldsymbol{\lambda}_{\text{PY}} = [V \;\; h]^{\text{T}}$. For the flight conditions corresponding to the projectile guided phase, all of the trajectories belong to the controller scheduling envelope $\boldsymbol{\Gamma}^{\boldsymbol{\lambda}}_{\text{PY}}$.

Concerning the second scenario, the MATLAB/Simulink `Horizontal Wind Model 07` is used for a latitude of 47.1° north, longitude of 2.4° east and altitude covering the interval [0.12000m], at 1 a.m. UTC of October 2nd 2015, using an Ap index of 48. As seen from the 3D projectile trajectories given in Fig. 34b, even though the wind leads to significantly modifying the projectile trajectory compared to the no-wind case, the wind disturbances are very well rejected by the autopilot and the projectile hits the target.

Concerning the third scenario, 300 trajectories are simulated using for each of them independent, uniformly distributed, random values for the 16 aerodynamic coefficients and the 5 coaxial motor parameters, along with random perturbed systems for the pitch/yaw-channel actuator and sensor uncertain models. Figure 34d shows that closed-loop system robust stability is ensured and that the guidance commands are successfully followed, permitting the projectile to hit the target in each case.

Concluding Remarks

This paper deals with the development of guidance and control functions for the roll, pitch and yaw-channels of a 155 mm Skid-To-Turn canard-guided spin-stabilized projectile. The complete 7DoF nonlinear and subsequently derived linearized models are addressed, and those consider the actual nose-mounted sensor position for modeling realism improvement. The application of an $\mathcal{H}_\infty$ loop-shaping design approach provides a linear autopilot for the nose roll-channel, along with a gain-scheduled controller for the complete airframe pitch/yaw-channels. Both separately designed autopilots offer high performance and robustness linear properties despite their quite simple fixed and reduced order structures. The proposed pure proportional navigation guidance and gain-scheduled control scheme is proved to be very efficient for hitting a ballistic target with a high level of precision and accuracy, through various guided flight scenarios considering nominal, perturbed or uncertain nonlinear operating conditions.

Future works for autopilot design could focus on developing an anti-windup control scheme for handling potential actuator amplitude and rate saturations. Alternative controller interpolation laws, theoretically guaranteeing global closed-loop system stability, contrary to the linear interpolation technique used here, could also be studied. In addition, it would be interesting to design a purely LPV controller and compare it to the gain-scheduled autopilot proposed here ■

Aknowledgment

The authors would like to thank the French Ministry of Defence Procurement Agency (*Direction Générale de l'Armement – DGA*) for financial support.

References

[1] P. APKARIAN, D. NOLL - *Nonsmooth $\mathcal{H}_\infty$ Synthesis*. IEEE Transactions on Automatic Control, 51(1), p. 71-86, January 2006.

[2] K. J. ÅSTRÖM - *Limitations on Control System Performance*. European Journal of Control, 6(1), p. 2-20, 2000.

[3] J.-M. BIANNIC, P. APKARIAN - *Missile Autopilot Design via a Modified LPV Synthesis Technique*. Aerospace Science and Technology, 3(3), p. 153-160, April 1999.

[4] J.-D. BLIGHT, R. L. DAILEY, D. GANGSAAS - *Practical Control Law Design for Aircraft using Multivariable Techniques*. International Journal of Control, 59(1), p. 93-137, January 1994.

[5] B. BURCHETT, A. PETERSON, M. COSTELLO - *Prediction of Swerving Motion of a Dual-Spin Projectile with Lateral Pulse Jets in Atmospheric Flight*. Mathematical and Computer Modelling, 35(7-8), p. 821-834, April 2002.

[6] D. CARLUCCI , S. JACOBSON - *Ballistics: Theory and Design of Guns and Ammunition*. CRC Press, 2007.

[7] B. CHOI, S. KANG, H. J. KIM, B.-E. JUN, J.-I. LEE, M.-J. TAHK, C. PARK - *Roll-Pitch-Yaw Integrated μ-Synthesis for High Angle-of-Attack Missiles*. Aerospace Science and Technology, 23(1), p. 270-279, December 2012.

[8] M. COSTELLO, A. PETERSON - *Linear Theory of a Dual-Spin Projectile in Atmospheric Flight*. Journal of Guidance, Control, and Dynamics, 23(5), p. 789-797, September-October 2000.

[9] G. COOPER, F. FRESCONI, M. COSTELLO - *Flight Stability of an Asymmetric Projectile with Activating Canards*. Journal of Spacecraft and Rockets, 49(1), p. 130-135, January-February 2012.

[10] M. A. CREAGH, D. J. MEE - *Attitude Guidance for Spinning Vehicles with Independent Pitch and Yaw Control*. Journal of Guidance, Control, and Dynamics, 33(3), p. 915-922, May-June 2010.

[11] J. C. DOYLE, G. STEIN - *Multivariable Feedback Design: Concepts for a Classical/Modern Synthesis.* IEEE Transactions on Automatic Control, 26(1), p. 4-16, February 1981.

[12] F. FRESCONI - *Guidance and Control of a Projectile with Reduced Sensor and Actuator Requirements*. Journal of Guidance, Control, and Dynamics, 34(6), p. 1757-1766, November-December 2011.

[13] F. FRESCONI, I. CELMINS, S. SILTON, M. COSTELLO - *High Maneuverability Projectile Flight using Low Cost Components*. Aerospace Science and Technology, 41, p. 175-188, February 2015.

[14] D. W. C. HO, J. LAM, T. W. K. CHAN - *An Application of $\mathcal{H}_\infty$ Design to Model-Following.* International Journal of Control, 55(2), p. 483-509, 1992.

[15] J. B. HOAGG, D. S. BERNSTEIN - *Nonminimum-Phase Zeros: Much to Do about Nothing - Classical Control Revisited*. Part II. IEEE Control Systems Magazine, 27(3), p. 45-57, June 2007.

[16] P. B. JACKSON - *Overview of Missile Flight Control Systems.* Johns Hopkins APL Technical Digest, 29(1), p. 9-24, 2010.

[17] P. B. JACKSON - *Robust Control and $\mathcal{H}_\infty$-Optimization-Tutorial Paper.* Automatica, 29(2), p. 255-273, March 1993.

[18] G. A. LAWRENCE, W. J. RUGH - *Gain Scheduling Dynamic Linear Controllers for a Nonlinear Plant.* Automatica, 31(3), p. 381-390, March 1995.

[19] D. J. LEITH, W. E. LEITHEAD - *Survey of Gain-Scheduling Analysis and Design.* International Journal of Control, 73(11), p. 1001-1025, January 2000.

[20] A. MARCOS, G. J. BALAS - *Development of Linear-Parameter-Varying Models for Aircraft.* Journal of Guidance, Control, and Dynamics, 27(2), p. 218-228, March-April 2004.

[21] R. L. McCOY - *Modern Exterior Ballistics: The Launch and Flight Dynamics of Symmetric Projectiles.* Schiffer Publishing, Ltd., 2012.

[22] D. C. McFARLANE, K. GLOVER - *Robust Controller Design Using Normalized Coprime Factor Plant Descriptions.* Springer-Verlag New York, 1990.

[23] D. C. McFARLANE, K. GLOVER - *A Loop-Shaping Design Procedure using $\mathcal{H}_\infty$ Synthesis.* IEEE Transactions on Automatic Control, 37(6), p. 759-769, June 1992.

[24] D. OLLERENSHAW, M. COSTELLO - *Model Predictive Control of a Direct Fire Projectile Equipped With Canards.* Journal of Dynamic Systems, Measurement, and Control, 130(6), p. 61010-1–61010-11, November 2008.

[25] P. C. PELLANDA, P. APKARIAN, H. D. TUAN - *Missile Autopilot Design via a Multi-Channel LFT/LPV Control Method.* International Journal of Robust and Nonlinear Control, 12(1), p. 1-20, January 2002.

[26] J. ROGERS, M. COSTELLO - *Design of a Roll-Stabilized Mortar Projectile with Reciprocating Canards.* Journal of Guidance, Control, and Dynamics, 33(4), p. 1026-1034, July-August 2010.

[27] W. J. RUGH, J. S. SHAMMA - *Research on Gain Scheduling.* Automatica, 36(10), p. 1401-1425, October 2000.

[28] F. SÈVE, S. THEODOULIS, P. WERNERT, M. ZASADZINSKI, M. BOUTAYEB - *Sensor Position Influence on Modeling and Control of 155mm Canard-Guided Spin-Stabilized Projectiles.* IEEE International Conference on Control, Decision and Information Technologies (CoDIT), p. 358-363, Metz, France, November 2014.

[29] J. S. SHAMMA, J. R. CLOUTIER - *Gain-Scheduled Missile Autopilot Design Using Linear Parameter Varying Transformations.* Journal of Guidance, Control, and Dynamics, 16(2), p. 256-263, March-April 1993.

[30] S. SKOGESTAD, I. POSTLETHWAITE - *Multivariable Feedback Control: Analysis and Design.* John Wiley & Sons, Ltd, 2005.

[31] N. SLEGERS - *Predictive Control of a Munition Using Low-Speed Linear Theory.* Journal of Guidance, Control, and Dynamics, 31(3), p. 768-775, May-June 2008.

[32] B. L. STEVENS, F. L. LEWIS - *Aircraft Control and Simulation.* John Wiley & Sons, Inc., 2003.

[33] S. THEODOULIS, V. GASSMANN, P. WERNERT, L. DRITSAS, I. KITSIOS, A. TZES - *Guidance and Control Design for a Class of Spin-Stabilized Fin-Controlled Projectiles.* Journal of Guidance, Control, and Dynamics, 36(2), p. 517-531, March-April 2013.

[34] S. THEODOULIS, F. SÈVE, P. WERNERT - *Robust Gain-Scheduled Autopilot Design for Spin-Stabilized Projectiles with a Course-Correction Fuze.* Aerospace Science and Technology, 42, p. 477-489, April-May 2015.

[35] K. A. WISE - *Bank-to-turn Missile Autopilot Design using Loop Transfer Recovery.* Journal of Guidance, Control, and Dynamics, 13(1), p. 145-152, January-February 1990.
[36] K. A. WISE, D. J. BROY - *Agile Missile Dynamics and Control.* Journal of Guidance, Control, and Dynamics, 21(3), p. 441-449, May-June 1998.
[37] B. A. WHITE, L. BRUYERE, A. TSOURDOS - *Missile Autopilot Design using Quasi-LPV Polynomial Eigenstructure Assignment.* IEEE Transactions on Aerospace and Electronic Systems, 43(4), p. 1470-1483, October 2007.
[38] R. YANUSHEVSKY - *Modern Missile Guidance.* CRC Press, 2008.
[39] P. ZARCHAN - *Tactical and Strategic Missile Guidance.* American Institute of Aeronautics and Astronautics, Inc., 2012.
[40] P. H. ZIPFEL - *Modeling and Simulation of Aerospace Vehicle Dynamics.* American Institute of Aeronautics and Astronautics, Inc., 2014.
[41] K. ZHOU, J. C. DOYLE, K. GLOVER - *Robust and Optimal Control.* Prentice-Hall, Inc., 1996.

Acronyms

CNRS	(Centre National de la Recherche Scientifique - *National Center for Scientific Research*)
CRAN	(Centre de Recherche en Automatique de Nancy - *Research Center for Automatic Control of Nancy*)
DGA	(Direction Générale de l'Armement - *French Ministry of Defence Procurement Agency*)
ISL	(Institut Franco-Allemand de Recherches de Saint-Louis - *French-German Research Institute of Saint-Louis*)

AUTHORS

Florian Sève received the Engineering degree in automatic control engineering from Télécom Physique Strasbourg, Strasbourg, France, in 2011, and the M.Sc. degree in automatic control and robotics from the University of Strasbourg, Strasbourg, France, in 2011. Since 2011, he had been a Ph.D. student at both the French-German Research Institute of Saint-Louis (ISL), Saint-Louis, France, and the University of Lorraine, Longwy, France, and in 2016, he received the Ph.D. degree in automatic control engineering from the University of Lorraine, France. During 2014-2015, he was a Research Assistant and a Teaching Assistant at the University of Lorraine. Since 2016, he has been a Research Associate in the Department of Guidance, Navigation and Control, French-German Research Institute of Saint-Louis. His research interests include flight dynamics modeling and development of control and guidance algorithms for guided ammunition.

Spilios Theodoulis received the diploma degree in Electrical Engineering from the University of Patras, Patras, Greece, in 2004, the M.Sc. in systems and control from Université Paul Sabatier, Toulouse, France, in 2005, and the Ph.D. degree in control systems from Université Paris Sud, Orsay, France, in 2008. Since 2009, he has been a tenured Researcher in the Department of Guidance, Navigation and Control, French-German Research Institute of Saint-Louis (ISL), Saint-Louis, France. His research interests include flight dynamics and control as well as system and hardware in the loop simulation for guided ammunition and UAV's.

Philippe Wernert studied aeronautics engineering at Ecole Nationale Supérieure de Méchanique et d'Aérotechnique (ENSMA Poitiers in France) and received the *Diplôme d'Ingénieur* in 1989. He joined the French-German Research Institute of Saint-Louis (ISL) in 1990 and graduated (Ph.D. summa cum laude) with University of Marseille (France) in 1997. From 1990 to 2000, he was mainly involved in the development and application of measuring techniques for the study of projectiles aerodynamics in subsonic and supersonic wind tunnels. Since 2000, he is in charge of the study, development and expertise of existing or new concepts of guided flying vehicles (mainly gun launched guided projectiles and microdrones). To this purpose, he developed specific trajectory and system analysis simulation programs. He is now head of the GNC (Guidance, Navigation and Control) department at ISL.

Michel Zasadzinski received the Ph.D. degree in automatic control from the Université de Lorraine, Nancy, France, in 1990. He has been an Assistant Professor at the Université de Lorraine and from 1992 to 2000, he has been a CNRS Researcher in the *Centre de Recherche en Automatique de Nancy* (CRAN, CNRS), Nancy, France. He is currently a Professor at the Institut Universitaire de Technologie (Longwy, Université de Lorraine), Lorraine, France. His research interests include the theory and application of robust control and filtering for linear and nonlinear systems, and for stochastic differential equations.

Mohamed Boutayeb received the Electrical Engineer degree from the *Ecole Hassania des Travaux Publics*, Casablanca, Morocco, in 1988 and the Ph.D. and H.D.R. degrees in automatic control from the University of Lorraine, Lorraine, France, in 1992 and 2000, respectively. From 1996 to 1997, he was an Invited Researcher at the Alexander von Humboldt Foundation, Germany. From 1997 to 1999, he was a Researcher at the *Centre National de la Recherche Scientifique* (CNRS), France. Since 2002, he has been a Full Professor at the University of Strasbourg, Strasbourg, France, and the University of Lorraine, respectively. His research interests include identification, state estimation, and control of dynamical systems. He is author and co-author of more than 200 publications in international journals and conferences.

Randomized and Robust Methods for Uncertain Systems using R-RoMulOC, with Applications to DEMETER Satellite Benchmark

M. Chamanbaz
(Arak University of Technology, Arak, Iran)

F. Dabbene, R. Tempo
(CNR-IEIIT Politecnico di Torino, Italy)

D. Peaucelle
(LAAS-CNRS, Université de Toulouse, CNRS, Toulouse, France)

C. Pittet
(CNES, Toulouse, France)

E-mail: mrchamanbaz@gmail.com

DOI: 10.12762/2017.AL13-04

R-RoMulOC is a freely distributed toolbox aimed at making easily available to the users various optimization-based methods for dealing with uncertain systems. It implements both deterministic LMI-based results, which provide guaranteed performance for all values of the uncertainties, and probabilistic randomization-based approaches, which guarantee performance for all values of the uncertainties except for a subset with arbitrary small probability measure. The paper is devoted to the description of these two approaches for analysis and control design when applied to a satellite benchmark proposed by the CNES, the French Space Agency. The paper also describes the modeling of the DEMETER satellite and its integration into the R-RoMulOC toolbox as a challenging test example. Design of state-feedback controllers and closed-loop performance analysis are carried out with the randomized and robust methods available in the R-RoMulOC toolbox.

Introduction

The last decades have witnessed an increase of interest in the area of analysis and design of systems in the presence of uncertainty. This is due to the continuous development of novel and efficient theoretical and numerical tools for robustness (ability of the system to maintain stability and performance under large variations of the system parameters), see [18] for a recent overview.

In particular, two main paradigmatic approaches have gained popularity. On one side, the worst-case, or deterministic, paradigm is aimed at guaranteeing a desired level of performance *for all* system configurations. This approach has largely benefited from the introduction of the linear matrix inequality (LMI) formalism, which led to many important results, enabling a large variety of uncertainty models and performance requirements to be tackled. Recently, the corresponding numerical tools have been collected in a Matlab toolbox named Robust Multi Objective Control toolbox (RoMulOC) [16]. The toolbox provides a variety of functions for describing and manipulating uncertain systems, and for building LMI optimization problems related to robust multiobjective control problems. We refer to [18] for and extensive review of deterministic and probabilistic methods in robust control design and analysis.

The deterministic approach can be seen as "pessimistic", in the sense that the guaranteed (and certified) performance is usually significantly worse than the actual worst case performance, due to unavoidable conservatism of the developed methodologies. This fact motivated the introduction of a probabilistic approach [23, 4], which consists in testing a finite number of configurations among the infinitely many admissible ones. This approach is said to be "optimistic", in the sense that even if a level of performance is valid for all tested cases, it may not hold for some of the unseen instances. However, rigorous theoretical results, based on large-deviation inequalities, have been derived to bound the probability of performance violation. This theory has now reached a good level of maturity, and the main algorithms have been coded in the Randomized Algorithm Control Toolbox (RACT) [24], which can be freely downloaded from http://ract.sourceforge.net/pmwiki/pmwiki.php/. This toolbox allows the user to define and manipulate various types of probabilistic uncertainties, providing efficient sampling algorithms for the various uncertainty types commonly encountered in robust control. Furthermore, it includes sequential and batch randomized algorithms for control system design.

It is important to remark that these two paradigms are not in competition, but rather they represent complementary approaches that provide additional tools to the systems engineer for the design of control systems under uncertainty. Inspired by these considerations, a joint effort between the two teams at the core of RoMulOC and RACT has been recently carried out, with the aim of merging the features of the two toolboxes in an integrated framework. This led to the development of R-RoMulOC. The main feature of this toolbox is to allow the user to input the system's description only once, using the well tested formalism of RoMulOC. Then, both deterministic and probabilistic methods can be applied to the same system, efficiently moving from a deterministic to a probabilistic description of the uncertainty, by simply changing some parameters in the code.

Like the two tools from which it originates, R-RoMulOC is freely distributed, and can be downloaded from http://projects.laas.fr/OLOCEP/rromuloc/. We refer the interested reader to this webpage for a detailed list of references to the various worst-case and probabilistic methods coded in R-RoMulOC. For a description of the R-RoMulOC toolbox, the reader is referred to [5].

In this paper, the effectiveness of the toolbox is shown by introducing the modeling of the DEMETER satellite [19] in the R-RoMulOC toolbox. Then, we show how the design of state-feedback controllers and the analysis of closed-loop performance can be performed with the randomized and robust methods available in the R-RoMulOC toolbox.

Notation

I_n stands for the identity matrix of dimension n. A^T is the transpose of A. $\{A\}^S$ represents the symmetric matrix $\{A\}^S = A + A^T$. $Tr(A)$ is the trace of A. $A \succ (\succeq) B$ means $A - B$ is positive (semi-)definite. $diag\left[\cdots \quad F_i \quad \cdots\right]$ is a block-diagonal matrix whose diagonal blocks are F_i. The symbol $\otimes$ refers to the Kronecker product. Given vectors $v, w \in \mathbb{R}^3$, the matrix $v^\times \in \mathbb{R}^{3\times 3}$ is a skew-symmetric matrix defined in such a way that $v \times w = v^\times w$; *i.e.*,

$$v^\times = \begin{bmatrix} 0 & -v_z & v_y \\ v_z & 0 & -v_x \\ -v_y & v_x & 0 \end{bmatrix}$$

for $v = [v_x \quad v_y \quad v_z]^T$. The three-dimensional sphere $\mathbb{S}^3$ is parameterized by quartenions $q \in \mathbb{R}^4$ satisfying the constraint $|q| = 1$. Finally, thestar-product describes Linear-Fractional Transformations (LFT)

$$M_a + M_b \Delta \left(I - M_d \Delta\right)^{-1} M_c = \Delta \star \left[\begin{array}{c|c} M_d & M_c \\ \hline M_b & M_a \end{array}\right].$$

DEMETER benchmark

DEMETER is a satellite of the CNES Myriade series. Launched in 2004, it observed electric and magnetic signals in Earth's ionosphere for more than 6 years. Its characteristic is to be composed of a central body and four long and flexible appendices – as shown in Figure 1 – oriented in different directions and fixed to the rigid-body at different positions distinct from the center of gravity. The model of this satellite has been provided as a benchmark in [19]. This model with uncertainties is revisited in the following. A specific function incorporated in R-RoMulOC allows variants of the complete benchmark to be generated. The variants are such that the user can generate models of various sizes, both in terms of order of the plant and in terms of the number of uncertainties involved.

Nonlinear model without flexible modes

Assuming full actuation for attitude control $u \in \mathbb{R}^3$ and modeling in the body-fixed frame, the nonlinear dynamics of the satellite are

$$J\dot{\omega} + \omega^\times J\omega = u \quad , \quad \dot{q} = \frac{1}{2}\begin{bmatrix} -\omega^\times & \omega \\ -\omega^T & 0 \end{bmatrix} q, \tag{1}$$

where $\omega \in \mathbb{R}^3$ is the rotational velocity of the satellite body-fixed frame with respect to the inertial frame, $J \in \mathbb{R}^{3\times 3}$ is the symmetric positive definite matrix corresponding to its moment of inertia and $q \in \mathbb{S}^3$ are the quaternion coordinates. A classical control problem related to this nonlinear model is to build an ideal state-feedback control law $u^\star(\omega, q)$ guaranteeing global stability. A more involved problem is to take into account in the design phase implementation issues such as saturation of reaction wheels, sensor delays and failures, the periodic sub-actuated character of magneto-torquers, etc. The model complexity depends on the considered actuators. For example, considering reaction wheel control, the model becomes

$$J\dot{\omega} + \omega^\times (J\omega + h) = -T + T_{ext} \ , \ \dot{h} = T \ , \ \dot{q} = \frac{1}{2}\begin{bmatrix} -\omega^\times & \omega \\ -\omega^T & 0 \end{bmatrix} q, \tag{2}$$

where $h \in \mathbb{R}^3$ is the vector of the angular momenta of the wheels, T is the vector of the torques applied to the wheels, and T_{ext} represents the external disturbances that the controller should reject.

Linear model with flexible modes

Let $\theta \in \mathbb{R}^3$ be the three-axis angular deviation of the satellite from some reference constant orientation. The linearized model of (1) is

$$J\ddot{\theta} = u, \tag{3}$$

which is a three-dimensional double integrator. We remark that, so far, we assumed that the satellite is composed only of a rigid body. Unfortunately, this is not the case because of solar panels and other scientific equipment onboard. At small pointing errors (the attitude control is required to have less than 0.1 degree precision), the flexibility of

Figure 1 – DEMETER satellite. ©CNES November 2003, ill. D. Ducros

appendices is not negligible and needs to be considered in the model. The linearized model including flexible modes is [19]

$$\begin{bmatrix} J & J^{1/2}L \\ L^T J^{1/2} & I \end{bmatrix}\begin{pmatrix}\ddot{\theta}\\ \ddot{\eta}\end{pmatrix}+\begin{bmatrix} 0 & 0 \\ 2Z\Omega & \Omega^2 \end{bmatrix}\begin{pmatrix}\dot{\eta}\\ \eta\end{pmatrix}=\begin{bmatrix} I \\ 0 \end{bmatrix}u, \qquad (4)$$

where $\eta \in \mathbb{R}^{2n_f}$ is the vector of angular deviations in torsion and bending of the flexible appendices (up to $n_f = 4$ in the DEMETER model), L is a matrix modeling the cross influence of flexible modes on the rigid body, which depends on how the appendices are attached to the rigid body, $Z = diag\begin{bmatrix}\cdots & \zeta_i I_2 & \cdots\end{bmatrix}$ is a diagonal matrix of all flexible mode damping factors and $\Omega = diag\begin{bmatrix}\cdots & \omega_i I_2 & \cdots\end{bmatrix}$ is a diagonal matrix of all flexible mode natural frequencies (the low damped oscillatory flexible dynamics are such that $\ddot{\eta}_i + 2\zeta_i\omega_i\dot{\eta}_i + \omega_i^2\eta_i = -L_i^T J^{1/2}\ddot{\theta}$). The same parameters apply for the bending and torsion effects and, in most cases, one can assume that the appendices are identical ($\zeta_i = \zeta \forall i = 1,\ldots,n_f$ and $\omega_i = \omega \forall i =,1\ldots,n_f$). In (4), the force $L^T J^{1/2}\ddot{\theta}$ that acts on the flexible modes comes from the derivative of the angular momentum of the rigid body, and its symmetric feedback reaction on the rigid body is $J^{1/2}L\ddot{\eta}$. An analysis in the frequency domain shows that only the first flexible modes of the appendices have significant influence on the system dynamics, while all other flexible modes, including those of the solar panels, can be neglected.

Parametric uncertainties

In (4) the matrix L, which is only due to positioning of the appendices, is assumed to be perfectly known. All other parameters, *i.e.,* J, ζ_i and ω_i, cannot be precisely measured on the Earth due to gravity, and hence are considered to be uncertain. The damping ratio and natural frequencies ζ_i, ω_i describe the first flexible modes of the four appendices. These appendices are of same length and same material, and hence their flexible modes are almost identical. However, there are discrepancies from one appendix to another, which are not known. The damping ratio and natural frequencies are assumed to be bounded in the intervals

$$\omega_i \in [\,0.2\cdot 2\pi\,,\,0.6\cdot 2\pi\,]\,,\ \zeta_i \in [\,5\cdot 10^{-4}\,,\,5\cdot 10^{-3}\,]\ \ \forall i = 1,\ldots,4.$$

The inertia J has the following nominal value on the ground

$$J_o = \begin{bmatrix} J_{o11} & J_{o12} & J_{o13} \\ J_{o12} & J_{o22} & J_{o23} \\ J_{o13} & J_{o23} & J_{o33} \end{bmatrix} = \begin{bmatrix} 31.38 & -1.11 & -0.26 \\ -1.11 & 21.19 & -0.78 \\ -0.26 & -0.78 & 35.70 \end{bmatrix}.$$

Uncertainties in J are assumed to be at most of 30% for the diagonal entries and ± 3 for the off-diagonal entries. That is, for example, $J_{11} \in [\,0.7J_{o11}\,,1.3J_{o11}\,] = [\,21.97\,,40.80\,]$ and $J_{12} \in [\,J_{o12} - 3\,,\, J_{o12} + 3\,] = [\,-4.11\,,1.89\,]$.

LFT modeling of uncertain matrices

We first derive the LFT model of the $[2Z\Omega \quad \Omega^2]$ matrix. Note that the uncertain matrices Ω and Z are defined as a nominal matrix with normalized discrepancies around the nominal value. Hence, one can write Ω as

$$\Omega = \omega_a I + \omega_b \delta_\Omega = \delta_\Omega \star \left[\begin{array}{c|c} 0 & I \\ \hline \omega_b I & \omega_a I \end{array}\right]$$
$$\delta_\Omega = diag\begin{bmatrix}\delta_{\omega_1} I_2 & \delta_{\omega_2} I_2 & \delta_{\omega_3} I_2 & \delta_{\omega_4} I_2\end{bmatrix},$$

where $\omega_a = \frac{1}{2}(0.6\cdot 2\pi + 0.2\cdot 2\pi) = 0.4\cdot 2\pi$ is the mean between the two extreme values, $\omega_b = \frac{1}{2}(0.6\cdot 2\pi - 0.2\cdot 2\pi) = 0.2\cdot 2\pi$ is the maximal deviation and $|\,\delta_{\omega_i}\,| \le 1, i = 1,\ldots,4$ are norm bounded uncertainties. The uncertain matrix Z can be derived in a similar way

$$Z = \zeta_a I + \zeta_b \delta_Z = \delta_Z \star \left[\begin{array}{c|c} 0 & I \\ \hline \zeta_b I & \zeta_a I \end{array}\right]$$
$$\delta_Z = diag\begin{bmatrix}\delta_{\zeta_1} I_2 & \delta_{\zeta_2} I_2 & \delta_{\zeta_3} I_2 & \delta_{\zeta_4} I_2\end{bmatrix},$$

with $\zeta_a = \frac{1}{2}(5\cdot 10^{-3} + 5\cdot 10^{-4}) = 2.75\cdot 10^{-3}$ being the mean between the two extreme values, $\zeta_b = \frac{1}{2}(5\cdot 10^{-3} - 5\cdot 10^{-4}) = 2.25\cdot 10^{-3}$ being the maximal deviation and $|\,\delta_{\zeta_i}\,| \le 1, i = 1,\ldots,4$ being the norm bounded uncertainties. Using properties of the star-product we have

$$\begin{bmatrix} 2Z & \Omega \end{bmatrix} = \begin{bmatrix} \delta_Z & 0 \\ 0 & \delta_\Omega \end{bmatrix} \star \left[\begin{array}{cc|cc} 0 & 0 & I & 0 \\ 0 & 0 & 0 & I \\ \hline 2\zeta_b I & \omega_b I & 2\zeta_a I & \omega_a I \end{array}\right],$$

and

$$\begin{bmatrix} 2Z\Omega & \Omega^2 \end{bmatrix} = \Omega\begin{bmatrix} 2Z & \Omega \end{bmatrix}$$
$$= \begin{bmatrix} \delta_\Omega & 0 & 0 \\ 0 & \delta_Z & 0 \\ 0 & 0 & \delta_\Omega \end{bmatrix} \star \left[\begin{array}{ccc|cc} 0 & 2\zeta_b I & \omega_b I & 2\zeta_a I & \omega_a I \\ 0 & 0 & 0 & I & 0 \\ 0 & 0 & 0 & 0 & I \\ \hline \omega_b I & 2\omega_a\zeta_b I & \omega_a\omega_b I & 2\omega_a\zeta_a I & \omega_a^2 I \end{array}\right].$$

We remark that the LFT defined in this way is minimal. An alternative is to build separately the LFTs for $2Z\Omega$ and Ω^2 matrices and then to concatenate the two. This alternative gives an LFT with δ_Ω repeated 3 times, which is clearly non-minimal.

We next focus on the LFT modeling of the matrix depending on the uncertain matrix J. The difficulty can be observed arising from modeling the square-root of J. In [19], it is implicitly assumed that off-diagonal terms in $J^{1/2}$ are sufficiently small to be neglected in the computation of $J^{1/2}$. That is, defining

$$J = J_1 + J_1^T + J_2 \ :\ J_1 = \begin{bmatrix} 0 & J_{12} & J_{13} \\ 0 & 0 & J_{23} \\ 0 & 0 & 0 \end{bmatrix},$$
$$J_2 = diag\begin{bmatrix} J_{11} & J_{22} & J_{33} \end{bmatrix},$$

it is assumed that $J^{1/2} \simeq J_2^{1/2}$. Then, in order to further simplify the model, the paper [19] makes the second assumption that the square root can be replaced by a first order approximation $(J_{2a} + J_{2b}\delta_{J_2})^{1/2} \simeq J_{2a}^{1/2} + \frac{1}{2}J_{2b}\delta_{J_2}$. The relative error of this last approximation is less than 2%, which is indeed reasonable. Based on this approximation, the minimal LFT model is such that δ_{J_2} is repeated twice. As we will show next, there is no reason for performing the first order approximation, and this can be avoided without increasing the size of the LFT.

Two ways for improving the square root LFT modeling are explored next. The first still assumes that $J^{1/2} \simeq J_2^{1/2}$ but avoids the first-order approximation of the square root. To this end, we define the following LFT model of the square root of inertia diagonal components

$$J_2^{1/2} = \hat{J}_{2a} + \hat{J}_{2b}\delta_{J_2} = \delta_{J_2} \star \left[\begin{array}{c|c} 0 & I \\ \hline \hat{J}_{2b} & \hat{J}_{2a} \end{array}\right],$$

where $\hat{J}_{2a} = \frac{1}{2}((1.3J_{2a})^{1/2} + (0.7J_{2a})^{1/2})$ is the mean between the two extreme values, $\hat{J}_{2b} = \frac{1}{2}((1.3J_{2a})^{1/2} - (0.7J_{2a})^{1/2})$ is the maximal deviation, $\delta_{\hat{J}_2} = diag[\delta_{\hat{J}_{11}} \quad \delta_{\hat{J}_{22}} \quad \delta_{\hat{J}_{33}}]$ and $|\delta_{\hat{J}_{ii}}| \leq 1$ are the norm bounded uncertainties. Using properties of the star-product, one obtains

$$\begin{bmatrix} J_2 & J_2^{1/2}L \\ L^T J_2^{1/2} & L^T L \end{bmatrix} = \begin{bmatrix} J_2^{1/2} \\ L^T \end{bmatrix} \begin{bmatrix} J_2^{1/2} & L \end{bmatrix}$$

$$= \begin{bmatrix} \delta_{\hat{J}_2} & 0 \\ 0 & \delta_{\hat{J}_2} \end{bmatrix} \star \left[\begin{array}{cc|cc} 0 & \hat{J}_{2b}^2 & \hat{J}_{2b}\hat{J}_{2a} & \hat{J}_{2b}L \\ 0 & 0 & I & 0 \\ \hline I & \hat{J}_{2a}\hat{J}_{2b} & \hat{J}_{2a}^2 & \hat{J}_{2a}L \\ 0 & L^T\hat{J}_{2b} & L^T\hat{J}_{2a} & L^T L \end{array}\right].$$

Notice that – as in [19] – the uncertainties $\delta_{\hat{J}_2}$ are repeated only twice; hence, the LFT size is not increased by precise modeling of the square root.

Next, consider the cross inertia dependent matrix

$$J_1 = \hat{J}_{1a} + \hat{J}_{1b}\delta_{J_1}\hat{J}_{1c} = \delta_{J_1} \star \left[\begin{array}{c|c} 0 & J_{1c} \\ \hline J_{1b} & J_{1a} \end{array}\right],$$

$$J_{1a} = \begin{bmatrix} 0 & J_{o12} & J_{o13} \\ 0 & 0 & J_{o23} \\ 0 & 0 & 0 \end{bmatrix} \quad J_{1b} = \begin{bmatrix} 3 & 3 & 0 \\ 0 & 0 & 3 \\ 0 & 0 & 0 \end{bmatrix} \quad J_{1c} = \begin{bmatrix} 0 & 1 & 0 \\ 0 & 0 & 1 \\ 0 & 0 & 1 \end{bmatrix},$$

$$\delta_{J_1} = diag\begin{bmatrix} \delta_{J_{12}} & \delta_{J_{13}} & \delta_{J_{23}} \end{bmatrix} \ : \ |\delta_{J_{ij}}| \leq 1.$$

Using properties of the star-product we finally arrive at

$$\begin{bmatrix} J_1 + J_1^T + J_2 & J_2^{1/2}L \\ LJ_2^{1/2} & I \end{bmatrix}$$

$$= diag\begin{bmatrix} \delta_{J_1} \\ \delta_{J_1} \\ \delta_{\hat{J}_2} \\ \delta_{\hat{J}_2} \end{bmatrix} \star \left[\begin{array}{cccc|cc} 0 & 0 & 0 & 0 & J_{1c} & 0 \\ 0 & 0 & 0 & 0 & J_{1b}^T & 0 \\ 0 & 0 & 0 & \hat{J}_{2b}^2 & \hat{J}_{2b}\hat{J}_{2a} & \hat{J}_{2b}L \\ 0 & 0 & 0 & 0 & I & 0 \\ \hline J_{1b} & J_{1c}^T & I & \hat{J}_{2a}\hat{J}_{2b} & J_{1a} + J_{1a}^T + \hat{J}_{2a}^2 & \hat{J}_{2a}L \\ 0 & 0 & 0 & L^T\hat{J}_{2b} & L^T\hat{J}_{2a} & I \end{array}\right].$$

The second approach for improving the LFT modeling of the square-root $J^{1/2}$ first requires the relevance of modeling the coefficients of J in intervals to be questioned. The matrix J is symmetric positive definite, which can be defined as $J = (J_o^{1/2} + \Delta_{\hat{J}})^2$ with an uncertain symmetric matrix $\Delta_{\hat{J}}$ constrained by a convex quadratic constraint

$$X + Y\Delta_{\hat{J}} + \Delta_{\hat{J}}Y + \Delta_{\hat{J}}Z\Delta_{\hat{J}} \preceq 0 \ , \ Z \succeq I,$$

where all X, Y and Z matrices are chosen as symmetric, to match the symmetric nature of $\Delta_{\hat{J}}$. The set is also written as

$$(\Delta_{\hat{J}} - \Delta_o)Z(\Delta_{\hat{J}} - \Delta_o) \preceq \Delta_o Z \Delta_o - X,$$

where $\Delta_o = -YZ^{-1}$ is the center of the set. Recall that $J = (J_o^{1/2} + \Delta_{\hat{J}})^2$ is (as formulated in [19]) a matrix whose 6 independent coefficients are in intervals. The matrix J can therefore be defined as the convex linear combination of 2^6 vertices – denoted as $J^{[v]}, v = 1, \ldots, 2^6$ – and constructed taking all of the extreme combinations of the interval uncertainties. A natural way of defining X, Y, Z matrices is to impose on the set the requirement of containing the convex combination of the square-roots of extremal values, that is, the matrices $\Delta_{\hat{J}}^{[v]} = J^{[v]1/2} - J_o^{1/2}$

$$(\Delta_{\hat{J}}^{[v]} - \Delta_o)Z(\Delta_{\hat{J}}^{[v]} - \Delta_o) \preceq \Delta_o Z \Delta_o - X \ \ \forall v = 1, \ldots, 2^6. \qquad (5)$$

A natural choice for the center of the set is to take the mean value of all vertices

$$\Delta_o = \frac{1}{2^6}\sum_{v=1}^{2^6} \Delta_{\hat{J}}^{[v]}. \qquad (6)$$

Of course, one aims at defining the smallest set containing the matrices $\Delta_{\hat{J}}^{[v]}$. It is rather easy to see that the size of the set is highly dependent on the matrix $\Delta_o Z \Delta_o - X$. The smaller it is, the smaller the set of $\Delta_{\hat{J}}$ matrices will be. It is suggested to minimize this matrix with respect to its Frobenius norm, which amounts to taking

$$(X^*, Z^*) = \arg \min_{Z \succeq I, (5)} Tr(\Delta_o Z \Delta_o - X),$$

and $Y^* = -\Delta_o Z^{*-1}$. Having performed this LMI optimization, the inertia of the satellite is now defined as

$$J = (J_o^{1/2} + \Delta_{\hat{J}})^2 \ , \ \Delta_{\hat{J}} \in \left\{ \Delta = \Delta^T : \begin{bmatrix} I & \Delta \end{bmatrix} \begin{bmatrix} X^* & Y^* \\ Y^* & Z^* \end{bmatrix} \begin{bmatrix} I \\ \Delta \end{bmatrix} \preceq 0 \right\}.$$

LFT modeling with respect to this newly defined uncertainty is rather simple, following the same lines as the first method, and gives

$$\begin{bmatrix} J & J^{1/2}L \\ L^T J^{1/2} & I \end{bmatrix} = \begin{bmatrix} \Delta_{\hat{J}} & 0 \\ 0 & \Delta_{\hat{J}} \end{bmatrix} \star \left[\begin{array}{cc|cc} 0 & I & J_o^{1/2} & L \\ 0 & 0 & I & 0 \\ \hline I & J_o^{1/2} & J_o & J_o^{1/2}L \\ 0 & L^T & L^T J_o^{1/2} & I \end{array}\right].$$

The LFT built in this way has two remarkable features: *i)* to the best of our knowledge, it is the first time that the modeling involves an uncertain matrix that is constrained to be symmetric, *ii)* this matrix is repeated twice $\begin{bmatrix} \Delta_{\hat{J}} & 0 \\ 0 & \Delta_{\hat{J}} \end{bmatrix} = \Delta_{\hat{J}} \otimes I_2$. To build LMI type results for such uncertainties one needs to build some DG-scaling like result [11]. That is, to characterize, via linear matrix equalities and inequalities, the matrices $\Theta_{\hat{J}}$ that satisfy

$$\begin{bmatrix} I & \Delta_{\hat{J}} \otimes I_2 \end{bmatrix} \Theta_{\hat{J}} \begin{bmatrix} I \\ \Delta_{\hat{J}} \otimes I_2 \end{bmatrix} \preceq 0$$

$$\forall \Delta_{\hat{J}} \in \left\{ \Delta = \Delta^T : \begin{bmatrix} I & \Delta \end{bmatrix} \begin{bmatrix} X^* & Y^* \\ Y^* & Z^* \end{bmatrix} \begin{bmatrix} I \\ \Delta \end{bmatrix} \preceq 0 \right\}.$$

A choice of such matrices DG is a natural generalization of the well-known DG-scalings that work for scalar repeated uncertainties

$$\Theta_{\hat{J}} = \begin{bmatrix} X^* \otimes D & Y^* \otimes D + I \otimes G \\ Y^* \otimes D - I \otimes G & Z^* \otimes D \end{bmatrix} : \begin{array}{l} D = D^T \succ 0 \in \mathbb{R}^{2\times 2} \\ G = -G^T \in \mathbb{R}^{2\times 2}. \end{array}$$

The proof of this fact is trivial: in the formula below, the G dependent terms cancel one another thanks to the fact that Δ is symmetric and remains only

$$\begin{bmatrix} I & \Delta\otimes I_2 \end{bmatrix}\Theta\begin{bmatrix} I \\ \Delta\otimes I_2 \end{bmatrix} = D\otimes\left(\begin{bmatrix} I & \Delta \end{bmatrix}\begin{bmatrix} X^* & Y^* \\ Y^* & Z^* \end{bmatrix}\begin{bmatrix} I \\ \Delta \end{bmatrix}\right),$$

which is negative semi-definite because it is the result of a Kronecker product of a positive definite matrix and a negative semi-definite matrix.

LFT modeling of the uncertain system

Based on the described modeling of uncertain matrices discussed in the previous section and with some rather trivial additional manipulations – independent from the choice of model for the inertia J – the system dynamics can be converted to the following descriptor state-space form

$$\left(\Delta_E \star \begin{bmatrix} E_d & E_c \\ E_b & E_a \end{bmatrix}\right)\dot{X} = \left(\Delta_A \star \begin{bmatrix} A_d & A_c \\ A_b & A_a \end{bmatrix}\right)X + Bu, \qquad (7)$$

where $X = \begin{pmatrix} \dot{\theta}^T & \dot{\eta}^T & \theta^T & \eta^T \end{pmatrix}^T$ is the state of the satellite including its flexible modes; $\Delta_A = diag\begin{bmatrix} \delta_\Omega & \delta_Z & \delta_\Omega \end{bmatrix}$; $\Delta_E = diag\begin{bmatrix} \delta_{J_1} & \delta_{J_1} & \delta_{J_2} & \delta_{J_2} \end{bmatrix}$ or $\Delta_E = \Delta_J I\otimes_2$ depending on the choice of model for the inertia; E and A matrices are built accordingly. Taking the inverse of the left-hand side of (7) this formula allows a usual state-space model to be built,

$$\dot{X} = \left(diag\begin{bmatrix} \Delta_E \\ \Delta_A \end{bmatrix} \star \left[\begin{array}{cc|cc} E_d - E_cE_a^{-1}E_b & -E_cE_a^{-1}A_b & -E_cE_a^{-1}A_a & -E_cE_a^{-1}B \\ 0 & A_d & A_c & 0 \\ \hline E_a^{-1}E_b & E_a^{-1}A_b & E_a^{-1}A_a & E_a^{-1}B \end{array}\right]\right)\begin{pmatrix} X \\ u \end{pmatrix},$$

which is the same as the following linear system

$$\begin{cases} \dot{X} = E_a^{-1}A_aX + \begin{bmatrix} E_a^{-1}E_b & E_a^{-1}A_b \end{bmatrix}w_\Delta + E_a^{-1}Bu \\ z_\Delta = \begin{bmatrix} -E_cE_a^{-1}A_a \\ A_c \end{bmatrix}X + \begin{bmatrix} E_d - E_cE_a^{-1}E_b & -E_cE_a^{-1}A_b \\ 0 & A_d \end{bmatrix}w_\Delta + \begin{bmatrix} -E_cE_a^{-1}B \\ 0 \end{bmatrix}u, \end{cases}$$

in a feedback loop with the uncertainty $w_\Delta = diag\begin{bmatrix} \Delta_E \\ \Delta_A \end{bmatrix}z_\Delta$. Such a system with feedback uncertainties can be easily defined in the R-RoMulOC toolbox. A dedicated function has been developed that yields this model. The output is of the following type

$$\begin{cases} \dot{X} = AX + B_\Delta w_\Delta + B_u u \\ z_\Delta = C_\Delta X + D_{\Delta\Delta}w_\Delta + D_{\Delta u}u \qquad w_\Delta = \Delta z_\Delta . \\ y = C_y X + D_{y\Delta}w_\Delta + D_{yu}u \end{cases}$$

Reduced size variations of the uncertain model

In order to test methods with respect to the dimensions of the problem to be solved (both in terms of order of the systems and in terms of size of the uncertainty block) several variants have been coded. The variations are threefold:

- Select only one or two of the three axes. This of course reduces the number of states describing the satellite attitude. Moreover, in the case when only one axis is considered, the torsion and bending effects of the flexible modes can be combined. It produces models with twice less flexible mode states and twice smaller matrices Δ_A.
- Select only some of the appendices. One can (virtually of course) remove any of the appendices. It produces models with reduced number of flexible modes and smaller matrices Δ_A.
- Impose that all appendices have the same frequency and damping characteristics, $\omega_i = \omega$ and $\zeta_i = \zeta$. In such case, the number of flexible modes can be reduced to only three modes (one per axis) that are the projections of all bending and torsion modes on the attitude axes.

The simplest and rather realistic models amount to assuming (a) zero cross influence between satellite axes and (c) that all appendices have exactly identical characteristics. Such assumptions reduce the study to three fourth-order models, one per angular axis. Each of these models ($i = 1,2,3$) are described by two scalar equations

$$\begin{cases} J_{ii}\ddot{\theta}_i + \sqrt{J_{ii}}l_i\ddot{\eta}_i = u_i \\ \sqrt{J_{ii}}l_i\ddot{\theta}_i + \ddot{\eta}_i + 2\zeta\omega\dot{\eta}_i + \omega^2\eta_i = 0 \end{cases}, \qquad (8)$$

and illustrated in Figure 2 (where $\alpha = \sqrt{J_{ii}}l_i$). Corresponding LFT models have a 5 × 5 uncertain matrix where scalar uncertainties on J_{ii} appear twice, scalar uncertainties on ω appear twice and scalar uncertainties on ζ appear once.

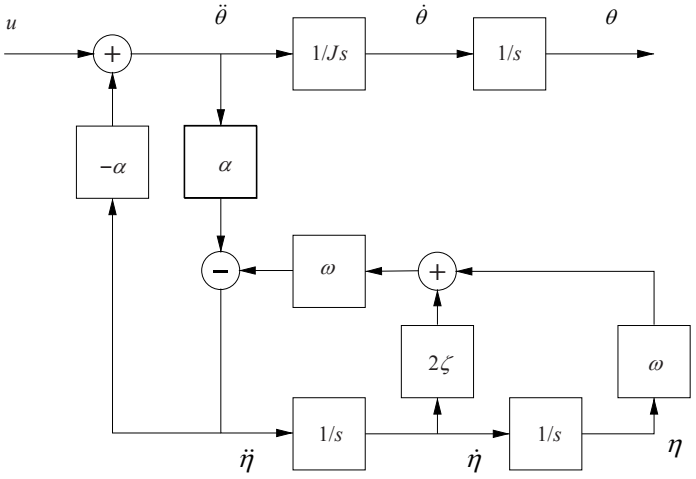

Figure 2 – Block diagram of a one axis model with one flexible mode

State-feedback design model

The control design problem is to build a control that ensures the following performances:

- As small as possible pointing error. To this end, the control should contain an integrator to improve the low frequency disturbing torque rejection.
- Avoid saturation of the reaction wheel actuators. These actuators have the following nonlinear model

$$u = sH(s)\,sat_W\left(\frac{1}{s}sat_T(u_c)\right),$$

where u_c stands for the torque control input computed by the controller and u is the actual torque applied by the reaction wheel. sat_T is a saturation on the torque to be applied, which is of 5×10^{-3} Nm. It is, in general, not critical and can be neglected. The term $\frac{1}{s}$ is an integrator that yields the reaction wheel angular momentum. This angular

momentum is saturated (sat_W), with a saturation level of 0.12 Nms. This saturation is critical: when it occurs, the system is no longer actuated and is open-loop unstable. Finally, $sH(s)$ is a transfer function describing the dynamics of the reaction wheel.

- Other specifications, such as noise rejection, robustness to time-delays in the control, etc., as discussed in [19].

In order to take into account the two specifications (i) and (ii), we add to the model an integrator of the output and a pseudo integrator $I(s) = \frac{1}{s+0.001}$ of the input. We remark that an integrator in the input – instead of a pseudo integrator – would result in instability since the states of the integrator are not controllable in the formulation. These are represented with dotted lines in Figure 3. The dotted lines indicate that these blocks are added by the designer, and are hence part of the control law.

For that augmented model we seek a robust state-feedback control, as illustrated in Figure 3. The dotted lines represent the state-feedback with eight gains. k_P, k_I, k_D are the feedback gains with respect to the angular error θ, its integral, and its derivative, respectively. k_{Pf} and k_{Df} are the gains on the angular position of the flexible mode η and on its derivative, respectively. k_W is the gain on the state of the pseudo-integrator that models the reaction wheel speed. $K_H \in \mathbb{R}^{1\times 2}$ is the gain on the states of the reaction wheels. The aim of the control is to minimize the peak of z_2 (the reaction wheel speed), especially when the satellite starts from a large non-zero angle and angular rate initial conditions that are represented as input signals w_2. We assume a maximal ± 0.08 deg/s angular rate initial deviation and ± 15 deg angular initial deviation. Simultaneously, the control should minimize the effect of unknown input perturbations on the system precision; that is to minimize the transfer for w_1 to z_1.

The design of such a state-feedback controller is possible using the R-RoMulOC toolbox [5, 16]. In particular, a function named `demeterPerformance` is developed to generate models required for controller design. The following lines of codes define three models being:

- The augmented model with integrator on the output, reaction wheel model and pseudo-integrator of the input.
- Model with w_1 / z_1 performance input output.
- Model with w_2 / z_2 performance input output.

```
usysIW=demeterPerformance(ConsideredAxis,Considered
Appendices,... model_type,uncertainty_type, rwheels,0);

usysIW1=demeterPerformance(ConsideredAxis,Considered
Appendices,... model_type,uncertainty_type, rwheels,1);

usysIW2=demeterPerformance(ConsideredAxis,Considered
Appendices,... model_type,uncertainty_type, rwheels,2);
```

Next, we briefly explain various arguments of the `demeterPerformance` function.

The parameters `ConsideredAxis` and `ConsideredAppendices` define the number of axes and appendices used in the model respectively. If `model_type=2`, all flexible modes have the same frequency and damping characteristic with the same uncertain parameters but, if `model_type=1`, uncertain parameters are allowed to be independent for different appendices. If `uncertainty_type=1`, all uncertainties are norm-bounded scalars; if `uncertainty_type=2`, all uncertainties are scalars in intervals; and if `uncertainty_type=3`, uncertainties on inertia are norm-bounded deterministic; others are uniformly distributed in intervals. If `rwheels=1`, the reaction wheels are included in the model and if `rwheels=0`, the model does not include reaction wheel dynamics.

Let N_a be the number of considered axes and N_f be the number of appendices. The satellite dynamics involve $2*N_a+4*N_f$ states, to

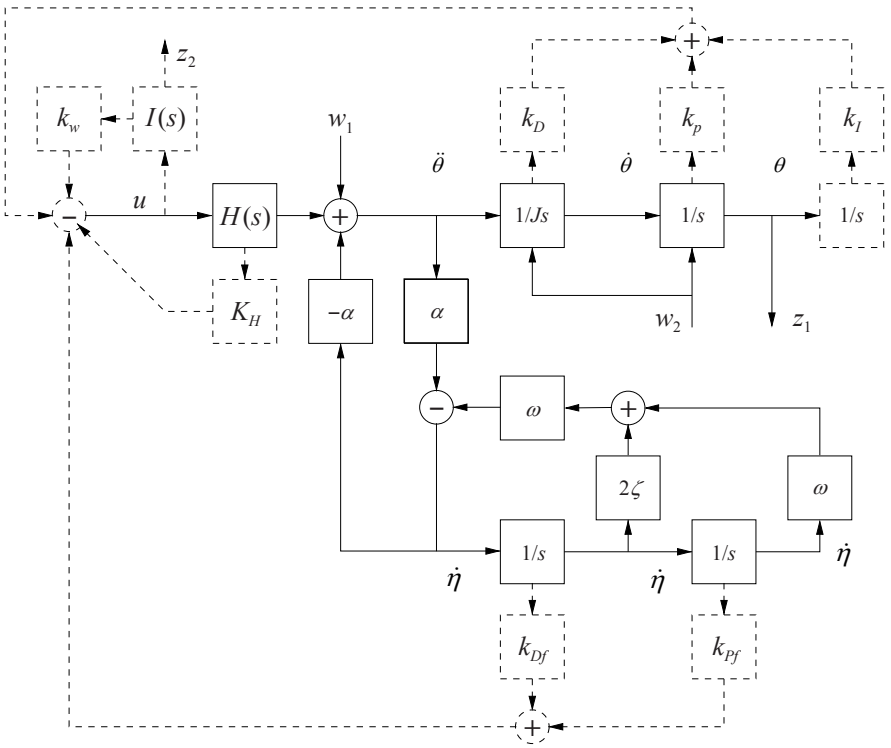

Figure 3 – Block diagram of a state-feedback design model.

which one adds actuator models and N_a integrators of the control law. If `model_type=1` (all appendices have different characteristics) the satellite dynamics involve $N_a(N_a+1)/2+2*N_f$ scalar uncertainties. If `model_type=2` (all appendices have identical characteristics) the satellite dynamics involve $N_a(N_a+1)/2+2$ scalar uncertainties. A special case is when $N_a=1$ and all appendices are considered identical. In such a case, the satellite dynamics involve only 4 states and 3 uncertainties, see (8).

In R-RoMulOC there are two approaches to design the robust state feedback controller. The first approach is based on deterministic multiobjective methods, in which the performance specifications are enforced to hold for the entire set of uncertainties. The second paradigm is probabilistic and randomized methods, in which the design specifications (including stability) are enforced to hold up to a probability level. In the next two subsections, we study the two mentioned approaches in state feedback design.

Controller design

Deterministic approach

In R-RoMulOC the deterministic state-feedback design LMI problem is defined as

```
quiz=ctrpb('state-feedback','unique')...
   +1*hinfty(usysIW1)...
   +100*i2p(usysIW2)...
   +dstability(usysIW,region('plane',-1e-4))...
   +dstability(usysIW,region('plane',-10,pi));
```

The LMI problem built in this way is based on quadratic stability type results with Lyapunov shaping paradigm [21], that is, a unique Lyapunov matrix is used for assessing all four specified performances and for all values of uncertainties. The four specifications are: the H_∞ performance with respect to the input/outputs w_1/z_1; the impulse-to-peak performance with respect to the input/outputs w_2/z_2 (which is equivalent to looking at peak response to the initial conditions); the pole location performance such that all closed-loop poles should have a real part smaller than -1×10^{-4} and greater than –10 (which influences the rapidity of the time response). The LMI problem is solved in R-RoMulOC using the following commands that return the state-feedback gain

```
Ksf_det=solvesdp(quiz,sdpsettings('verbose',1,'solver',
'mosek'));
```

Probabilistic Design

There are two paradigms in probabilistic techniques for controller design. The first approach is non-sequential, in which a sampled version of the original problem is solved in one shot. The scenario approach [2, 3] is a non-sequential approach for solving uncertain convex problems. The main idea in this approach is to reformulate a semi-infinite convex optimization problem as a sampled convex optimization problem subject to a finite number of random constraints extracted from the uncertainty set. The second class of probabilistic design algorithms are sequential methods, in which, at each iteration, a candidate solution is constructed – based on the gradient [20], ellipsoid [14], cutting plane [9] or sampling based technique [7] – and its robustness is verified through a sequential probabilistic validation algorithm [1]. In R-RoMulOC, the scenario approach and sequential algorithms based on the gradient update rule [20] and the sequential approach presented in [7] are used to solve the uncertain state-feedback design problem. A controller addressing the same performance requirements as in the deterministic case can be formulated and solved using the sequential algorithm [6, 7]

```
quiz = ctrpb('state-feedback','rand')...
   +1*hinfty(usysIW1)...
   +100*i2p(usysIW2)...
   +dstability(usysIW,region('plane',-1e-4))...
   +dstability(usysIW,region('plane',-10,pi));
opts=randsettings('epsilon',0.1,'delta',1e-9,...
'method','sequential','sdpopts',...
sdpsettings('verbose',0,'solver','mosek'));
Ksf_prob=solvesdp(quiz,opts);
```

The parameters `epsilon` and `delta` defined in the `randsettings` function are the required accuracy and confidence levels of the solution. In words, the probability that the solution does not satisfy constraints is smaller than `epsilon` and this statement holds with a probability of at least `1-delta`. We refer to [4, 23] for the exact definition of accuracy and confidence levels. We remark that one can solve the same problem using the scenario approach [2, 3] by changing `'sequential'` to `'scenario'` in the code.

Closed-loop analysis of the state-feedback law

An important feature of R-RoMulOC is to provide, within a unified framework, a variety of available tools for analyzing the robust performance of uncertain closed-loop systems. In particular, a user can check whether several performance criteria, such as for instance the H_2 and H_∞ norms, impulse-to-peak response, pole location, etc., hold either robustly or with a guaranteed level of probability. Similar to design techniques, analysis can be performed either in a deterministic setting or through randomized algorithms resulting in a probabilistic estimate of robust performance.

Deterministic analysis

The deterministic analysis methods implemented in R-RoMulOC are based on Lyapunov-type certificates. In particular, it can be based on either a parameter-dependent Lyapunov function [10, 13, 15] or a common Lyapunov function [21]. An upper bound of the closed-loop H_∞ norm for the transfer z_1/w_1 can be computed using parameter-dependent Lyapunov matrices, as follows

```
usysIW1cl=sfeedback(usysIW1,Ksf_det);
quiz = ctrpb('analysis', 'PDLF')+hinfty(usysIW1cl);
solvesdp(quiz,sdpopts);
```

Probabilistic analysis

The probabilistic analysis is based on a Monte Carlo algorithm, in which a number of random samples are extracted from the uncertainty set and the performance index is measured only for the extracted samples. There are two probabilistic analysis algorithms: 1) Worst-case performance estimation, in which an estimate of the

ConsideredAxis	ConsideredAppendices	model_type	uncertainty_type	rwheels	Design			Analysis				
								Det		Prob		Complexity(s)
					Design Method	Impulse to Peak	Infinity Norm	Impulse to Peak	Infinity Norm	Impulse to Peak	Infinity Norm	
1	1	1	1	1	Prob	22.3	2.9	0.36	1.5	0.13	1.01	160
	1	1	1	1	Det	22.3	4.7	0.41	1.5	0.16	1.16	1
1	1,2	1	1	1	Prob	Inf	Inf	NA	NA	NA	NA	NA
	1,2	1	1	1	Det	Inf	Inf	NA	NA	NA	NA	NA
1	1,2,3,4	2	1	1	Prob	22.5	3	0.42	1.3	0.14	0.84	520
	1,2,3,4	2	1	1	Det	22.5	3	0.43	1.3	0.13	0.99	1.3
1,2	1,2,3,4	2	1	1	Prob	Inf	Inf	NA	NA	NA	NA	NA
1,2	1,2,3,4	2	1	1	Det	Inf	Inf	NA	NA	NA	NA	NA
1,2	1,2	2	1	1	Prob	22.4	2.8	0.67	Inf	0.2	0.06	2215
1,2	1,2	2	1	1	Det	22.7	5	Inf	Inf	0.16	0.5	142
1,2	1,2	2	2	1	Prob	22.46	2.69	0.7	1.38	0.19	0.08	1750
1,2	1,2	2	2	1	Det	22.6	4.24	0.75	1.03	0.19	0.14	46
1,2,3	1,2	2	2	1	Prob	22.5	3.3	Inf	Inf	0.23	0.66	16387
1,2,3	1,2	2	2	1	Det	22.7	8.1	Inf	Inf	0.2	1.34	14111

Table 1 – Simulation results for various probabilistic and deterministic controllers designed using R-RoMulOC for the DEMETER model. "Inf" indicates the cases where the optimization problem is infeasible; "NA" also refers to Not Applicable.

worst-case performance is defined as the worst-case performance among all extracted samples. The sample size in this case is defined by a log-over-log bound [22]. 2) Randomized performance verification, where the objective is to estimate the probability of a given level of performance being satisfied, for instance, estimating the probability of instability or the probability that the H_∞ norm of the system is below a given level. The number of samples in this case is defined by the Chernoff bound [8]. The next command computes the wost-case H_∞ norm of the closed-loop system `usysIW1cl` using a randomized worst-case performance estimation algorithm.

```
quiz = ctrpb('analysis', 'rand')+hinfty(usysIW1cl);
opts=randsettings('epsilon',1e-1,'delta',1e-6);
solvesdp(quiz,opts);
```

Numerical tests

In this section, we compare probabilistic and deterministic approaches in terms of performance and complexity. To this end, we generate a number of DEMETER models – based on the discussion of Subsection "Reduced size variations of the uncertain model", by changing the parameters `ConsideredAxis`, `ConsideredAppendices`, `model_type`, `uncertainty_type` and `rwheels` – and design various deterministic and probabilistic controllers. Next, the performance of the designed controllers is measured using the deterministic and probabilistic analysis methods of Section "Closed-loop analysis of the state-feedback law", in order to quantify the level of conservatism associated with different design approaches. The result of these numerical tests is reported in Table 1, where we consider different numbers of axes and appendices, and different model and uncertainty types, and design probabilistic and deterministic controllers for the generated models. The probabilistic controller is designed using the scenario approach, and the probabilistic accuracy `epsilon` and confidence `delta` levels are set to 0.1 and 10^{-9}, respectively. In most cases – as expected – the probabilistic controller achieves less conservative performance levels in handling various uncertainties. In terms of computational complexity, the deterministic approach is less computationally demanding for the case in which all uncertainties are considered to be norm bounded. However, if we require uncertainties to be defined in intervals (and hence in polytopes), the computational complexity associated with the deterministic approach increases significantly. For such uncertainties, R-RoMulOC applies a vertex-separator result, as proposed in [12]. Unlike highly sparse DG-scaling type separators with few constraints built in the case of norm-bounded uncertainties, the vertex-separator is known to be less conservative but with an increased number of decision variables (full matrices) and an increased number of constraints (one for each vertex, and the number of vertices is 2^N where N is the number of uncertain parameters). We remark that in some problem instances of Table 1 the optimization problem – for controller design – is infeasible; there does not exists a "robust" state-feedback controller satisfying all required specifications and the optimization problem becomes infeasible, even for large probabilistic accuracy `epsilon` and confidence `delta` levels.

To further validate our design, *a posteriori* analysis using Monte-Carlo simulation was carried out for the controller designed in the second row of Table 1. To do so, we extracted 100 random samples from the uncertainty set, closed the loop for each of them and measured the impulse response – from w_2 to z_2 – of each sampled closed-loop

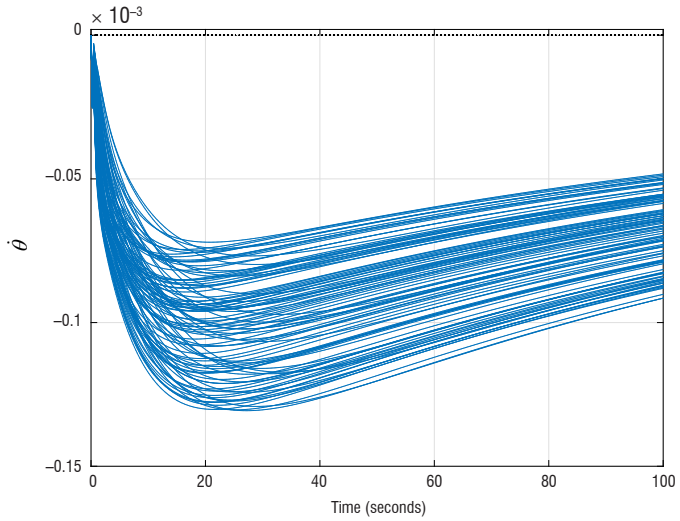

Figure 4 – Impulse response of 100 randomly generated closed-loop systems from w_2 to z_2 with the controller designed in the second row of Table 1

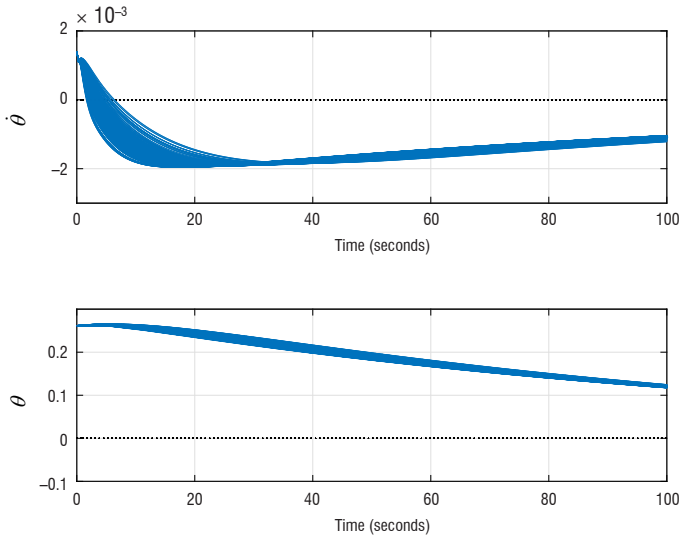

Figure 5 – Time trajectories of the satellite angular rate $\dot{\theta}$ (top figure) and angular deviation θ (bottom figure) for 100 randomly generated closed-loop systems from w_2 to z_2 with the controller designed in the second row of Table 1.

system. Figure 4 shows the result of this simulation. Figure 5 also demonstrates the time trajectories of the angular rate $\dot{\theta}$ and angular deviation θ of the satellite for the same sampled closed-loop systems. One can see that $\dot{\theta}$ starts from the initial condition 0.08π / 180 = 1.4×10^{-3} rad/s and θ starts from 15π / 180 = 0.262 rad. This is considered as the worst-case initial configuration. It is such that the pointing error θ tends to increase at the start due to the positive angular rate.

An interesting feature of randomized methods is that the computational complexity does not depend on the number of uncertain parameters. This feature is known as "breaking the curse of dimensionality". Therefore, increasing the number of uncertain parameters does not influence the complexity of solving a state-feedback problem using randomized methods. On the other hand, the stability and performance achieved using the controller designed by this approach is not guaranteed to hold for the entire set of uncertainties. That is, there might exist a subset of the uncertain set – although with very small probability measure – for which the guaranteed performance level is not attained.

It is noted that the designed controllers referred to in this paper are of the state-feedback type, requiring all of the states to be available for feedback. This requirement is not realistic in practice. In fact, in practice, sensors report $\theta, \dot{\theta}$ and $\int\theta$. Observers are needed for flexible modes $\eta, \dot{\eta}$. Therefore, an observer can be designed using the approach presented in [17], in order to estimate the states of the system and then use the state-feedback controller formulated in this paper to control the DEMETER satellite.

Conclusions

This paper shows how the features of the recently released Matlab toolbox R-RoMulOC can be exploited to perform both deterministic and probabilistic analysis, and the design of systems in the presence of uncertainty. The potentialities of R-RoMulOC are illustrated on the DEMETER satellite benchmark. The performed numerical simulations are fully reproducible, since both the DEMETER model and the R-RoMulOC toolbox are freely downloadable at http://projects.laas.fr/OLOCEP/rromuloc/ ■

Acknowledgments

Acknowledgments to all those who contributed to R-RoMulOC in many different ways: D. Arzelier, A. Bortott, G. Calafiore, G. Chevarria, E. Gryazina, B. Polyak, P. Shcherbakov, M. Sevin, P. Spiesser, and A. Tremba.

References

[1] T. ALAMO, R. TEMPO, A. LUQUE, D. R. RAMIREZ - *Randomized Methods for Design of Uncertain Systems: Sample Complexity and Sequential Algorithms*. Automatica, 52:160-172, 2015.

[2] G. C. CALAFIORE, M. C. CAMPI - *Uncertain Convex Programs: Randomized Solutions and Confidence Levels.* Mathematical Programming, 102:25-46, 2004.

[3] G. C. CALAFIORE, M. C. CAMPI - *The Scenario Approach to Robust Control Design*. IEEE Transactions on Automatic Control, 51:742-753, 2006.

[4] G. C. CALAFIORE, F. DABBENE, R. TEMPO - *Research on Probabilistic Methods for Control System Design.* Automatica, 47:1279-1293, 2011.

[5] M. CHAMANBAZ, F. DABBENE, D. PEAUCELLE, R. TEMPO - *R-RoMulOC: A Unified Tool for Randomized and Robust Multiobjective Control.* 8th IFAC Symposium on Robust Control Design, Bratislava, July 2015.

[6] M. CHAMANBAZ, F. DABBENE, R. TEMPO, V. VENKATARAMANAN, Q-G. WANG - *Sequential Randomized Algorithms for Sampled Convex Optimization.* Proc. IEEE Multi-Conference on Systems and Control, p. 182-187, Hyderabad, India, 2013.

[7] M. CHAMANBAZ, F. DABBENE, R. TEMPO, V. VENKATARAMANAN, Q-G. WANG - *Sequential Randomized Algorithms for Convex Optimization in the Presence Of Uncertainty.* IEEE Transactions on Automatic Control, 61:2565-2571, 2016.

[8] H. CHERNOFF - *A Measure of Asymptotic Efficiency for Tests of a Hypothesis Based on the Sum of Observations*. The Annals of Mathematical Statistics, 23:493-507, 1952.

[9] F. DABBENE, P. S. SHCHERBAKOV, B. T. POLYAK - *A Randomized Cutting Plane Method with Probabilistic Geometric Convergence.* SIAM Journal on Optimization, 20, 2010.

[10] Y. EBIHARA, D. PEAUCELLE, D. ARZELIER - *S-Variable Approach to LMI-Based Robust Control.* Springer London, 2015.

[11] M. FAN, A. TITS, J. DOYLE - *Robustness in the Presence of Mixed Parametric Uncertainty and Unmodelled Dynamics.* 36(1):25-38, January 1991.

[12] T. IWASAKI, S. HARA - *Well-Posedness of Feedback Systems: Insights into Exact Robustness Analysis and Approximate Computations.* IEEE Trans. on Automat. Control, 43(5):619-630, 1998.

[13] T. IWASAKI, G. SHIBATA - *LPV System Analysis via Quadratic Separator for Uncertain Implicit Systems.* IEEE Transactions on Automatic Control, 46:1195-1208, 2001.

[14] S. KANEV, B. DE SCHUTTER, M. VERHAEGEN - *An Ellipsoid Algorithm for Probabilistic Robust Controller Design.* Systems & Control Letters, 49:365-375, 2003.

[15] D. PEAUCELLE, D. ARZELIER, D. HENRION, F. GOUAISBAUT - *Quadratic Separation for Feedback Connection of an Uncertain Matrix and an Implicit Linear Transformation.* Automatica, 43:795-804, 2007.

[16] D. PEAUCELLE, D. ARZELIER - *Robust Multi-Objective Control Toolbox*. Proc. of the CACSD Conference, Munich, Germany, 2006.

[17] D. PEAUCELLE, Y. EBIHARA. *LMI Results for Robust Control Design of Observer-Based Controllers, the Discrete-Time Case with Polytopic Uncertainties.* Proc. 19th IFAC world congress, p. 6527-6532, 2014.

[18] I. R. PETERSEN, R. TEMPO - *Robust Control of Uncertain Systems: Classical Results and Recent Developments.* Automatica, 50:1315-1335, 2014.

[19] C. PITTET, D. ARZELIER - *Demeter: A Benchmark for Robust Analysis and Control of the Attitude of Flexible Micro Satellites*. Proc. 6th IFAC Symposium on Robust Control Design, p. 661-666, Toulouse, France, 2006.

[20] B. T. POLYAK, R. TEMPO - *Probabilistic Robust Design with Linear Quadratic Regulators.* Systems & Control Letters, 43:343-353, 2001.

[21] C. SCHERER, P. GAHINET, M. CHILALI - *Multiobjective Output-Feedback Control via LMI Optimization.* IEEE Transactions on Automatic Control, 42:896-911, 1997.

[22] R. TEMPO, E.-W. BAI, F. DABBENE - *Probabilistic Robustness Analysis: Explicit Bounds for The Minimum Number of Samples.* Systems and Control Letters, 30:237-242, 1997.

[23] R. TEMPO, G. C. CALAFIORE, F. DABBENE - *Randomized Algorithms for Analysis and Control of Uncertain Systems: With Applications.* Springer, 2nd edition, 2013.

[24] A. TREMBA, G. C. CALAFIORE, F. DABBENE, E. GRYAZINA, B. POLYAK, P. SHCHERBAKOV, R. TEMPO. *RACT: Randomized Algorithms Control Toolbox for MATLAB.* Proc. 17th World Congress of IFAC, Seoul, p. 390-395, 2008.

AUTHORS

Mohammadreza Chamanbaz was born in Shiraz, Iran in 1985. In 2008 he received his BSc in Electrical Engineering from Shiraz University of Technology, Shiraz, Iran. In 2014 he received his PhD in control science from the Department of Electrical & Computer Engineering, National University of Singapore. He was with Data Storage Institute, Singapore as research scholar from 2010 to 2014 and with Singapore University of Technology and Design as postdoctoral research fellow from 2014 to 2017. He is now Assistant Professor in Arak University of Technology, Arak, Iran. He is a member of IEEE Technical Committee on Computational Aspects of Control System Design (CACSD). His research activities are mainly focused on probabilistic and randomized algorithms for analysis and control of uncertain systems, convex optimization and robust control.

Fabrizio Dabbene received the Laurea degree in 1995 and the Ph.D. degree in 1999, both from *Politecnico di Torino*, Italy. He is currently Senior Researcher at the CNR-IEIIT institute. His research interests include randomized and robust methods for systems and control, and modeling of environmental systems. He published more than 100 research papers and two books, and is recipient of the 2010 EurAgeng Outstanding Paper Award. He served as Associate Editor for Automatica (2008-2014) and IEEE Transactions on Automatic Control (2008-2012). Dr. Dabbene is a Senior Member of the IEEE, and has taken various responsibilities within the IEEE-CSS: he served as elected member of the Board of Governors (2014-2016) and as Vice President for Publications (2015-2016).

Roberto Tempo graduated from *Politecnico di Torino*, Italy. He was a Director of Research of Systems and Computer Engineering since 1991. He has held visiting positions at Tsinghua University and Chinese Academy of Sciences, Beijing; Kyoto University, Japan; the University of Tokyo, Japan; University of Illinois at Urbana-Champaign, IL, USA, German Aerospace Research Organization, Oberpfaffenhofen; and Columbia University, New York. Dr. Tempo's research activities were mainly focused on the analysis and design of complex networked systems subject to uncertainty, and various applications within information technology. Dr. Tempo was a Fellow of the IEEE and of the IFAC. He has been a recipient of the IEEE Control Systems Magazine Outstanding Paper Award, of the Automatica Outstanding Paper Prize Award, and of the Distinguished Member Award from the IEEE Control Systems Society. In 2010 Dr. Tempo was President of the IEEE Control Systems Society. He served as Editor-in-Chief of Automatica. He has been Editor for Technical Notes and Correspondence of the IEEE TRANSACTIONS ON AUTOMATIC CONTROL in 2005–2009 and a Senior Editor of the same journal in 2011–2014. He was General Co-Chair for the IEEE Conference on Decision and Control, Florence, Italy, 2013 and Program Chair of the first joint IEEE Conference on Decision and Control and European Control Conference, Seville, Spain, 2005.

Dimitri Peaucelle was born in Leningrad, USSR, on 2 March 1974. He is a full-time researcher at the French National Center for Scientific Research (CNRS), working at LAAS in Toulouse. He obtained his Ph.D. degree in 2000 from Toulouse University. His research interests are in robust control, and extend to convex optimization over linear matrix inequalities (LMIs), periodic systems, positive systems, time-delay systems and direct adaptive control. He is also involved in computer-aided control design activities and is the main contributor to the Randomized and Robust Multiobjective Control (R-RoMulOC) Toolbox. He has been involved in several industrial projects with aerospace partners for launcher, aircraft, and satellite robust control. In 2017 he serves as General Chair of the IFAC World Congress.

Christelle Pittet received the Engineering degree in aeronautics from *Ecole Nationale de l'Aviation Civile*, Toulouse, France in 1995 and the PhD degree in 1998 from University Paul Sabatier of Toulouse, France. She has been with the French Space Agency (CNES), Toulouse, France, as Attitude and Orbit Control System expert, where she is in charge of advanced control studies, project development and in flight analysis.

F. Demourant
(ONERA)

E-mail: fabrice.demourant@onera.fr

DOI: 10.12762/2017.AL13-05

Stability Analysis by a New Algorithmic Approach Based on Integral Quadratic Constraints: Application to an Aircraft Benchmark

To analyze a non-linear, uncertain and time-varying closed loop representing a fighter aircraft model interconnected with a control law, an Integral Quadratic Constraint (IQC) approach has been used. This approach is particularly interesting for two reasons. The first one is that it is possible with the same stability criterion to analyze a large class of stability problems. The second reason is that the stability criterion is based on frequency dependent inequalities (FDI). Usually, the Kalman-Yakubovich-Popov (KYP) lemma is used, in order to transform this infinite set of inequalities into one linear matrix inequality (LMI). However, this kind of approach leads to a steep increase in the number of optimization variables. Consequently, a new FDI-based algorithmic approach has been developed. Usually, the number of FDI that must be satisfied is infinite or, thanks to a frequency domain gridding, it is possible to avoid this problem but with the drawback of not being able to guarantee the validity of the solution throughout the frequency domain continuum. To tackle this problem, a specific technique has been developed. It consists in computing a frequency domain where the solution is valid. By an iterative approach, this domain is extended to cover $[0,+\infty[$. Thus, the solution obtained from the FDI is necessarily valid throughout the frequency domain continuum and the number of optimization variables remains limited, which makes the IQC approach tractable for high-order models.

Introduction

The IQC technique, which appeared during the nineties, at least in its modern form [13], can be viewed as the merging of two well-known robustness analysis techniques, namely the (scaled) small gain techniques, the best known of these being μ analysis [3], and the positivity/passivity techniques, which study the interconnection of a linear time invariant (LTI) operator with non-linearity (the famous "Lur'e problem"). As a consequence, the IQC technique enables a wide range of problems to be studied, namely the robust stability and performance properties of the interconnection $G(s)-\Delta$ of an LTI operator $G(s)$, with a structured model uncertainty Δ containing non-linearities, LTI and/or linear time-varying (LTV) parameters, neglected dynamics, delays, and specific non-linearities such as friction or hysteresis, etc. The principle is to replace each block of uncertainty by an IQC description of its inputs/outputs, *i.e.*, the inputs/outputs of the block (e.g., a non-linearity inside a sector, possibly with a bound on its slope) are assumed to satisfy a set of Integral Quadratic Constraints [13, 7]. The finer the IQC description of the block is, the less conservative the result will be. This approach is very interesting for two reasons. It includes in the same formalism a large set of linear and non-linear stability theorems. The formalism used in the IQC approach can be described as a unified formalism. Secondly, this unified formalism is based on an input/output approach, namely a frequency domain approach.

In the context of our fighter aircraft application, we use standard IQC descriptions of the uncertainties and focus on the algorithmic issue. Let us recall that the stability criterion of this approach is based on FDI. Thus, the most classical way to solve an IQC analysis problem consists in solving the state-space LMI conditions derived from the KYP lemma, so that the optimization variables come from the IQC multipliers, but also from the Lyapunov matrix P. However, this solution becomes intractable when the order n of the state-space

representation becomes too high, since the number of scalar optimization variables in P grows quadratically with n. Note moreover that the initial state-space representation of $G(s)$ is augmented with the state-space representations of the dynamic multipliers, so that even if the order of the initial state-space representation is low, it may increase very fast when introducing dynamic multipliers. Various approaches based on a Hamiltonian matrix have been developed [9, 14, 15] to avoid this problem. Other references propose new multipliers or methodologies to improve results [5, 16, 12, 11]. Here, an alternative technique is implemented.

A first solution is to solve frequency-dependent LMIs, *i.e.*, the FDI, on a frequency domain gridding. However, the main drawback is that it is not possible to guarantee the validity of the solution between the gridding points, even if it is possible to analyze the result *a posteriori* with a very fine frequency domain gridding. However, formally the solution cannot be validated throughout the frequency domain continuum.

A second and more interesting approach, which consists in checking the validity of the solution over the entire frequency domain, has been developed. More precisely, the validation of the solution is done during the optimization problem resolution. In other terms, when the final solution is obtained, this solution is necessarily valid over the entire frequency domain. This validation step is based on a mathematical result for the singular-value maximum of an LFT structure [18] where the Δ block is a real perturbation model. More precisely, when a solution is obtained from a frequency domain gridding, the stability criterion, which depends on frequencies, is written in an LFT form in order to make the frequency ω appear as a real parameter in the Δ block of the LFT [4]. Then, the validity domain of the solution is computed using an algebraic approach. If this domain is $[0,+\infty[$ the solution is valid over the entire frequency domain. Otherwise, frequencies for which the FDI are not satisfied are detected and are added to the initial frequency domain gridding and a new solution is computed with the new gridding, and so on. If no solution is obtained on the gridding, the problem is considered as unfeasible. In brief, the stability problem is recast as an LMI feasibility problem, where the constraints (FDI) are added iteratively. Finally, the number of optimization variables is completely independent from the model order.

However, it remains a problem, since the IQC stability criterion is based on FDI, *i.e.*, a positivity constraint and not a weak gain constraint [18]. However, thanks to a specific bilinear transformation, namely the Cayley transformation [1], this positivity condition, which corresponds to our stability criterion, is replaced by a weak gain condition. By this transformation these two kinds of inequalities are perfectly equivalent. Consequently, it becomes straightforward to evaluate the validity of the solution for the stability criterion.

This is applied to a fighter aircraft interconnected with a control law. The closed loop is written in LFT form, where the Δ block contains one non-linearity, LTV, and LTI parameters. The LTV parameters correspond to the scheduling parameters $Mach$ and V_c (calibrated airspeed), represented by repeated real scalars. Moreover the scheduling parameters are known to be rather slowly time-varying, so that considering arbitrarily time-varying scheduling parameters will lead to conservative results. Thus, the IQC description of time-varying parameters with a bounded rate of variation is used [8]. LTI parameters represent parametric uncertainties of the aircraft model. The non-linearity corresponds to a saturation/dead-zone on the actuator rate output. The objective is to analyze the stability of this non-linear, uncertain and time-varying closed loop.

Notations

Given three operators $P(\cdot)$, $M(\cdot)$ and $\Delta(\cdot)$ of compatible dimensions, the lower and upper Linear Fractional Transformations (LFTs) are respectively defined (for appropriate partitions of P and M) by $\mathcal{F}_l(P,\Delta) = P_{11} + P_{12}\Delta(I - P_{22})^{-1}P_{21}$ and $\mathcal{F}_u(M,\Delta) = M_{22} + M_{21}\Delta(I - M_{11})^{-1}M_{12}$. The star product $\star$ of P and M is defined by:

$$P \star M = \begin{bmatrix} \mathcal{F}_l(P, M_{11}) & P_{12}(I - M_{11}P_{22})^{-1}M_{12} \\ M_{21}(I - P_{22}M_{11})^{-1}P_{21} & \mathcal{F}_u(M, P_{22}) \end{bmatrix} \quad (1)$$

IQC generalities

IQC-based analysis techniques enable us to study a wide range of problems, namely, the robust stability and performance properties of the interconnection $G(s) - \Delta$ of an LTI operator $G(s)$ with a structured model uncertainty Δ containing non-linearities, LTI and/or linear time-varying parameters, neglected dynamics, delays, and specific non-linearities such as friction and hysteresis.

Here, standard IQC descriptions are used for both LTI uncertainties/LTV parameters, Δ, and sector non-linearities, denoted by φ. The originality of our approach resides in the specific algorithm that has been developed to reduce the computational burden. Indeed, standard IQC-oriented analysis methods consist in solving Kalman-Yakubovitch-Popov-based LMI conditions [13]. These standard approaches are, however, intractable for high-order models, since the number of scalar optimization variables quadratically increases with the closed-loop order [2, 19].

An IQC describes a relation between input and output signals of an operator. Since these two formulations are completely equivalent, these constraints can be defined either in the time or the frequency domain. Nevertheless, frequency-domain constraints are often preferred, since this leads to obtaining stability conditions that are easier to handle in comparison with the impulse response for the time domain representation. The definition of an IQC is given in the frequency domain.

Definition 1

Two signals, respectively of dimension m and p, square-integrable over the interval $[0,\infty)$, i.e.: $v \in L_2^m[0,\infty)$, $w \in L_2^p[0,\infty)$, satisfy the IQC defined by $\Pi : jR \to C^{(m+p)\times(m+p)}$, and the Hermitian-valued function, if

$$\int_{-\infty}^{\infty} \begin{bmatrix} \tilde{v}(j\omega) \\ \tilde{w}(j\omega) \end{bmatrix}^* \Pi(j\omega) \begin{bmatrix} \tilde{v}(j\omega) \\ \tilde{w}(j\omega) \end{bmatrix} d\omega \geq 0 \quad (2)$$

where $\tilde{v}(j\omega)$ and $\tilde{w}(j\omega)$ respectively correspond to Fourier transforms of v and w, such as $w = \Delta v$.

A priori, the operator Π, called the multiplier, defined from jR in $C^{(m+p)\times(m+p)}$ can be any measurable Hermitian-valued function. In most situations, it is sufficient to use rational operators that are bounded on the imaginary axis.

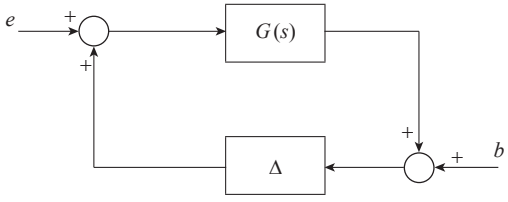

Figure 1 – non-linear, uncertain and time-varying closed loop

The problem consists in analyzing the closed loop that corresponds to the interconnection by a positive feedback of $G(s)$ with Δ, where Δ can be nonlinear and non-stationary. Let us suppose that the input and output signals of Δ satisfy the IQC defined by Π. The following result gives the stability criterion [13].

Theorem 1

Let us assume that $G(s)$ is stable and that Δ is a causal and bounded operator; if

- *the interconnection G-$\tau\Delta$ is well posed for any $\tau \in [0,1]$,*
- *$\tau\Delta$ satisfies the IQCs defined by Π, $\forall \tau \in [0,1]$,*
- *there exists $\varepsilon > 0$ such that:*

$$\forall \omega \in R \quad \underbrace{\begin{bmatrix} G(j\omega) \\ I \end{bmatrix}^* \Pi(j\omega) \begin{bmatrix} G(j\omega) \\ I \end{bmatrix}}_{Z(j\omega)} \leq -\varepsilon I \qquad (3)$$

then, the closed-loop system is stable in the sense of the global asymptotic stability.

It is important to note that if $\tau\Delta$ satisfies several IQC $\Pi_1, \ldots, \Pi_n$, then a sufficient condition for the stability is that $x_1, \ldots, x_n \geq 0$ exist such that the inequality (3) is satisfied for $\Pi = x_1\Pi_1 + \ldots + x_n\Pi_n$, which is a variant of the S-procedure.

The following proposition is very useful to consider the case with several multipliers [6].

Proposition 1

Let us assume a block-diagonal structure $\Delta = diag(\Delta_1, \ldots, \Delta_n)$ and that each Δ_i satisfies the IQC defined by Π_i, where $i = 1, \ldots, n$. Then, Δ satisfies the IQC defined by $\Pi = daug(\Pi_1, \ldots, \Pi_n)$, where the operator $daug$ is defined as follows. If

$$\Pi_i = \begin{bmatrix} \Pi_{i1} & \Pi_{i2} \\ \Pi_{i2}^* & \Pi_{i3} \end{bmatrix} \qquad (4)$$

then

$$daug(\Pi_1, \Pi_2) = \left[\begin{array}{cc|cc} \Pi_{11} & 0 & \Pi_{12} & 0 \\ 0 & \Pi_{21} & 0 & \Pi_{22} \\ \hline \Pi_{12}^* & 0 & \Pi_{13} & 0 \\ 0 & \Pi_{22}^* & 0 & \Pi_{23} \end{array}\right] \qquad (5)$$

List and parameterization of IQCs and stability

In this section, the parameterization of the global multiplier is built to be implemented and solved using the Matlab LMI toolbox.

Sector non-linearities

Let us consider a non-linearity that is memoryless, possibly time-varying, piecewise continuous in t and locally Lipschitz in y. The non-linearity is required that to satisfy a sector condition.

Definition 2

A memoryless non-linearity $\psi : [0,\infty) \times \mathbb{R}^p \to \mathbb{R}^p$ is said to satisfy a sector condition if

$$(w - \underline{k}v)^T (w - \overline{k}v) \leq 0 \qquad (6)$$

where $\underline{k}$ and $\overline{k}$ are gains that represent the limits of the sector and w and v represent the inputs/outputs of the non-linearity.

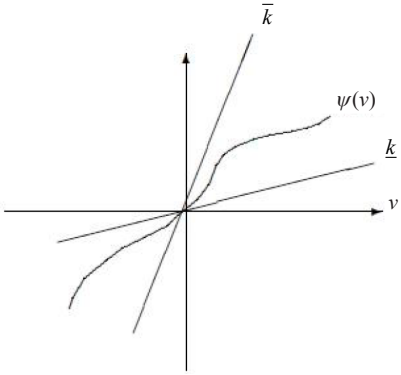

Figure 2 – Sector non-linearity

This definition is illustrated by Figure 2 in the SISO case. The IQC for sector non-linearity φ with a sector (0,1) is the following one [13]:

$$\Pi_\varphi = x\Pi_{sector} + \Pi_{Popov} = \begin{bmatrix} 0 & x + j\omega\lambda \\ x - j\omega\lambda & -2x \end{bmatrix}, \quad x \geq 0, \quad \lambda \in R \qquad (7)$$

Readers can refer to the literature for more details.

Slowly time varying real parameter

Here, $|\delta(t)| \leq 1$, $\dot{\delta}(t) \leq d$, $X = R^*R$ and $Y = S - S^*$. Let us define:

$$R_C(s) = C_R(sI - A_R)^{-1}$$

$$R_B(s) = (sI - A_R)^{-1} B_R$$

$$S_C(s) = C_S(sI - A_R)^{-1}$$

$$S_B(s) = (sI - A_R)^{-1} B_S$$

Let us consider the multiplier that corresponds to LTV parameters [8]:

$$\Pi_{\delta(t)} = \begin{bmatrix} R^*R + d\Gamma^*\Gamma & S - S^* \\ S^* - S & R^*R + d\Upsilon^*\Upsilon \end{bmatrix} \qquad (8)$$

with $\Gamma = \begin{bmatrix} R_B \\ S_B \\ S_C^* \end{bmatrix}$ and $\Upsilon = R_C^* R$. From the parameterization

$$X(j\omega) = \tilde{R}(j\omega)^* U \tilde{R}(j\omega) = R(j\omega)^* R(j\omega)$$

$$Y(j\omega) = V\tilde{S}(j\omega) - \tilde{S}(j\omega)^* V^T = S - S^* \qquad (9)$$

with $U = U^T$, the following multiplier is obtained:

$$\Pi_{\delta(t)} = \begin{bmatrix} \tilde{R}^*U\tilde{R} + d\left(\tilde{R}_B^*\tilde{R}_B + \tilde{S}_B^*\tilde{S}_B + V\tilde{S}_C\tilde{S}_C^*V^T\right) & V\tilde{S} - \tilde{S}^*V^T \\ \tilde{S}^*V^T - V\tilde{S} & -\tilde{R}^*U\tilde{R} + d\tilde{R}^*U\tilde{R}_C\tilde{R}_C^*U\tilde{R} \end{bmatrix}$$

We can clearly see that this multiplier is bilinear in U and V. Then, to satisfy the following inequality

$$\begin{bmatrix} G(j\omega) \\ I \end{bmatrix}^* \left\{ \begin{bmatrix} dV\tilde{S}_C\tilde{S}_C^*V^T & 0 \\ 0 & d\tilde{R}^*U\tilde{R}_C\tilde{R}_C^*U\tilde{R} \end{bmatrix} + \Pi_{lin} \right\} \begin{bmatrix} G(j\omega) \\ I \end{bmatrix} \leq 0 \qquad (10)$$

with $\Pi_{lin} = \begin{bmatrix} \tilde{R}^* U \tilde{R} + d\left(\tilde{R}_B^* \tilde{R}_B + \tilde{S}_B^* \tilde{S}_B\right) & V\tilde{S} - \tilde{S}^* V^T \\ \tilde{S}^* V^T - V\tilde{S} & -\tilde{R}^* U \tilde{R} \end{bmatrix}$

is not a convex problem.

In order to make this problem convex, let $\Lambda = \begin{bmatrix} G(j\omega) \\ I \end{bmatrix}$ and $W = \begin{bmatrix} \sqrt{d} V\tilde{S} & 0 \\ 0 & \sqrt{d}\tilde{R}^* U \tilde{R}_C \end{bmatrix}$; then, the inequality (10) becomes:

$$\Lambda^* \Pi_{lin} \Lambda + \Lambda^* W W^* \Lambda \le 0 \qquad (11)$$

From this relation, it is possible to use the Schur lemma to obtain the following LMI constraint:

$$\begin{bmatrix} \Lambda^* \Pi_{lin} \Lambda & \Lambda^* W \\ W^* \Lambda & -I \end{bmatrix} < 0 \qquad (12)$$

where Π_{lin} and W are affine in U and V. Of course, if $d = 0$ then $W = 0$, and only the first term of the LMI remains, $\Lambda^* \Pi_{lin} \Lambda$, which corresponds to the constant real scalar.

The global multiplier

In this section, the global multiplier, which corresponds to the general analysis problem, is presented. If φ is the sector non-linearity and $\delta(t) = diag[\delta_1(t) I_n, \ldots, \delta_k(t) I_k]$ the time varying real vector, the closed loop to analyze corresponds to the interconnection of $G(s)$ with $\Phi = diag(\varphi, \delta(t))$. Also, $|\delta_i(t)| \le 1$, $|\dot{\delta}_i(t)| \le d_i$ and $d = diag[d_1 I_n, \ldots, d_k I_k]$. In the case of a constant real scalar it suffices to set $d_i = 0$.

Thus, the global multiplier, which corresponds to Φ, is obtained from Proposition 1:

$$\Pi_{lin} = \begin{bmatrix} 0 & 0 & x + j\omega\lambda & 0 \\ 0 & \tilde{R}^* U \tilde{R} + d\left(\tilde{R}_B^* \tilde{R}_B + \tilde{S}_B^* \tilde{S}_B\right) & 0 & V\tilde{S} - \tilde{S}^* V^T \\ x - j\omega\lambda & 0 & -2x & 0 \\ 0 & \tilde{S}^* V^T - V\tilde{S} & 0 & -\tilde{R}^* U \tilde{R} \end{bmatrix} \qquad (13)$$

The LMI feasibility problem

In brief, the stability of the closed loop, which corresponds to the interconnection by a positive feedback of a sector non-linearity (0,1) and time-varying and/or constant real scalars with a linear part $G(s)$, is ensured by solving the following LMI feasibility problem.

Find $\lambda, x, U = U^T, V$ such that:

$$\begin{bmatrix} \Lambda^* \Pi_{lin}(x, \lambda, U, V) \Lambda & \Lambda^* W(U, V) \\ W(U, V)^* \Lambda & -I \end{bmatrix} < 0 \quad \forall \omega \in R \qquad (14)$$

$$\tilde{R}(j\omega)^* U \tilde{R}(j\omega) > 0 \quad \forall \omega \in R \qquad (15)$$

$$x > 0 \qquad (16)$$

If a solution exists, the closed loop is stable.

Remark 1
This form cannot be directly implemented; a factorized form allowing the dynamic part to be separated into decision variables is involved.

Remark 2
If n_f frequencies are considered, then a problem with $2n_f + 1$ LMI constraints is obtained.

Remark 3
The number of decision variables is completely independent from the closed loop order, but only depends on the structure and the size of the Δ block.

Proposed method

State space approach

The classical approach is based on the Kalman-Yakubovitch-Popov lemma.

Lemma 1
Let us consider M a symmetric matrix, A, B, C, D a state space representation of Φ such as $\Phi(s) = C(sI - A)^{-1} B + D$, and $\forall \omega \in R$ $det(j\omega I - A) \ne 0$; then, the two following propositions are equivalent:
(i) the quadratic constraint

$$\forall \omega \quad \Phi(j\omega)^* M \Phi(j\omega) < 0 \qquad (17)$$

is satisfied

(ii) there exists $P = P^T > 0$ such that

$$\begin{bmatrix} C^T \\ D^T \end{bmatrix} M \begin{bmatrix} C & D \end{bmatrix} + \begin{bmatrix} I & 0 \\ A & B \end{bmatrix}^T \begin{bmatrix} 0 & P \\ P & 0 \end{bmatrix} \begin{bmatrix} I & 0 \\ A & B \end{bmatrix} < 0 \qquad (18)$$

The important point is that the second proposition can easily be solved, since it is a feasibility problem under LMI constraints. We notice that the inequality does not depend on the frequency, but a new optimization matrix P has appeared. In other terms, an infinite set of constraints has been transformed into one constraint with a new optimization variable P. To involve the stability criterion (3) in Theorem 1 it suffices to choose a multiplier such as:

$$\sum_{i=1}^{r} x_i \Pi(j\omega) = \Psi(j\omega)^* M \Psi(j\omega) \qquad (19)$$

where M is a symmetric matrix, structured according to the problem considered. This matrix contains a set of optimization variables. With

$$\Psi(j\omega) \begin{bmatrix} G(j\omega) \\ I \end{bmatrix} = C(j\omega I - A)^{-1} B + D \qquad (20)$$

the previous lemma allows the inequality (3) to be transformed into an LMI with respect to the optimization matrices P, and M.

Proposed innovative method

An infinite number of LMI constraints has been replaced by one LMI constraint. Nevertheless, this transformation has a major drawback since a new optimization matrix P appears whose size depends on the order of G plus the dynamics of Ψ. More precisely, the number

of decision variables grows quadratically, which can lead to a computational problem.

In this paper, the optimization problem is directly solved from frequency-domain inequalities, through a grid-based approach. Of course, the drawback to this approach is the lack of guarantee of the validity of the solution throughout the frequency domain continuum.

To guarantee that the solution is valid over the entire frequency domain, a specific technique based on [4] and [18] is adapted. Also, another advantage is to limit the number of LMI constraints, since only active constraints are added in the LMI optimization problem. Here, the main result is presented:

Let $\Xi = (A_\Xi, B_\Xi, C_\Xi, D_\Xi)$ be the realization of $\Xi(s)$ (of order m), with $\Xi(j\omega) = (I - Z(j\omega))(I + Z(j\omega))^{-1}$ ($(I+Z)$ is invertible) where $Z(j\omega) = Z^*(j\omega)$ is the stability criterion (3), and $\Xi(j(\omega_0 + \delta\omega)) = \mathcal{F}_l(S(\omega_0), \delta\omega I_m)$, with $\forall\, \delta\omega \geq -\omega_0$, *i.e.,* $S(\omega_0)$ is interconnected to $\delta\omega$ as a lower LFT, where $\delta\omega$ is a real parameter. $S(\omega_0)$ is written as

$$S(\omega_0) = \begin{pmatrix} D_\Xi & \frac{C_\Xi}{\sqrt{j}} \\ \frac{B_\Xi}{\sqrt{j}} & -jA_\Xi \end{pmatrix} \star \left(\frac{1}{\omega_0} \begin{pmatrix} I & I \\ -I & -I \end{pmatrix} \right) \tag{21}$$

Proposition 2

If $\bar{\sigma}(\Xi(\omega_0)) < 1$ *then* $\bar{\sigma}(\mathcal{F}_l(S(\omega_0), \delta\omega I_m)) < 1$ *holds true for* $\omega_0 + \delta\omega \in [\underline{\omega}, \bar{\omega}]$, *where* $\underline{\omega}$ *and* $\bar{\omega}$ *are computed as* $\underline{\omega} = \omega_0 + \frac{1}{\eta_n}$ *and* $\bar{\omega} = \omega_0 + \frac{1}{\eta_p}$, *where* η_n *and* η_p *are the maximal magnitude real negative and positive eigenvalues of* T, *respectively, defined as*

$$T = \begin{bmatrix} S_{22} & 0 \\ 0 & S_{22}^* \end{bmatrix} - \begin{bmatrix} 0 & S_{21} \\ S_{12}^* & 0 \end{bmatrix} X^{-1} \begin{bmatrix} S_{12} & 0 \\ 0 & S_{21}^* \end{bmatrix} \tag{22}$$

where,

$$S(\omega_0) = \begin{bmatrix} S_{11} & S_{12} \\ S_{21} & S_{22} \end{bmatrix} \quad \text{and} \quad X = \begin{bmatrix} I & S_{11} \\ S_{11}^* & I \end{bmatrix} \tag{23}$$

Remark 4

When $\bar{\sigma}(\Xi(+\infty)) = 1$, $\bar{\omega} = +\infty \Leftrightarrow \eta_p = 0$, *a null eigenvalue is obtained, which means that* $\bar{\sigma}(\Xi(\omega))$ *crosses the 0 dB axis for* $\omega = +\infty$. *However, the intersection of the stability criterion with the 0 dB axis has no physical meaning.*

Remark 5

The bilinear transformation $\Xi(j\omega) = (I - Z(j\omega))(I + Z(j\omega))^{-1}$ *with* $(I+Z)$ *invertible allows a positivity condition to be transformed into a weak gain condition:*

$$\bar{\sigma}(\Xi) \leq 1 \Leftrightarrow Z + Z^* \geq 0 \tag{24}$$

In brief, if we consider a transfer matrix Ξ, in order to determine the frequency domain containing ω_0 such as the maximal singular value of $\Xi(j\omega)$ is inferior to 1, it suffices to evaluate $\bar{\omega}$ and $\underline{\omega}$ as above.

In the iterative approach, proposed in Algorithm 4.2.1, the validation step is performed *a priori* and during the LMI optimization problem resolution. The choice of the initial grid has no influence on the feasibility problem. It is possible to choose a singleton at the first iteration. However, in order to limit the number of iterations, and consequently the calculation time, without any *a priori* knowledge, it is recommended to take some frequencies roughly spread over the frequency domain. It is possible, when first solutions are obtained, to tune this initial frequency grid, in order to decrease the number of iterations.

Sketch of the algorithm

The algorithm can be summarized by the following steps:

Algorithm 1: Iterative IQC resolution

Data: $G(j\omega)$ the stable fixed block of the LFR, multiplier $\Pi(\omega_i)$ and $\omega_i \in R_+$, $i = 1, \ldots n_f$.
Result: A stability proof of the LFR model, including nonlinear sector saturations.
while *Stability not checked* **do**

For $i = 1, \ldots n_f$, check the stability criterion

$$\begin{bmatrix} G(j\omega_i) \\ I \end{bmatrix}^* \Pi(\omega_i) \begin{bmatrix} G(j\omega_i) \\ I \end{bmatrix} < 0\,. \tag{25}$$

if (25) *has solutions* **then**

- Set $\Pi_i \leftarrow \Pi(\omega_i)$ be the solution obtained at ω_i.
- Set $\omega_0 \leftarrow w_i$ and apply Proposition 2.
- For each solution Π_i, a frequency-domain $\Omega_i = [\underline{\omega}_i, \bar{\omega}_i]$ is obtained. $\Omega_{valid} = \bigcup_{i=1,\ldots,n_f} \Omega_i$.

if $\Omega_{valid} = [0 + \infty)$ **then**

The solution composed by the set of Π_i is validated over the entire frequency domain.
Stability is proved, **stop**.

else

- Determine the complementary set $\Omega_{novalid} = C_{[0,+\infty)}\Omega_{valid}$.
- Select one or several frequencies in $\Omega_{novalid}$ and update the grid.

Stability cannot be proved, **stop**.

This algorithm is a specific case of outer approximation algorithms [17, 14]. Of course, if no solution is obtained on the finite set of frequencies, the problem is considered as infeasible. If a solution is obtained, necessarily this solution is valid over the entire frequency domain.

Remark 6

The stability condition is checked as described in Section 4.2, where critical frequencies are added iteratively. However, it is necessary to check the positivity constraint of the multiplier $X(j\omega) = \tilde{R}(j\omega)^* U \tilde{R}(j\omega)$ *for all* ω. *Of course, it is possible to proceed in the same way: frequencies for which the multiplier is negative are added in the optimization problem by an iterative approach. However, this approach is useless and increases the computational burden. By noting that* X *is hardly ever positive when the stability condition is satisfied for any frequency, the positivity condition of* X *is checked by the technique presented previously just once at the end of the algorithm, i.e., when the stability criterion is satisfied over the entire frequency domain. In the exceptional case where a frequency exists such that* $X(j\omega) < 0$, *then this frequency is added in the optimization problem and another solution is sought, to satisfy the stability condition and the positivity of* X.

Remark 7

It is possible by this approach to solve directly over the frequency domain without any approximation based on rational functions. A solution based on irrational multipliers is proposed in [19].

Application

The objective is to analyze the stability problem with a fighter aircraft model. For the problem considered, the critical static non-linearity is the rate limiter, which has been transformed into a dead zone. In brief, the analysis is performed as follows. For specific values of the speed variation d, a sector size $(0,k)$ is determined by a dichotomic approach, so the closed loop stability is guaranteed. This analysis is performed for two cases essentially: one case with one static non-linearity, which corresponds to the rate limiter, and another case with one non-linearity and all other LTV and LTI parameters. The LTV parameters are the Mach number and calibrated air speed. These two time-varying parameters represent the flight case. The Mach number and the calibrated airspeed, respectively, vary from 0 to 1 and from 150 to 275 kts. The nominal rate of variation is $d = 0.2$ for both. The LTI parameters correspond to real uncertainties on the model. This LFT real uncertainties are a combination of various physical real uncertainties, such as mass, center of gravity position, etc. This transformation is necessary to obtain a limited size for the LFT model. In brief, it is not possible to associate a real uncertainty of the LFT model to a physical parameter of the aircraft model. However, the important fact to keep in mind is that the stability analysis is performed for the maximum variation of real uncertainties and not for a restricted domain. In other words, if the stability is guaranteed with all LTI parameters for all possible uncertainty values, the stability is guaranteed for the entire domain of physical parameters. Of course, this kind of transformation can lead to a difficult interpretation if the analysis is performed over a restricted domain for LTI parameters, since it is not possible to easily link this restricted domain to the physical domain; however, this is not the case here.

Another and last point is the following one. The sector size is determined by the value k. However, this value can be interpreted as an amplitude of the non-linearity input u. Since the problem has been normalized, for a rate limiter of 80 deg / s, $u = 1$ corresponds to 80 deg / s and, more generally, to a physical signal equal to u*80 deg / s, For example if $k = 0.5$, this value corresponds to a normalized non-linearity input $u = \frac{1}{1-k} = 2$. It means that, for any normalized $u \leq 2$, or equivalently 160 deg / s, the stability of the non-linear closed loop is ensured. In other words, if any realistic pilot order, turbulence or discrete gust leads to having $u \leq 2$ for the normalized signal, the stability is ensured. If there exists a realistic input signal that leads to having $u > 2$ for the normalized non-linearity input, then the stability cannot be guaranteed. In brief, the stability can be interpreted as an input/output approach: for any bounded input signal; any output signal of the non-linear closed loop is bounded. This bound corresponds to classical norms of signals, as $l_1, l_2, l_\infty, \ldots$. To be complete, the case where $k = 1$ corresponds to an infinite stability domain.

The parameter occurrence is the following: 1 for the rate limiter, 2 and 8 for the 2 LTV parameters, and 1,1,1,1 and 1 for the 5 LTI parameters. The dynamic for the multipliers $\tilde{R}$ and $\tilde{S}$ is a first order low-pass filter with a pole at 10 rad/s.

Analysis with one rate limiter

In this section, the analysis is performed with just one non-linearity of sector $(0,1)$. This case is interesting for several reasons:

- This case represents the best result that can be expected, since the size of the sector decreases with the number of LPV and LTI parameters that are considered in the analysis problem.
- This case can be interpreted very easily using a SISO representation like the Popov and Nyquist plot.

Let us recall that the Popov plot represents the plot $Re[G(j\omega)]$ versus $\omega Im[G(j\omega)]$. The closed loop stability is ensured if the Popov plot of $G(j\omega)$ lies to the right of the line that intercepts the point $-1+0j$ with a slope 1 / λ [10].

- The size of the sector is consistent with the Popov and the Nyquist plot, since the value obtained for the sector leads the Nyquist and the Popov plot to be very close to the critical point -1.

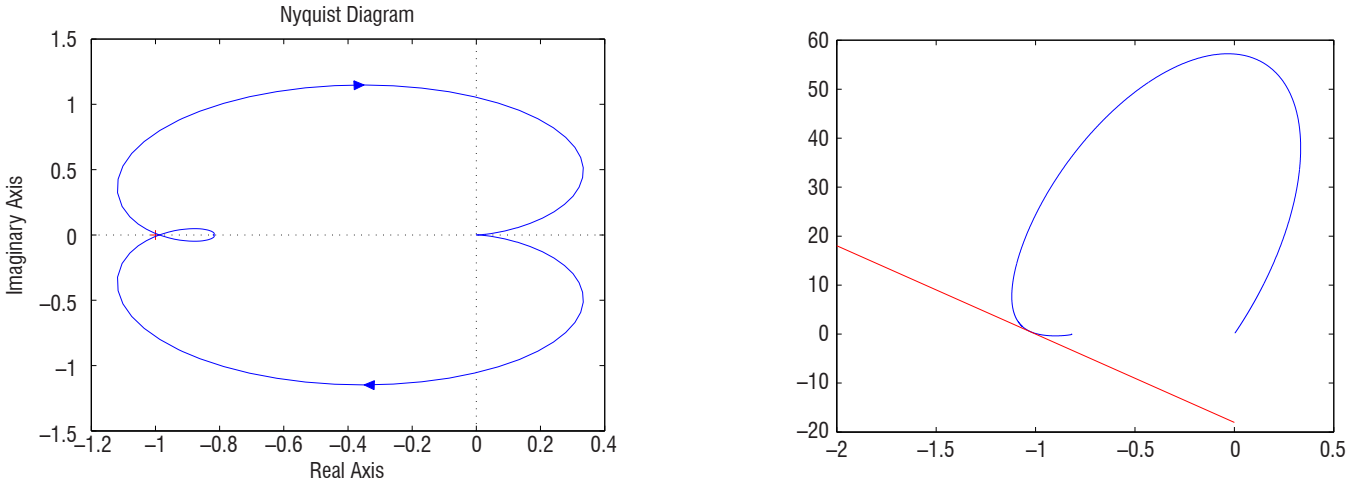

Figure 3 – Popov plot

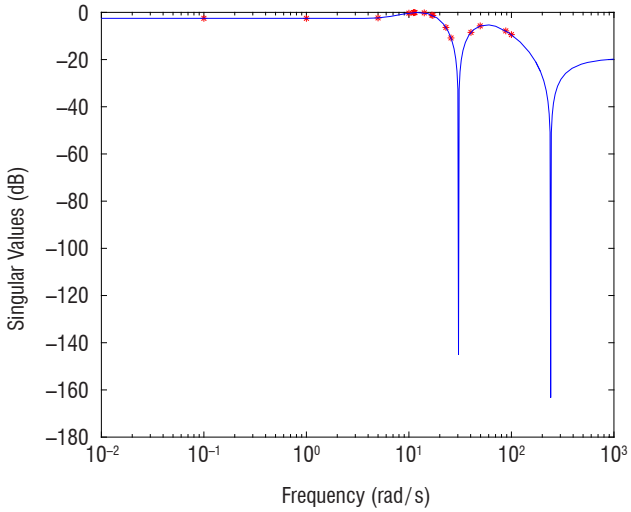

Figure 4 – Singular values

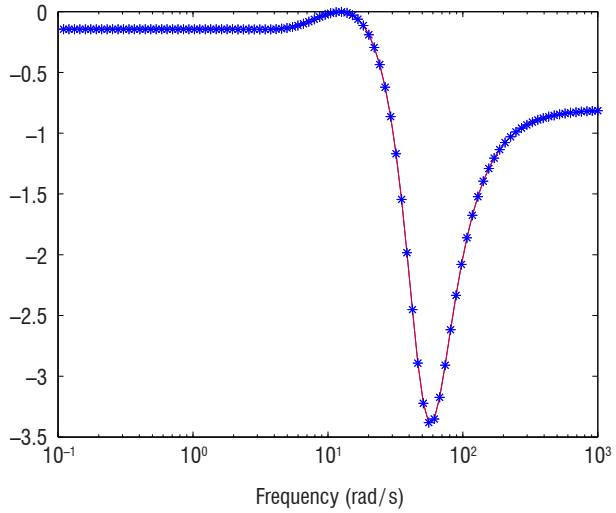

Figure 5 – Eigenvalues

- The solution obtained by the IQC approach is consistent with the graphical interpretation, since we note that the Popov plot lies to the right of the red line whose slope is $1 / \lambda$.

- To confirm the solution, the eigenvalues of the stability criterion and singular values of the transformed criterion by the Cayley method are respectively negative and inferior to $k = 0.81 \Leftrightarrow u = 5.26$.

The limit of the sector is $k = 0.81 \Leftrightarrow u = 5.26$. Of course, this size is determined for the nominal case, *i.e.*, without uncertainties and LTV parameters.

Analysis with one rate limiter, LTV Mach number, and five real uncertainties

This case is interesting, since it combines three kinds of problem: a static non-linearity, LTV parameter and LTI real uncertainties. It is the typical problem treated by the IQC approach. In addition, since the Δ block is not very large, the computational burden is very limited and it is possible to perform several simulations with different bounded rates d to test the algorithm. The LTV parameter considered is the Mach number. Finally, the Δ block has 8 inputs/outputs.

	LTI	d=0	d=0.1	d=0.2	d=0.5	d=0.8	d=10	d=100	d=1000	X,Yconstant
k	0.89	0.89	0.86	0.85	0.85	0.84	0.81	0.80	0.74	0.78
u	9.09	9.09	7.14	6.67	6.67	6.25	5.26	5.00	3.85	4.55

From this table, we can make several remarks:

- For the LTV case, we note that the size of the sector decreases with the rate of variation, which is consistent physically and mathematically since d appears as a penalty in the LMI constraints.

- The LTV case with $d = 0$ is equivalent to the LTI case, from a mathematical point of view. However, it is important to check this point from an algorithmic point of view. The results are the same, or very similar.

- The LTV case with $d \to \infty$ is equivalent to the case where the multipliers X and Y are chosen as constant. Indeed, as indicated previously, if the rate of variation is arbitrary high, the multiplier must be constant. In brief, the size of the sector is evaluated in the LPV context with $d = 100$ or 1000 and compared to the solution obtained with constant multipliers. The results are very closed in terms of sector limits.

To complete these previous results, the stability analysis is performed when the LTV calibrated air speed V_c is replaced by a specific value and $d = 0.2$. Of course, the nominal case is represented by the value 0.

	V_c=+1	V_c=+0.5	V_c=0	V_c=–0.5	V_c=–1
k	0.81	0.83	0.85	0.80	0.77
u	5.26	5.88	6.67	5.00	4.35

Analysis with one rate limiter, LTV Mach number and airspeed, and five real uncertainties

This system represents the final case, which combines all LTV and LTI parameters. The Δ block has 16 inputs/outputs.

Two results have been obtained: for the LTI case ($d = 0$) and the nominal case ($d = 0.2$).

- With $d = 0$ the sector obtained is $k = 0.45 \Leftrightarrow u = 1.82$.

- With $d = 0.2$ the sector obtained is $k = 0.31 \Leftrightarrow u = 1.45$.

In this last case, the number of optimization variables is 309, with some dozens of constraints. The calculation time varies from a few to ten minutes.

Conclusion

In this article, a new algorithmic approach based on IQC technique has been presented. Usually, the KYP lemma is used to transform the stability criterion, which consists in an infinite set of LMI constraints, into one LMI. The main drawback is that a decision matrix P is added and consequently the number of decision variables grows quadratically. To avoid this kind of problem, the frequency domain criterion is explicitly used. To guarantee the solution over the entire frequency domain and not only over the frequency domain gridding, an LFT structure is involved where Δ contains the frequency ω. Then, it becomes possible to treat this variable as a continuous variable, as for any μ analysis problem, and to check the validity of the solution over the frequency domain continuum. In brief, the number of decision variables is independent from the order of $G(s)$ and the solution obtained using the gridding is valid over the entire frequency domain. Finally, to illustrate the approach, this is applied to a fighter aircraft. This application presents one sector non-linearity, two LTV parameters, which correspond to the flight case, and five real uncertainties. The results show that the algorithm is effective for dealing with a large class of stability analysis problems ■

Acronyms

KYP	(Kalman-Yakubovich-Popov)
FDI	(Frequency Dependent Inequalities)
LTI	(Linear Time Invariant)
LTV	(Linear Time-Varying)
IQC	(Integral Quadratic Constraints)
LMI	(Linear Matrix Inequalities)
LFT	(Linear Fractional Transformation)

References

[1] S. BOYD, Q. YANG - *Structured Lyapunov Functions for System Stability Problems*. International Journal of Control, 49(6):819-829, 1989.

[2] F. DEMOURANT - *New Algorithmic Approach Based on Integral Quadratic Constraints for Stability Analysis of High Order Models*. Control Conference (ECC), 2013 European, p. 359-364, July 2013.

[3] M. K. H. FAN, A. L. TITS, J. C. DOYLE - *Robustness in the Presence of Mixed Parametric Uncertainty and Unmodeled Dynamics*. IEEE Transactions on Automatic Control, 36(1):25-38, 1991.

[4] G. FERRERES, J-M. BIANNIC - *A μ Analysis Technique Without Frequency Gridding*. American Control Conference, 1998. Proceedings of the 1998, vol. 4, p. 2294-2298 Jun 1998.

[5] T. IWASAKI, S. HARA, A. L. FRADKOV - *Time Domain Interpretations of Frequency Domain Inequalities on (Semi)Finite Ranges*. Systems & Control Letters, 54(7):681-691, 2005.

[6] U. JONSSON, A. RANTZER - *A Unifying Format for Multiplier Optimization.* American Control Conference, Proceedings of the 1995, vol. 5, p. 3859-3860, Jun 1995.

[7] U. T. JONSSON - *Lecture Notes on Integral Quadratic Constraints*. 2001.

[8] U. T. JONSSON, A. RANTZER - *Systems with Uncertain Parameters - Time Variations with Bounded Derivatives*. International Journal of Robust and Nonlinear Control, 6:969-982, 1996.

[9] C.-Y. KAO, A. MEGRETSKI, U. JONSSON - *Specialized Fast Algorithms for Iqc Feasibility and Optimization Problems*. Automatica, 40(2):239-252, 2004.

[10] H. K. KHALIL - *Nonlinear Systems*. Pearson Education. Prentice Hall, 2002.

[11] H. KOROGLU, C. W. SCHERER - *Robust Performance Analysis for Structured Linear Time-Varying Perturbations with Bounded Rates-of-Variation.* IEEE Transactions on Automatic Control, 52(2):197-211, Feb 2007.

[12] R. MANCERA, M. G. SAFONOV - *Stability Multipliers for Mimo Monotone Nonlinearities.* American Control Conference, 2003. Proceedings of the 2003, volume 3, vol. 3, p. 1861-1866, June 2003.

[13] A. MEGRETSKI, A. RANTZER - *System Analysis via Integral Quadratic Constraints.* Automatic Control, IEEE Transactions, 42(6):819-830, Jun 1997.

[14] P. A. PARRILO - *On the Numerical Solution of Lmis Derived from the Kyp Lemma.* Decision and Control, 1999. Proceedings of the 38th IEEE Conference, vol. 3, p. 2334-2338, 1999.

[15] P. A. PARRILO - *Outer Approximation Algorithms for Kyp-Based Lmis.* American Control Conference, 2001. Proceedings of the 2001, vol. 4, p. 3025-3028, 2001.

[16] H. PFIFER, P. SEILER - *Robustness Analysis with Parameter-Varying Integral Quadratic Constraints.* 2015 American Control Conference (ACC), p. 138-143, July 2015.

[17] E. POLAK - *Optimization Algorithms and Consistent Approximations.* Springer-Verlag New York, 1997.

[18] A. SIDERIS, R. S. SANCHEZ PENA - *Robustness Margin Calculation with Dynamic and Real Parametric Uncertainty.* IEEE Transactions on Automatic Control, 35(8):970-974, Aug. 1990.

[19] P. VUILLEMIN, F. DEMOURANT, J.-M. BIANNIC, C. POUSSOT-VASSAL - *Stability Analysis of a Set of Uncertain Large-Scale Dynamical Models with Saturations: Application to an Aircraft System*. IEEE Transactions on Control Systems Technology, 25(5):1736-1749, 2017.

AUTHOR

Fabrice Demourant was born in Istres, France, in 1975. He received the Engineering Degree and M.Sc. degree in control and signal processing from ENSICAEN, Caen, France, and the Ph.D. degree in control systems theory within System Control and Flight Dynamics Department, ONERA, Toulouse, France, in 2002. In 2003, he worked as engineer with AIRBUS, Toulouse, in the load control domain. Since 2005, he is Researcher with ONERA, where he is in charge of the methods and tools activities. He has a consolidated experience in control law design, analysis, modeling, and load/vibration control.

A-K. Schug
(Hamburg University of Technology)

P. Seiler
(University of Minnesota)

H. Pfifer
(University of Nottingham)

E-mail: ann.schug@tuhh.de

DOI: 10.12762/2017.AL13-06

Robustness Margins for Linear Parameter Varying Systems

An approach for extending classical robustness margins to linear parameter varying (LPV) systems is presented. LPV systems are often used to model aircraft dynamics that are highly dependent on the operating conditions such as altitude and airspeed. Classical gain and phase margins are evaluated in the frequency domain and therefore cannot be applied to LPV systems. The proposed approach is based on a time-domain interpretation for disk margins. Specifically, a norm bounded linear time invariant (LTI) uncertainty is interconnected to the nominal LPV system. Next, a time-domain worst-case metric is applied to evaluate both the robustness margin and also the robust performance degradation. The approach does not require detailed uncertainty modeling. In addition, the analysis can be formulated as a convex optimization leading to reliable numerical analysis tools. As an example, the LPV gain margin of a flutter suppression controller for a flexible aircraft is evaluated.

Introduction

This paper presents a method for extending the notion of gain and phase margins to linear parameter varying (LPV) systems. LPV systems are often used in aerospace engineering to model dynamics that strongly depend on the operating conditions, where the state matrices depend on measurable exogenous parameters that vary over time. If the state matrices of the LPV model have a rational dependence on the scheduling parameters, finite dimensional semi-definite programs (SDPs) can be formulated for controller synthesis and analysis [1],[8],[14]. However, in many engineering applications the state matrices have an arbitrary dependence on the parameters. In this case, the analysis and synthesis problem leads to an infinite-dimensional set of linear matrix inequalities (LMIs). A finite approximation approach based on gridding is proposed in [19]. The existing results on LPV modeling, as well as controller design and synthesis have been widely studied and successfully used for many industrial applications. Results on robustness analysis for LPV systems, which depend rationally on the scheduling parameter, can be found, for example, in [18]. However, there is still a gap in the literature when it comes to standard robustness analysis tools for LPV systems with arbitrary parameter dependence. The classical phase and gain margins are evaluated in the frequency domain and can therefore not be applied to LPV systems due to their time varying dynamics. A standard approach is to impose a grid on the scheduling-parameter space and to evaluate the robustness margins at each grid point. However, this does not guarantee the robustness for the entire LPV system. This paper seeks to combine the knowledge about standard robustness margin analysis for linear time invariant (LTI) systems and new results for the analysis of uncertain LPV systems.

Recently, the framework of Integral Quadratic Constraints (IQCs) has gained a lot of attention in the research community. IQCs where first introduced in [7] as a general robustness analysis framework for LTI systems. The authors in [11] propose a time domain interpretation that can be used to extend the IQC framework to LPV systems. Specifically, a worst-case gain metric was proposed to extend the known performance analysis conditions for nominal LPV systems [19] to uncertain LPV systems. Here, the uncertain system is divided into a nominal system and a perturbation block. The IQC can then be imposed on the input/output behavior of the latter. The focus in this paper is on norm bounded LTI uncertainties, used to model simultaneous phase and gain variations in a system. The constraint can be directly obtained by reformulating the norm bound conditions of the uncertainty without having to go into too much detail concerning the IQC framework. The main contributions of this paper are based on the theoretical results in [12]. First, the worst-case metric is used to provide a notion of LPV stability margins. These margins are then used to formulate a simple robustness test for a gain scheduled controller, similar to the classical stability margins in LTI control. Additionally to the single margin point where instability occurs, this new technique can also be used to determine the robust performance of the LPV systems. The theory is finally applied to an aerospace engineering example. Here, the LPV robustness margins of a flutter suppression controller for a flexible aircraft are evaluated and compared to classical LTI analysis results based on μ-theory at each grid point.

Background

In many aerospace applications the dynamics strongly depend on the operating conditions of the aircraft, such as altitude or airspeed. The LPV framework can be used to consider this dependency in the modeling procedure as well as the controller synthesis. The dynamics are expressed as a function of a scheduling parameter. This section provides a brief summary of LPV modeling and introduces the performance of nominal LPV systems. This work is aimed at extending classical (LTI) robustness margins and robust performance analysis to LPV systems. The approach is based on the concept of disk margins for LTI systems as reviewed in Section "Disk Margins for LTI Systems".

Linear Parameter Varying Systems

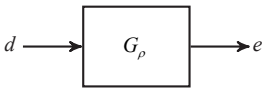

Figure 1 – LPV System

Linear parameter varying (LPV) systems are a special class of time varying systems where the dynamics depend on an exogenous parameter vector $\rho(t)$ restricted to remain in a compact set $\rho(t)\in\mathcal{P}\subset\mathbb{R}^{n_\rho}$ for all $t\geq 0$. An n^{th}-order LPV system G_ρ as depicted in Figure 1 has the form

$$\dot{x}(t)=A\big(\rho(t)\big)x(t)+B\big(\rho(t)\big)d(t) \tag{1}$$
$$e(t)=C\big(\rho(t)\big)x(t)+D\big(\rho(t)\big)d(t)$$

with the continuous functions $A:\mathbb{R}^{n_\rho}\to\mathbb{R}^{n_x\times n_x}$, $B:\mathbb{R}^{n_\rho}\to\mathbb{R}^{n_x\times n_d}$, $C:\mathbb{R}^{n_\rho}\to\mathbb{R}^{n_e\times n_x}$ and $D:\mathbb{R}^{n_\rho}\to\mathbb{R}^{n_e\times n_d}$. In addition, $x(t)\in\mathbb{R}^{n_x}$ is the vector containing the states of the system, $e(t)\in\mathbb{R}^{n_y}$ is the output vector and $d(t)\in\mathbb{R}^{n_u}$ the input vector. Given by the physical restrictions of most practical applications the admissible parameter trajectories are defined by

$$\mathcal{A}:=\left\{\rho:\mathbb{R}^+\to\mathbb{R}^{n_\rho}\,|\,\rho(t)\in\mathcal{P},\ \dot{\rho}(t)\in\dot{\mathcal{P}}\ \forall\, t\geq 0\right\} \tag{2}$$

where the admissible parameter rate is given by the subset

$$\dot{\mathcal{P}}:=\left\{\dot{\rho}\in\mathbb{R}^{n_\rho}\,|\,|\dot{\rho}_i|\leq\nu_i,\ i=1,\ldots,n_\rho\right\}$$

ν_i is the fastest admissible parameter variation rate.

The performance of an LPV system G_ρ can be measured in terms of the induced $\mathcal{L}_2$-norm. First define the norm of a signal d as $\|d\|_2=\sqrt{\int_0^\infty d^T(t)d(t)dt}$. The set of bounded signals, *i.e.* $d\in\mathcal{L}_2$, are those that satisfy $\|d\|_2<\infty$. The gain of the system from the input d to the output e can be defined using the signal $\mathcal{L}_2$-norm:

$$\|G_\rho\|:=\sup_{0\neq d\in\mathcal{L}_2,\ \rho\in\mathcal{A},\ x(0)=0}\frac{\|e\|_2}{\|d\|_2} \tag{3}$$

A bounded-real type result exists to bound the induced $\mathcal{L}_2$-norm of an LPV system. First, define the following differential operator for a symmetric matrix function $P:\mathcal{P}\to\mathbb{S}^{n_x}$:

$$\partial P(\rho,\dot{\rho})=\sum_{i=1}^{n_\rho}\frac{\partial P(\rho)}{\partial\rho_i}\dot{\rho}_i \tag{4}$$

The theorem below provides a matrix inequality condition to prove stability and bound the induced $\mathcal{L}_2$ gain of an LPV system with bounded parameter variation rate.

Theorem 2.1 (Bounded Real Lemma [20])
An LPV System G_ρ as defined in (1) is exponentially stable and $\|G_\rho\|<\gamma$ if there exists a continuously differentiable symmetric matrix function $P:\mathcal{P}\to\mathbb{S}^{n_x}$ such that the following two conditions hold $\forall(\rho,\dot{\rho})\in\mathcal{P}\times\dot{\mathcal{P}}$

$$P(\rho)>0 \tag{5}$$

$$\begin{bmatrix}P(\rho)A(\rho)+A(\rho)^TP(\rho)+\partial P(\rho,\dot{\rho}) & P(\rho)B(\rho)\\ B(\rho)^TP(\rho) & -I\end{bmatrix}+\frac{1}{\gamma^2}\begin{bmatrix}C(\rho)^T\\ D(\rho)^T\end{bmatrix}\begin{bmatrix}C(\rho) & D(\rho)\end{bmatrix}<0 \tag{6}$$

Proof. This is a standard result but a sketch of the proof is provided since it will be extended for the robustness result. Multiply (6) on the left and right by $\begin{bmatrix}x^T,d^T\end{bmatrix}$ and $\begin{bmatrix}x^T,d^T\end{bmatrix}^T$, respectively, to obtain (neglecting the dependence on time):

$$\dot{x}^TP(\rho)x+x^TP(\rho)\dot{x}+x^T\partial P(\rho,\dot{\rho})x+\frac{1}{\gamma^2}e^Te-d^Td<0 \tag{7}$$

Define a storage function $V:\mathbb{R}^{n_x}\times\mathcal{P}\to\mathbb{R}^+$ as $V(x,\rho)=x^TP(\rho)x$. Evaluating V along the state and parameter trajectory gives

$$\dot{V}+\frac{1}{\gamma^2}e^Te-d^Td<0 \tag{8}$$

Integrating over the time interval $[0,T]$ and applying $x(0)=0$ yields

$$V(T)+\frac{1}{\gamma^2}\int_0^T e(t)^Te(t)dt-\int_0^T d(t)^Td(t)dt<0 \tag{9}$$

Let $T\to\infty$ and use $V(T)\geq 0$, as well as the definition of the $\mathcal{L}_2$-norm, to obtain bound $\|e\|_2\leq\gamma\|d\|_2$. A slight modification of the arguments (using the compactness of $\mathcal{P}$) yields the strict inequality $\|e\|_2<\gamma\|d\|_2$.

Disk Margins for LTI Systems

In many applications, it is important to provide a high level of robustness. Specifically, the system performance should be insensitive to deviations between the model used for the controller synthesis and the actual system dynamics. Classical robustness measures, e.g., gain and phase margins, can be easily evaluated given the frequency response of the nominal system dynamics. More modern tools, e.g. μ analysis, require more detailed descriptions of the uncertainty. In general, an uncertain system can be described by "pulling out the uncertainty", as shown in Figure 2 [21]. This corresponds to an interconnection of a nominal (not-uncertain) system G and an uncertainty block Δ, as shown in Figure 2. The signals d and e correspond to exogenous inputs and system outputs, respectively. The signals v and w correspond to the signals related to the modeling uncertainty. The notation $F_u(G,\Delta)$ is used to represent this interconnection structure.

As noted above, classical gain and phase margins are common robustness metrics. These margins measure the amount of (individual) gain or phase that can be tolerated before a single closed-loop

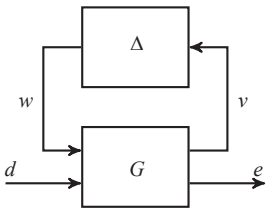

Figure 2 – Uncertain LTI System

becomes unstable. On the other hand, symmetric disk margins, as described in [3, 5], allow for simultaneous variations in both gain and phase within a prescribed disk. The remainder of the section briefly reviews the disk margin concept, since this will be used to formulate the proposed robustness margins for LPV systems. Consider the interconnection shown in Figure 3 where G and K are single input/single output (SISO) LTI systems and Δ is an LTI uncertainty. The symmetric disk margins are related to robustness with respect to this uncertainty interconnection.

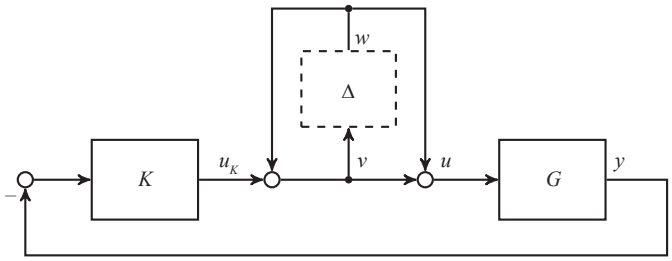

Figure 3 – Input Disk Margin Interconnection

The open loop transfer function, without Δ, from input w to output v is given by $\frac{1}{S_i - T_i}$, where $S_i := \frac{1}{1+GK}$ and $T_i := \frac{GK}{1+GK}$ are the sensitivity and complementary sensitivity functions at the plant input. Thus the disk margin interconnection is equivalent to $F_u\left(\frac{1}{S_i - T_k}, \Delta\right)$ (with no disturbance and error channels). By the small gain theorem [6, 21], the uncertain disk margin interconnection is stable if and only if $\|\Delta\|_\infty < \left\|\frac{1}{S_i - T_i}\right\|_\infty$. Thus, the stability radius (margin) can be defined as $r := 1/\|S_i - T_i\|$ where $0 < r < 1$ typically satisfies $0 < r < 1$.

Block diagram manipulation can be used to bring the disk margin interconnection into the equivalent form shown in Figure 4. This alternative form provides a useful connection back to classical gain and phase margins. This implies that the interconnection is stable for all real gains from u_K to u in the interval $\left[\frac{1-r}{1+r}, \frac{1+r}{1-r}\right]$. This proves the following symmetric lower and upper disk gain margins:

$$\mathrm{GM}_l = \frac{1-r}{1+r}, \quad \mathrm{GM}_u = \frac{1+r}{1-r} \tag{10}$$

Similarly, stability of Figure 4 for all $\|\Delta\|_\infty < r$ can be used to show that the loop is stable for all additional phase (from u_K to u) within the following disk phase margin limits:

$$\mathrm{PM}_l = -2\cot(r), \quad \mathrm{PM}_u = 2\cot(r) \tag{11}$$

These are called disk margins due to a connection in the Nyquist domain. Specifically, stability of the interconnection in Figure 4 for all $\|\Delta\|_\infty < r$ implies that the open loop Nyquist curve of GK remains outside the disk containing –1 and with diameter passing through $[-GM_u, -GM_l]$. Figure 5 shows the disk margins for an example transfer function. The critical point (–1,0) is marked in red. The interval on the real axis between the disk (orange) and the critical point corresponds to the gain margin and the intersection of the disk and the circle around the origin with radius 1 marks the arc of the phase margin. For further information on disk margins the reader is referred to [5], for example.

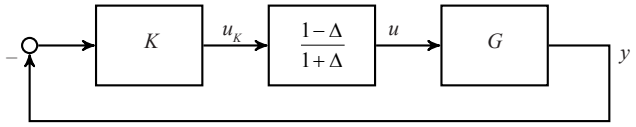

Figure 4 – Equivalent Input Disk Margin Interconnection

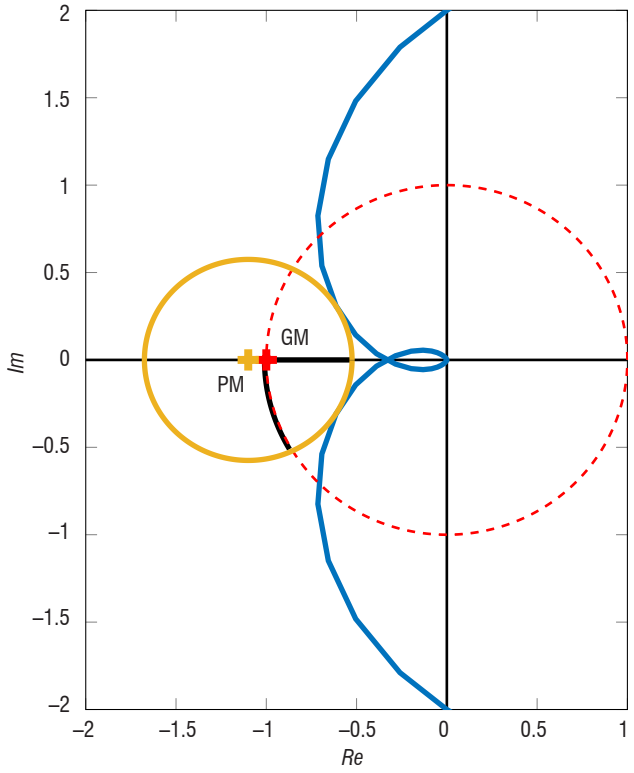

Figure 5 – Disk Margin in the Nyquist Plane

LPV Robustness Margins

Classical gain and phase margins are widely used as a standard formulation for robustness requirements in the aerospace industry. They do not require specific, detailed uncertainty models and, hence, these margins are easy to evaluate. Additionally, engineers have significant experience on the interpretation of the analysis results. At the same time, gain scheduling is a commonly used design method in aerospace. Since the classical margins are evaluated in the frequency domain, they cannot be directly applied to LPV systems due to the time varying nature of the dynamics. It is typical to simply evaluate the margins at "frozen" flight conditions. However, this fails to capture the effects of varying flight conditions. This motivates the proposed generalized robustness margins for LPV systems. The approach presented in this section provides two main extensions to the classical margins. A time domain worst-case metric can be used to formulate a generalized robustness margin for LPV systems. Additionally, this approach also considers the performance degradation before instability occurs.

LPV Disk Margins

The generalized disk margin interconnection in Figure 6 will be used for the analysis. This contains two significant differences from the previous disk margin interconnection in Figure 3. First, the plant G_ρ and controller K_ρ are allowed to be LPV systems. Here ρ is a parameter vector defining the flight condition. Second, an input d and output e are added in order to consider performance criteria. This corresponds to a plant input disturbance and plant output error. More generally, performance inputs/outputs can be included at any point in the feedback diagram depending on the specific application.

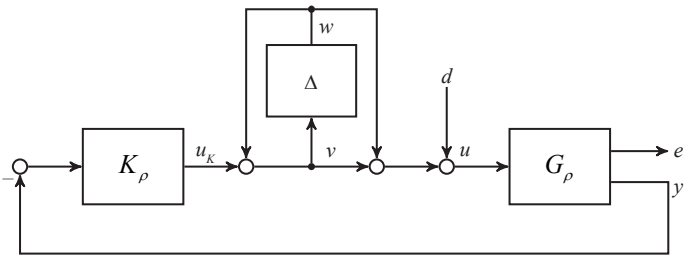

Figure 6 – Input Disk Margin Interconnection for LPV Systems

It is common to evaluate the classical margins with G_ρ and K_ρ evaluated at specific grid points of ρ. With a constant ρ, both the plant and controller are then LTI systems at the fixed operating condition. The disk margin analysis presented in Section "Disk Margins for LTI Systems" can be directly applied to this LTI interconnection. However, the resulting analysis does not consider the actual time varying nature of ρ. The approach proposed in this paper directly deals with the time varying operating conditions using the framework developed in [12].

Two basic robustness analysis problems will be considered, based on the LPV interconnection in Figure 6:

- **LPV Disk Margins**: Let Δ be an LTI uncertainty. Compute a stability margin r such that the LPV interconnection is stable for all $\|\Delta\|_\infty < r$ and all $\rho \in \mathcal{A}$.
- **Worst-Case Gain**: Again let Δ be an LTI uncertainty. In addition, assume that the uncertainty satisfies a given norm-bound $b < r$, *i.e.*, $\|\Delta\|_\infty < b$. Compute the worst-case gain from d to e over this set of uncertainties and all $\rho \in \mathcal{A}$.

The analysis requires a time-domain characterization of the uncertainty. Let $w = \Delta(v)$, where both w and v are assumed to be scalar signals, in order to simplify this discussion. The norm-bound $\|\Delta\|_\infty < b$ implies the following frequency-domain constraint on the input-output signals:

$$\begin{aligned} &\int_{-\infty}^{\infty} b^2 |V(j\omega)|^2 - |W(j\omega)|^2 d\omega = \\ &\int_{-\infty}^{\infty} V(j\omega)^* \left(b^2 - \Delta(j\omega)^* \Delta(j\omega)\right) V(j\omega) d\omega \geq 0 \end{aligned} \tag{12}$$

where $V(j\omega)$ and $W(j\omega)$ are the transforms of the signals $v(t)$ and $w(t)$. By Parseval's theorem [21], this inequality is equivalent to an infinite-horizon, time-domain constraint:

$$\int_0^\infty \begin{bmatrix} v(t) \\ w(t) \end{bmatrix}^T \begin{bmatrix} b^2 & 0 \\ 0 & -1 \end{bmatrix} \begin{bmatrix} v(t) \\ w(t) \end{bmatrix} dt \geq 0 \tag{13}$$

The causality of Δ implies that this constraint also holds for all finite intervals $[0,T]$, for all $v \in \mathcal{L}_2$, $w = \Delta(v)$ and $T > 0$ [12]. The time-invariance of Δ can be used to formulate a tighter constraint, as is standard in structured singular value (μ) analysis [9, 13]. Specifically, Δ is LTI and, hence, it commutes with any stable, minimum-phase LTI system D, *i.e.*, $D(s)\Delta(s) = \Delta(s)D(s)$. This property is the basis for the use of frequency-domain "D"-scale conditions in μ analysis [9, 13]. The equivalent time-domain formulation is obtained by noting that if $w = \Delta v$ then $Dw = \Delta Dv$. Hence, the filtered signals $(\tilde{v}, \tilde{w}) := (Dv, Dw)$ satisfy the same norm bound constraints as D. To simplify notation, combine the scalings D and stack the filtered signals as follows:

$$z := \begin{bmatrix} \tilde{v} \\ \tilde{w} \end{bmatrix} = \Psi \begin{bmatrix} v \\ w \end{bmatrix} \quad where \ \Psi := \begin{bmatrix} D & 0 \\ 0 & D \end{bmatrix} \tag{14}$$

As noted above, the filtered signals $(\tilde{v}, \tilde{w}) := (Dv, Dw)$ satisfy the same norm bound constraints as (v, w). This leads to the following time-domain inequality.

Definition 3.1
Let Δ be an LTI system satisfying $\|Delta\|_\infty < b$. In addition, let D be a stable, minimum phase LTI system. Define Ψ as in Equation 14 and $M = \begin{bmatrix} b^2 & 0 \\ 0 & -1 \end{bmatrix}$. Then Δ satisfies

$$\int_0^T z(t)^T M z(t) dt \geq 0 \tag{15}$$

for all $v \in \mathcal{L}_2$, $w = \Delta(v)$ and $T \geq 0$.

Equation 15 is a specific example of a time-domain *Integral Quadratic Constraint* (IQC). It is worth noting that IQCs provide a general framework, introduced in [7], for studying various uncertainties, such as infinite dimensional systems or hard non-linearities. There is an existing library of IQCs (Ψ, M) for particular classes of uncertainties. The (Ψ, M) given in Definition 3.1 is for the particular class of LTI norm-bounded uncertainty. The more general IQC framework can be used to obtain worst-case stability margins for other cases, e.g., systems with saturation. However, this paper will focus on norm bounded LTI uncertainties, in order to assess LPV disk margins.

LPV Worst-Case Gain

The (nominal) stability conditions of Section "Linear Parameter Varying Systems" can now be combined with the time domain constraint on the input/output behavior of the uncertainty block Δ. This can be used to assess the robust performance of an uncertain LPV system. First note that the LPV disk margin interconnection (Figure 6) is a special instance of the more general uncertain LPV system interconnection in Figure 7. Here, the nominal (not uncertain) LPV system T_ρ is connected to the uncertainty block. In addition, the dynamic filter Ψ, used to describe the IQC in Definition 3.1, is also appended to the diagram. The combined dynamics of T_ρ and Ψ are described by the following LPV system:

$$\begin{aligned} \dot{x} &= A(\rho)x + B_1(\rho)w + B_2(\rho)d \\ z &= C_1(\rho)x + D_{11}(\rho)w + D_{12}(\rho)d \\ e &= C_2(\rho)x + D_{21}(\rho)w + D_{22}(\rho)d \end{aligned} \tag{16}$$

The state vector combines the state of G and the state of Ψ, *i.e.*, $x = [x_G^T, x_\Psi^T]^T$. The perturbation block Δ is unknown and is not

considered for the purposes of analysis. Instead, w is treated as an external signal subject to the constraint on z given in Equation 15. This effectively replaces the precise relation $w=\Delta(v)$ by the imprecise time domain inequality.

The robust performance of this general uncertain LPV system (Figure 7) can be measured by the worst-case induced $\mathcal{L}_2$ gain from input d to output e over all uncertainties Δ satisfying the finite-time horizon constraint in (15). The following Theorem (from [12]) provides a matrix inequality condition to compute the upper bound on the worst case $\mathcal{L}_2$ -gain of $\mathcal{F}_u\left(T_\rho,\Delta\right)$.

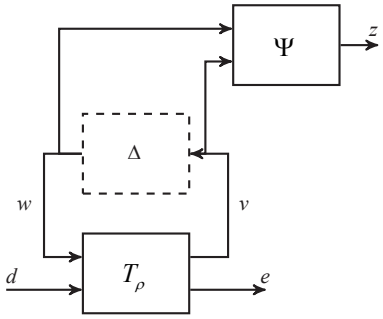

Figure 7 – Worst-Case Gain Analysis Interconnection

Theorem 3.2 (Extended Bounded Real Lemma [11])
Let $\mathcal{F}_u\left(T_\rho,\Delta\right)$ be well posed for any $\Delta\in IQC\left(\Psi,M\right)$. Then, the worst case gain of $F_u\left(T_\rho,\Delta\right)$ is upper bounded by $\gamma<\infty$ if there exists a continuously differentiable $P:\mathcal{P}\to\mathbb{S}^{n_x}$ and a scalar $\lambda>0$ such that the following conditions hold for all $\left(\rho,\dot\rho\right)\in\mathcal{P}\times\dot{\mathcal{P}}$:

$$P(\rho)>0, \tag{17}$$

$$\begin{bmatrix} P(\rho)A(\rho)+A(\rho)^TP(\rho)+\partial P(\rho,\dot\rho) & P(\rho)B_1(\rho) & P(\rho)B_2(\rho)\\ B_1(\rho)^TP(\rho) & 0 & 0\\ B_2(\rho)^TP(\rho) & 0 & -I\end{bmatrix}$$
$$+\lambda\begin{bmatrix}C_1(\rho)^T\\ D_{11}^T(\rho)^T\\ D_{12}^T(\rho)^T\end{bmatrix}M\begin{bmatrix}C_1(\rho) & D_{11}(\rho) & D_{12}(\rho)\end{bmatrix} \tag{18}$$
$$+\frac{1}{\gamma^2}\begin{bmatrix}C_2(\rho)^T\\ D_{21}(\rho)^T\\ D_{22}(\rho)^T\end{bmatrix}\begin{bmatrix}C_2(\rho) & D_{21}(\rho) & D_{22}(\rho)\end{bmatrix}<0$$

Proof. The proof is similar to Theorem 2.1. The uncertainty Δ is assumed to satisfy the IQC defined by $\left(\Psi,M\right)$, and therefore the signal z satisfies (15) for any $T>0$. Define a storage function $V\left(x,\rho\right)=x^TP(\rho)x$ as in the proof of Theorem 2.1. Left/right multiplication of Equation 18 by $\left[x^T,w^T,d^T\right]$ and $\left[x^T,w^T,d^T\right]^T$ leads to the following dissipation inequality

$$\dot V-d^Td+\lambda z^TMz+\frac{1}{\gamma^2}e^Te<0 \tag{19}$$

Integrating (19) over the finite time horizon $\left[0,T\right]$ and using the initial condition $x(0)=0$ along with the conditions $\lambda>0$ and $P(\rho)>0$ leads to the gain bound $\|e\|\le\gamma\|d\|$. This holds for any input $d\in\mathcal{L}_2$, admissible parameter trajectory $\rho\in\mathcal{A}$ and uncertainty $\Delta\in IQC\left(\Psi,M\right)$. Therefore the worst-case gain is upper bounded by γ.

The robustness analysis therefore consists in searching for decision variables, namely the matrix function $P(\rho)$, gain bound γ, and the constant λ, that lead to the feasibility of the conditions in Theorem 3.2. If the linear matrix inequality (LMI) conditions are feasible, then the system is stable for the selected uncertainty bound b. A bisection can be used to find the largest value of b for which the LMI is feasible. This largest uncertainty bound corresponds to the stability (disk) margin, denoted by r, for the LPV system. For example, the interconnection in Figure 6 is stable for all real gains from u_K to u in the interval $\left[\frac{1-r}{1+r},\frac{1+r}{1-r}\right]$. The other disk margin interpretations given in Section "Disk Margins for LTI Systems" have similar extensions to the LPV interconnection. The key point is that the plant and controller are LPV and the time-domain analysis enables the robustness with respect to LTI (disk-margin) uncertainty to be evaluated.

Theorem 3.2 can also be used to evaluate performance, in addition to the stability margin. In particular, it is important to emphasize that the performance can become unacceptable before the system becomes unstable. Thus, it is useful to evaluate the performance degradation for uncertainty bounds within the stability margin. In other words, a plot of worst-case gain vs. uncertainty bound b will approach infinity as $b\to r$. The performance degradation as the bound b increases provides additional useful information beyond simply knowing the stability margin r. It should also be mentioned that this approach can be used to obtain generalized delay margins for LPV systems, using existing time-domain IQCs for time delays. The work in [10] provides detailed information on IQCs for time-delayed LPV systems.

Numerical Implementation

The conditions in Theorem 3.2 involve infinite dimensional LMIs, *i.e.,* the conditions must hold for all $\rho\in\mathcal{P}$. In the case of System (1),depending only rationally on ρ, a guaranteed solution of the parameter dependent LMI conditions can be found, as proposed in [14]. In many practical applications, for example, the aeroelastic vehicle considered here, (1) depends arbitrarily on ρ. For this class of systems, an approximation of the parameter dependent constraints based on gridding is proposed in [19]. Specifically, the parameter space is approximated by a finite grid over $\left(\mathcal{P}\times\dot{\mathcal{P}}\right)$. It should be emphasized that the gridding approach is only an approximation for the parameter-dependent LMI conditions. Hence, no rigorous performance guarantees are provided by this approach, and special care must be taken when drawing conclusions. A pragmatic implementation of this approach is as follows: Enforce the LMI conditions on a "coarse" grid consisting of a small number of points, in order to reduce computation time. The resulting solution can then be checked on a "dense" grid of many points to ensure the accuracy of the solution. The SDP can be re-solved on a less coarse grid if required.

Another issue is that the matrix function P in Theorem 3.2 is itself parameter dependent. This function P can be expanded in terms of a finite number of basis functions:

$$P(\rho)=\sum_j^{n_\rho}b_j(\rho)P_j \tag{20}$$

where $b_j : \mathbb{R}^{n_\rho} \to \mathbb{R}$ can be any user-defined differentiable basis functions. The matrices P_j appearing in this expansion describe the function P with a (finite) number of decision variables. In general, there is no specific rule on how to choose the basis function. It has been reported that a similar parameter dependence as that in the system equations leads to satisfying results [2]. However, there is no scientific validation of this method in the literature. The choice of basis function used in the following application example will be described in Section "Robustness Analysis".

The final issue is the description of the IQC, which involves the scaling D. In μ-analysis the search over the D-scales is performed in the frequency domain on a grid of frequencies. This approach cannot be replicated for LPV analysis, since the condition in Theorem 3.2 is formulated in the time domain. Instead, many different D-scales, e.g., $\{D_i\}_{i=1}^{N}$ can be selected. Each D_i defines a valid IQC with corresponding filter Ψ_i. An approach for selecting basis functions for IQCs is proposed in [17]. The LMI conditions in Theorem 3.2 can be augmented in order to handle these multiple dynamic filters Ψ_i. The extended system then includes the additional dynamics of all Ψ_i. The corresponding LMI condition in (18) is modified to include one term corresponding to each selected D_i:

$$\sum_{i=1}^{N} \lambda_i \begin{bmatrix} C_{1i}(\rho)^T \\ D_{11i}(\rho)^T \\ D_{12i}(\rho)^T \end{bmatrix} M_i \begin{bmatrix} C_{1i}(\rho) & D_{11i}(\rho) & D_{12i}(\rho) \end{bmatrix} \qquad (21)$$

The constants λ_i are decision variables each of which must be ≥ 0. The output state matrices $(C_{1i}(\rho), D_{11i}(\rho), D_{12i})$ corresponding to the output z_i of filter Ψ_i. The analysis includes a search for the constants λ_i that lead to the feasibility of the LMI conditions in Theorem 3.2. It is worth noting that, in principle, Ψ and M do not have to be LTI but could potentially be LPV. However, the use of LPV (Ψ, M) has not been fully developed in the literature and will not be pursued here.

Application on a Flexible Aircraft

The proposed method is used to evaluate the LPV robustness margins of a flutter suppression controller for a flexible aircraft. The airframe is a small, radio-controlled aircraft denoted *mini-MUTT*, as shown in Figure 8. The design is based on Lockheed Martin's Body Freedom Flutter vehicle [4]. The mini-Mutt has a mass of 6.7 kg and a wing span of 3 meters. It was built completely in-house at the University of Minnesota to study the usage of active control for suppressing detrimental structural and aerodynamic interactions. These undesired interactions lead to a phenomenon called flutter, which is an unstable oscillation that can potentially destroy the aircraft. Given the catastrophic consequences of flutter, it is paramount to have an insightful and accurate robustness metric available.

Figure 8 – mini MUTT

System Description

The modeling of the aircraft incorporates structural and rigid body dynamics, as well as aerodynamics. The procedure can be found in [15]. The final model which is used is adapted from [11] and describes the longitudinal dynamics for straight and level flight. The system has a total of six states as well as one input and three output signals.

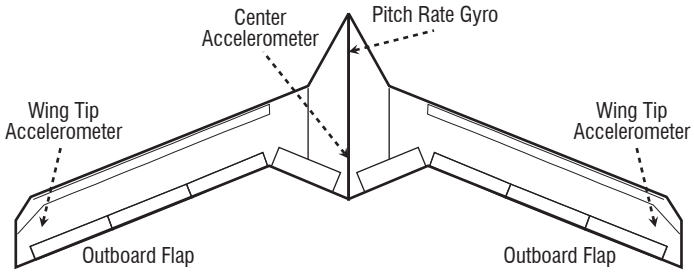

Figure 9 – Schematic Overview

A schematic overview of the aircraft is depicted in Figure 9, showing the available sensors and actuators. The aircraft has a total of 8 flaps on the back of the wing. The body flaps are unused in this example, while the inner two are the aileron and elevator, respectively. The flutter suppression controller has full authority over the outboard flap deflection denoted by δ, such that $u = \delta$. The plant output signals are the pitch rate q and the vertical acceleration at the center of gravity a_{CG} and the wing tips a_{WT}, such that $y = [q\, a_{CG}\, a_{WT}]$. A short period approximation of the full model as proposed in [16] is used. The first two states of the state space representation are associated with the rigid body dynamics and consist of the angle of attack α and pitch rate q. The remaining states represent the generalized displacement and velocity of the first flexible mode, denoted by η and $\dot{\eta}$, respectively. Therefore, the approximated plant model is of 4th-order and consists of the four states $\alpha, q, \eta, \dot{\eta}$. The dynamics strongly depend on the airspeed and it is therefore straightforward to represent the aircraft model as a parameter varying model. Specifically, the airspeed is assumed to be a measurable exogenous signal, which can be used as the scheduling parameter $\rho(t)$. Additionally, the sensor and actuator dynamics and the assumed time delay as described in [16] are included, leading to the final 6th-order LPV model.

The LPV controller is mainly based on the H_∞ design, which is also proposed in [16]. In this work, the airspeed is assumed to be constant, 30 m/s. To adapt the controller design to the LPV description of the system, the loopshaping approach can be systematically extended using the synthesis algorithm provided in [20]. Weighting filters can be used to shape the individual transfer functions of the individual performance channels. The modal velocity $\dot{\eta}$ of the first flexible mode is used as a non-measurable performance output. Since the main objective of the flutter suppression controller is to attenuate the mode, this can be achieved by pushing down the peak in the associated transfer function using a constant weighting filter.

Robustness Analysis

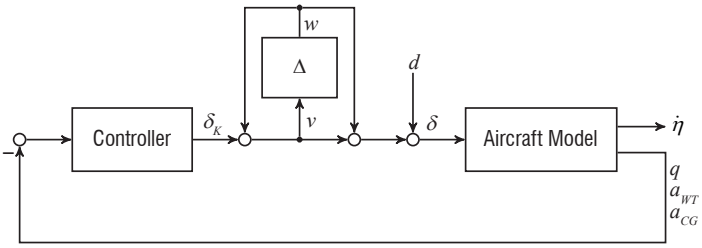

Figure 10 – Equivalent Input Disk Margin Interconnection

The LPV robustness margin analysis is performed on the closed-loop system of the aircraft and the LPV flutter suppression controller as shown in Figure 10. The parameter range is assumed to be $\rho = [20,\ldots,40]$ m/s and the parameter variation rate is bounded by ± 10 m/s^2. The worst-case performance is computed for increasing values of b by solving the LMI conditions in Theorem 3.2. The results are then normalized by the $\mathcal{L}_2$ gain of the nominal system $(b = 0)$. Let us recall that a norm bounded uncertainty is assumed to satisfy an IQC of the form

$$\Psi_1 = I_2 \qquad M = \begin{bmatrix} b^2 & 0 \\ 0 & -1 \end{bmatrix} \tag{22}$$

A second filter with simple first order dynamics

$$\Psi_2 = \begin{bmatrix} \frac{1}{s+1} & 0 \\ 0 & \frac{1}{s+1} \end{bmatrix} \tag{23}$$

is added to the analysis. Let us recall that, in general, it is possible to choose any stable minimum phase LTI system as a basis for the filter Ψ. However, including more complicated filters into the analysis did not lead to a significant improvement of the results. Initially, a constant matrix function P is used for the LMI conditions in Theorem 3.2. The analysis is then repeated, using linear and quadratic basis functions for the approximation of $P(\rho)$, *i.e.*, $P(\rho) = P_0 + \rho P_1$ and $P(\rho) = P_0 + \rho P_1 + \rho^2 P_2$. As a comparison, for each value of b the largest worst-case gain of the LTI systems over all individual grid points is computed, using the μ-Analysis framework and the Matlab function `wcgain`. Specifically, for a fixed value of b the LTI worst-case gain is computed at each grid point. The largest gain of all grid points is then plotted as a function of the uncertainty norm bound b.

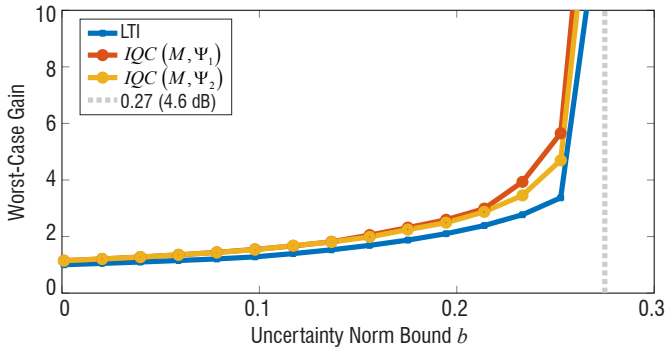

Figure 11 – Norm Bounded Uncertainty Worst-Case Gain

Evaluation

The optimization algorithm could not find any feasible solutions using a constant P and a linear basis functions. The analysis results using quadratic basis functions are shown in Figure 11. It can be seen that the worst-case gain using `wcgain` as well as the proposed method for LPV systems converges to the gain of the nominal plant $(b = 0)$. The gain slowly increases for uncertainty bounds below 0.1. Even further, the upper bound on the worst-case LPV gain is very close to the lower bound given by the largest LTI worst-case gain over all grid points. Using a constant matrix P as well as affine parameter dependence clearly introduces too much conservatism. Additional basis functions for the matrix function $P(\rho)$, such as a third-order polynomial were tested as well, but did not lead to a significant improvement of the results. Adding an additional IQC with internal dynamics shows only minimal improvement of the results. Both curves indicate an upper bound for the robustness margin of $b_{max} \approx 0.27$, corresponding to a real gain at the plant input of about 1.7 (4.6 dB). In comparison, the lowest LTI input-disk margin over all individual grid points is 4.9 dB. Let us recall that evaluating the classical LTI margins at each grid point has only been assumed to give a valid statement for the overall LPV system, so far. However, the results obtained by the worst-case LPV gain are very close to the LTI margin results, which indicates that the LTI analysis is indeed a useful first indicator of the LPV robustness in this application.

Conclusion

The IQCs framework can be used to extend classical robustness margins to LPV systems. The approach is independent from the plant and therefore no specific uncertainty modeling is required. Simultaneous gain and phase variations can be expressed using a norm bounded LTI perturbation block in connection to the nominal LPV system. The worst-case gain metric can be used to determine the robustness margins in the time domain, as well as the robust performance. The applicability was demonstrated on a flutter suppression controller ■

Acknowledgments

The work was supported by the National Science Foundation under Grant No. NSF-CMMI-1254129 entitled "CAREER: Probabilistic Tools for High-Reliability Monitoring and Control of Wind Farms".

Acronyms

IQC (Integral Quadratic Constraint)
LMI (Linear Matrix Inequality)
LPV (Linear Parameter Varying)
LTI (Linear Time Invariant)
SDP (Semidefinite Program)
SISO (Single Input/Single Output)

References

[1] P. APKARIAN, P. GAHINET - *A Convex Characterization of Gain-Scheduled H/Sub ∞ / Controllers.* IEEE Transactions on Automatic Control, 40(5):853-864, 1995.

[2] G. J. BALAS - *Linear, Parameter-Varying Control and its Application to a Turbofan Engine.* International Journal of Robust and Nonlinear Control, 12(9):763-796, 2002.

[3] D. BATES, I. POSTLETHWAITE - *Robust Multivariable Control of Aerospace Systems.* IOS Press, 8th edition, 2002.

[4] J. BERANEK, L. NICOLAI, M. BUONANNO, E. BURNETT, C. ATKINSON, B. HOLM-HANSEN, P. FLICK - *Conceptual Design of a Multi-Utility Aeroelastic Demonstrator*. 13th AIAA/ISSMO Multidisciplinary Analysis Optimization Conference, 3:2194-2208, 2010.

[5] J. D. BLIGHT, R. L. DAILEY, D. GANGSAAS - *Practical Control Law Design for Aircraft Using Multivariable Techniques.* International Journal of Control, 59(1):93-137, 1994.

[6] C. A. DESOER, M. VIDYASAGAR - *Feedback Systems: Input-Output Properties.* Academic Press, New York, 1975.

[7] A. MEGRETSKI, A. RANTZER - *System Analysis via Integral Quadratic Constraints.* IEEE Transactions on Automatic Control, 42(6):819-830, 1997.

[8] A. PACKARD - *Gain Scheduling via Linear Fractional Transformations.* Systems & Control Letters, 22(2):79-92, 1994.

[9] A. PACKARD, J. DOYLE - *The Complex Structured Singular Value.* Automatica, 29(1):71-109, 1993.

[10] H. PFIFER, P. SEILER - *Integral Quadratic Constraints for Delayed Nonlinear and Parameter-Varying Systems.* Automatica, 56:36-43, 2015.

[11] H. PFIFER, P. SEILER - *Less Conservative Robustness Analysis of Linear Parameter Varying Systems Using Integral Quadratic Constraints.* International Journal of Robust and Nonlinear Control, 26(16):3580-3594, 2016.

[12] H. PFIFER, P. SEILER - *Robustness Analysis of Linear Parameter Varying Systems Using Integral Quadratic Constraints.* International Journal of Robust and Nonlinear Control, 25(15):2843-2864, 2015.

[13] M. G. SAFONOV - *Stability and Robustness of Multivariable Feedback Systems.* MIT Press, Cambridge, MA, USA, 1980.

[14] C. W. SCHERER - *LMI Relaxations in Robust Control.* European Journal of Control, 12(1):3-29, 2006.

[15] D. K. SCHMIDT, W. ZHAO, R. K. KAPANIA - *Flight-Dynamics and Flutter Modeling and Analyses of a Flexible Flying-Wing Drone*. Proceedings of the AIAA SciTech Conference, :4-8, 2016.

[16] J. THEIS, H. PFIFER, P. J. SEILER - *Robust Control Design for Active Flutter Suppression.* AIAA Atmospheric Flight Mechanics Conference, p.1751, 2016.

[17] J. VEENMAN, C. W. SCHERER, H. KÖROGLU - *Robust Stability and Performance Analysis Based on Integral Quadratic Constraints.* European Journal of Control, 31:1-32, 2016.

[18] J. VEENMAN, C. W. SCHERER, I. E. KÖSE - *Robust Estimation with Partial Gain-Scheduling Through Convex Optimization.* Control of Linear Parameter Varying Systems with Applications, pages 253-278. Springer US, Boston, MA, 2012.

[19] F. WU - *Control of Linear Parameter Varying Systems.* Dissertation, University of California at Berkeley, 1995.

[20] F. WU, X. H. YANG, A. PACKARD, G. BECKER - *Induced L_2-Norm Control for LPV System with Bounded Parameter Variation Rates.* American Control Conference, Proceedings of 1995, 1995.

[21] K. ZHOU, J. C. DOYLE, K. GLOVER - *Robust and Optimal Control.* Prentice Hall, New Jersey, 1996.

Ann-Kathrin Schug graduated from the Hamburg University of Technology (TUHH), Germany in 2016. In early 2016 she joined the Aerospace Engineering and Mechanics Department of the University of Minnesota to work on robust control of a flexible aircraft. She is now a Ph.D. student at the Institute of Control Systems (TUHH) working on distributed control of spatially-interconnected systems.

Peter Seiler received his Ph.D. from the University of California, Berkeley in 2001. His graduate research focused on coordinated control of unmanned aerial vehicles and control over wireless networks. From 2004-2008, he worked at the Honeywell Research Labs on various aerospace and automotive applications including the redundancy management system for the Boeing 787, sensor fusion algorithms for automotive active safety systems and re-entry flight control laws for NASA's Orion vehicle. Since joining the University of Minnesota in 2008, he has been working on fault-detection methods for safety-critical systems and advanced control techniques for wind turbines and unmanned aircraft.

Harald Pfifer received his Ph.D. from the Technical University Munich, Germany in 2013. From 2008 till 2013, he has been a Research Associate with the Institute of Robotics and Mechatronics, German Aerospace Center (DLR), Oberpfaffenhofen, Germany. From 2013 to 2016 he has been a post-doctoral associate at the Aerospace Engineering and Mechanics Department of the University of Minnesota after which he joined the University of Nottingham as an assistant professor. His main research interests include aeroservoelastic control, modeling of uncertain dynamical system and robust and linear parameter varying control.

I. Queinnec, S. Tarbouriech
(LAAS-CNRS, Université de Toulouse, CNRS)

J.-M. Biannic
(ONERA)

C. Prieur
(Univ. Grenoble Alpes, CNRS, Gipsa-lab)

E-mail: queinnec@laas.fr

DOI: 10.12762/2017.AL13-07

Anti-Windup Algorithms for Pilot-Induced-Oscillation Alleviation

The paper deals with the development of anti-windup schemes and related numerical oriented tools. The objective is then to design anti-windup compensators to guarantee stability and performance for some particular classes of nonlinear actuators presenting both magnitude and rate saturations. The lateral flying case for a civil aircraft undergoing aggressive maneuvering by the pilot is addressed. A complete methodology including theoretical conditions and associated toolbox is then proposed and compared to solutions based on anti-PIO filters.

Introduction

The paper is aimed at developing anti-windup schemes and related numerical tools, in order to alleviate the Pilot-Induced-Oscillations in the lateral flying case for a civil aircraft undergoing aggressive maneuvering by the pilot. Indeed, anti-windup strategies represent an appropriate framework to mitigate the undesired saturation effects [24], [31]. Thus, the general principle of the anti-windup scheme can be depicted in Figure 1, where the (unconstrained) signal produced by the controller is compared to what is actually fed into the plant (the constrained signal). This difference is then used to adjust the control strategy by preserving stability and performance.

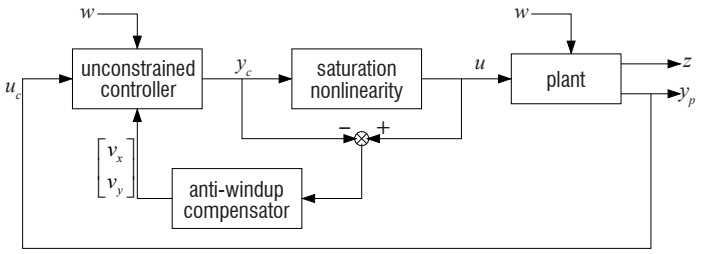

Figure 1 – Anti-windup principle

Such an anti-windup scheme is crucial for many control plants, since adding such a compensator to a previously computed control loop enables the performance of the closed-loop system to be improved, and could even prevent dramatic behavior, such as diverging solutions, when starting from bad initial conditions. For instance, [2], [3], [13], [14], [11], [12], [24] discuss several examples of open-loop unstable or stable physical systems presenting diverging solutions due to the presence of saturations. In particular, this undesirable nonlinear behavior appears for all exponentially unstable open-loop control systems, as well as for some marginally stable open-loop systems, as established in [23], [29].

Actually, this problem is particularly crucial for the space and aeronautical fields, where the Pilot-Induced-Oscillation (PIO) phenomenon is observed; that is, the existence of a particular external excitation (signal w in the notation of Figure 1) renders the closed-loop system unstable without anti-windup compensator [1], [15]. Thus, *ad-hoc* [22], [16] or advanced anti-windup strategies [8], [9], [18] for PIO suppression have been proposed in the literature and applied in practice.

For a given plant in closed loop with a pre-designed controller (designed without taking into account the saturation constraint) and a saturating input, the design of the anti-windup compensator is usually split into two steps, as explained in [26]. First, an analysis study is performed to estimate the effect of the isolated nonlinearity on the performance of the closed-loop system. Then, the second step is the design of an anti-windup compensator to improve the performance. By "performance", various notions could be considered, such as the $\mathcal{L}_2$ gain between a perturbation w and the regulated output z, as depicted in Figure 1. Of course, this performance estimation is associated with an estimation of the region where the initial conditions need to be restricted, in order to guarantee the asymptotic or exponential stability of the origin.

Numerous methods exist for the design of anti-windup compensators for control systems in the presence of magnitude or rate saturation constraints. See, for example, [11], [30], [10], [28], [24], [31] to cite just a few books, surveys or special issues on this subject. Of course, the aim of this paper is not to give an exhaustive perspective about anti-windup compensator design, but rather to present some hints and algorithms on how to solve numerically the anti-windup compensator design problem for an application purpose. Actually, due to the classical tradeoff between performance and estimation of the suitable region of initial conditions, the design of anti-windup

compensators is cast into a static optimization problem, written in terms of Linear Matrix Inequalities (LMIs). Such an optimization problem can be solved numerically in an efficient way using classical software in a Matlab environment. To illustrate the approach and algorithms, the anti-windup compensator design methods are applied to a lateral aircraft model, in order to provide a systematic way to mitigate the PIO phenomenon. Although actuator loss is not exactly the subject of the paper, we illustrate the case where only one aileron is available, allowing us to consider a harsh limit on the actuator bounds to better exhibit the effect of saturation and anti-windup actions.

This paper is organized as follows. First, the model and the problem under consideration are stated in Section "Model description and problem formulation". The main results are presented in Section "Main anti-windup design conditions", where numerically tractable conditions are given to solve the anti-windup compensator design problem and some efficient algorithms are given. The numerical tools used to actually solve the problem are focused on in Section "Dedicated software tools for solving saturated and anti-windup problems". These tools are then illustrated through an application to a realistic model for a civil transport aircraft in Section "PIO alleviation using an anti-windup loop". Some concluding remarks and perspectives end the paper.

Model description and problem formulation

The full model, including the plant, actuator, controller and anti-windup loop, is precisely defined below.

Plant model

We assume that the output of the controller is not affected in a same way by the nonlinear elements. The vector $u \in \Re^m$ building the m inputs of the plant is broken down into two subvectors: the first one, denoted by $u_s \in \Re^{m_s}$, corresponds to m_s saturated inputs, whereas the second one, denoted by $u_{ns} \in \Re^{m-m_s}$, corresponds to the linear inputs (unsaturated inputs). The plant model can be defined by:

$$\text{sysP}: \begin{cases} \dot{x}_p &= A_p x_p + B_{pu}^s u_s + B_{pu}^{ns} u_{ns} + B_{pw} w \\ y_p &= C_p x_p + D_{pu}^s u_s + D_{pu}^{ns} u_{ns} + D_{pw} w \\ z &= C_z x_p + D_{zu}^s u_s + D_{zu}^{ns} u_{ns} + D_{zw} w \end{cases} \quad (1)$$

where $x_p \in \Re^{n_p}$ and $w \in \Re^q$ are the state and the measured output of the plant. $w \in \Re^q$ generally represents an exogenous perturbation, but may also be used to represent a reference signal (or both). Furthermore, $z \in \Re^l$ represents the regulated output, which is used to evaluate the performance of the system with respect to the perturbation w via some appropriate optimization criteria.

Controller model

Unlike the classical anti-windup loops, in which the output of the anti-windup controller is injected into the dynamics of the controller and/or the output of the controller, we consider here that the output of the anti-windup controller modifies only partially the dynamics of the controller and/or the output of the controller. Thus, the dynamical controller is described as follows:

$$\text{sysC}: \begin{cases} \dot{x}_c &= A_c x_c + B_c u_c + B_{cw} w + B_{ca} v_x \\ y_{cs} &= C_c^s x_c + D_c^s u_c + D_{cw}^s w + D_{ca} v_y \\ y_{cns} &= C_c^{ns} x_c + D_c^{ns} u_c + D_{cw}^{ns} w \end{cases} \quad (2)$$

where $x_c \in \Re^{n_c}$ and $u_c \in \Re^p$ are the state and the input of the controller. The output of the controller is broken down into two signals: $y_{cs} \in \Re^{m_s}$, which will be interconnected u_s through a saturated actuator, and $y_{cns} \in \Re^{m-m_s}$, which will be interconnected with the linear (unsaturated) input u_{ns}. Moreover, v_x and v_y are the additional inputs that will be connected to the anti-windup controller. B_{ca} and D_{ca} are matrices of dimensions $n_c \times n_{cr}$ and $m_s \times m_r$, and make it possible to specify what the n_{cr} states and m_r outputs modified by the anti-windup action are.

Actuator model

The actuator block between the output of the controller y_c and the input of the plant u is divided into two blocks: the first one corresponding to the nonlinear (saturated) part and the second one corresponding to the linear (unsaturated) part. The nonlinear actuator part involves n_{dz} nested saturations, including the case of rate and magnitude saturations, as depicted in Figure 2(a). Such nonlinearities are tackled via the use of dead-zone, denoted by $\phi_i(.)$, $i = 1,...,n_{dz}$.

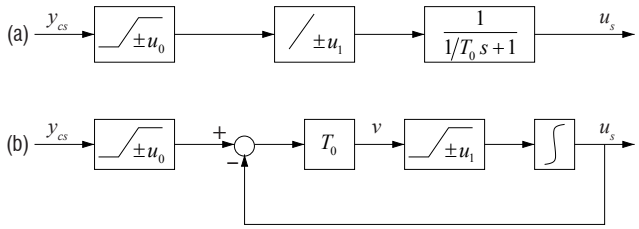

Figure 2 – (a) Actuator with rate and magnitude saturations. (b) Model used to represent such an actuator (scalar case)

The dynamical model of the actuator is based on Scheme 2(b) as follows:

$$\text{with} \quad sysACT: \begin{cases} \dot{x}_a &= v + \phi_1(v) \\ v &= T_0 y_{cs} + T_0 \phi_0(y_{cs}) - T_0 x_a \\ u_s &= x_a \end{cases} \quad (3)$$

where $\phi_0(y_{cs}) = sat_{u_0}(y_{cs}) - y_{cs}$ and $\phi_1(v) = sat_{u_1}(v) - v$. $sat_{u_0}(.)$ and $sat_{u_1}(.)$ are classical saturation functions and u_0 and u_1 are the levels of saturation in magnitude and rate, respectively. The elements of the diagonal matrix $T_0 \in \Re^{m_s \times m_s}$ classically take on large enough values, in order to avoid affecting the linear dynamics of the closed-loop system.

Anti-windup compensator

In the DLAW (Direct Linear Anti-Windup) strategy, the anti-windup controller uses as input the difference between the signals issued either from the input and the output of the whole actuator or from the input and the output of the nonlinear elements included in the actuator. Then, the anti-windup loop under consideration in the paper considers that the inputs of the anti-windup controller are the dead-zones associated with each saturation. Hence, the anti-windup controller of order n_{aw} is written as:

$$AW_\phi: \begin{cases} \dot{x}_{aw} &= A_{aw} x_{aw} + B_{aw}^0 \phi_0(y_c) + B_{aw}^1 \phi_1(v) \\ \begin{bmatrix} v_x \\ v_y \end{bmatrix} &= C_{aw} x_{aw} + D_{aw}^0 \phi_0(y_c) + D_{aw}^1 \phi_1(v) \end{cases} \quad (4)$$

where v_x and v_y are of dimensions n_{cr} and m_r, respectively.

Interconnections

The interconnections considered can be described as follows:

- linear link between the output of the plant and the input of the controller: $u_c = y_p$;

- the first part of the output of the controller (y_{cs}) is linked to the corresponding inputs of the plant (u_s) through the actuator model (3);
- the second part of the output of the controller is directly connected to the corresponding inputs of the plant: $u_{ns} = y_{cns}$;
- v_x and v_y are built from the anti-windup compensator.

Remark 2.1

An important fact is that the anti-windup model (4) imposes the assumption that the input and output signals of each saturation block in Figure 2 are available. To overcome this assumption, alternative strategies can be investigated. For example, the anti-windup may use the difference between the nonlinear actuator and a linear fictitious one (with the same dynamics but without saturation blocks) to explicitly take into account the dynamics of the actuator (present in the rate limiter) [20]. Another option would be to build an observer to evaluate the internal state of the actuator [27].

Standard formulation

In [24], a standard formulation of the anti-windup design has been proposed for various kinds of actuators. In the current case, by considering an augmented state of dimensions $n = n_p + m_s + n_c + n_{aw}$ including the state of the plant, the state of the actuator, the state of the controller and the state of the anti-windup controller, the following standard model of the complete closed-loop system can be defined by:

$$\begin{cases} \dot{x} &= \mathcal{A}x + \mathcal{B}_0\phi_0(y_c) + \mathcal{B}_1\phi_1(v) + \mathcal{B}_2 w \\ y_c &= \mathcal{C}_0 x + \mathcal{D}_{00}\phi_0(y_c) + \mathcal{D}_{01}\phi_1(v) + \mathcal{D}_{0w} w \\ v &= \mathcal{C}_1 x + \mathcal{D}_{10}\phi_0(y_c) + \mathcal{D}_{11}\phi_1(v) + \mathcal{D}_{1w} w \\ z &= \mathcal{C}_2 x + \mathcal{D}_{20}\phi_0(y_c) + \mathcal{D}_{21}\phi_1(v) + \mathcal{D}_{2w} w \end{cases} \quad (5)$$

where the matrices of the anti-windup controller are encapsulated into the matrices of system (5). Details of these matrices are given in Section "Algorithms for AW_ϕ design".

The design procedure of the anti-windup controller consists in optimizing some quantities, such as the size of the region of stability of the closed-loop system or the guaranteed level of performance. In particular, the idea when adding the anti-windup loop is to maximize the basin of attraction of the origin for the closed-loop system and/or to minimize the $\mathcal{L}_2$ gain between w and z or to maximize the set of perturbation w, which can be rejected. Then, the perturbation signal is assumed to be bounded in energy, as follows:

$$\|w\|_2^2 = \int_0^\infty w'(t)w(t)dt \le \delta^{-1};\ 0 \le \delta^{-1} < \infty \quad (6)$$

The problem that we intend to address is summarized below.

Problem 2.2

Determine an anti-windup controller AW_ϕ and a region $\mathcal{E}$, as large as possible, such that

- *Internal stability. When $w = 0$, the closed-loop system (5) is asymptotically stable for any initial conditions belonging to $\mathcal{E}$ (which is a region of asymptotic stability (RAS));*
- *Performance. When $w \neq 0$, satisfying (6), and for $x(0) = 0$, the $\mathcal{L}_2$ gain between w and z is finite and equal to $\gamma > 0$. Furthermore, the trajectories of the closed-loop system (5) remain bounded in the set $\mathcal{E}$.*

The convex optimization problems associated with Problem 2.2 are specified in Section "Algorithms for AW_ϕ design".

Main anti-windup design conditions

Solution to standard anti-windup design

The following proposition provides conditions of local stability and $\mathcal{L}_2$ performance for the closed-loop system (5). The result considers existence conditions to solve Problem 2.2.

Proposition 3.1

If there exist a symmetric positive definite matrix $Q \in \Re^{n\times n}$, two matrices Z_0 and $Z_1 \in \Re^{m\times n}$, two positive diagonal matrices S_0 and $S_1 \in \Re^{m\times m}$ and a positive scalar γ such that the following conditions are met:

$$\begin{bmatrix} Q\mathcal{A}' + \mathcal{A}Q & \mathcal{B}_0S_0 - Q\mathcal{C}_0' - Z_0' & \mathcal{B}_1S_1 - Q\mathcal{C}_1' - Z_1' & \mathcal{B}_2 & Q\mathcal{C}_2' \\ \star & -2S_0 - \mathcal{D}_{00}S_0 - S_0\mathcal{D}_{00}' & -\mathcal{D}_{01}S_1 - S_0\mathcal{D}_{10}' & -\mathcal{D}_{0w} & S_0\mathcal{D}_{20}' \\ \star & \star & -2S_1 - \mathcal{D}_{11}S_1 - S_1\mathcal{D}_{11}' & -\mathcal{D}_{1w} & S_1\mathcal{D}_{21}' \\ \star & \star & \star & -I & \mathcal{D}_{2w}' \\ \star & \star & \star & \star & -\gamma I \end{bmatrix} < 0 \quad (7)$$

$$\begin{bmatrix} Q & Z_{0(i)}' \\ \star & \delta u_{0(i)}^2 \end{bmatrix} \ge 0,\ i = 1,\ldots,m \quad (8)$$

$$\begin{bmatrix} Q & Z_{1(i)}' \\ \star & \delta u_{1(i)}^2 \end{bmatrix} \ge 0, i = 1,\ldots,m \quad (9)$$

then,

1. *when $w = 0$, the set $E(Q^{-1},\delta) = \{x \in \Re^n; x'Q^{-1}x \le \delta^{-1}\}$ is RAS for the closed-loop system (5);*
2. *when $x(0) = 0$, satisfying (6), and for $x(0) = 0$,*
   - *the trajectories of the closed-loop system remain bounded in the set $\mathcal{E}(Q^{-1},\delta)$;*
   - *the $\mathcal{L}_2$ gain is finite and one obtains:*

$$\int_0^T z(t)'\,z(t)dt \le \gamma \int_0^T w(t)'\,w(t)dt,\ \forall T \ge 0 \quad (10)$$

The detailed way to derive the conditions and to prove them can be found, for example, in [24], [31].

Remark 3.2

The interest of the anti-windup structure resides in the simplicity of the design conditions. Indeed, the design of a static anti-windup gain (only matrices D_{aw}^0 and D_{aw}^1 are used) is the result of a fully linear problem. In the case of the design of a dynamical anti-windup controller, for a priori given matrices A_{aw} and C_{aw}, the determination of the input and transmission matrices is also obtained by solving a linear problem. In the case where $n_{aw} = n_p + n_{m_s} + n_c$, the resolution of a linear problem can also be considered through an iterative procedure [24].

For analysis purposes (the anti-windup controller being given), the conditions of Proposition 3.1 are linear and can be directly used to solve adequate optimization problems. Moreover, in the design context, the conditions of Proposition 3.1 are non-convex, matrices A_{aw}, B_{aw}, C_{aw} and D_{aw}, hidden in matrices $\mathcal{A}$, $\mathcal{B}_i$, $\mathcal{C}_i$, $\mathcal{D}_{ij}$, $i,j = 0,1$. Conditions with linear decision variables can be obtained, more or less directly, by slightly modifying the original conditions, or even by considering iterative procedures (including D-K iteration process)

allowing a Lyapunov matrix and anti-windup matrices to be sought. These situations are detailed in the next subsection.

Remark 3.3

In the sequel, one considers a set $\mathcal{X}_0$, defined by some directions in the plant state space $v_i \in \Re^{n_p}$, $i = 1,...,q$, to provide a desired shape of the region $E(Q^{-1},\delta)$ to be maximized when solving Problem 2.2. Then, considering $\overline{v}_i = \begin{bmatrix} v_i' & 0 \end{bmatrix}' \in \Re^n$, $i = 1,...,q$ and β a scaling factor such that $\beta\overline{v}_i \in E(Q^{-1},\delta)$, $i = 1,...,q$ (which corresponds to imposing $\beta\mathcal{X}_0 \subset E(Q^{-1},\delta)$), an additional condition to those of Proposition 3.1 must be considered in the algorithms, as follows:

$$\begin{bmatrix} \delta\dfrac{1}{\beta^2} & \delta\overline{v}_i' \\ \delta\overline{v}_i & Q \end{bmatrix} > 0,\ i = 1,...,q \tag{11}$$

This means that β is used to maximize the region of attraction of the system and $\mathcal{X}_0$ allows the directions of interest for this region of attraction to be oriented.

Algorithms for AW_ϕ design

From (1), (2), (3) and (4), the matrices of system (5) are defined by:

$$\begin{gathered}
\mathcal{A} = \begin{bmatrix} \mathbb{A} & B_v C_{aw} \\ 0 & A_{aw} \end{bmatrix} \qquad \mathcal{B}_0 = \begin{bmatrix} B_{\phi 0} + B_v D_{aw}^0 \\ B_{aw}^0 \end{bmatrix} \qquad \mathcal{B}_1 = \begin{bmatrix} B_{\phi 1} + B_v D_{aw}^1 \\ B_{aw}^1 \end{bmatrix} \\
\mathcal{C}_0 = \begin{bmatrix} C_0 & C_{v0} C_{aw} \end{bmatrix} \qquad \mathcal{C}_1 = \begin{bmatrix} C_1 & C_{v1} C_{aw} \end{bmatrix} \qquad \mathcal{C}_2 = \begin{bmatrix} C_2 & 0 \end{bmatrix} \\
\mathcal{D}_{00} = C_{v0} D_{aw}^0 \qquad \mathcal{D}_{01} = C_{v0} D_{aw}^1 \qquad \mathcal{D}_{10} = D_1 + C_{v1} D_{aw}^0 \qquad \mathcal{D}_{11} = C_{v1} D_{aw}^1 \\
\mathcal{B}_2 = \begin{bmatrix} B_2 \\ 0 \end{bmatrix} \qquad \mathcal{D}_{20} = 0 \qquad \mathcal{D}_{21} = 0
\end{gathered} \tag{12}$$

with

$$\mathbb{A} = \begin{bmatrix} A_p + B_{pu}^{ns}\Delta^{-1} D_c^{ns} C_p & B_{pu}^s + B_{pu}^{ns}\Delta^{-1} D_c^{ns} D_{pu}^s & B_{pu}^{ns}\Delta^{-1} C_c^{ns} \\ T_0 D_c^s \left(C_p + D_{pu}^{ns}\Delta^{-1} D_c^{ns} C_p \right) & T_0 \left(D_c^s D_{pu}^s - I_{ms} + D_c^s D_{pu}^{ns}\Delta^{-1} D_c^{ns} D_{pu}^s \right) & T_0 \left(C_c^s + D_c^s D_{pu}^{ns}\Delta^{-1} C_c^{ns} \right) \\ B_c C_p + B_c D_{pu}^{ns}\Delta^{-1} D_c^{ns} C_p & B_c D_{pu}^s + B_c D_{pu}^{ns}\Delta^{-1} D_c^{ns} D_{pu}^s & A_c + B_c D_{pu}^{ns}\Delta^{-1} C_c^{ns} \end{bmatrix}$$

$$B_2 = \begin{bmatrix} B_{pw} + B_{pu}^{ns}\Delta^{-1}\left(D_c^{ns} D_{pw} + D_{cw}^{ns} \right) \\ T_0 \left(D_c^s D_{pw} + D_{cw}^s + D_c^s D_{pu}^{ns}\Delta^{-1}\left(D_c^{ns} D_{pw} + D_{cw}^{ns} \right) \right) \\ B_{cw} + B_c D_{pw} + B_c D_{pu}^{ns}\Delta^{-1}\left(D_c^{ns} D_{pw} + D_{cw}^{ns} \right) \end{bmatrix}$$

$$B_{\phi 0} = \begin{bmatrix} 0 \\ T_0 \\ 0 \end{bmatrix} \qquad B_{\phi 1} = \begin{bmatrix} 0 \\ I_{m_s} \\ 0 \end{bmatrix} \qquad D_1 = T_0$$

$$\begin{aligned}
C_0 &= \begin{bmatrix} D_c^s \left(I_p + D_{pu}^{ns}\Delta^{-1} D_c^{ns} \right) C_p & D_c^s \left(I_p + D_{pu}^{ns}\Delta^{-1} D_c^{ns} \right) D_{pu}^s & C_c^s + D_c^s D_{pu}^{ns}\Delta^{-1} C_c^{ns} \end{bmatrix} \\
C_1 &= \begin{bmatrix} T_0 D_c^s \left(I_p + D_{pu}^{ns}\Delta^{-1} D_c^{ns} \right) C_p & T_0 D_c^s \left(I_p + D_{pu}^{ns}\Delta^{-1} D_c^{ns} \right) D_{pu}^s - T_0 T_0 \left(C_c^s + D_c^s D_{pu}^{ns}\Delta^{-1} C_c^{ns} \right) \end{bmatrix} \\
C_2 &= \begin{bmatrix} C_z + D_{zu}^{ns}\Delta^{-1} D_c^{ns} C_p & D_{zu}^s + D_{zu}^{ns}\Delta^{-1} D_c^{ns} D_{pu}^s & D_{zu}^{ns}\Delta^{-1} C_c^{ns} \end{bmatrix}
\end{aligned}$$

$$\begin{aligned}
D_{0w} &= D_{cw}^s + D_c^s D_{pw} + D_c^s D_{pu}^{ns}\Delta^{-1}\left(D_c^{ns} D_{pw} + D_{cw}^{ns} \right) \\
D_{1w} &= T_0 \left(D_{cw}^s + D_c^s D_{pw} + D_c^s D_{pu}^{ns}\Delta^{-1}\left(D_c^{ns} D_{pw} + D_{cw}^{ns} \right) \right) \\
D_{2w} &= D_{zw} + D_{zu}^{ns}\Delta^{-1}\left(D_c^{ns} D_{pw} + D_{cw}^{ns} \right)
\end{aligned}$$

Furthermore, matrices defining the interconnection between the anti-windup loop and the system are:

$$B_v = \begin{bmatrix} 0 \\ T_0 D_{ca} \begin{bmatrix} 0 & I_{m_r} \end{bmatrix} \\ B_{ca} \begin{bmatrix} I_{n_{cr}} & 0 \end{bmatrix} \end{bmatrix} \qquad C_{v0} = D_{ca} \begin{bmatrix} 0 & I_{m_r} \end{bmatrix} \qquad C_{v1} = T_0 D_{ca} \begin{bmatrix} 0 & I_{m_r} \end{bmatrix}$$

The analysis problem (Algorithm 3.4) is linear and the synthesis problem of the anti-windup is nonlinear, including products between decision variables and, in particular, between the Lyapunov matrix Q and the anti-windup elements. A D-K iteration procedure may then be considered for the synthesis problem (Algorithm 3.6). However, the synthesis optimization problem may be partially linearized and, for given matrices A_{aw} and C_{aw}, the design of matrices B_{aw}^i and D_{aw}^i, $i = 0,1$ can be handled via a linear optimization problem (Algorithm 3.5).

Algorithm 3.4

Analysis of a given AW_ϕ anti-windup controller

1. *Select matrices A_{aw}, B_{aw}^0, B_{aw}^1, D_{aw}^0, D_{aw}^0 and D_{aw}^1.*
2. *Choose directions to be optimized $v_i \in \Re^{n_p}$, $i = 1,...,q$ and a known perturbation bound δ.*
3. *Solve*

$$\min_{Q, S_0, S_1, Z_0, Z_1, \gamma, \mu} f_{cost}(\gamma, \mu)$$

subject to LMI (7), (8), (9) *and* (11)

where γ is the $\mathcal{L}_2$ gain between w and z and $\mu = 1/\beta^2$.

Algorithm 3.5

Design of an AW_ϕ anti-windup controller with fixed dynamics

1. *Select matrices A_{aw} and C_{aw}. A static anti-windup AW_ϕ may also be used by considering $n_{aw} = 0$.*
2. *Choose directions to be optimized $v_i \in \Re^{n_p}$, $i = 1,...,q$ and a known perturbation bound δ.*
3. *Solve*

$$\min_{Q, S_0, S_1, Z_0, Z_1, \bar{B}_{aw}^0, \bar{B}_{aw}^1, \bar{D}_{aw}^0, \bar{D}_{aw}^1, \gamma, \mu} f_{cost}(\gamma, \mu)$$

subject to LMI (7), (8), (9) *and* (11)

where γ is the $\mathcal{L}_2$ gain between w and z and $\mu = 1/\beta^2$.

4. *Compute $B_{aw}^0 = \bar{B}_{aw}^0 S_0^{-1}$, $B_{aw}^1 = \bar{B}_{aw}^1 S_1^{-1}$, $D_{aw}^0 = \bar{D}_{aw}^0 S_0^{-1}$ and $D_{aw}^1 = \bar{D}_{aw}^1 S_1^{-1}$.*

Algorithm 3.6

Design of an AW_ϕ anti-windup controller – full design

1. *Select matrices A_{aw}, C_{aw} of appropriate dimensions, in order to build the desired anti-windup loop.*
2. *Choose the directions to be optimized $v_i \in \Re^{n_p}$, $i = 1,...,q$ and a known perturbation bound δ.*
3. *Pre-synthesis step – Solve*

$$\min_{Q, S_0, S_1, Z_0, Z_1, \bar{B}_{aw}^0, \bar{B}_{aw}^1, \bar{D}_{aw}^0, \bar{D}_{aw}^1, \gamma, \mu} f_{cost}(\gamma, \mu)$$

subject to LMI (7), (8), (9) *and* (11)

where γ is the $\mathcal{L}_2$ gain between w and z and $\mu = 1/\beta^2$.

4. *Compute $B_{aw}^1 = \bar{B}_{aw}^1 S_1^{-1}$, $B_{aw}^1 = \bar{B}_{aw}^1 S_1^{-1}$, $D_{aw}^0 = \bar{D}_{aw}^0 S_0^{-1}$ and $D_{aw}^1 = \bar{D}_{aw}^1 S_1^{-1}$.*
5. *If the solution obtained is satisfactory (some accuracy has to be fixed), or no longer improved compared to the previous steps, then STOP. Otherwise, go to the next iteration (the idea is to finish by a pre-synthesis step).*
6. *Synthesis step – Pick the solution Q obtained at Step 3 and solve*

$$\min_{S_0, S_1, Z_0, Z_1, A_{aw}, C_{aw}, B_{aw}^0, B_{aw}^1, D_{aw}^0, D_{aw}^1, \gamma} \gamma$$

subject to LMI (7), (8), (9) *and* (11)

7. Go to Step 3.

Remark 3.7

The optimization cost function f_{cost} is typically related to the performance of the disturbance rejection ($min\ \gamma$) and/or to the size of the domain of safe behavior in which the trajectories of the system may be initiated. In this paper, we consider inequalities (11) and $min\ \mu$, with $\mu = 1/\beta^2$ but any other criterion of the matrix B_{aw}^i could be used.

Remark 3.8

In Algorithm 3.5 and in Step 3 of Algorithm 3.6, condition (7) is not directly applied. The products between B_{aw}^i and D_{aw}^i with the matrices S_i are replaced by the change of variables $\bar{B}_{aw}^i$ and $\bar{D}_{aw}^i$, $i = 0,1$, which allows the problem to be linearized.

Remark 3.9

An interesting case is the static anti-windup one, for which matrices A_{aw} and C_{aw} are null matrices of appropriate dimensions. It implies that B_{aw}^i, $i = 0,1$, are also null matrices of appropriate dimensions and only matrices D_{aw}^i, $i = 0,1$, are computed in Algorithm 3.5.

Remark 3.10

Matrices A_{aw} and C_{aw} to be used in Algorithm 3.5 may be selected as the solution to a full-order ($n_{aw} = n_p + n_c + m_s$) anti-windup compensator design where the actuator is just a saturation in magnitude (see, for example, the conditions provided in [24]), i.e., *via a linear optimization problem. Eventually, an order-reduction step may also be considered in order to select matrices A_{aw} and C_{aw} (see Example 8.5 in [24]). Other procedures developed in [31], such as the Model Recovery Anti-Windup (MRAW), could be used.*

Dedicated software tools for solving saturated and anti-windup problems

For numerical evaluations, Semi-Definite Programming (SDP) solvers are easily available in a Matlab environment, either considering the MathWorks® package LMI Lab included in the Robust Control Toolbox™ or any freely available solvers. Similarly, in addition to the original parser of the LMI Lab package, one may prefer YALMIP format [17] to specify LMIs systems, convex optimization costs and associated solvers.

SATAW toolbox [19] has been developed to perform analysis and control design operations for linear systems interconnected with saturation elements. The toolbox manipulates a flexible description of the continuous-time system, controller and actuator using simple structure elements, as they are described in Section "Main anti-windup design conditions". For the saturation modeling, sector conditions are used. In this representation, the saturation term is replaced by a dead-zone nonlinearity. Hence, sector conditions, locally or globally valid, can be used to provide stability and stabilization conditions. The package then includes several functions for:

- state feedback or output feedback analysis, in the presence of position saturation and/or rate saturation;
- state feedback or output feedback design, in the presence of position saturation;
- static and dynamic anti-windup analysis, in the presence of position saturation;
- static anti-windup design, in the presence of position saturation.

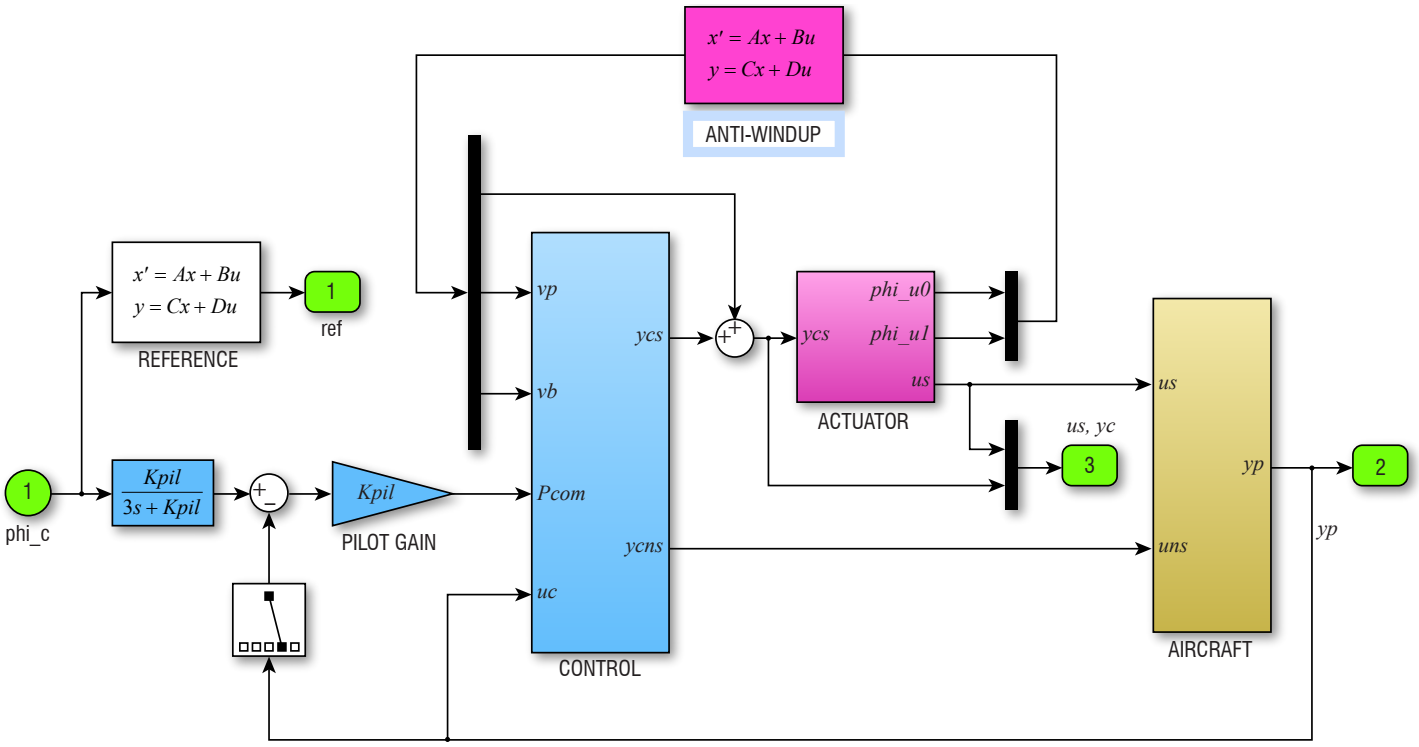

Figure 3 – Nonlinear closed-loop Simulink implementation of anti-windup AW_ϕ for lateral aircraft simulations

Actually, the current published version of the toolbox does not allow the dynamic anti-windup design problem to be formally solved in the presence of position and rate saturation, but gives many elements to extend the functions to the case addressed in this paper.

Alternatively, the AWAST Tools [5], which were recently updated and integrated as a library (SAW Library) of the SMAC Toolbox [4], enable rather general anti-windup problems to be formalized and solved, following the practical framework proposed in [6].

PIO alleviation using an anti-windup loop

The design and analysis algorithms of Section "Main anti-windup design conditions" are now applied and compared in the realistic context of lateral maneuvers of a civil transport aircraft. Specific attention is devoted to aggressive pilot demands in conjunction with actuator loss.

To do this, the pilot's activity is modeled as a static gain K_{pil}. For this application, a normal activity would correspond to $K_{pil} = 1$. Actually, in stressful situations, notably in case of actuator loss, a more aggressive pilot behavior is generally observed, resulting in much higher gains. Here, the gain is set to $K_{pil} = 2$.

Problem setup and objectives

A nonlinear closed-loop Simulink implementation of the anti-windup structure is depicted in Figure 3. The "aircraft" block is a linearized version (for fixed airspeed and altitude under cruise flight conditions) of the lateral dynamics of the system, including structural filters and delays, resulting in a state-space model of dimension 63. The controller block includes a dynamical controller of dimension 29. Its central objective is to provide good damping for the Dutch roll and to enable a safe control of the roll rate so that the bank angle ϕ is then easily controlled by the pilot with a simple gain K_{pil}. The state-space models $sysP$ and $sysC$ are then readily obtained from the Simulink diagrams of Figure 3, with the help of the Matlab **linmod** function. The plant corresponds to the "yellow box" depicting the aircraft system while the global controller (including pilot actions) is obtained by extraction of the 3 blue boxes. A standard balanced reduction technique is finally applied to obtain reasonably sized models. The reduced orders obtained, respectively $n_p = 8$ and $n_c = 20$, are compatible with the proposed algorithms.

The aircraft system involves 2 control inputs ($m = 2$): ailerons and rudder deflections. Note that only the aileron deflection actuator is assumed to saturate ($m_s = 1$) for the considered maneuvers. Moreover, 5 outputs ($p = 5$) are available for feedback ($y_p = [\beta, p, r, \phi, \dot{\phi}]'$). The performance is evaluated via the tracking accuracy on the fourth bank-angle output ϕ (then, $l = 1$). The disturbance input of System (1) is used to express the perturbing effect of the saturation of the system input, that is, $B_{pw} = B^s_{pu}$ ($q = 1$).

In the AW_ϕ strategy, two signals (one for the magnitude limitation and one for the rate limitation) are used by the anti-windup device. Their generation is detailed in the Simulink implementation of Figure 4.

The anti-windup controller acts on the internal dynamics of the nominal lateral controller of the aircraft through two scalar signals v_p and $v_{b,}$ which respectively affect roll and sideslip angle dynamics ($v_x = [v_p \;\; v_b]$ and $v_y = 0$, $n_{cr}=2$, $m_r = 0$). This means that matrix B_{ca} appearing in Equation (2) is of dimension $n_c \times 2$.

The chosen strategy offers some flexibility, with the possibility of a direct anti-windup action at the controller output. However, no significant improvement has been observed with this additional feature, which has thus not been further considered in this application. This means that D_{ca} appearing in Equation (2) is equal to 0.

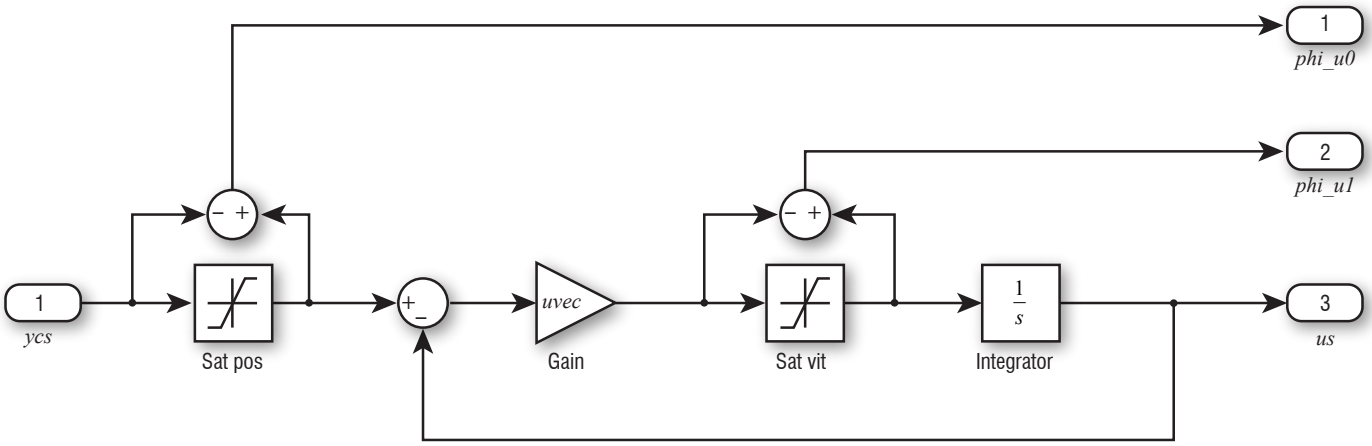

Figure 4 – Detailed view of the magnitude and rate limitation system

The main objective of this application is to design and evaluate anti-windup compensators to improve the aircraft response to roll angle solicitations while limiting oscillations despite actuator loss [18]. During such maneuvers, a significant control activity is observed on the ailerons. This is why the effects of saturations are modeled and taken into account for these actuators in the diagram of Figure 3, while no saturation is introduced on the rudders. The effects of saturations become even more penalizing in case of a partial loss of control capability. Assume indeed that the aircraft is controlled by a pair of ailerons on each wing, but that only one is operational. In that case, the activity of the remaining actuators is doubled, as well as the risk of magnitude and rate saturations. Then, the magnitude and rate limits in the following are halved. We consider $u_0 = L_m = 10$ deg (instead of 20 under normal conditions) and $u_1 = L_r = 20$ deg (instead of 40).

In the following, various cases studies are implemented and compared:

- Unsaturated – A non-saturated case where saturation elements are removed allows an ideal behavior of the closed-loop system to be exhibited;
- Saturated – A saturated case without compensation strategy is used as the nominal behavior of the closed-loop saturated system;
- Anti-PIO filter – The standard anti-PIO filter used in the industry is an "open-loop" solution that does not exploit the information relative to the saturation of the signal (see [7]). It may be considered as the basic solution from the industry. This strategy consists in adding a dynamical block with pre-saturation between the pilot gain (K_{pil}) and the control block. The full scheme is hidden in the block REFERENCE in Figure 3;
- Static AW_ϕ – A static version of our anti-windup strategy is designed with Algorithm 3.5. This strategy is an alternative to the standard anti-PIO filter, since it is very easy to implement (no additional dynamical system to introduce in the controller block);
- Dynamic AW_ϕ – A dynamic version of our anti-windup is designed with Algorithm 3.5. Various cases initializing the procedures with given matrices A_{aw} and C_{aw} are investigated;
- $\mathcal{H}_\infty AW_e$ – A dynamic anti-windup built using a structured $\mathcal{H}_\infty$ design method [18] is also implemented to compare dynamic anti-windup strategies. The advantage of such a strategy is that it circumvents some limitations of LMI-based strategies (limitation on the problem size when manipulating LMIs, conservatism of sufficient conditions), but to the detriment of ease of construction for engineers who are not always specialists in advanced control theories. Note that, unlike the approach addressed in this paper, the signal used as input for the anti-windup scheme is the difference between the output and the input of the nonlinear block (denoted by e).

In what follows, reduced size models are used for stability analysis and to compute the anti-windup controllers. Full size models of the aircraft and controllers are used for all of the simulations.

Design of a static anti-windup AW_ϕ

Let us first consider the design of a static AW_ϕ anti-windup where only matrices D_{aw}^i, $i = 0,1$ (see Equation (4)), have to be designed ($n_{aw} = 0$). The main advantage is that Condition (7) becomes linear and that the anti-windup block does not involve any additional dynamics. The optimization problem is solved by considering the bound on perturbation $\delta = 0.1$ and $v_1 = \left[C_p(4;:)\,0\right]$, corresponding to the roll angle, as the direction to be optimized over the set $E\left(Q^{-1},\delta\right)$. Algorithm 3.5, followed by Algorithm 3.4, provide the following optimal solution:

Static AW_ϕ design: $\gamma = 1.18110$; $\beta = 0.7808$

with the static anti-windup gains:

$$D_{aw}^0 = \begin{bmatrix} -14.7887 \\ 8.6544 \\ 0 \end{bmatrix} \quad D_{aw}^1 = \begin{bmatrix} -0.0042 \\ 0.0392 \\ 0 \end{bmatrix}$$

which shows that the anti-windup hardly uses the rate saturation information. Moreover, it is interesting to perform the same analysis for the saturated closed-loop system without anti-windup. The feasibility is also obtained and the solution is:

Analysis without anti-widup: $\gamma = 1.8560$; $\beta = 0.7796$

The solution with the static AW_ϕ anti-windup described through γ and β as performance indicators does not appear to be much better than the one without anti-windup: the anti-windup allows γ to be decreased and β to be increased, but only slightly. This does not reflect, however, the simulations described below, which show that the anti-windup action significantly improves the transient behavior of the roll angle, avoiding a large overshoot and degraded time evolution

with respect to the saturated case. The meaning of this is that the considered optimization criterion, which does not explicitly include the time response performance, does not exactly fit the analysis or design of the anti-windup loop. Nevertheless, considering criteria on time response performance is a difficult task and the optimization criterion used here gives a reasonable trade-off between stability guarantee, performance and time response.

Figures 5 and 6 illustrate the time evolution of the closed-loop system to a roll solicitation of 40 deg at time $t = 1$ s followed by a step of –60 deg at time $t = 15$ s and a step of +60 deg at time $t = 30$ s. The responses are compared by considering the case with saturation and no compensation (saturated), a standard anti-PIO strategy (anti-PIO filter) and the static AW_ϕ anti-windup strategy. It is important to underline that a simple static anti-windup strategy enables better performance than the standard anti-PIO case to be obtained, which adds dynamics to the system.

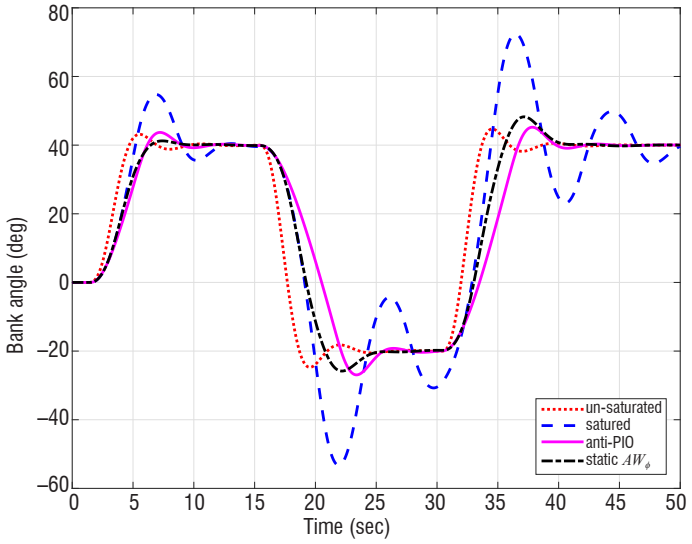

Figure 5 – roll solicitation of +40 deg at time $t = 1$ s followed by a step of –60 deg at time $t = 15$ s and a step of +60 deg at time $t = 30$ s: comparison of the performance output for the un-saturated, saturated (no compensation of the saturation), standard anti-PIO and static anti-windup AW_ϕ simulations

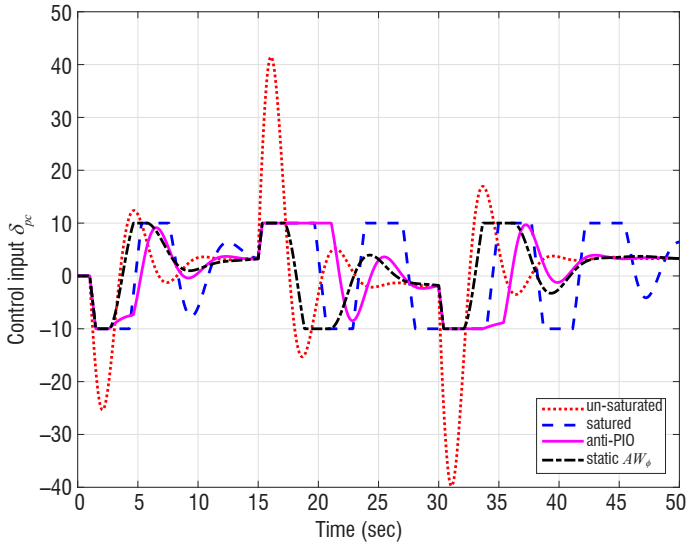

Figure 6 – roll solicitation of +40 deg at time $t = 1$ s followed by a step of –60 deg at time $t = 15$ s and a step of +60 deg at time $t = 30$ s: comparison of the saturating input for the un-saturated, saturated (no compensation of the saturation), standard anti-PIO and static anti-windup AW_ϕ simulations

Design of a dynamic anti-windup AW_ϕ

To go further, let us now consider the design of a dynamic anti-windup AW_ϕ. The difficulty in that case is to initialize the iterative procedure described in Algorithm 3.6, or to select matrices A_{aw} and C_{aw} used in Algorithm 3.5. As for the static case, the optimization problem is solved by considering the bound on perturbation $\delta = 0.1$ and $v_1 = \left[C_p(4;:)\ 0 \right]$ as the direction to be optimized over the set $\varepsilon(Q^{-1}, \delta)$.

Let us first consider a very simple structure to set matrices A_{aw} and C_{aw}, namely a modal structure for A_{aw} allowing its dynamics to be set slightly faster than those of the closed-loop linear system:

$$A_{aw} = \begin{bmatrix} -100 & 50 \\ -50 & -100 \end{bmatrix} \quad C_{aw} = \begin{bmatrix} -10 & 0 \\ 0 & 10 \\ 0 & 0 \end{bmatrix}$$

Algorithm 3.5 followed by Algorithm 3.4 provides the following optimal solution:

Dynamic AW_ϕ design 1: $\gamma = 1.7863$; $\beta = 0.8334$

with the anti-windup terms:

$$B_{aw}^0 = \begin{bmatrix} 9461.4 \\ -7872.5 \end{bmatrix} \quad B_{aw}^1 = \begin{bmatrix} 60.6 \\ -32.9 \end{bmatrix} \quad D_{aw}^0 = \begin{bmatrix} 438.2 \\ 1009 \\ 0 \end{bmatrix} \quad D_{aw}^1 = \begin{bmatrix} 3.5 \\ 5.1 \\ 0 \end{bmatrix}$$

Another option is to use matrices A_{aw} and C_{aw}, which are the solution to another dynamic anti-windup scheme implemented on the same application. The idea is to circumvent the nonlinear problem of the dynamic anti-windup by pre-selecting matrices A_{aw} and C_{aw} obtained from other approaches, when they exist, with the expectation of obtaining better results than with a "random" selection as done above. In the current case, we consider the solution obtained with a structured $\mathcal{H}_\infty$ design method [18], and previously applied on the same numerical evaluation [7]. In that case, Algorithm 3.5 gives matrices B_{aw}^i and D_{aw}^i, $i = 0,1$, (not provided here for readability reasons) and the following optimal solution:

Dynamical AW_ϕ design 2: $\gamma = 1.7395$; $\beta = 0.9147$

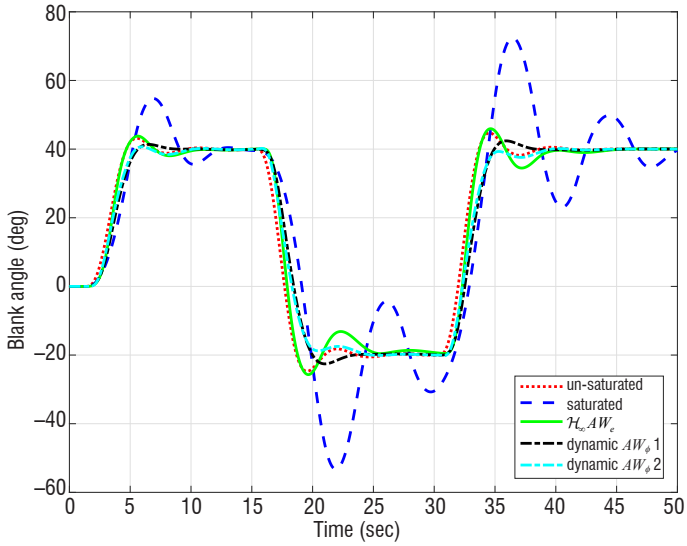

Figure 7 – roll solicitation of +40 deg at time $t = 1$ s followed by a step of –60 deg at time $t = 15$ s and a step of +60 deg at time $t = 30$ s: comparison of the performance outputs for the un-saturated, saturated (no compensation of the saturation), $\mathcal{H}_\infty AW_e$ anti-windup and designed anti-windup AW_ϕ cases

A roll solicitation of 40 deg at time $t = 1$ s followed by a step of –60 deg at time $t = 15$ s and a step of +60 deg at time $t = 30$ s is considered to compare the results. The time responses of the roll angle for the case without saturation, with the $\mathcal{H}_\infty AW_e$ anti-windup resulting from [7] and the designed dynamic AW_ϕ anti-windups are plotted in Figure 7. Similarly, the time evolutions of the control input δ_{pc} in these cases are depicted in Figure 8.

One can observe that the level of performance of the very well-tuned $\mathcal{H}_\infty AW_e$ anti-windup is slightly degraded in comparison with the two cases of AW_ϕ design, but it remains acceptable and close to the ideal response that would be obtained if no saturation was present in the actuator block. One can also remark that the dynamic anti-windup design makes it possible to speed-up the rising time (less than 6 seconds) toward the set-point, with respect to the static anti-windup design (more than 6 seconds), even with very basic anti-windup dynamics (AW_ϕ design 1).

Complementary illustrations

The rate-saturation effectiveness is illustrated in Figures 9 and 10, where the signals v and $\dot{x}_a$ are plotted, respectively, for the case with and without anti-windup. One can check that the anti-windup action both reduces the number of rate-saturation events and the amplitude of the signal v entering the saturation element (see Equation (3)).

Moreover, the stick response of the system, *i.e.*, the output of the pilot gain block, is plotted in Figure 11 to illustrate the efficiency of the anti-windup design. In this case, with a moderately aggressive pilot ($K_{pil} = 2$), one can check that the pilot workload increases in

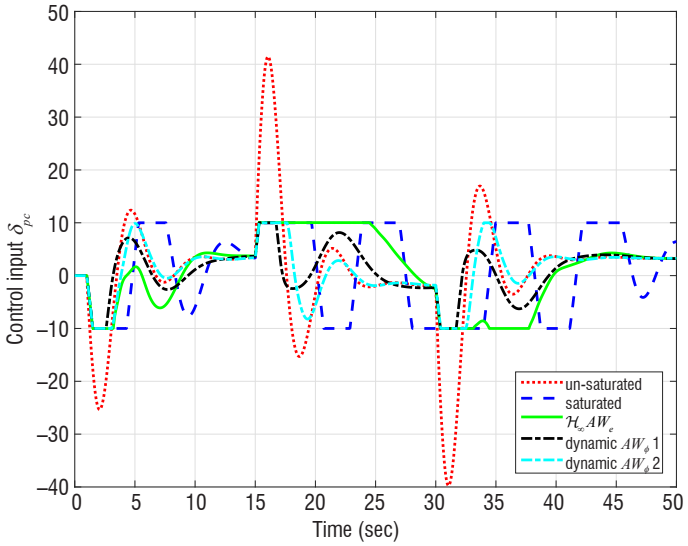

Figure 8 – roll solicitation of +40 deg at time $t = 1$ s followed by a step of –60 deg at time $t = 15$ s and a step of +60 deg at time $t = 30$ s: comparison of the saturating input for the un-saturated, saturated (no compensation of the saturation), $\mathcal{H}_\infty AW_e$ anti-windup and designed anti-windup AW_ϕ cases

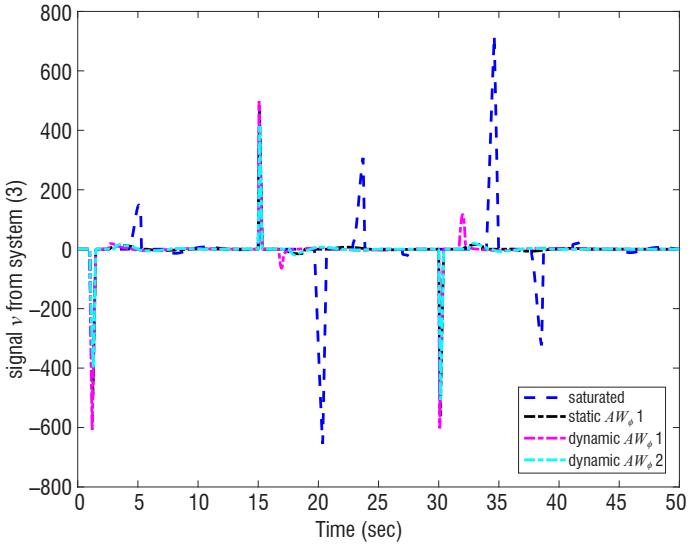

Figure 9 – roll solicitation of +40 deg at time $t = 1$ s followed by a step of –60 deg at time $t = 15$ s and a step of +60 deg at time $t = 30$ s: comparison of the signal v used in Equation (3) for the saturated (no compensation of the saturation) and designed static and anti-windup cases

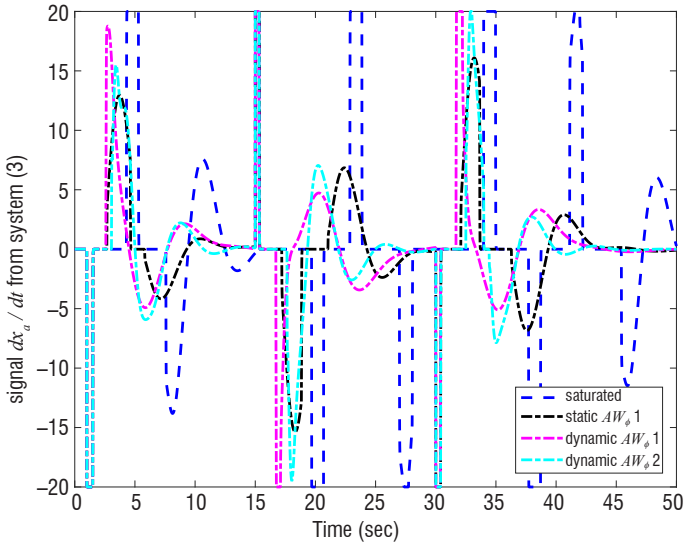

Figure 10 – roll solicitation of +40 deg at time $t = 1$ s followed by a step of –60 deg at time $t = 15$ s and a step of +60 deg at time $t = 30$ s: comparison of the signal $\dot{x}_a$ used in Equation (3) for the saturated (no compensation of the saturation) and designed static and anti-windup cases

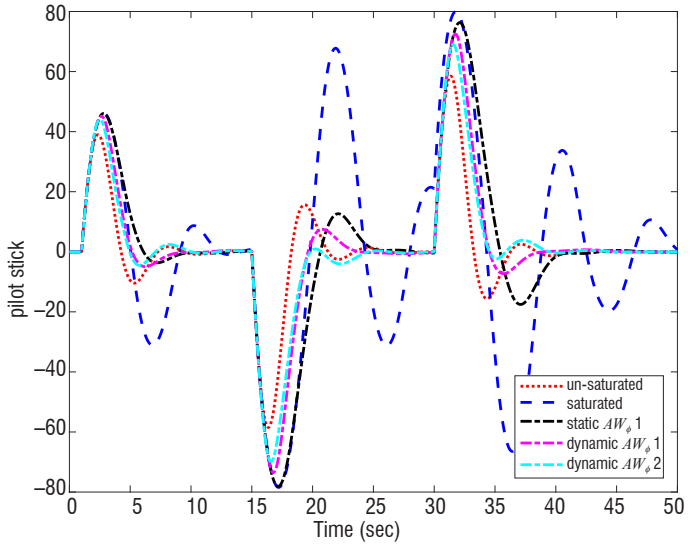

Figure 11 – roll solicitation of +40 deg at time $t = 1$ s followed by a step of –60 deg at time $t = 15$ s and a step of +60 deg at time $t = 30$ s: comparison of the pilot stick output for the un-saturated, saturated (no compensation of the saturation) and designed static and anti-windup cases

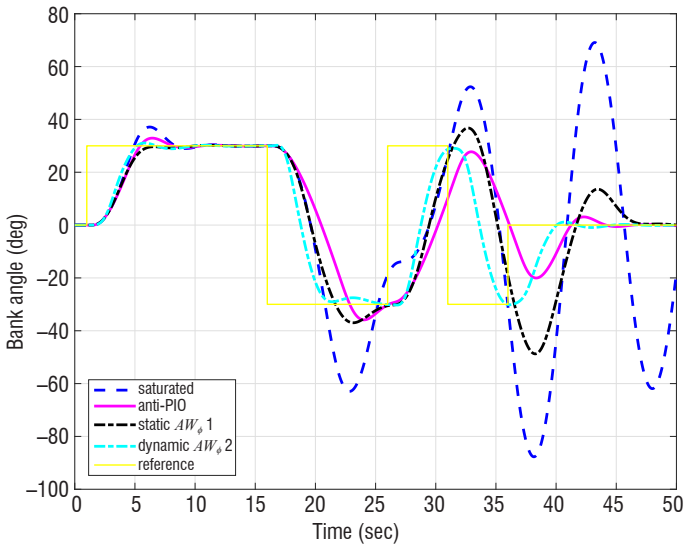

Figure 12 – roll solicitation with a 3211 type input of amplitude ± 30 deg with a $\Delta t = 5$ s: comparison between the performance outputs for the saturated (no compensation of the saturation), standard anti-PIO and designed static and anti-windup cases

the presence of saturation, and returns to the order of magnitude of the unsaturated case when anti-windup actions are present. Note also that when a more aggressive pilot is investigated (not shown here), with $K_{pil} = 3$, the saturated system becomes instable as soon as no anti-windup is present, but its stability is preserved in the presence of static or dynamic anti-windup actions.

Finally, the time evolution of the fourth bank-angle output (roll angle) in response to a 3211 type input is shown in Figure 12 for various configurations (with or without anti-windup). This type of input allows to effectively excite the aircraft modes of motion. The time unit Δt is set to 5 s to generate sufficient excitation in the aircraft modes of motion.

This illustrates the situation where strong excitation of the lateral aircraft modes of motion may result in the instability of the saturation response. Anti-PIO and anti-windup strategies allow stability to be preserved. Moreover, the dynamic anti-windup strategy enables a good tracking of the reference to be preserved, when the standard anti-PIO and the static anti-windup induce degraded responses with overshoot even if stable.

Conclusion

An anti-windup design strategy has been proposed for systems involving both magnitude and rate saturations, and taking into consideration that such saturations elements only affect some of the inputs. Such a situation is illustrated on a lateral flying model of a civil aircraft undergoing moderately aggressive maneuvering by the pilot. For this kind of systems, it is well known that magnitude and rate saturations of the aileron deflection actuator may lead to an undesirable behavior, often called Pilot-Induced-Oscillation (PIO). Anti-windup compensators have been designed through adequate convex optimization schemes, and a comparison with given dynamic anti-PIO filters already developed has also been provided. The numerical evaluation has made it possible to show, first, that a static strategy provides better results than classical anti-PIO filters basically used in industry. Moreover, the increase in the complexity of dynamic anti-windup compensators (both in terms of structure and computation) is compensated by the fact that they make it possible to recover behaviors very close to that which would be obtained if the actuators were linear. In any case, there is room for future work, such as the design of other anti-windup schemes, which may include the parameter-varying approach [21] or reset controllers [25]■

Acronyms

AW (Anti-Windup)
DLAW (Direct Linear Anti-Windup)
LMI (Linear Matrix Inequality)
MRAW (Model Recovery Anti-Windup)
PIO (Pilot-Induced-Oscillation)

References

[1] *Why the Gripen Crashed.* Aerospace America, 32(2):11, 1994.

[2] K. J. ÅSTRÖM, L. RUNDQWIST - *Integrator Windup and how to Avoid it.* American Control Conference, p. 1693-1698, Pittsburgh, PA, 1989.

[3] D.S. BERNSTEIN, A.N. MICHEL - *A Chronological Bibliography on Saturating Actuators.* International Journal of Robust and Nonlinear Control, 5:375-380, 1995.

[4] J-M. BIANNIC, L. BURLION, F. DEMOURANT, G. FERRERES, G. HARDIER, T. LOQUEN, C. ROOS - *SMAC: A Toolbox for Systems Modeling*. Analysis and Control with Matlab/Simulink. Available at: http://w3.onera.fr/smac, 2015.

[5] J-M BIANNIC, C. ROOS - *Introduction to AWAST : The Anti-Windup Analysis and Synthesis Toolbox.* IEEE CACSD Conference, San Antonio, TX, USA, September 2008.

[6] J-M. BIANNIC, S. TARBOURIECH - *Optimization and Implementation of Dynamic Anti-Windup Compensators in Aircraft Control Systems with Multiple Saturations.* Control Engineering Practice, 17(6):703-713, June 2009.

[7] J.-M. BIANNIC, S. TARBOURIECH - *Analyse et ajustement de lois de commande en présence de saturations implantation de filtres anti-PIO générés par synthèse anti-windup.* Technical report, Rapport COCKPIT/OCKF/CO1.1, 2011.

[8] O. BRIEGER, M. KERR, D. LEISSLING, I. POSTLETHWAITE, J. SOFRONY, M. C. TURNER - *Flight Testing of a Rate Saturation Compensation Scheme on the Attas Aircraft.* Aerospace Science and Technology, 13:92-104, 2009.

[9] O. BRIEGER, M. KERR, I. POSTLETHWAITE, M. C. TURNER, J. SOFRONY - *Pilot-Involved-Oscillation Suppression Using Low-Order Antiwindup: Flight-Test Evaluation.* AIAA Journal of Guidance, Control and Dynamics, 35(2):471-483, 2012.

[10] S. GALEANI, S. TARBOURIECH, M. C. TURNER, L. ZACCARIAN - *A Tutorial on Modern Anti-Windup Design.* European Journal of Control, 15(3-4):418-440, 2009.

[11] A. H. GLATTFELDER, W. SCHAUFELBERGER - *Control Systems with Input and Output Constraints.* Springer-Verlag, London, 2003.

[12] P. HIPPE - *Windup in Control. Its Effects and their Prevention.* AIC, Springer, Germany, 2006.

[13] T. HU, Z. LIN - *Control Systems with Actuator Saturation: Analysis and Design.* Birkhäuser, Boston, 2001.

[14] V. KAPILA, K. GRIGORIADIS (Eds.) - *Actuator Saturation Control.* Marcel Dekker, Inc., 2002.

[15] D. H. KLYDE, D. T. MCRUER, T. T. MYERS - *Pilot-Induced Oscillation Analysis and Prediction with Actuator Rate Limiting.* Journal of Guidance, Control and Dynamics, 20(1):81-89, 1997.

[16] B. S. LIEBST, M. J. CHAPA, D. B. LEGGETT - *Nonlinear Prefilter to Prevent Pilot-Induced Oscillations Due to Actuator Rate Limiting.* AIAA Journal of Guidance, Control and Dynamics, 25(4):740-747, 2002.

[17] J. LÖFBERG - *Yalmip - A Toolbox for Modeling and Optimization in Matlab.* Proceedings of the CACSD Conference, Taipei, Taiwan, 2004.

[18] G. PUYOU, J.-M. BIANNIC - *Application of Robust Antiwindup Design to the Longitudinal Aircraft Control to Cover Actuator Loss.* 19th IFAC Symposium on Automatic Control in Aerospace, University of Wurzburg, Germany, September 2013.

[19] I. QUEINNEC, S. TARBOURIECH - *SATAW-Tool - A Saturation Aware Toolbox.* Available at: http://homepages.laas.fr/queinnec/sataw-tool.html, 2012.

[20] I. QUEINNEC, S. TARBOURIECH, G. GARCIA - *Anti-Windup Design for Aircraft Control.* IEEE Conference on Control Applications (CCA), Munich, Germany, 2006.

[21] C. ROOS, J-M. BIANNIC, S. TARBOURIECH, C. PRIEUR, M. JEANNEAU - *On-Ground Aircraft Control Design Using a Parameter-Varying Anti-Windup Approach.* Aerospace Science and Technology, 14(7):459-471, 2010.

[22] L. RUNDQUIST, K. STAHL-GUNNARSSON - *Phase Compensation of Rate-Limiters in Unstable Aircraft.* IEEE Conference on Control Applications, 1996.

[23] H. J. SUSSMANN, E. D. SONTAG, Y. YANG - *A General Result on the Stabilization of Linear Systems Using Bounded Controls.* IEEE Transactions on Automatic Control, 39(12):2411-2425, 1994.

[24] S. TARBOURIECH, G. GARCIA, J. M. GOMES DA SILVA JR., I. QUEINNEC - *Stability and Stabilization of Linear Systems with Saturating Actuators.* Springer, 2011.

[25] S. TARBOURIECH, T. LOQUEN, C. PRIEUR - *Anti-Windup Strategy for Reset Control Systems.* International Journal of Robust and Nonlinear Control, 21(10):1159-1177, 2011.

[26] S. TARBOURIECH, I. QUEINNEC, J.-M. BIANNIC, C. PRIEUR - *Pilot-Induced-Oscillations Alleviation through Anti-Windup Based Approach,* volume VOL TITLE, G. Fasano and J. D. Pinter (eds). Springer, 2016.

[27] S. TARBOURIECH, I. QUEINNEC, M. C. TURNER - *Anti-Windup Design with Rate and Magnitude Actuator and Sensor Saturations.* European Control Conference, Budapest, Hungary, 2009.

[28] S. TARBOURIECH, M. C. TURNER - *Anti-Windup Design: an Overview of Some Recent Advances and Open Problems.* IET Control Theory and Application, 3(1):1-19, 2009.

[29] A. R. TEEL - *Global Stabilization and Restricted Tracking for Multiple Integrators with Bounded Controls.* Systems Control Lett, 18(3):165-171, 1992.

[30] M. C. TURNER, L. ZACCARIAN (Editors) - *Special Issue: Anti-Windup.* International Journal of Systems Science, 37(2):65-139, 2006.

[31] L. ZACCARIAN, A. R. TEEL - *Modern Anti-Windup Synthesis.* Princeton University Press, 2011.

Isabelle Queinnec is currently CNRS researcher at LAAS-CNRS, Toulouse University. She received her PhD degree and HDR degree in automatic control in 1990 and 2000, respectively, from University Paul Sabatier, Toulouse. Her current research interests include constrained control and robust control of processes with limited information, with particular interest in applications on aeronautical systems, robotic, electronic, biochemical and environmental processes. She has been serving as member of the IFAC technical committees on "Biosystems and Bioprocesses" and on "Modelling and Control of Environmental Systems", respectively from 2002 and 2005 and of the IEEE CSS-CEB from 2013. She is currently AE for IET Control Theory and Applications and for the IFAC Journal NAHS (Nonlinear Analysis: Hybrid systems). She is co-author of a book on saturated systems and of more than 50 journal papers, both in control theory and in process engineering.

Sophie Tarbouriech received the PhD degree in Control Theory in 1991 and the HDR degree (*Habilitation à Diriger des Recherches*) in 1998 from University Paul Sabatier, Toulouse, France. Currently, she is full-time researcher (*Directeur de Recherche*) in LAAS-CNRS, Toulouse. Her main research interests include analysis and control of linear and nonlinear systems with constraints (limited information), hybrid dynamical systems. She is currently Associate Editor for IEEE Transactions on Automatic Control, IEEE Transactions on Control Systems Technology, Automatica and European Journal of Control. She is also in the Editorial Board of International Journal of Robust and Nonlinear Control. She is also co-Editor-in-Chief of the French journal JESA (*Journal Européen des Systèmes Automatisés*). Since January 2017, she is Senior Editor of the journal IEEE Control Systems Letters. Since 1999, she is Associate Editor at the Conference Editorial Board of the IEEE Control Systems Society. She is a member of the IFAC Technical Committees on Robust Control and Nonlinear Systems. She is also member of the IEEE Technical Committee on Hybrid Systems.

Jean-Marc Biannic graduated from SUPAERO Engineering School in 1992 and received the PhD degree in Robust Control Theory with the highest honors in 1996 from SUPAERO as well. He joined ONERA as a research scientist in 1997 and received the HDR degree (French habilitation as PhD supervisor) from Paul Sabatier's University of Toulouse in 2010. Jean-Marc Biannic has supervised 6 PhD students. He is the author or co-author of 20 journal papers, beyond 50 conference papers, many book chapters, teaching documents, a tutorial book on multivariable control and Matlab toolboxes. He received in 2011 the second research distinction grade(MR2) from ONERA and the "ERE" distinction from ISAE (Aeronautics and Space Institute) thanks to which he is recognized as a full-professor in PhD committees. Jean-Marc Biannic has participated to several European projects and Garteur Groups (on PIO and nonlinear control). From 2012 to 2016, he has led a research project involving 10 research scientists for the development of the SMAC toolbox (w3.onera.fr/smac) for systems modeling, analysis and control.

Christophe Prieur was born in Essey-les-Nancy, France, in 1974. He graduated in Mathematics from the Ecole Normale Supérieure de Cachan, France in 2000. He received the Ph.D degree in 2001 in Applied Mathematics from the Université Paris-Sud, France, and the "*Habilitation à Diriger des Recherches*" (HDR degree) in 2009. From 2002 he was an associate researcher CNRS at the laboratory SATIE, Cachan, France, and at the LAAS, Toulouse, France (2004-2010). In 2010 he joined the Gipsa-lab, Grenoble, France where he is currently a senior researcher of the CNRS (since 2011). His current research interests include nonlinear control theory, hybrid systems, and control of partial differential equations. He was the Program Chair of the 9th IFAC Symposium on Nonlinear Control Systems (NOLCOS 2013) and of the 14th European Control Conference (ECC 2015). He has been a member of the IEEE-CSS Conference Editorial Board and an associate editor for IMA J. Mathematical Control and Information. He is currently a member of the EUCA-CEB, an associate editor for the IEEE Trans. on Automatic Control, European J. of Control, and IEEE Trans. on Control Systems Technology, and a senior editor for the IEEE Control Systems Letters.

M. Ganet-Schoeller
(Ariane Group)

J. Desmariaux
(CNES)

C. Combier
(ISAE)

E-mail: martine.ganet@airbusafran-launchers.com

DOI: 10.12762/2017.AL13-08

Structured Control for Future European Launchers

Control of a flexible launcher during the atmospheric flight phase is a highly challenging control problem involving multiple and concurrent design requirements: stability (stabilization of unstable rigid dynamics, sloshing modes and flexible structural modes), performance (guidance tracking, structural load minimization) and robustness (physical parameter uncertainties and accommodation to multiple vehicle configurations) on a non-stationary system. This paper focuses on co-funded AG/CNES research activities on the development of an advanced modular control strategy using recent advances in structured control design. We demonstrate here that structured H_∞ synthesis could give a gain scheduling solution to full time-varying flexible launcher control problems during the non-stationary ascent phase, enabling load performance improvement between complex sets of requirements, and, design cost improvements through simplification of the tuning process. We also present a generic framework for rapid control design that is now applicable both for European launcher families already in activity (with existing S/W and fixed controller structure) and for future expendable and reusable launchers.

Introduction

Ariane Group (AG) and the CNES (French Space Agency) aim to safeguard the exceptional quality and reliability of Ariane 5, while developing a family of next-generation rocket launchers designed to consolidate Europe's leadership in the space industry. In this frame, this paper focuses on co-funded AG/CNES R&D activities for developing *launcher advanced control strategies* applicable both for launchers already in activity (with existing S/W and fixed controller structure) and for future expendable and reusable launchers. Motivation for this research is twofold: improve performance and reduce development cost focusing on modularity and accommodation to multiple vehicle configurations.

Conventional launcher control design during the ascent phase is a challenging robust control problem. Key challenges to be tackled to ensure performance and robustness are:

- aerodynamic instability during atmospheric flight, which represents a high level of risk [1],
- presence of multiple badly damped bending and sloshing modes,
- disturbances from the external environment (mainly wind turbulences),
- non-linearity of sensors and actuators (delays, noises, limited control authority, etc.),
- uncertainties and dispersions on all physical parameters that characterize launcher dynamics, actuators and sensors,
- mission dependency of all the parameters; e.g., launcher characteristics such as MCI and bending modes depend on the payload,
- varying launcher characteristics throughout the flight (mass, thrust, aerodynamics, bending modes, etc.), as well as varying objectives (perturbations attenuation, consumption, accuracy, etc.) and constraints (loads, actuator limitations).

Therefore, to improve launcher performance, a first research direction is to improve model knowledge and accuracy, which is usually done on operational launchers using post flight analysis as per ARIANE or VEGA. Another research direction is to use recent developments in robust control methods. Indeed, during the two last decades, Europe has been successfully working on robust control techniques, such as Ariane 5 LQG and H_∞ control, the VEGA robust modal control, adaptive control, optimization methods, or LPV control. Research and applications were also performed all over the world. Complementary results on adaptive control and optimization methods for flexible launcher control of the Ares launch vehicle could be found in the literature. All of these design methods were successfully tested

and presented at various AIAA, IFAC, ESA or EUCASS conferences. However, despite their satisfying performances, their implementation could be complex due to the high order of the synthesized controllers required to ensure the desired dynamics and performance.

It was not until recently that structured control developments opened new perspectives for control design: by combining *robust control with controller structure requirements*, it is now possible to directly synthesize a low-order controller or fixed-structure controller. This problem is often that of a non-convex and typically non-smooth (non-differentiable) optimization [2, 3]. Recent research has led to the development of new powerful tools, such as structured synthesis `hinfstruct` *[3]* and `systune` [4,10], available in the Matlab Robust Control Toolbox (RCT) [15].

The purposes of this paper are, on the one hand, to demonstrate that structured H_∞ synthesis could solve full time-varying flexible launcher control problems, enabling performance and cost improvement and, on the other hand, to present the resulting generic framework for rapid launcher control design. This framework was developed on a representative benchmark before being used both for the improvement of existing launcher control laws and for future launcher pre-development phases.

This paper is organized as follows: in Section 3 we give an overview of the launcher control problem, then in Section 4 H_∞ and structured H_∞ theory are recalled, focusing on their respective advantages and drawbacks for launcher control. A generic framework for rapid launcher control design is presented in Section 5. Sections 6 and 7 gather results from various applications.

Launcher control

Launcher control overview

The automatic control of a launcher is one of the four main functions of the overall flight-control system, which also encompasses redundancy, navigation and guidance functions. Since the roll, pitch and yaw axes are weakly coupled, the control design is based on the assumption that each axis can be controlled independently of the other two. *A-posteriori* verifications of global performance and stability are, of course, performed. An example of a 1-axis control loop for atmospheric flight is depicted for illustration in Figure 1.

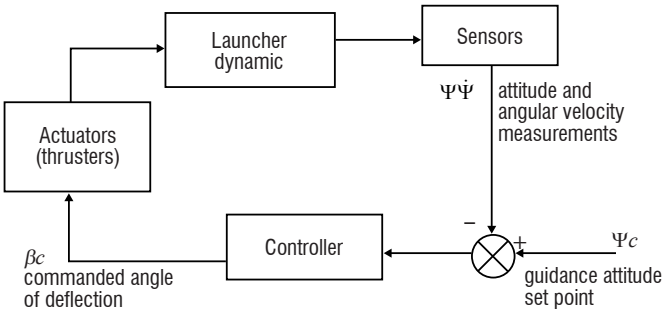

Figure 1 – Flight control loop (one axis)

In this figure, corresponding to the launcher benchmark, inputs for the controller are the angular and angular rate measurements (additional acceleration measurement could also be used as proposed in [5]). The controller outputs a commanded thrust deflection angle. As far as the control function is concerned, the atmospheric phase (flight from lift-off to the jettisoning of the solid propellant boosters) is the most critical one. During this phase, the control requirements are, by decreasing order of importance:

- to ensure the stability of the launcher rigid, bending and propellant sloshing modes, with sufficient stability margins,
- to compensate for external (wind, wind gusts) and internal (thrust misalignment, static error of the servo-actuators, thrust asymmetry) disturbances, while minimizing angle-of-attack, for structural sizing reasons,
- to follow the guidance orders (attitude set points), by ensuring a static error and a response time compatible with guidance requirements,
- to minimize the cumulated commanded thrust deflections (hereafter called consumption), since the hydraulic activation devices use a blow-down system.

All of the uncertainties and dispersions associated with launcher and trajectory parameters (mass, inertia, location of the center of gravity, bending and sloshing modes, propulsion and aerodynamic characteristics, etc.) must be taken into account for the tuning of the control law. All of these parameters also fluctuate during the flight, which makes the control problem essentially non-stationary (time-variant).

The control function must therefore simultaneously fulfill:

- *Performance requirements:*
  the control law must ensure the required launcher flight behavior, while compensating for the various disturbances.

- *Robustness requirements:*
  this behavior must be preserved regardless of the internal and external fluctuations that may adversely affect the vehicle during the flight.

The main issues of launcher control lies in the trade-off between these two sets of requirements that are essentially contradictory, since an ill-known system cannot be controlled in a highly efficient way.

Launcher applications

The generic framework for rapid launcher control design was developed on a representative benchmark before being applied to the European launcher control design. This benchmark that can now be used, on request, for internal and external research studies on control design and validation, is presented here. European launcher models and data are not presented here for industrial confidentiality reasons; however, for the development of the generic framework, their main added value concerns the fixed discrete time controller structure, as well as the number and type of actuators and sensors.

Launcher benchmark models

This benchmark deals with pitch control of a symmetric launcher during the atmospheric flight phase from take-off to tail-off. Launcher dynamic equations are linearized around reference trajectory in the body frame

(Figure 2), leading to a state space representation in continuous time defined by Equation (1). Launcher benchmark dynamics contain:

- rigid mode dynamics defined by a bi-dimensional linear perturbation model already described in detail in the literature [6],
- bending modes represented by a second-order model with low damping,
- an actuator model described by a second-order transfer function,
- sensor delays (IMU and gyrometer) that are directly included during discretization of continuous time launcher models.

$$\begin{cases} \dfrac{d}{dt}X = AX + BU \\ Y = CX \end{cases} \quad (1)$$

With

$$X = \begin{pmatrix} \Delta\dot{\theta} \\ \Delta\theta \\ \Delta\dot{z} \\ \Delta\dot{\beta}_R \\ \Delta\beta_R \\ \dot{q}_i \\ q_i \end{pmatrix} \quad U = \begin{pmatrix} \Delta\beta_c \\ \Delta W \end{pmatrix} \quad Y = \begin{bmatrix} \Delta\theta_m \\ \Delta\dot{\theta}_m \end{bmatrix}$$

$$A = \begin{pmatrix} 0 & A_6 & A_3 & 0 & K_1 & 0 & 0 \\ 1 & 0 & 0 & 0 & 0 & 0 & 0 \\ 0 & A_1 & A_2 & 0 & K_2 & 0 & 0 \\ 0 & 0 & 0 & -2\xi_\beta\omega_\beta & -\omega_\beta^2 & 0 & 0 \\ 0 & 0 & 0 & 1 & 0 & 0 & 0 \\ 0 & 0 & 0 & -2\xi_\beta\omega_\beta Mb_i & -\omega_\beta^2 Mb_i - P_c htu_i & -2\xi_i\omega_i & -\omega_i^2 \\ 0 & 0 & 0 & 0 & 0 & 1 & 0 \end{pmatrix}$$

$$B = \begin{pmatrix} 0 & B_1 \\ 0 & 0 \\ 0 & B_2 \\ \omega_\beta^2 & 0 \\ 0 & 0 \\ \omega_\beta^2 Mb_i & 0 \\ 0 & 0 \end{pmatrix} \quad C = \begin{pmatrix} 0 & 1 & 0 & 0 & 0 & 0 & -hp_{IMUi} \\ 1 & 0 & 0 & 0 & 0 & -hp_{GYi} & 0 \end{pmatrix}$$

Where $\begin{cases} A_1 = -\dfrac{P_C}{m} + (T - D) \\ A_2 = -\dfrac{D}{V_R} \\ A_3 = \dfrac{A_6}{V_R} \\ A_6 = \dfrac{mDL_F}{I} \end{cases}$ and $\begin{cases} K_1 = \dfrac{P_C l_{tu}}{I} \\ K_2 = -\dfrac{P_C}{m} \\ B_1 = -\dfrac{A_6}{V_R} \\ B_2 = -A_2 \end{cases}$

All rigid and bending mode coefficients of Equation (1) are *time-varying* along a given trajectory; they are also subject to *uncertainties* leading to more than 20 uncertain parameters. Finally, *three payload* configurations are considered (1000 kg, 2000 kg and 6000 kg).), with their associated impact on rigid and flexible mode characteristics. For each payload, a *Model DataBase (MDB)* covering the worst uncertain cases is included in the benchmark.

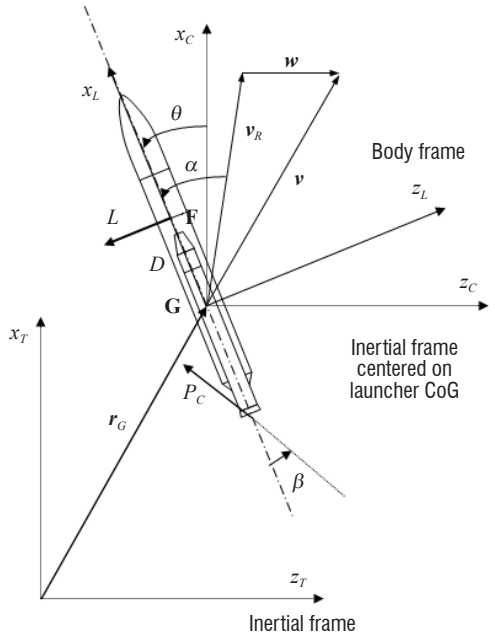

Figure 2. Launcher reference frames

Launcher control objectives and validation means

Stability requirements

Stability margins shall be computed using the Nichols or Bode diagrams *in discrete time*. The stability margin requirements shall be respected for the entire set of pre-defined *worst cases* located on the bounds of the uncertainty domain, as described in the user manual, for all instants and for all payload configurations.

	Stability margins
LF open-loop gain margin	1 dB
HF open-loop gain margin	3 dB
Phase margin	-
Delay margin	50 ms
Bending mode delay margin	50 ms
Bending mode gain margin	Overshoot < -6 dB

Table 1 – Stability margin requirements Performance requirements

The control function shall guarantee the following stability margins (with equipment characteristics) on the SISO system.

Performance requirements

All of the *time domain requirements* shall be respected for the time varying launcher, in the *nominal case*, for the whole set of payload configuration and for 4 different wind profiles. This validation shall be done using the Simulink models delivered with the benchmark.

Disturbance rejection

Disturbance rejection need is mainly linked to atmospheric wind disturbance impact on angle of attack, and to the measurement noise impact on cumulated deflection.

- The control function shall maintain the induced aerodynamic angle of attack compatible with general load specification $Q\alpha < 150$ kPadeg.

- Thruster misalignment impact on load shall not exceed 10% of the specification.
- Cumulated deflection shall remain lower than 200° during the 100s of the flight phase.

Guidance tracking constraints

In the steady state, under nominal conditions, the control function shall be able to control the attitude with the following accuracy:

- attitude ≤ 2° (compromise with $Q\alpha$ minimization),
- attitude rate ≤ 1°/s during thrust steady state and 0.5°/s at the end of tail off.

Technical constraints

The controller shall be implemented in discrete time with a sampling frequency of 20 Hz.

Actuator constraints:

- maximal deflection angle ≤ 6°,
- maximal deflection rate ≤ 15°/s.

Reference H_∞ controller

In this benchmark, we have defined a non-structured gain scheduled H_∞ control law that will serve as a reference. This reference controller was fully validated and respects all stability and performance objectives; even if a small margin is left for optimization.

H_∞ and structured H_∞ synthesis – theory and analysis

In this section, we give an overview of (non-structured) H_∞ theory and structured H_∞ theory focusing on their respective advantages and drawbacks for launcher control application.

H_∞ synthesis

H_∞ synthesis was developed in the eighties [7]. It is based on the use of the H_∞ norm, which measures the maximum amplification that a system can apply to any input signal. For SISO systems, this norm is equivalent to the peak gain value. H_∞ synthesis is a frequency domain robust control method applicable for MIMO, LTI, causal and proper systems, that guarantees nominal stability, nominal performance and robust stability. H_∞ synthesis uses the standard form of Figure 3.

Where $P(s)$ is the system model augmented by objective-linked weighting functions, $C(s)$ is the controller; u is the command vector, y is the measurement vector, $w=[w_1, w_2, ..., w_N]^T$ is the disturbance vector and $z=[z_1, z_2, ..., z_M]^T$ is the error vector that will be minimized.

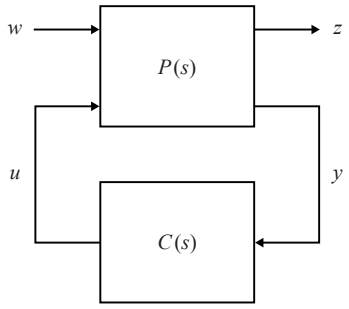

Figure 3 – H_∞ standard form

H_∞ synthesis sub-optimal problem is to find a controller C (or K) that internally stabilizes the augmented system P and such that:

$$\left\| \frac{z}{w} \right\|_\infty < \gamma \qquad (2)$$

Many solutions exist for this synthesis, which can be transformed into a convex problem by means of additional variables, through γ-iteration in continuous time [7] or in discrete time [8], or, LMI approaches [9]

Numerous examples using H_∞ controllers are described in the literature and those controllers are currently used in industry. With regard to launcher control, H_∞ synthesis was successfully developed and implemented on Ariane 5 following a test flight in 2001. During this development, performance gain and development cost reduction were demonstrated through H_∞ synthesis roll-off effect and frequency domain compromise between objectives; however, some drawbacks were identified:

- The H_∞ controller order is equal to the augmented system order; therefore, it directly increases with the level of representativeness of the model and with the number of objectives. Thus, for the Ariane 5 application, design choices were limited to avoid controller post-reduction.

- Minimizing the whole transfer matrix including non-diagonal terms could induce conservatism and tuning difficulties when considering multiple objectives, which was the case for Ariane 5 control.

Non-smooth optimization and structured H_∞ synthesis

Structured H_∞ synthesis uses non-smooth optimization techniques to locally solve H_∞ synthesis problems under additional structural constraints on the controller. Structured H_∞ uses the standard form described in Figure 4. This form is similar to the non-structured H_∞ form, except that the transfer functions are decoupled.

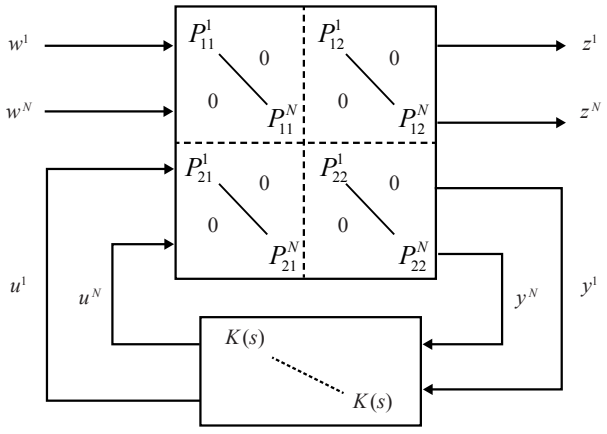

Figure 4 – Structured H_∞ standard form

Structured H_∞ synthesis consists in finding an internally stabilizing controller such that:

$$\exists\ K : \min \left\| \begin{bmatrix} F_l(P,K)_{11} & 0 & \dots & 0 \\ 0 & F_l(P,K)_{22} & \dots & 0 \\ \dots & \dots & \dots & \dots \\ \dots & \dots & \dots & \dots \\ 0 & 0 & \dots & F_l(P,K)_{NN} \end{bmatrix} \right\|_\infty \quad (3)$$

$$\Leftrightarrow \min_{x \in \Re^k} \max\left(\left\| F_l(P,K)_{11} \right\|_\infty, \left\| F_l(P,K)_{22} \right\|_\infty, \dots, \left\| F_l(P,K)_{NN} \right\|_\infty \right)$$

Where K is the structured controller and the vector x contains all tunable elements of K.

The problem described above is usually that of a non-convex and non-differentiable optimization. It was not until recently that algorithms and solvers for this type of problem began to appear [2, 3]. To date, as far as we know, there are two MATLAB® packages that are capable of addressing this problem via non-smooth optimization: the *HIFOO* packages [2] and the RCT packages `hinfstruct` *[3] and* `systune` [4,10]. In this paper, we will expand work processed with `hinfstruct` in [11] and tackle the launcher control problem with `systune` [4].

Structured H_∞ Advantages and Drawbacks for launcher control

For launcher applications, fixed-order controllers using non-smooth H_∞ algorithms solve most of the drawbacks of H_∞ synthesis. Indeed, its main advantages are:

- use of a *reduced-order fixed-structure* control law,
- *direct quantification* of stability and performance requirements in simple weighting functions, thanks to multi-model approaches and frequency domain limitations, with loop shaping and/or sensitivity function criteria,
- use of Soft/Hard constraints, enabling the automatic minimization of structural loads and consumption.

The disadvantages of fixed-order H_∞ synthesis methods for launcher applications are fading with recent developments and applications.

- One remaining drawback for non-stationary launcher control design is that, today, to our knowledge, *no LPV design* for a fixed-structure controller is sufficiently mature. An alternative is the use of gain surfaces, developed and applied in [12], or, applied in [13]; however, this approach could lead both to an increasing number of controller parameters and to some conservatism linked to gain surface selection. Additional developments in this field would be of great interest. However, in practice, we will show in this paper that, with an adequate initialization process and additional constraints on the controller pole and zero characteristics, the *gain scheduling* approach traditionally used for non-structured H_∞ launcher control is also well suited for structured control design.

- *Local optimization:* non-smooth optimization algorithms are only local algorithms and there is no guarantee of convergence towards a global optimum. *Non-repeatability* can be an issue for industrial implementations of gain scheduling control. This drawback was softened by considering additional constraints for gain scheduling control design. This last point is the only one that still requires attention from an industrial point of view.

Control design framework

The generic framework for control design was developed on the launcher benchmark; it contains both specific functions depending on launcher application, with dedicated interfaces with launcher data, modeling and validation tools, and generic functions for controller design unrelated to launcher applications. Its architecture is described in Figure 5, and the main functions are detailed in this section.

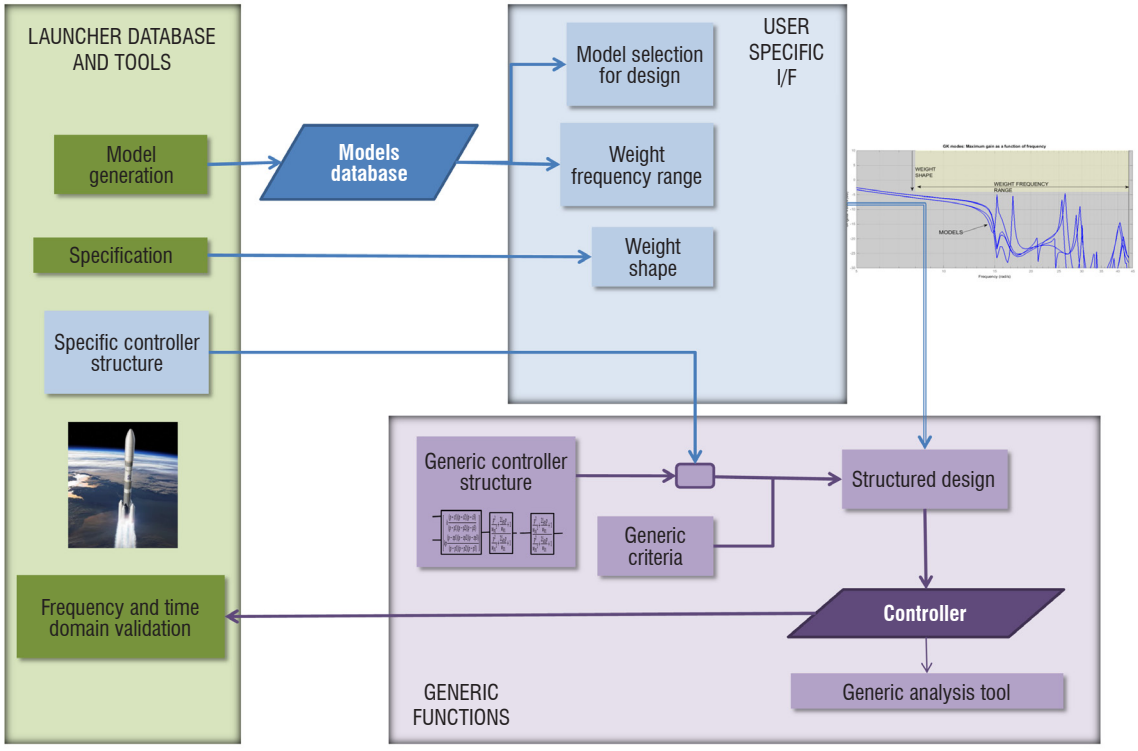

Figure 5 – Control Design Framework

Model generation and selection

A complete launcher Model DataBase (MDB) is generated covering rigid and flexible mode dynamics, nominal and uncertain cases, in continuous time and/or discrete time representations. Then, for each requirement, a single model or multiple models are selected for control design, e.g., worst uncertain case for the Low Frequency (LF) stability margin requirement, worst uncertain case for High Frequency (HF) stability margin requirement, etc.). These models also serve for frequency range definition of weighting functions, as described in the objective transcription.

Controller structure

The controller structure can be specific, or the user can select the default structure defined in [11] for the launcher benchmark. In this case, a MISO structured controller is selected that makes use of both the attitude and angular rate measurements to compute the commanded thruster deflection. Controller structure is separated into a so-called "rigid mode controller" for low-frequency rigid-dynamics control and a "bending mode filter" for high-frequency command filtering.

The generic controller structure contains:

- for rigid mode control, a reduced order controller with constraints on the pole and zero characteristics to avoid interpolation issues,
- for bending mode filtering, a reduced order filter, for which the range of variation of the poles and zeros is limited to enable gain scheduling and to avoid filtering overshoots.

Objective transcription

Problem definition and tuning of robust flexible launcher control design are greatly simplified thanks to the use of structured design: each objective is associated with a generic criterion (transfer function independent from the launcher model) and with mission data (models, frequency range or numerical objective value).

Structured H_∞ design generic criteria

All of the control stability, robustness and performance objectives were translated into *generic criteria* within the `systune` [4, 10] function framework. In this approach, both traditional H_∞ techniques and loop shaping were used, combined with multi-model design and frequency-limited requirements. The traditional approach [14] uses a closed loop sensitivity function S, KS, KG or T described in Figure 6, while loop shaping uses an open-loop transfer function K or KG. Generic criteria used for launcher control design are gathered in Table 1.

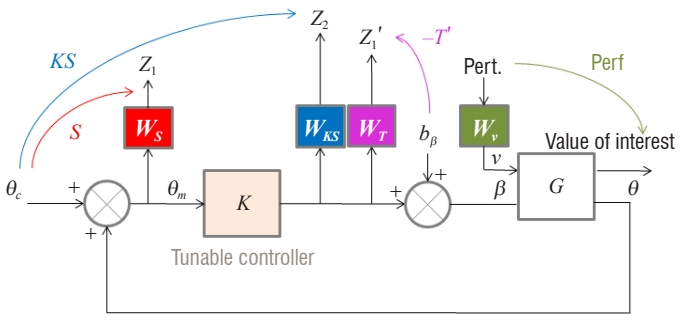

Figure 6 – Closed loop sensitivity functions

Mission data

For each of these generic criteria, a user I/F enables the selection of the following:

- worst case models in launcher MDB,
- the frequency range, determined by model analysis; e.g., the bending mode control objective is applicable for the bending mode frequency range over the launcher configurations,
- once the frequency range has been selected, launcher control requirements (or mission specification) are directly used for weighting function shape definition.

For each objective, Table 2 gathers the constrained sensitivity function used in the classical robust control approach and models that could be used for design.

Objective	Models (MDB)	Sensitivity function or transfer function
LF Margin	Worst Case 1	*S*
HF Margin	Worst Case 2	*S*
Bending mode passive stabilization (gain control)	N uncertain models / Mission-dependent	*KG*
Bending mode active stabilization (phase control)	N uncertain models / Mission-dependent	*T*
Consumption and filtering authority	NA	*K*

Table 2 – Structured H_∞ criterion, models and sensitivity functions

Controller synthesis

Depending on the sampling frequency, it could be advisable to perform the launcher control design in discrete time. Therefore, the use of both continuous and discrete time versions of the `systune` [4, 10] function was validated during the development of this framework.

Gain scheduling was applied using the following process:

- Structured control design for one reference flight point (instant of maximum dynamic pressure).
- We use an automatic load minimization criterion with guarantee of compliance of all other requirements (directly for stability margins and frequency domain requirement / indirectly for time domain requirements); therefore, *reducing the cost of iterative design.*
- Ascent front synthesis with reasonable time interval from the reference flight point until the end of the flight, with initialization using the controller from the previous instant.
- Descent front synthesis with reasonable time interval from the reference flight point down to the beginning of the flight, with initialization using the controller from the next instant.

Then, the set of structured controllers are linearly interpolated along the flight.

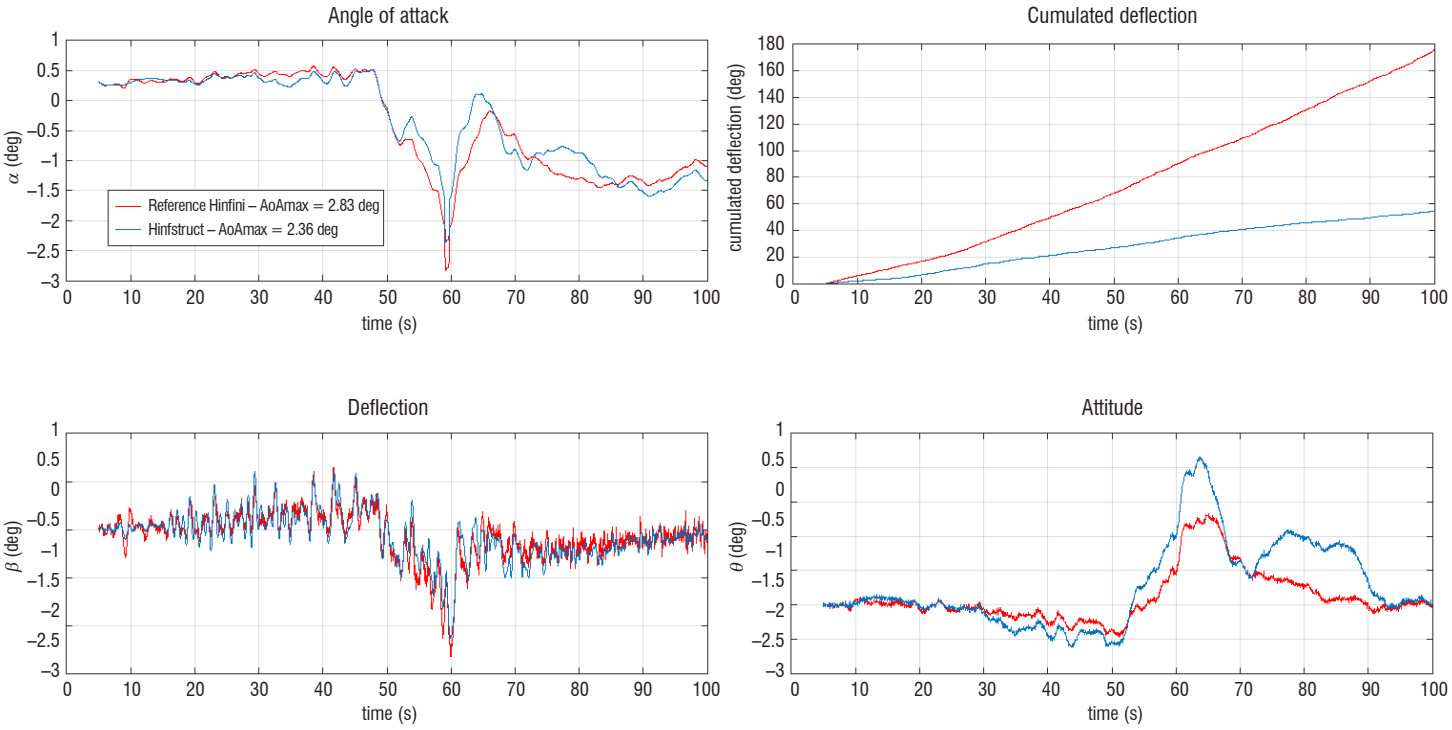

Figure 7 – Simulation results for the reference controller and gain-scheduled structured controller

We have included slight evolutions in the weighting functions and requirements along the trajectory, in order to take into account the objective variation during the flight.

Analysis

A set of generic analysis functions are associated with control design tools for fast validation on control design models. Complete validation is then performed on full MDB with industrial validation tools.

Feasibility demonstration – benchmark application

In this section, structured H_∞ control design feasibility is demonstrated on the launcher benchmark. A summary of structured H_∞ results obtained for the entire flight phase and for the three payload cases is presented and compared with the reference non-structured H_∞ controller. These results were extended to other applications in Section 7, thereby validating the genericity of the control design framework on different launcher configurations. These results also illustrate the advantages of structured design for rapid controllability and control design.

One can see, in the simulation results of Figure 7 that the gain scheduling process, using gain scheduled weighting functions, is quite efficient, without presenting interpolation issues.

All stability requirements, both for rigid dynamics and bending modes, are respected (Figure 8), as well as all performance requirements (Figure 9). In this last figure, performance of the reference non-structured controller is also plotted, highlighting loads and consumption improvements. Indeed, the gain-scheduled structured controller design leads to a reduction in the loads of about 5 to 15%, depending on wind disturbance, and a consumption reduction of about 60% with respect to the reference controller.

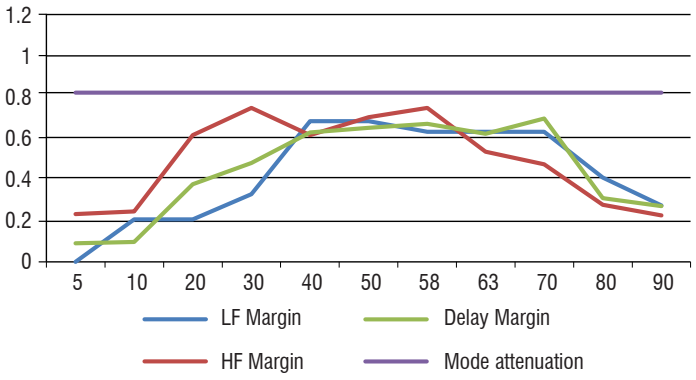

Figure 8 – Gain-scheduled structured controller - Normalized stability margins (with respect to the requirement)

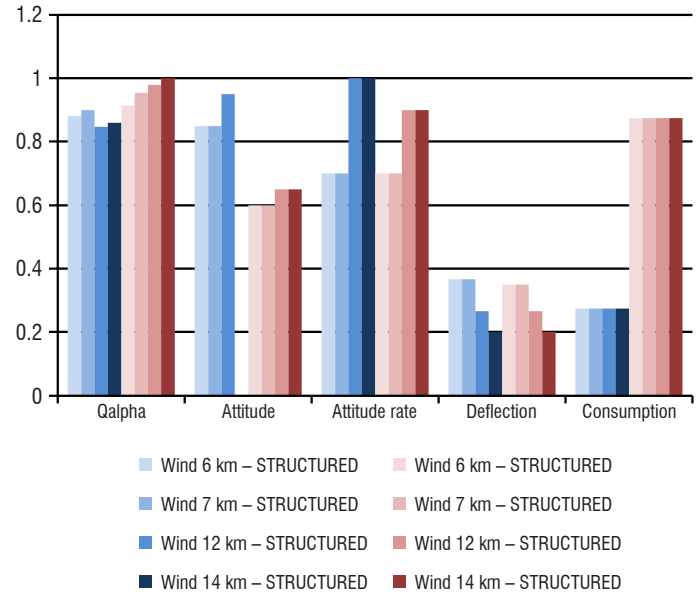

Figure 9 – Gain-scheduled structured controller and reference controller - Normalized performance (with respect to the requirement)

European launcher applications

In this section, we present some results of this generic framework, obtained from a multipurpose application for different launcher configurations; these results illustrate its strengths for rapid control design.

On the one hand, simplification in the control design process that was shown during the development of the launcher benchmark was confirmed on different European launcher configurations. Low and high frequency control design requirements are simultaneously tackled on worst cases extracted from each launcher MDB without design iterations. Resulting performances are always better, or at least equivalent to those obtained with traditional approaches. Figure 10 illustrates the time-varying compromise between low and high frequency objectives on the Bode plot of the controller for an IMU measurement. Figure 11 clearly shows the respect of stability margin requirements for all of the instants and models used for the design. Figure 12 demonstrates the respect of load requirements for a complete real wind database measured at the Kourou launchpad.

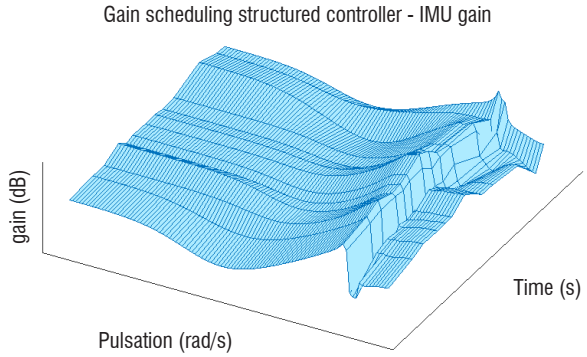

Figure 10 – Example of IMU controller Bode plot

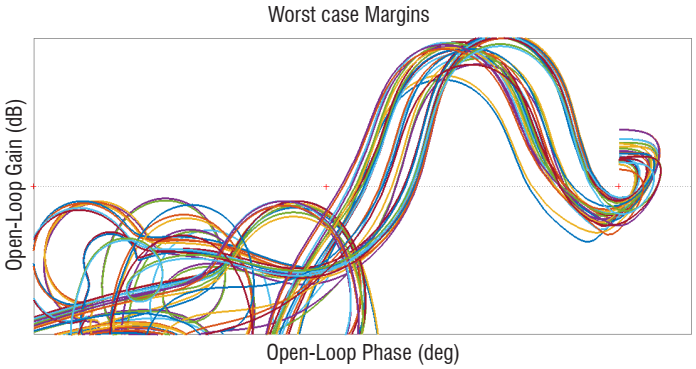

Figure 11 – Illustration of stability margin requirement respect

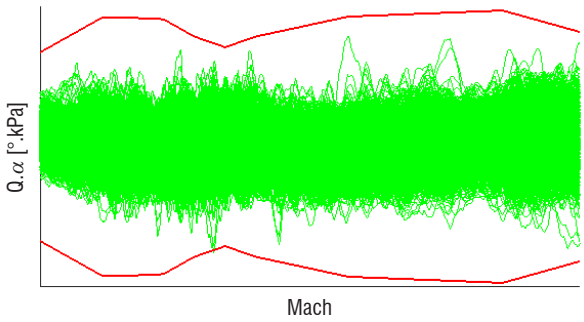

Figure 12 – Illustration of load requirement respect when facing real winds at Kourou

On the other hand, these tools are perfectly suited to perform numerous trade-offs and concept choices for future launchers through preliminary performance analysis in an automated way without manual retuning. They were used for:

- automatic trade-off between sensor selection and location, with performance assessment, thereby improving the process proposed in [5],
- trade-off between robustness and performance requirements. An example of the impact of stability margin relaxation on angle of attack performance is shown in Figure 13,
- trade-off between phase or gain control of the first bending mode. An example of the impact of gain or phase control of the first bending mode on the angle attack performance is shown in Figure 14,
- trade-off between mission dependence and robustness.

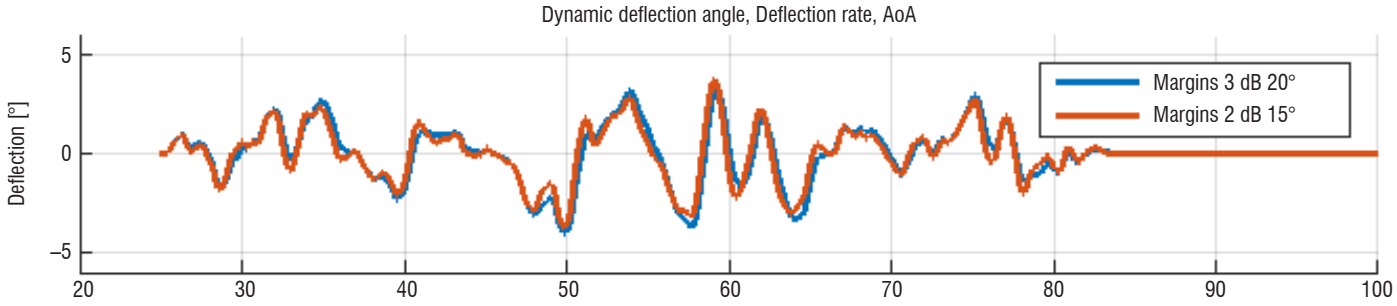

Figure 13 – Trade-off between stability margins and performance results

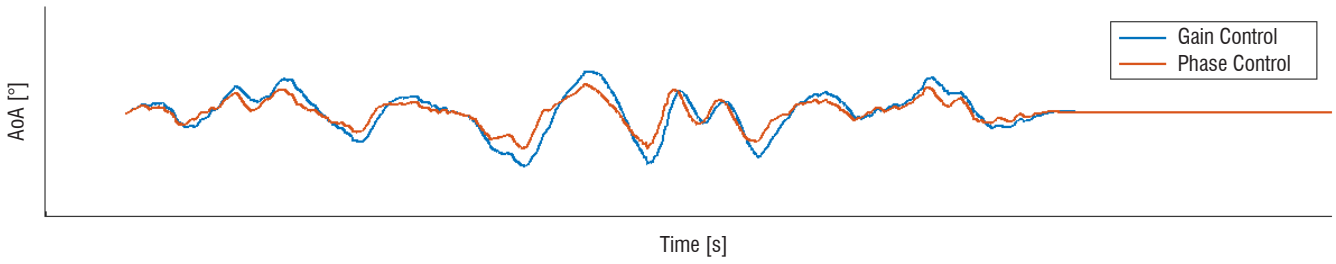

Figure 14 – Trade-off between bending mode gain or phase control and performance results

Conclusion

In this study, we have taken advantage of all of the enhancements of structured control design (fixed controller structure, multi-model, band-limited objectives, Soft/Hard constraints, etc.) to develop a *generic framework for rapid control design*. This framework was developed on a representative benchmark (with complete freedom on controller structure) before being proposed for the improvement of existing control laws and for future launcher pre-development phases.

In these examples, we have shown that load performance was improved with respect to pre-existing non-structured controllers. Simplifications in the design process were highlighted, providing flight control development cost reduction perspectives. These results pave the way for the industrial application of a structured H_∞ framework for fast retuning of existing controllers and development of new controller structures for future launchers ■

Nomenclature

AG	(Ariane Group)
α	(Angle of attack)
$\Delta\beta_c$	(Commanded deflection around nominal deflection)
$\Delta\beta_R$	(Realized deflection around nominal deflection)
CNES	(*Centre National d'Etudes Spatiales*)
D	(Drag in body axis)
F	(Aerodynamic Center)
G	(Center of Gravity)
HF	(High Frequency)
hp_{GYi}	(i^{th} bending mode slope at gyrometer location)
hp_{IMUi}	(i^{th} bending mode slope at IMU location)
htu_i	(i^{th} bending mode deformation at nozzle rotation point)
I	(Launcher pitch inertia)
I/F	(Interface)
IMU	(Inertial Measurement Unit)
ξ_i	(i^{th} bending mode damping)
ξ_β	(Damping of actuator model)
L	(Lift in body axis)
LF	(Low Frequency)
LMI	(Linear Matrix Inequality)
LQG	(Linear Quadratic Gaussian)
LPV	(Linear Parameter Varying)
LTI	(Linear Time Invariant)
L_F	(Distance between CoG and Centre of Pressure)
l_{tu}	(Position of nozzle rotation point with respect to the launcher CoG)
m	(Launcher total mass)
Mb_i	(i^{th} mode nozzle rotation point slope contribution)
MCI	(Mass Balance and Inertia Data)
MDB	(Model DataBase)
MIMO	(Multi-Input Multi-Output)
MISO	(Multi-Input Single-Ouptut)
P_c	(Commanded thrust)
q_i	(i^{th} bending mode generalized coordinates)
R_c	(Barycentric reference frame)
R_l	(Body reference frame)
R_t	(Terrestrial reference frame)
$\Delta\theta$	(Launcher pitch angle deviation with respect to commanded angle)
SISO	(Single-Input Single-Output)
S_{ref}	(Reference area)
T	(Thrust in body axis)
V_R	(Relative velocity)
ΔW	(Wind perturbation)
ω_i	(i^{th} bending mode pulsation)
ω_β	(Pulsation of actuator model)
$\Delta\dot{z}$	(Launcher lateral velocity)

References

[1] G. STEIN - *Respect the Unstable*. IEEE Control Systems Magazine, 23(4): 12-25, Aug. 2003.

[2] J. V. BURKE, D. HENRION, A. S. LEWIS, M. L. OVERTON - *HIFOO – A Matlab Package for Fixed Order Controller Design and H-Infinity Optimization*. Proc. IFAC Symp. Robust Control Design, Toulouse, France, 2006.

[3] P. APKARIAN, D. NOLL - *Nonsmooth H_∞ Synthesis*. IEEE Transactions on Automatic Control, 51(1): 71-86, 2006.

[4] P. APKARIAN, D. NOLL - *Nonsmooth Optimization for Multiband Frequency-Domain Control Design*. Automatica Journal, vol. 43, no. 4, p. 724-731, 2007.

[5] J. S. ORR *et. al.* - *Space Launch System Ascent Flight Control Design*. AAS GNC Conference, 14-038, 2014.

[6] B. WIE, W. DU, M. WHORTON - *Analysis and Design of Launch Vehicle Flight.* AIAA Guidance, Navigation, and Control Conference and Exhibit, August 2008.

[7] J. C. DOYLE, K. GLOVER, P. P. KHARGONEKAR, B. A. FRANCIS - *State-Space Solutions to Standard H2 and H_∞ Control Problems*. IEEE Transactions on Automatic Control, 34(8), August 1989.

[8] P. A. IGLESIAS, K. GLOVER - *State-Space Discrete Time H_∞ Control Theory.* ECC 91, Grenoble, France, July 1991.

[9] P. GAHINET, P. APKARIAN - *A Linear Matrix Inequality Approach to H_∞ Control*. International Journal of Robust and Nonlinear Control, Vol 4: 421-448, 1994.

[10] P. GAHINET, P. APKARIAN - *Structured H_∞ Synthesis in MATLAB*. Proc. 18th IFAC World Congress, Milano, August 2011.

[11] M. GANET-SCHOELLER - *Towards Structured H_∞ Synthesis for Flexible Launcher*. CEAS, 2015.

[12] P. GAHINET, P. APKARIAN - *Automated Tuning of Gain-Scheduled Control Systems.* Proc. IEEE Conf. on Decision and Control, 2740-2745, December 2013.

[13] H. LHACHEMI, D. SAUSSIE, G. ZHU - *A Structured H_∞-Based Optimization Approach for Integrated Plant and Self-Scheduled Flight Control System Design*. Aerospace Science and Technology 45, 30-38, 2015.

[14] S. SKOGESTAD, I. POSTLETHWAITE - *Multivariable Feedback Control: Analysis and Design.* 2nd ed., Wiley, 2005.

[15] *Matlab Robust Control Toolbox (RCT)*. 2013.

AUTHORS

Martine Ganet-Schoeller is currently a flight control engineer at Ariane Group in Les Mureaux, France.

Clément Combier: ISAE student.

Jean Desmariaux is currently a flight control engineer at CNES Launchers Directorate in Paris, France.

A. Kamath
(GE Global Research Centre)

P. P. Menon
(College of Engineering, Mathematics and Physical Sciences, University of Exeter)

M. Ganet-Schoeller, G. Maurice
(Ariane Group)

S. Bennani
(Guidance, Navigation and Control Section, ESA/ESTEC)

E-mail: p.m.prathyush@exeter.ac.uk

DOI: 10.12762/2017.AL13-09

Surrogate Assisted Computation of the Parametric Safety Margin for a Flexible Launcher

In order to assess the robustness of dynamical systems, an approach is to demarcate the uncertain parameter space as safe set and unsafe set. Unsafe set represents the region within which the system lacks the required level of performance, or even loses its stability. However, determining the minimum distance metric for the unsafe set from the nominal operating point, the so-called parametric safety margin, for a higher dimensional dynamical system is not trivial and is often computationally demanding. In this paper, the parametric safety margin for a closed loop industrial standard launch vehicle simulator during its thrust vector control phase is computed. Imposing certain basic topological restrictions for the multi-dimensional uncertain parameter space, the computation of the parametric safety margin can be posed as a constrained non-convex global optimization problem, and is thus extremely challenging in the case of high-fidelity aerospace simulators. Various performance requirements become the constraints in the optimization problem. An approach exploiting the use of non-intrusive polynomial surrogate modeling is proposed for the efficient computation of the parametric safety margin for the industrial standard launch vehicle simulator.

Introduction

In order to ensure the safety of a space mission, the controller needs to ensure robust stability and performance in the presence of various uncertainties and disturbances[1]. Uncertainties emanating from the mission parameters, such as aero-thermodynamic parameters, physical configuration parameters such as mass, inertia, actuator and sensor uncertain parameters, and flexible mode parameters, are to be considered. During the design cycle [2], the performance of the controller is assessed using a range of methods, such as analytical techniques that could be employed on lower order models, simulation-based techniques that are applicable to more detailed, complex and high-fidelity models [3], hardware in loop analysis, where actual subsystems replace some of the mathematical models [4] and the flight tests [5]. Analytical techniques, such as gain/phase margins [6] and the nonlinear continuation/bifurcation analysis against single parameter variations [7] can be considered as the traditional analytical tools for worst-case analysis in the early phase of the design cycle. Multivariable methodologies, such as μ-analysis and ν-gap metric analysis (Chapters 17 and 18, of Ref. [1]) became modern candidates for carrying out worst-case analysis based on a robust control theory, representing a given closed-loop system in a Linear Fractional Transformation (LFT)-based representation ([8] and Chapter 3, 4 and 5 of Ref. [9]). These techniques and their variants deal with multiple sources of uncertainty; however, the complexity in determining the exact μ value is claimed to be an NP-hard problem [10] and an excellent bound comparison using several variants of the algorithm on various benchmark problems can be found in [11]. Useful extensions of these approaches, which can handle certain types of nonlinear dynamics, have also recently been developed, such as Integral Quadratic Constraints (IQC)([12, 13] and Chapter 10 of Ref. [9]) and Sum Of Squares (SOS) programming [14].

The key advantages, as well as the conservatism and the limitations from the perspective of the requirements of the underlying uncertain model for many of these analytical methods, can be found in the conclusions of Chapter 3, 4, 5 and 10 of Ref [9]. Sampling and simulation-based analysis techniques, such as Monte Carlo and optimization methods, have specific advantages when dealing with nonlinear and complex models. Determining the worst case perturbations that lead to large excursions of the desired design metrics can be formulated as maximization problems and can be solved using various optimization algorithms [3, 1, 15, 16, 17, 9]. Despite the common generic mathematical formulation of the maximization problem, the quality of the worst-case solution and the computational complexity depend on the underlying methods selected for the

analysis. However, relatively fewer limitations are imposed on the requirements of the closed-loop mathematical models. That said, the computational time required for each simulation can possibly impose restrictions, if excessive. In that case, one would be forced to limit their analysis based on the available computational budget, or depend on other surrogate modeling techniques.

Parametric safety margin metric estimation provides another method (based on a simulation and optimization-based analysis concept) to assess the robustness of the controller [18]. This metric is defined in the parameter space as the distance between the nominal parameter value and the parameter value that corresponds to the first violation instance of a performance criterion. The implementation of this method on an aerospace benchmark with a complex nonlinear model is computationally challenging. When dealing with highly complex nonlinear models, a single function evaluation might take several seconds, which when used in an optimizer can take several hours until a global optimum is reached. The computation requirement for the parametric safety margin may benefit from the use of surrogate models instead of the actual full-order model. The use of surrogate models to evaluate the parametric safety margin will give the control system designer an estimate of the robustness of the designed controller within a matter of minutes. The designer can then evaluate the full-order model only in the zone of interest to check the validity of the parametric safety margin. Although in the literature there are plethora of methods available to build surrogate models,[19, 20, 21, 22, 23], to name a few. This paper focuses on the use of the polynomial chaos methodology, since it utilizes a limited number of input configurations to derive a surrogate model. In order to avoid large computation times to evaluate the complex nonlinear model, a surrogate model is developed using just a minimal number of evaluations of the original model, without compromising on accuracy as per the polynomial chaos methodology. Such a surrogate model provides an approximation to the simulator for any input configurations, and hence may be used to replace the original simulator for the fast computation of responses. The contribution of this paper is in the application of three different schemes, such as the parametric safety margin method, surrogate modeling using polynomial chaos, and optimization-based worst case analysis, which are integrated with the analysis of a flexible launcher model.

This paper is organized as follows: at first, the problem definition is provided. The description of the launcher model along with its functional performance criteria is given in Section "Closed-Loop System Description". A brief description of the theory of parametric safety margin estimation and the surrogate polynomial model is provided in Section "Analysis Methods". Section "Main Results" presents the results of the parametric safety margin with launcher, as well as polynomial models. Finally, a worst-case analysis is performed, in order to ascertain the maximum deviations of the performance criteria.

Problem Definition

A closed-loop dynamical system representation of a flexible launcher is provided, and the control law design is carried out to meet a set of mission performance objectives in a robust manner. The given model is treated as a "black-box" with access limited to certain input and output parameters, as is often the case with many other industrial models that are used for the purpose of validating and verifying the controllers. Given a bounded, multi-dimensional uncertain space, $\Delta \subset \mathcal{R}^m$, the questions that we are trying to answer are the following:

- Determine an operational parametric safety margin; *i.e.*, the set within which all different mission performance objectives associated with the closed-loop design are satisfied.
- Determine the combination of uncertain parameters associated with a maximum possible violation of a mission performance objective, $\delta^* \in \Delta \subset \mathcal{R}^m$, which is identified as the worst-case perturbation.
- Address computational complexities due to the time consuming simulations, while determining the parametric safety margin, by replacing the actual closed-loop dynamics model with its representative meta/surrogate model.

A constrained optimization problem is employed, in order to determine the parametric safety margin. The closed-loop functional performance requirements are written as a set of inequality constraints $\mathbf{s}(\delta, \mathcal{C}_{\mathcal{H}_\infty}, W) < 0$, where $\mathcal{C}_{\mathcal{H}_\infty}$ is the class of control law used and W is the wind gust disturbance profile and $\delta \in \Delta \subset \mathbb{R}^{dim(\delta)}$. The closed-loop design is said to be robust and acceptable if all of the constraints $\mathbf{s}(\delta, \mathcal{C}_{\mathcal{H}_\infty}, W) < 0$ are satisfied in the presence of various combinations of uncertain parameter perturbations.

The uncertain parameter space (Δ - space) can be classified as a safe or unsafe region, depending on whether the constraints $\mathbf{s}(\delta, \mathcal{C}_{\mathcal{H}_\infty}, W) < 0$ are satisfied or not, respectively. The unsafe region, denoted as $\mathcal{S}^u(\mathbf{s}) \subset \mathbb{R}^{dim(\delta)}$, is given by

$$\mathcal{S}^u(\mathbf{s}) = \bigcup_{i=1}^{dim(\mathbf{s})} \mathcal{S}_i^u(\mathbf{s})$$

where, for $1 \le i \le dim(\mathbf{s})$,

$$\mathcal{S}_i^u(\mathbf{s}) = \left\{ \delta \in \mathbb{R}^{dim(\delta)} : \mathbf{s}_i\left(\delta, \mathcal{C}_{\mathcal{H}_\infty}, W\right) > 0 \right\}$$

$\mathcal{S}^u(\mathbf{s})$ is the union of all unsafe regions defined by the individual constraints. The boundary of the set is on $\mathbf{s}(\delta, \mathcal{C}_{\mathcal{H}_\infty}, W) = 0$. The complementary set $\mathcal{S}'^u(\mathbf{s})$ becomes the safe set. At least one constraint must be violated in the unsafe region, while in the safe region all of the performance constraints are satisfied.

The method involves the definition of a reference set in the parameter space, with the nominal parameter vector δ_0 as the geometric center. This reference set is then subjected to homothetic dilations (*i.e.*, expansion and contraction) until the first instance of violation of the constraints $\mathbf{s} < 0$ occurs. In other words, we are interested in evaluating the largest safe set, $\mathcal{S}'^u(\mathbf{s})$, around the nominal parameter value. The size of this set is directly related to the operational uncertainty margin. Further details on the evaluation of the operational uncertainty margin can be found in Section "Analysis Methods".

The evaluation of the operational uncertainty margin becomes computationally very expensive when applying it to an industry standard problem. Given that performance criteria are treated as constraints, a closed-loop dynamical system is simulated and performance criteria are evaluated in the constraint function of the optimization scheme. Since the dynamical system is evaluated in the constraint function, the process of evaluating the operational uncertainty margin becomes computationally expensive. Identifying the exact operational

uncertainty margin, which may be a non-convex multidimensional surface, or even disconnected regions, with an attractive and feasible computational effort is challenging. Hence, an approximate operational margin that could be conservative, yet determined with a reduced computational effort, is preferred.

Computational effort could be considerably reduced if the constraint function were in polynomial form. Hence, a polynomial model is preferred instead of a closed-loop dynamical model. However, depending on the accuracy of the polynomial model, the safety margin could be optimistic or conservative. A conservative margin will always be safe, but optimistic safety margins may contain regions of the parametric space where constraints are violated. In order to be absolutely sure that the uncertainty margin truly contains no constraint violation, we perform a worst-case analysis on the reduced region defined by the margin. If no worst cases are found inside this region, then the margin is valid.

Closed-Loop System Description

Launcher Model and Control

A single-axis, parameter-varying model [24], derived by linearization of complete non-linear dynamic equations of motion for a flexible launcher under various equilibrium flight conditions, is considered as the benchmark for this study. A H_∞ controller is provided for the pitch control of the launcher during the atmospheric flight phase, from take-off to tail-off [24]. Rigid and bending mode dynamics together with an actuator, bending mode filter and H_∞ controller are modeled and implemented in MATLAB R2008b Simulink. The rigid-body dynamics during the atmospheric flight phase are described by the following three state representations:

$$\begin{bmatrix}\ddot{\theta}\\ \dot{\theta}\\ \dot{Z}\end{bmatrix}=\begin{bmatrix}0 & A_6(t) & A_6(t)/V(t)\\ 1 & 0 & 0\\ 0 & A_1(t) & -A_6(t)\alpha_3(t)\end{bmatrix}\begin{bmatrix}\dot{\theta}\\ \theta\\ \dot{Z}\end{bmatrix}+\begin{bmatrix}K_1(t) & -A_6(t)/V(t)\\ 0 & 0\\ K_2(t) & A_6(t)\alpha_3(t)\end{bmatrix}\begin{bmatrix}\beta\\ W\end{bmatrix} \quad (1)$$

In which parameters such as aerodynamic efficiency $A_6(t)$, aerodynamic coefficient $A_1(t)$, aero thruster efficiency $K_1(t)$ and $K_2(t)$, and $\alpha_3(t)$ are time-varying along the trajectory and are defined as follows [24]:

$$A_1=-\frac{P_C+P_S}{m}+\frac{QS_{ref}}{m}\left(C_A-C_{N\alpha}\right)$$

$$A_6=\frac{QS_{ref}C_{N\alpha}L_F}{I}$$

$$K_1=\frac{P_C l_{tu}}{I}\qquad K_2=-\frac{P_C}{m}\qquad \alpha_3=\frac{I}{m(t)V}L_F$$

In (1), $Col(\dot{\theta},\theta,\dot{Z})$ are states of the rigid mode dynamics and correspond to the launcher pitch rate (deg/sec), pitch angle (deg) and drift velocity (m/s) in the body frame, respectively. β and W represent the control input deflections and the wind perturbation, respectively. In the definitions of the aerodynamic and thruster efficiency parameters $A_i(t)$ and $K_i(t)$: $V, P_C, P_S, Q, S_{ref}, C_A, C_{N\alpha}, L_F, l_{tu}, I$ and m represent the absolute velocity, commanded thrust level, thrust level along the longitudinal axis, dynamic pressure, reference area, axial force coefficient, normal aerodynamic force coefficient with respect to the angle of attack, distance between the center of gravity and center of pressure on longitudinal axis, position of nozzle rotation with respect to the center of gravity, total inertia and total mass, respectively.

A second-order model with a small damping value represents the flexible bending mode dynamics associated with the flexible launcher, and is modeled as an additive perturbation on the rigid-body model. The flexible mode dynamics are represented as follows [24]:

$$\ddot{q}_i+2\xi_i\omega_i\dot{q}_i+\omega_i^2 q_i=-P_C h_{tu_i}\beta_C+\left(I_T h_{ptu_i}-M_{tu}L_{tu}\left(h_{tu_i}-L_{tu}h_{ptu_i}\right)\right)\ddot{\beta}_C \quad (2)$$

where q_i, ξ_i, ω_i, h_{tu_i}, I_T, h_{ptu_i}, M_{tu}, L_{tu} and β_C represent the i^{th} bending mode state, i^{th} bending mode damping, i^{th} bending mode pulsation, i^{th} bending mode deformation at the nozzle rotation point, total pitch inertia, i^{th} bending mode slide of deformation at the nozzle rotation point, nozzle mass, position of nozzle CoG respective to the nozzle rotation point and the commanded deflections around the nominal value to follow the reference trajectory. A total of five bending modes are considered in this benchmark. The actuator model for the pitch control is characterized by a second-order system having commanded deflection as a single input, and the realized deflection and its two derivatives as the three outputs.

$$\ddot{\beta}_R+2\xi_\beta\omega_\beta\dot{\beta}_R+\omega_\beta^2\beta_R=\omega_\beta^2\beta_C \quad (3)$$

where, ξ_β and ω_β represent the damping of the actuator model and the actuator model pulsation. The final effective deflection angle β corresponds to the sum of the realized control input deflection (β_R) and the misalignment deflection (β_{FZ}), and is given as:

$$\beta=\beta_R+\beta_{FZ} \quad (4)$$

The pitch angle is derived from the attitude measurement by the Inertial Measurement Unit (IMU) and the pitch rate is derived from the angular rate measurement by the gyrometer. hp_{IMUi} is the i^{th} bending mode slide of deformation at the IMU location and hp_{GYi} is the i^{th} bending mode slide of deformation at the gyrometer location. Noises are added to these measurements. Angular noise and angular rate noises are treated as Gaussian with 0.02° and 0.15°/s standard deviation, respectively.

$$\theta_m=\theta-\sum_i hp_{IMUi}q_i+noises$$
$$\dot{\theta}_m=\dot{\theta}-\sum_i hp_{GYi}\dot{q}_i+noises \quad (5)$$

A discrete time-robust gain-scheduled controller is used with the benchmark model (see the block interconnection in Figure 1), which consists of an H_∞ rigid-mode controller and a filter, which is kept in

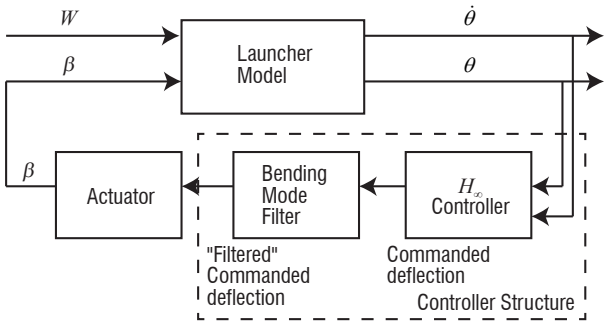

Figure 1 – Block description of the flexible launcher vehicle

series with the controller, for robust attenuation of the bending modes. The angular position and rate are the inputs of the controller and the filtered commanded deflection is the output. Further details on the model can be found in [24, 25].

Disturbances

The external disturbance corresponds to the wind gradient and the wind gust. The wind gust is a sudden increase/decrease in wind speed. This wind disturbance is assumed to be applied at the center of gravity of the flexible launcher vehicle. In this study, the wind perturbation is modeled by synthetic wind from a wind envelope, wind shear (wind speed change divided by the altitude interval) and wind gust according to a NASA specification in [26]. Synthetic wind is commonly used by aerospace organizations for vehicle design computations. Wind envelope and wind shear both come from wind measurements collected at the area of interest over a long period, and wind gust is an arbitrary characterization of the small scale motion. The NASA database given in [26] is followed. The synthetic wind is determined by an altitude, which corresponds to the maximum wind gradient. It is also the altitude at which the wind takes the value of the envelope. In this tool, the input is a flight instant and altitude is computed from the trajectory data using this instant. We have considered a deterministic wind profile occurring at five flight instances, 30, 35, 40, 45 and 50 seconds, as shown in Figure 2. Wind disturbance occurring early on in the flight interval can make the vehicle unstable and, hence, focus is on five instances between 30 to 50 seconds. Other wind instances were also considered during the analysis, but not reported here because they did not have any significant impact on the launch vehicle.

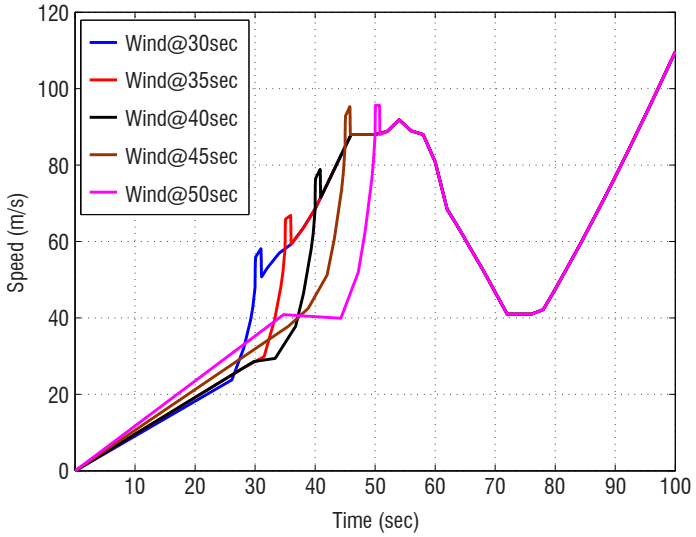

Figure 2 – Wind Profile

Uncertainties

For the given launcher controller/payload configuration, twenty eight uncertainties are considered in this study, which constitute eight rigid-mode parameters and five bending-mode parameters (i^{th} bending-mode pulsation, deformation at the nozzle position, slide deformation at the nozzle location, slide deformation at the IMU location and slide deformation at the gyrometer location), with four bending modes each, are considered. The entire list of uncertainties is given in Table 1. The uncertainty domain consists of two aspects: a possible nominal domain, which is not well-known prior to the flight, but can be known and reduced after the qualifications of the flights (reducible uncertainty) and, secondly, a dispersion domain in which the parameter value can change from one mission to another. In the framework of worst-case analysis, bounds on uncertain parameters are utilized by optimization tools to generate the worst case. These bounds should be able to incorporate both the uncertainties and the dispersions associated with the parameters. Such types of bounds were defined by ASTRIUM and the CNES for launcher application, as presented in [27], and are used in this study.

	Parameters	Uncertainty	Dispersion
Rigid	Inertia (MI)	±10%	±3%
	Thrust (MP)	±3%	±1%
	Aerodynamic coefficient(MCz)	±20%	±10%
	Centre of pressure (MXf)	±1.79 m	±0.2 m
	Dynamic pressure (MQ)	±20%	±4%
	Centre of gravity (MXg)	±0.3 m	±0.05 m
	Mass (MM)	5%	–
	Deflection Misalignment ($\Delta\beta$)	1°	–
Bending mode	Pulsation ($Mpuls$)	±20%	–
	Deformation at the nozzle location ($Mhtu$)	±30%	–
	Slide deformation at the nozzle location ($Mhptu$)	±30%	–
	Slide deformation at IMU location ($MhpIMU$)	±30%	–
	Slide deformation at the Gyrometer location ($MhpIMU$)	±30%	–

Table 1 – Variability of rigid and bending-mode uncertain parameters

Specifications

The controller structure ($\mathcal{C}_{H_\infty}$), consisting of the H_∞ controller and the bending-mode filter, must satisfy various functional performance requirements during the atmospheric phase control. The main functional requirements are the compensation for external wind and wind gust perturbations, and compensation for the internal perturbations, which include the thrust misalignment, the static error of the servo-actuators and thrust asymmetry. The compensation scheme must maintain minimum aerodynamic loads (Q_α, which is the angle of attack times the dynamic pressure), for structural sizing reasons. The main temporal performance specifications that are to be validated and the margins to be assessed, in the presence of multiple uncertain parameter perturbations and dispersions, are listed in Table 2.

Specification Description	Requirement	Cost function
$s_1(.)$: Maximum value of the aerodynamic angle of attack ($Q_\alpha(t)$) compatible with general load specification simulated over a finite time period	$< 500\ kPadeg$	$\max_{t\in[t_0 t_f]} \lvert Q_\alpha(t)\rvert$
$s_2(.)$: Maximum final value of the attitude ($\theta(t_f)$)	≤ 2°	$\max \lvert\theta(t_f)\rvert$
$s_3(.)$: Maximum final value of the attitude rate ($\dot{\theta}(t_f)$)	≤ 0.8°/s	$\max \lvert\dot{\theta}(t_f)\rvert$
$s_4(.)$: Maximum value of the deflection angle ($\beta(t)$) simulated over a finite time period	< 6°	$\max_{t\in[t_0 t_f]} \lvert\beta(t)\rvert$
$s_5(.)$: Cumulative deflection over a finite time period	< 200°	$\max \sum_{t_0}^{t_f} \lvert\Delta\beta_C\rvert$

Table 2 – Functional performance requirements

Analysis Methods

Parametric Safety Margin Assessment

The parameter space, $\Delta \subset \mathbb{R}^{dim(\delta)}$ can be divided into safe and unsafe regions, where the safe region corresponds to a region where all of the functional performance criteria are satisfied and the unsafe region corresponds to a region where at least one of the functional performance criteria is violated.

In this study, the chosen reference set, $\mathcal{M} \subset \Delta := \delta \in [\delta_{min}, \delta_{max}]$, is assumed to be a hyper rectangle with each component of the uncertain parameter vector, $\delta \in \mathbb{R}^{dim(\delta)}$, defined over a bounded interval. Assume symmetry around the geometric center, which corresponds to the nominal parameter value (δ_0). Let $\mathbf{m}$ be the vector of half-lengths of the sides of the hyper-rectangle. The hyper-rectangle $\mathcal{R}(\delta_0, \mathbf{m})$ is defined as

$$\mathcal{R}(\delta_0, \mathbf{m}) := \left\{ \delta \mid \delta^i \in [\delta_0^i - \mathbf{m}^i, \delta_0^i + \mathbf{m}^i], 1 \le i \le dim(\delta) \right\} \quad (6)$$

$\mathcal{R}(\delta_0, \mathbf{m})$ is called the reference set, which is chosen by selecting the values of the vector of half-lengths $\mathbf{m}$. This reference set, $\mathcal{R}(\delta_0, \mathbf{m})$, is depicted by a dashed blue line in Figures 3(a) and 3(b). A homothetic scaling of the reference set by a scaling factor λ is $\mathcal{R}(\delta_0, \lambda\mathbf{m}) := \{\delta_0 + \lambda(\delta - \delta_0) \mid \delta \in \mathcal{R}(\delta_0, \mathbf{m})\}$. Suppose that λ is positive; the resultant set is expanded with respect to the reference set, in Eq. 6 and if λ is negative, the resultant set is contracted with respect to the reference set in Eq. 6. The ratio of expansion or contraction is called the similitude ratio, $\lambda \in \mathbb{R}$. The similitude ratio is a positive scaling factor. The similitude ratio condition $\lambda > 1$ corresponds to the expansion, and the similitude ratio in the range of $0 < \lambda < 1$ corresponds to the contraction of the reference set, $\mathcal{R}(\delta_0, \mathbf{m})$. By successive dilations of the reference set, *i.e.*, expansions and contractions, the objective is to determine the largest safe set, $\mathcal{S}'^u(\mathbf{s})$, around the nominal parameter value. The largest set is depicted by the red line in Figures 3(a) and 3(b) and is represented as $\mathcal{R}(\delta_0, \tilde{\lambda}\mathbf{m})$, where $\tilde{\lambda}$ is called the critical similitude ratio. The critical similitude ratio is a non-dimensional positive scaling value denoted as $\tilde{\lambda}$. It is the similitude ratio of the dilation, and is interpreted as the operational parametric safety margin, ρ, for satisfaction of all of the functional performance requirements in the parameter space. The corresponding uncertain parameter combination is termed as a critical parameter vector. Hence, although conservative, this would be viewed as the onset of a violation of at least one performance criterion in the certain parameter space. There could be certain directions in which an expansion might still be possible, depending on the complex topology of the safe uncertainty set.

The sets $\mathcal{R}(\delta_0, \mathbf{m})$ and the scaled set $\mathcal{R}(\delta_0, \tilde{\lambda}\mathbf{m})$ are proportional. In Figure 2, the reference set, $\mathcal{R}(\delta_0, \mathbf{m})$ has expanded to $\mathcal{R}(\delta_0, \tilde{\lambda}\mathbf{m})$, which implies that the unsafe region $\mathcal{S}^u$ is outside the reference set. Whereas in Figure 2, the reference set $\mathcal{R}(\delta_0, \mathbf{m})$ has contracted to $\mathcal{R}(\delta_0, \tilde{\lambda}\mathbf{m})$, implying that the unsafe region is inside the reference set. Naturally, good robustness is associated with the expansion of the reference set, whereas the contraction implies poor robustness, since even a small perturbation around the nominal parameter value would result in violation of performance criteria. This is a measure of robustness of the controller, $\mathcal{C}_{\mathcal{H}_\infty}$, implying how large an uncertain parameter set can be to be identified as safe with respect to the nominal point. The constraint $\mathbf{s}(\delta, \mathcal{C}_{\mathcal{H}_\infty}, W)$ might have a nonlinear dependency on the parameters, and hence the computation of the critical parameter value becomes a non-convex global optimization problem. Furthermore, for the purpose of checking the satisfaction of the constraints, a simulation of the closed-loop model and the evaluation of each performance constraint is required.

The critical parameter value corresponding to the dilation of the reference set $\mathcal{R}(\delta_0, \mathbf{m})$ in the case of the i^{th} constraint can be computed by solving

$$\widetilde{\delta^i} = \arg\min_{\delta} \left\{ \|\delta - \delta_0\|_{\mathbf{m}}^{\infty} \mid \mathbf{s}_i\left(\delta, \mathcal{C}_{\mathcal{H}_\infty}, W\right) \ge 0 \right\} \quad (7)$$

where $\|\delta - \delta_0\|_{\mathbf{m}}^{\infty} := \arg\sup_i \left\{ \frac{|\delta - \delta_0|_i}{\mathbf{m}_i} \right\}$, is the $\mathbf{m}$-scaled norm. Considering all of the performances, the overall critical parameter value is $\tilde{\delta} = \tilde{\delta}_k$, where $k = \arg\min_{1 \le j \le dim\delta} \left\{ \|\tilde{\delta}_j^i - \delta_0\|_{\mathbf{m}}^{\infty} \right\}$, which is associated with the critical requirement. The resultant set $\mathcal{R}(\delta_0, \tilde{\lambda}\mathbf{m})$ is proportional to $\mathcal{R}(\delta_0, \mathbf{m})$, where $\tilde{\lambda} = \|\tilde{\delta} - \delta_0\|_{\mathbf{m}}^{\infty}$, in a non-dimensionalized setting.

The operational parametric safety margin is $\rho = \tilde{\lambda}\|\mathbf{m}\|$. The robustness is ensured when $\rho \ge \|\mathbf{m}\|$ for a given controller design. In such situation, all of the performance constraints $\mathbf{s}(\delta, \mathcal{C}_{H_\infty}, W) \le 0$ are

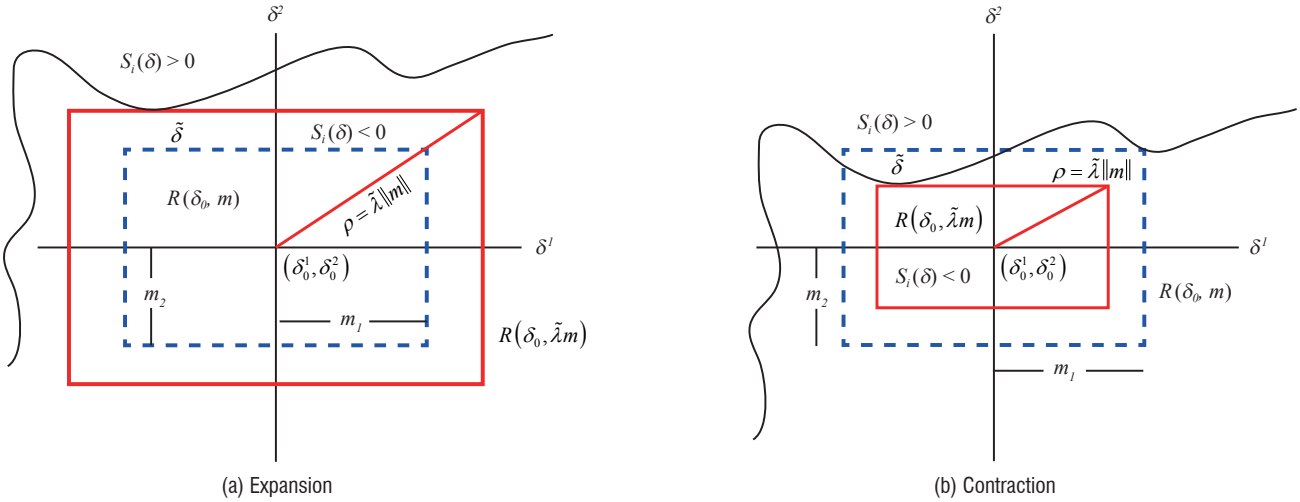

Figure 3 – Dilation of Uncertainty Set

satisfied in the region $\Delta = \mathcal{R}_{\delta}(\delta_0, \mathbf{m})$. Eq. 7 is reformulated as a constrained optimization problem, as follows:

$$\begin{aligned} \min \quad & \left\| \delta - \delta_0 \right\|_{\mathbf{m}}^{\infty} \\ \text{Subject to}: \quad & \mathbf{s}_i\left(\delta, \mathcal{C}_{H_\infty}, W\right) \geq 0 \end{aligned} \tag{8}$$

where $\mathbf{s}_i(.)$ are the functional performance constraints listed in Table 2.

Surrogate assisted analysis

The evaluation of a parametric safety margin metric is computationally very expensive. Often, simulation-based optimization techniques,[18, 28, 29], can be computationally expensive and thus very time consuming. Further, the complexity of models can contribute to the time complexity. Here, we investigate the potential of surrogate polynomial models instead of the original launcher model, in order to save in terms of computational time overhead.

Polynomial models have been used in various applications, including solid mechanics [30, 31], stochastic finite elements [32] and stochastic fluid dynamics [33, 34]. In [35], power series expansion and polynomial chaos expansion are used to quantify the uncertainty in the output of nonlinear systems, and to illustrate it on a batch crystallization process. In [36], Polynomial Chaos is used to analyze the stability and control of a dynamical system with probabilistic uncertainty on the system parameters. Singh, [37], used the generalized polynomial chaos (gPC) method to design robust input shapers for precise control of mechanical systems. In aerospace applications, Fisher, [38], provided a framework based on gPC to analyze a linear flight-control design for an F-16 aircraft model.

The basic concept is to approximate the response of the model using a polynomial function of uncertain parameters. The polynomial function is constructed using an orthogonal polynomial basis ($\Phi_q(\delta)$). The underlying idea is as follows: the random variables, *i.e.*, various uncertain parameters to be perturbed, are represented as orthogonal functions of a stochastic variable with deterministic coefficients:

$$F = \sum_{q=0}^{\infty} a_q \Phi_q(\delta) \tag{9}$$

As shown in [39], a truncated version of the expansion ($q = 0, 1, \ldots, M$) is possible, where the order M depends on the number of uncertain parameters and the order of the polynomial sought.

$$F = \sum_{q=0}^{M} a_q \Phi_q(\delta) \tag{10}$$

where $M = \frac{(q_v + q_o)!}{(q_v! q_o!)} - 1$, q_v is the number of independent sources of uncertainty and q_o is the maximum order of the polynomial. Here, the coefficients a_q for $q = 0, \ldots, M$ have to be determined.

In [40], Wiener introduced homogeneous chaos for the Gaussian process, which utilized the span of the Hermite polynomial functionals to quantify uncertain parameters. This was later expanded to incorporate a non-Gaussian random process with polynomials from the Wiener-Askey scheme [39]. The connections between the choice of distribution and random variable, the Wiener-Askey polynomial and the support set are listed in Table 3. For example, for a continuous uniform distributed random variable, a Legendre polynomial basis with corresponding support set $[a, b]$ is selected.

	Random variable δ	Wiener-Askey Scheme	Support Set
Continuous	Gaussian	Hermite	$(-\infty, \infty)$
	Gamma	Laguerre	$[0, \infty)$
	Uniform	Legendre	$[a, b]$
	Beta	Jacobi	$[a, b]$

Table 3 – Wiener-Askey polynomials with corresponding distribution

The Galerkin projection method is generally used to evaluate the coefficients (a_q) in Eq. 10 [39, 38, 30]. This projection method involves solving multiple definite integrals, which could be computationally expensive and time-consuming in the presence of a large number of uncertain parameters. A non-intrusive method, called the probabilistic collocation method [41], is used to evaluate the coefficients (Φ_q) of the surrogate polynomial model. The model is treated as a "black box" type with access limited to a few uncertain input parameters and the output response. The method involves evaluation of the original model at specific selected points in the uncertain parameter space, identified as collocation points. The required number of collocation points also depends on the order of the polynomial and the number of uncertainties. The collocation points are chosen in such a way that the dynamical behavior of the original model should be captured as closely as possible. In order to do this, the collocation points are generated by evaluating the roots of the next higher-order polynomial in the orthogonal polynomial basis Φ_q. The pseudo-code for deriving the surrogate model is given as Algorithm 1 in [42].

Polynomial model of the Launcher

A polynomial model is derived by treating the flexible launcher model in a closed loop with the H_∞ controller as a black box, and considering the uncertain parameters as inputs and the cost function value as the output. In order to incorporate the effect of the noise acting on the outputs, the original Simulink model in MATLAB uses a random number generator. A seed value of the random number generator ensures repeatability of the results. In order to truly randomize the noise acting on the outputs and also to incorporate the effect of noise in the surrogate model, we consider an additional uncertainty, which gives the seed values used by the random number generators in MATLAB to generate random noise signals in the original launcher model. This increases the total number of uncertainties considered to 29. The cost function is the performance specification against which the controller is validated. The entire list of cost functions is given in Table 2. Second-order polynomial models are generated for each of the cost functions. For a second-order model, the number of coefficients of the polynomial model is 465 (refer to Eq. 10). For each of the cost functions, 465 collocation points are generated and the flexible launcher model is evaluated at these points. These collocation points are common to all of the cost functions and, hence, all polynomials can be modeled by evaluating the original model just 465 times. A set of linear equations can be formed by substituting these collocation points and their corresponding output responses in Eq. 10. The coefficients of the polynomial are obtained by solving these set equations. comparison between the polynomial model and the original model is

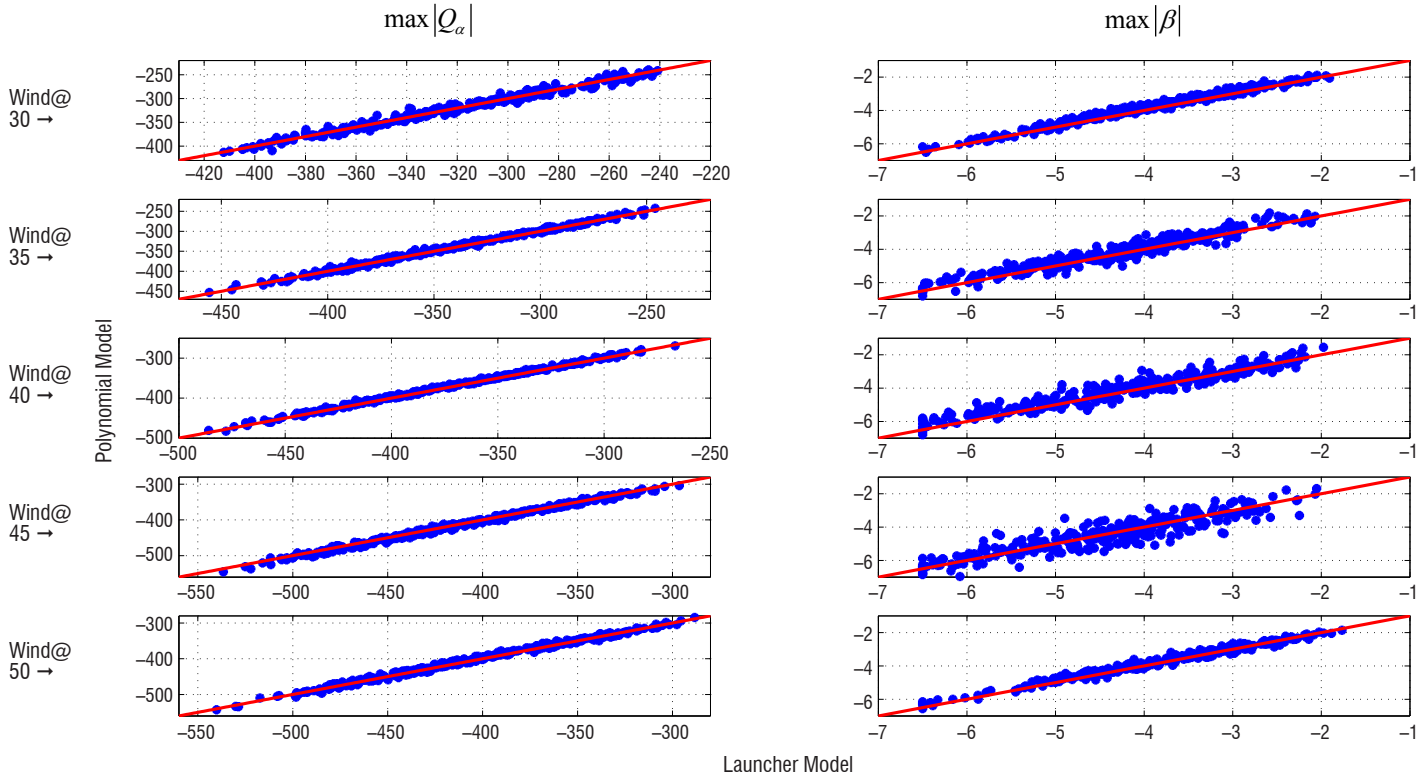

Figure 4 – Comparison between the launcher and polynomial models

shown in Figure 4. The comparison is shown for two performance criteria (along each column) at five different wind perturbations (along each row), which indicates a very good approximation.

Evolutionary-Based optimization: Hybrid Differential Evolution

The Differential Evolution (DE) method was first introduced by Storn and Price in [43] and is based on evolutionary principles. This method, like GA, starts with a random initial population. A new search point is generated by adding the weighted vector difference between two randomly selected individuals from the population with a third randomly chosen individual. The vector difference determines the search direction and a weighting factor decides the step size in that particular search direction. HDE employs a local optimization when no improvement is found from DE in successive iterations. Hybrid Differential Evolution (HDE) is used for optimization-based analysis in this paper. The results obtained by DE have been observed to be better than those of other evolutionary algorithms, both in terms of accuracy and computational overhead [44]. Please refer to [16, 17, 45] and the references therein for the HDE algorithm and its implementation.

Main Results

This section presents the results used to determine the efficacy of the controller. As a first step, a safety margin is evaluated and a comparison is made between the original launcher model and the polynomial model. The second step is to perform a worst-case analysis inside the safe region defined by the safety margin metric evaluated using the polynomial model. No constraint violations were found, thus indicating that the region defined by the metric is truly safe. Furthermore, a worst-case analysis is performed over the entire parameter space to gain insight into the level of performance deviations that could occur.

Results: Safety margin assessment

The safety margins for the given set of control laws $\mathcal{C}_{H_c}$ at five different wind perturbations occurring at 30, 35, 40, 45 and 50 seconds are determined by solving the constrained optimization in Eq. 8. A population-based optimization technique, specifically a Hybrid Differential Evolution (HDE) method, has been used to solve for the critical parameter values and the safety margins over the $\delta-$ space satisfying the performance requirements listed in Table 2. The critical similitude ratio ($\tilde{\lambda}$) and the safety margin (ρ) are evaluated for different wind perturbation cases, using a flexible launcher and polynomial model, and are given in Table 4. A high computation time, *i.e.*, more than 5 hours, is required to evaluate the parametric safety margin for each wind instance when the flexible launcher model is utilized.

		Wind perturbations				
		30 sec	35 sec	40 sec	45 sec	50 sec
Launcher Model	$\tilde{\lambda}$	1.05	0.71	0.66	0.68	0.88
	$\rho \geq 2.65$	2.78	1.88	1.75	1.8	2.32
	CPU Time (sec)	20914.33	16524.17	16948.07	18085.58	18381.9
Polynomial Model	$\tilde{\lambda}$	1.05	0.756	0.685	0.718	0.899
	$\rho \geq 2.65$	2.78	2	1.81	1.9	2.38
	CPU Time (sec)	181.27	442.16	211.41	366.65	204.07

Table 4 – Critical similitude ratio ($\tilde{\lambda}$) and safety margin (ρ) results for the launcher & the polynomial models

In order to reduce the computational time, surrogate polynomial models are utilized as constraints. It can be seen from Table 4 that the computational time is significantly reduced, by a factor of 100,

when the surrogate models are utilized. Due to the inherent error in the approximation, the critical parameter value found using the polynomial model is not the same as that found using the original launcher model.

It is found that $\tilde{\lambda} < 1$ for the wind perturbations occurring at 35, 40, 45 and 50 seconds. This indicates a reduced level of robustness, whereas for the wind perturbation occurring at 30 s, the value of λ is slightly greater than 1, indicating good robustness. For wind perturbations occurring at 40 and 45 seconds, the critical similitude ratio ($\tilde{\lambda}$) is 0.66 and 0.68 (for the launcher model), respectively, indicating that the reference set has contracted to a small safe region around the nominal parameter value.

Worst-case analysis inside the safe region

The worst-case analysis is carried out at five different wind perturbations occurring at 30, 35, 40, 45 and 50 seconds. The hybrid differential evolution is employed with a fixed termination criteria of 1200 simulations, a population size of 50, a mutation scale factor of 0.8 and a crossover factor of 0.8. The local optimization, sequential quadratic optimization "*fmincon*", is used for the hybridization purpose, and the maximum local iteration number is set to 30.

A worst-case analysis is performed on the original launcher model, in order to gain further insight about the levels of each performance deviation that could occur within the safe region defined by the parametric safety margin. In each case, the perturbations are limited within the set defined by the values of the parametric safety margin given in Table 4 respectively. Optimization-based worst-case analysis is performed for the cost functions listed in Table 2. The parameter space is restricted to be within the reference set defined by $\mathcal{R}(\delta_0, \tilde{\lambda}\mathbf{m})$, where $\mathbf{m}$ was kept fixed at 0.5 and $\tilde{\lambda}$ at the value from Table 4. The results of the worst-case analysis are shown in Table 5. None of the performance criteria were exceeded as expected and the maximum excursions for the performance requirements within the safe region are obtained. It is clear that the deflection angle performance requirement approached its limits and it is the first constraint violation in all of the cases.

Worst-case analysis over the entire parameter space

The numerical results for six different cost functions at five different wind perturbations are given in Table 6 - Table 7. In Table 6, consider the cost function representing the performance on the aerodynamic load $|Q(\alpha(t))|$ and wind occurring at 45 seconds. Among the 1200 candidate uncertain parameter vectors in the search space, the maximum cost function value associated with the worst case is 561.91 and has a mean of 436.11, with a standard deviation of 79.57. Mean and standard deviation statistics give us an idea of the variability of the cost function values in the search space. A high value of the standard deviation indicates that the cost function values are spread out over a large range in the search space, whereas a low value indicates that the cost function values lie too close to the mean. This shows the exploration property of the optimization algorithm, which is its ability to access uncertain parameter vectors spread out in the search space. In order to find the global solution, the optimization algorithm should be able to explore the search space as thoroughly as possible. In this case, the standard deviation is high and indicates that the algorithm was able to access uncertain parameter vectors spread out over the search space. Also, among the candidate points, 383 cases out

Cost Function		Worst case values				
		30s	35s	40s	45s	50s
$\max_{t\in[t_0 t_f]} \lvert Q_\alpha(t)\rvert$	max	388.11	393.44	423.09	467.65	476.51
	mean	340.85	355.41	385.65	425.83	423.46
	std	42.84	37.24	39.71	44.25	47.84
	failures	0	0	0	0	0
$\max_{t\in[t_0 t_f]} \lvert\beta(t)\rvert$	max	5.78	5.85	5.94	5.91	5.993
	mean	4.10	4.62	4.84	4.76	4.45
	std	0.85	0.71	0.67	0.68	0.83
	failures	0	0	0	0	0
$\max_{t\in[t_0 t_f]} \lvert\theta(t)\rvert$	max	4.51	4.24	4.21	4.53	4.13
	mean	3.51	3.46	3.56	3.51	3.04
	std	0.58	0.44	0.45	0.52	0.5
	failures	0	0	0	0	0
$\max \lvert\theta(t_{tf})\rvert$	max	0.199	0.152	0.144	0.145	0.138
	mean	0.038	0.033	0.032	0.035	0.034
	std	0.026	0.026	0.024	0.030	0.025
	failures	0	0	0	0	0
$\max \lvert\dot{\theta}(t_{tf})\rvert$	max	0.477	0.465	0.456	0.568	0.385
	mean	0.124	0.119	0.118	0.134	0.121
	std	0.095	0.095	0.090	0.101	0.101
	failures	0	0	0	0	0
Cumulated deflection	max	136.15	138.19	135.54	137.95	135.44
	mean	125.43	125.92	125.76	124.95	124.57
	std	12.1	12.31	12.00	11.81	11.42
	failures	0	0	0	0	0

Table 5 – Worst-case results inside the safe region

Cost Function			Worst-case values				
			30s	35s	40s	45s	50s
$\max_{t\in[t_0 t_f]} \lvert Q_\alpha(t)\rvert$	HDE	max	432.23	460.61	509.65	561.91	543.23
		mean	336.68	369.56	406.95	436.11	430.48
		std	62.53	66.12	75.46	79.57	77.49
		failures	0	0	37	383	370
	MC	max	424.74	449.14	493.08	549.26	532.14
		mean	319.58	340.42	376.16	411.67	402.38
		std	41.6	46.62	50.13	53.76	54.26
		failures	0	0	0	60	40
$\max_{t\in[t_0 t_f]} \lvert\beta(t)\rvert$	HDE	max	6.5	6.5	6.5	6.5	6.5
		mean	4.29	4.72	4.27	4.86	4.43
		std	1.32	1.38	1.44	1.35	1.38
		failures	187	516	582	517	366
	MC	max	6.47	6.5	6.5	6.5	6.5
		mean	3.79	4.26	4.36	4.4	3.88
		std	0.95	1.05	1.08	1.12	1.01
		failures	13	67	93	111	29
$\max_{t\in[t_0 t_f]} \lvert\theta(t)\rvert$	HDE	max	5.85	Unstable	Unstable	Unstable	6.91
		mean	3.51				3.41
		std	0.87				1.12
		failures	0				0
	MC	max	4.65	7.03	8.8	8.2	5.54
		mean	3.14	3.24	3.35	3.34	2.73
		std	0.59	0.7	0.76	0.95	0.63
		failures	0	0	0	0	0

Table 6 – Worst case results for entire parameter range

of 1200 violated the performance requirement on $Q(\alpha(t)) \leq 500$ kPa during the execution of the HDE optimization algorithm. It was noticed that the rigid uncertain parameters were the main cause for the worst-case performance in all of the cases, and the flexible modes were well suppressed by the bending-mode filters. Worst-case directions are oriented towards the parameters, which are simultaneously the most influent ones (dynamic pressure MQ, aerodynamic coefficient Cz, center of pressure Xf, center of gravity Xg) and the more dispersed ones (deflection misalignment).

Unstable cases are found for attitude when the wind perturbation corresponds to 35, 40, and 45 seconds. Sustained actuator saturation is observed in these cases. Monte Carlo analysis is also performed and the results are also tabulated in Table 6 - Table 7. These results are provided to compare with those found by optimization-based analysis. Due to the computational complexity involved with the original launcher model, 1000 Monte Carlo campaigns were performed for each cost function. It was observed that the optimization-based method is able to find more worst-cases and even better ones than those found by the Monte Carlo method, which can be attributed to the intelligence embedded in the search process of the optimization scheme. The Monte Carlo method is unable to capture any unstable cases corresponding to the performance criteria of attitude, attitude rate and cumulated deflection. Also, apart from Q_α and $\beta(t)$, no failures, *i.e.*, performance criteria violations, were recorded.

Cost Function			Worst case values				
			30s	35s	40s	45s	50s
$\max\lvert\theta(t_{tf})\rvert$	HDE	max	0.15	0.16	Unstable	Unstable	0.139
		mean	0.038	0.035			0.04
		std	0.027	0.029			0.03
		failures	0	0			0
	MC	max	0.22	0.18	0.19	0.184	0.177
		mean	0.04	0.04	0.04	0.04	0.04
		std	0.03	0.03	0.03	0.03	0.03
		failures	0	0	0	0	0
$\max\lvert\dot{\theta}(t_{tf})\rvert$	HDE	max	0.595	0.498	Unstable	Unstable	0.493
		mean	0.117	0.138			0.112
		std	0.09	0.101			0.088
		failures	0	0			0
	MC	max	0.556	0.54	0.53	0.58	0.536
		mean	0.13	0.13	0.13	0.13	0.122
		std	0.1	0.09	0.1	0.1	0.09
		failures	0	0	0	0	0
Cumulated Deflection	HDE	max	136.44	153.7	Unstable	Unstable	141.64
		mean	125.87	127.28			125.43
		std	14.05	13.55			12.85
		failures	0	0			0
	MC	max	136.52	142.51	151.14	142.18	135.63
		mean	126.81	127.3	127	127	126.36
		std	3.07	3.5	3.5	3.43	3.07
		failures	0	0	0	0	0

Table 7 – Worst-case results for the entire parameter range

Conclusion and future work

Parametric safety margin assessment provides means to quantify robustness in the parameter space. The methodology involves translating the performance criteria into constraints, which are used in an optimization problem. This optimization problem is formulated in such a way that dilations of the reference set are performed in order to find the largest hyper-rectangle in the parameter space around the nominal parameter value where all of the performance criteria/constraints are satisfied. This procedure involves a large number of simulations of the launch vehicle and the problem becomes computationally very expensive.

In order to reduce the computational burden, surrogate polynomial models were developed using the polynomial chaos theory. These models provided a relatively inexpensive way of calculating the operational parametric safety margin metric. Although polynomial models are computationally very cheap to utilize, they may be less accurate when compared with the original launcher model. The accuracy depends on the order of the polynomial. As the order is increased, the accuracy increases while significantly increasing the computation time to derive the polynomial models. Even so, this paper shows that the second order polynomial models could be used to generate results with a fair degree of accuracy.

Future work is aimed at investigating the method of Bernstein expansion on polynomial models to determine the parametric safety margin. The method of Bernstein expansion could further reduce the evaluation time of the safety margin by eliminating the use of the optimization procedure [46]; however, a stumbling block that needs to be overcome are the issues emanating from the dimensionality of the uncertainty space ■

References

[1] C. FIELDING, A. VARGA, S. BENNANI, M. SELIER - *Advanced Techniques for Clearance of Flight Control Laws*. Lecture Notes in Control and Information Sciences, Springer, 2002.

[2] R. W. PRATT, ED. - *Flight Control Systems.* Progress in Astronautics and Aeronautics, American Institute of Aeronautics and Astronautics, 2000.

[3] Y. JEPPU, K. KUNDAPUR, P. APTE - *Optimized Flight Control Component Testing Using Taguchi Design of Experiments*. American Institute of Aeronautics and Astronautics, 2014/11/19 2007. [Online]. Available: http://dx.doi.org/10.2514/6.2007-7824.

[4] A. PATEL, V. PATEL, G. DEODHARE, S. CHETTY - *Flight Control System Clearance Using Static Tests at Iron Bird*. American Institute of Aeronautics and Astronautics, 2014/11/19 2006. [Online]. Available: http://dx.doi.org/10.2514/6.2006-6203.

[5] V. PATEL, G. DEODHARE, S. CHETTY - *Near Real Time Stability Margin Estimation from Piloted 3-2-1-1 Inputs*. American Institute of Aeronautics and Astronautics, 2014/11/19 2002. [Online]. Available: http://dx.doi.org/10.2514/6.2002-5820.

[6] J. M. MACIEJOWSKI - *Multivariable Feedback Design*. Addison-Wesley, 1989.

[7] M. H. LOWENBERG - *Stability and Controllability Evaluation of Sustained Flight Manoeuvres*. Proceedings of 21st Atmospheric Flight Mechanics Conference. AIAA 1996-3422, July 1996.

[8] J. F. MAGNI - *Linear Fractional Representation Toolbox: Modelling, Order Reduction, Gain Scheduling*. System Control and Flight Dynamics Department, Onera, Toulouse, France, Tech. Rep., 2004.

[9] A. VARGA, A. HANSSON, G. PUYOU - *Optimization Based Clearance of Flight Control Laws: A Civil Aircraft Application*. Lecture Notes in Control and Information Sciences. Springer, 2011.

[10] R. P. BRAATZ, P. M. YOUNG, J. C. DOYLE, M. MORARI - *Compulational Complexity of μ Calculation*. IEEE Transactions on Automatic Control, vol. 39, no. 5, pp. 1000-1001, 1994.

[11] C. ROOS, J.-M. BIANNIC - *A Detailed Comparative Analysis of all Practical Algorithms to Compute Lower Bounds on the Structured Singular Value*. Control Engineering Practice, vol. 44, pp. 219–230, 2015.

[12] A. MEGRETSKI, A. RANTZER - *System Analysis via Integral Quadratic Constraints.* IEEE Transactions on Automatic Control, vol. 42, no. 6, pp. 819-830, 1997.

[13] J. M. BIANNIC, C. ROOS, A. KNAUF - *Design and Robustness Analysis of Fighter Aircraft Flight Control Laws*. European Journal of Control, vol. 12, no. 1, pp. 71-85, 2006.

[14] K. KRISHNASWAMY, G. PAPAGEORGIOU, S. GLAVASKI, A. PAPACHRISTODOULOU - *Analysis of Aircraft Pitch Axis Stability Augmentation System Using Sum of Squares Optimization*. Proceedings of American Control Conference, vol. 3, 2005, pp. 1497-1502.

[15] H. D. JOOS - *Flight Control Law Clearance Using Optimisation-Based Worst-Case Search*. Proceedings of 6th IFAC Symposium on Robust Control Design, vol. 6, no. 1, 2009, pp. 331-336.

[16] P. P. MENON, D. G. BATES, I. POSTLETHWAITE - *Nonlinear Robustness Analysis of Flight Control Laws for Highly Augmented Aircraft*. Control Engineering Practice, vol. 15, no. 6, pp. 655-662, 2007.

[17] P. P. MENON, I. POSTLETHWAITE, S. BENNANI, A. MARCOS, D. G. BATES - *Robustness Analysis of a Reusable Launch Vehicle Flight Control Law*. Control Engineering Practice, vol. 17, no. 7, pp. 751-765, 2009.

[18] L. G. CRESPO, D. P. GIESY, S. P. KENNY - *Robustness Analysis and Robust Design of Uncertain Systems*. AIAA Journal, vol. 46, pp. 388-396, 2008.

[19] H. S. CHUNG, J. J. ALONSO - *Comparison of Approximation Models with Merit Functions for Design Optimization*. Proceedings of 8th Symposium on Multidisciplinary Analysis and Optimization, vol. 200, AIAA 2000-4754, September 2000.

[20] R. JIN, W. CHEN, T. W. SIMPSON - *Comparative Studies of Metamodelling Techniques under Multiple Modeling Criteria*. Structural and Multidisciplinary Optimization, Springer-Verlag, vol. 23, no. 1, pp. 1-13, 2001.

[21] A. KHURI, S. MUKHOPADHYAY - *Response Surface Methodology*. Wiley Interdisciplinary Reviews: Computational Statistics, vol. 2, no. 2, pp. 128-149, 2010.

[22] J. P. C. KLEIJNEN - *Kriging Metamodeling in Simulation: A Review*. European Journal of Operational Research, vol. 192, no. 3, pp. 707-716, 2009.

[23] B. CHENG, D. M. TITTERINGTON - *Neural Networks: A Review from a Statistical Perspective*. Statistical Science, vol. 9, no. 1, pp. 2-30, 1994.

[24] M. GANET-SCHOELLER, M. DUCAMP - *LPV Control for Flexible Launcher*. Proceedings of AIAA Guidance, Navigation, and Control Conference. AIAA 2010-8193, 2010.

[25] M. GANET-SCHOELLER, J. BOURDON, G. GELLY - *Non-Linear and Robust Stability Analysis for ATV Rendezvous Control*. Proceedings of AIAA Guidance, Navigation, and Control Conference, AIAA 2009-5951, 2009.

[26] D. L. JOHNSON - *Terrestrial Environment (Climatic) - Criteria Guidelines for Use in Aerospace Vehicle Development*. NASA Technical Memorandum 4511, Revision, 1993.

[27] I. RONGIER, J. DROZ - *Robustness of Ariane 5 GNC Algorithms*. Proceedings of the 4th ESA International Conference on Spacecraft Guidance, Navigation and Control Systems, ESTEC, Noordwijk, The Netherlands, October, 1999.

[28] L. G. CRESPO, M. MATSUTANI, J. JANG, T. GIBSON, A. ANNASWAMY - *Design and Verification of an Adaptive Controller for the Generic Transport Model*. Proceedings of AIAA Guidance, Navigation, and Control Conference, AIAA 2009-5618, 2009.

[29] A. K. KAMATH, P. P. MENON, M. GANET-SCHOELLER, G. MAURICE, S. BENNANI, D. G. BATES - *Robust Safety Margin Assessment and Constrained Worst-Case Analysis of a Launcher Vehicle*. Proceedings of 7th IFAC Symposium on Robust Control Design, vol. 7, no. 1, 2012, pp. 254-259.

[30] R. GHANEM, J. RED-HORSE - *Propagation of Probabilistic Uncertainty in Complex Physical Systems Using a Stochastic Finite Element Approach*. Physica D: Nonlinear Phenomena, vol. 133, pp. 137-144, 1999.

[31] R. GHANEM - *Ingredients for a General Purpose Stochastic Finite Elements Implementation*. Computer Methods in Applied Mechanics and Engineering, vol. 168, no. 1, pp. 19-34, 1999.

[32] R. GHANEM, P. D. SPANOS - *Stochastic Finite Elements: A Spectral Approach*. Dover Publications, 2003.

[33] T. Y. HOU, W. LUO, B. ROZOVSKII, H. M. ZHOU - *Wiener Chaos Expansions and Numerical Solutions of Randomly Forced Equations of Fluid Mechanics*. Journal of Computational Physics, vol. 216, no. 2, pp. 687-706, 2006.

[34] D. XIU, G. E. KARNIADAKIS - *Modeling Uncertainty in Flow Simulations via Generalized Polynomial Chaos*. Journal of Computational Physics, vol. 187, no. 1, pp. 137-167, 2003.

[35] Z. K. NAGY, R. D. BRAATZ - *Distributional Uncertainty Analysis Using Polynomial Chaos Expansions*. Proceedings of IEEE International Symposium on Computer-Aided Control System Design, 2010, pp. 1103-1108.

[36] F. S. HOVER, M. S. TRIANTAFYLLOU - *Application of Polynomial Chaos in Stability and Control.* Automatica, vol. 42, no. 5, pp. 789-795, 2006.

[37] T. SINGH, P. SINGLA, U. KONDA - *Polynomial Chaos Based Design of Robust Input Shapers*. Journal of dynamic systems, measurement, and control, vol. 132, no. 5, 2010.

[38] J. FISHER, R. BHATTACHARYA - *Linear Quadratic Regulation of Systems with Stochastic Parameter Uncertainties*. Automatica, vol. 45, no. 12, pp. 2831-2841, 2009.

[39] D. XIU, G. KARNIADAKIS - *The Wiener-askey Polynomial Chaos for Stochastic Differential Equations*. SIAM Journal on Scientific Computing, vol. 24, no. 2, pp. 619-644, 2002.

[40] N. WIENER - *The Homogeneous Chaos.* American Journal of Mathematics, vol. 60, no. 4, pp. 897-936, 1938.

[41] M. D. WEBSTER, M. A. TATANF, G. J. MCRAE - *Application of the Probabilistic Collocation Method for an Uncertainty Analysis of a Simple Ocean Model*. Tech. Rep. 4, 1996.

[42] A. K. KAMATH, P. P. MENON, M. GANET-SCHOELLER, G. MAURICE, S. BENNANI, D. G. BATES - *Worst Case Analysis of a Launcher Vehicle Using Surrogate Models.* Proceedings of 7th IFAC Symposium on Robust Control Design, vol. 7, no. 1, 2012, pp. 260-265.

[43] R. STORN, K. PRICE - *Differential Evolution – A Simple and Efficient Heuristic for Global Optimization Over Continuous Spaces*. Journal of Global Optimization, vol. 11, no. 4, pp. 341-359, 1997.

[44] P. P. MENON, D. G. BATES, I. POSTLETHWAITE - *Hybrid Evolutionary Optimisation Methods for the Clearance of Nonlinear Flight Control Laws*. 44th IEEE Conference on Decision and Control, European Control Conference. CDC-ECC '05., December 2005, pp. 4053-4058.

[45] W. WANG, P. P. MENON, D. G. BATES, S. BENNANI - *Robustness Analysis of Attitude and Orbit Control Systems for Flexible Satellites*. Control Theory Applications, IET, vol. 4, no. 12, pp. 2958-2970, December.

[46] M. ZETTLER, J. GARLOFF - *Robustness Analysis of Polynomials with Polynomial Parameter Dependency Using Bernstein Expansion.* IEEE Transactions on Automatic Control, vol. 43, no. 3, pp. 425-431, 1998.

AUTHORS

Atul Kamath received the B.Eng. degree in electrical from Mumbai University, Mumbai, India, in 2005, the M.Tech. degree in control system engineering from Mumbai University, Mumbai, India., in 2008, and the Ph.D. degree in control engineering from the University of Exeter, Exeter, U.K., in 2014. He is currently working with General Electric's Global Research Center, Bangalore, India as a control system engineer. Email address: atul.kamath@ge.com

Prathyush P Menon is a senior lecturer in Mathematics. His research interests are control, optimisation, robustness analysis and autonomy.

Martine Ganet-Schoeller is currently a flight control engineer at Ariane Group in Les Mureaux, France.

Guillaume Maurice received a Master degree in engineering from ISAE Supaero, France in 2010. He is currently a flight control engineer at Ariane Group in Les Mureaux, France.

Samir Bennani has obtained a M.Sc. and a Ph.D from the TU Delft in aerospace engineering with specialisation in the field of systems theory and robust control applied to flight control systems. He is Guidance Navigation & Control System Engineer at European Space Agency (ESA), ESTEC. Within ESA, Samir Bennani has obtained the highest merit recognition in the field on Control being recommend as Ad Personal Control Systems Engineer to shape future needs and Competence Domain Lead Engineer for Space Transportation, Re-entry and Propulsion. He is a senior member of various international professional associations including the AIAA, IFAC and IEEE control systems society.

P. Vuillemin, F. Demourant, C. Poussot-Vassal
(ONERA)

E-mail: vuillemin@onera.fr

DOI: 10.12762/2017.AL13-10

Stability Analysis of a Set of Uncertain Large-Scale Dynamical Models with Saturations

From a sparse set of large-scale Linear Time Invariant (LTI) dynamical models, a methodology to generate a low-order parameter-dependent and uncertain model, with guaranteed bounds on the approximation error is firstly obtained using advanced approximation and interpolation techniques. Secondly, the stability of the aforementioned model, represented as a Linear Fractional Representation (LFR) and subject to actuator saturation and dynamical uncertainties, is addressed through the use of an irrational multiplier-based Integral Quadratic Constraint (IQC) approach. The effectiveness of the approach is assessed on a complex set of aeroservoelastic aircraft models used in an industrial framework for control design and validation purposes.

Introduction

Many techniques have been developed to model, control and assess the stability and performance of dynamical systems. When complex systems are considered, dedicated numerical software applications are usually used to accurately reproduce their dynamical behavior. The obtained models then result in large-scale ones equipped with a prohibitively high number of variables. Although complex models have a high degree of likeness with reality[1], in practice, due to finite machine precision and computational burden, they are problematic to manipulate. This is the case in many engineering fields, such as aerospace (e.g., aircraft [22], satellites, launchers, fluid flow mechanics), civilian structures, electronics (e.g., [11]), where control engineers have to cope with many practical problems, including lightly damped modes, nonlinear actuator(s), etc. Moreover, parametric uncertainties usually affect such models, accounting for variabilities and uncertainties. In most cases, the parametric dependency is not *a priori* known and local linear models, representing the system at frozen configurations, are often considered.

Let us consider a model $\mathbf{G}(\theta)$ of a physical dynamical system, which smoothly depends on a parameter $\theta \in \mathbb{R}^p$. This model is assumed to be only known through its linearized models $\mathbf{G}_i$ at some parametric points θ_i $(i = 1,\ldots,n_s)$. Let $\mathbf{G}_i$ be asymptotically stable large-scale Linear Time Invariant (LTI) dynamical models given by the state-space realizations:

$$\mathbf{G}(\theta_i) \overset{\text{lin.}}{=} \mathbf{G}_i : \begin{cases} \dot{x}_i(t) = A^{(i)}x_i(t) + B_1^{(i)}w(t) + B_2^{(i)}u(t) \\ z(t) = C_1^{(i)}x_i(t) + D_{11}^{(i)}w(t) + D_{12}^{(i)}u(t) \\ y(t) = C_2^{(i)}x_i(t) + D_{21}^{(i)}w(t) + D_{22}^{(i)}u(t) \end{cases} \quad (1)$$

where $x_i(t) \in \mathbb{R}^{n_i}$, $w(t) \in \mathbb{R}^{n_w}$, $u(t) \in \mathbb{R}$, $z(t) \in \mathbb{R}^{n_z}$ and $y(t) \in \mathbb{R}^{n_y}$ are the states, exogenous input, single control input, performance output and measurement signals, respectively. Moreover, let be given a robust n_k^{th} order LTI controller $\mathbf{K} = (A_K, B_K, C_K, D_K)$ with transfer $K(s) = C_K(sI_{n_k} - A_K)^{-1}B_K + D_K$, looped between $y(t)$ and $u(t)$, that ensures some robustness and performance specification(s) for all of the n_s models. Such a controller could, for instance, be obtained with robust optimization tools, such as [3]. For an example of synthesis, see [21] and the references therein.

The problem of assessing the stability of such a high-dimensional controlled system over the *continuum of parametric variations, when the single control input $u(t)$ is subject to saturations*, is addressed here. To this aim, as clarified in the rest of the paper and pursuant to Figure 1 and

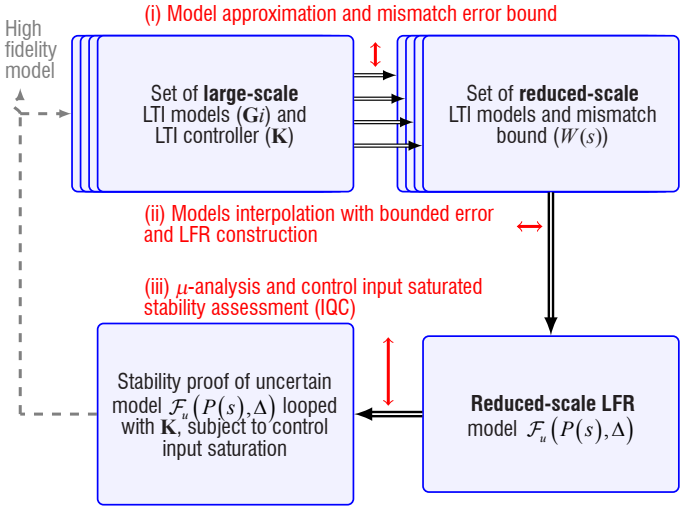

Figure 1 – Global process of the proposed approach (Algorithm 1)

[1] Of course, given that every model can always be questioned or amended, the approach is valid only according to the considered dynamical models, and additional precautions should be considered when it is applied to the real system.

Algorithm 1, a three-step methodology is proposed: *(i)* approximate the n_s dynamical models and bound the mismatch error, *(ii)* perform (inexact) interpolation of the reduced-order models with interpolation error bounds and, finally, *(iii)* assess the stability of the closed-loop model over both parametric variations and control input saturation limitations[2].

Algorithm 1 – Global procedure

Data: $\mathbf{G}_i(i=1,\ldots,n_s)$ describing a system at various **frozen** parameter combination values $\theta_i \in \mathbb{R}^p$ and a **robust** LTI controller $\mathbf{K}$.
Result: Stability assessment.
begin Step (*i*) (Section " Multi-LTI model approximation and error bound")

- Compute $\hat{G}_i(s)\ (i=1,\ldots,n_s)$ such that

$$\hat{G}_i := \arg \min_{H\in\mathcal{H}_\infty,\ \mathbf{rank}(H)=r} \left\| G_i - H \right\|_{\mathcal{H}_2,\Omega} \tag{2}$$

- Determine a low-order weighting function $W(s)$ s.t. $\forall i=1\ldots n_s,\ \exists \Delta_{R_i} \in \mathcal{H}_\infty\ ,\ \| \Delta_{R_i} \|_{\mathcal{H}_\infty} \le 1$ and:

$$F_i(s) = \hat{F}_i(s) + W(s)\Delta_{R_i}(s) \tag{3}$$

with $F_i(s) = K(s)\,G_i(s)$ and $\hat{F}_i(s) = K(s)\,\hat{G}_i(s)$.

return *A set of reduced-order approximations* $\hat{F}_i(s)$.
begin Step (*ii*) (Section "Bounded-error reduced-order LFR model generation")

- Compute a parameter-dependent LFR approximation $\hat{P}(s)$ associated with the normalized and lowest-size block-diagonal parametric structure $\Theta(\theta)$ such that, for each parametric configuration $\Theta_i = \Theta(\theta_i)$ there exists a real-valued norm-bounded structured uncertainty $\mathbf{\Delta}_P$ capturing the interpolation errors, such that:

$$\hat{F}_i(s) = \mathcal{F}_u\left(\hat{P}(s), \mathbf{diag}\left(\Theta_i, \Delta_P\right)\right) \tag{4}$$

- Combine (3) and (4), construct $P(s)$ including all errors, where $\mathbf{\Delta} = \mathbf{diag}\,(\Theta_i, \Delta_P, \Delta_R(s))$, such that,

$$F_i(s) = \mathcal{F}_u\left(P(s), \mathbf{\Delta}\right) \text{ with } \left\|\mathbf{\Delta}\right\|_{H_\infty} \le 1 \tag{5}$$

return *A low-order uncertain LFR model* $\mathcal{F}_u(P(s),\mathbf{\Delta})$ *covering the initial set* $\{F_i(s)\}_{i=1\ldots n_s}$.
begin Step (*iii*) (Section "Stability assessment")

- Close the open-loop LFR model $P(s)$ without input saturation, build the standard form $M(s)-\mathbf{\Delta}$ and check the robust stability by means of a μ test:

$$\forall \omega \ge 0,\ \ \mu_{\mathbf{\Delta}}\left(M(j\omega)\right) \le 1 \tag{6}$$

- Close the open-loop LFR model $P(s)$ with input saturation to obtain an augmented nonlinear standard form $M(s) - \mathbf{diag}\,(\varphi, \mathbf{\Delta})$ and check the robust stability by means of an IQC-based analysis test.

$$\forall \omega \in \mathbb{R}\ \ \left[M(j\omega)*I\right]\Pi(j\omega)\left[M(j\omega)*I\right]^* < 0 \tag{7}$$

return *A stability proof of the input-saturated closed-loop large-scale models.*

[2] Note that, in practice, people usually reduce and perform the analysis in a trial and error way, which is of course tedious and time-consuming.

In comparison to [22] and [26] contributions, the proposed approach is accompanied with both approximation (Step *(i)*) and interpolation (Step *(ii)*) errors. Hence, the μ (structured singular value) and Integral Quadratic Constraint (IQC) analysis (Step *(iii)*) respectively provide *sufficient stability conditions for the entire set of closed-loop models, without and with saturation*. This represents the *main contribution of this paper*. It is also worth mentioning that the irrational multiplier-based approach developed in Step *(iii)* is an extension of [6]. It is shown that no solution is obtained by means of a rational multiplier and only a frequency domain approach can be used here to assess the closed-loop stability.

The paper is organized following the schematic view of Figure 1. First, the main result, *i.e.*, the procedure to assess the stability of a set of large-scale models looped with a control law subject to saturations, is described. Then we illustrate the proposed procedure on a complex large-scale aeroservoelastic business jet aircraft model for various flight configurations, looped with an anti-vibration controller. To end, Conclusions are given.

Notations

Given three operators $P(\cdot)$, $M(\cdot)$ and $\Delta(\cdot)$ of compatible dimensions, the lower and upper Linear Fractional Transformations (LFTs) are respectively defined (for appropriate partitions of P and M) by $\mathcal{F}_l(P,\Delta) = P_{11} + P_{12}\Delta(I-P_{22})^{-1}P_{21}$ and $\mathcal{F}_u(M,\Delta) = M_{22} + M_{21}\Delta(I-M_{11})^{-1}M_{12}$. The star product $\star$ of P and M is defined by:

$$P \star M = \begin{bmatrix} \mathcal{F}_l\left(P, M_{11}\right) & P_{12}\left(I - M_{11}P_{22}\right)^{-1}M_{12} \\ M_{21}\left(I - P_{22}M_{11}\right)^{-1}P_{21} & \mathcal{F}_u\left(M, P_{22}\right) \end{bmatrix} \tag{8}$$

Given a matrix $M \in C^{p\times m}$, $M_{j,k} = M(j,k)$ (with $1 \le j \le p$ and $1 \le k \le m$) denotes the scalar coefficient in the j^{th} row and k^{th} column of M, M^* denotes the conjugate transpose of M and $\bar{\sigma}(M)$, its largest singular value. The frequency-limited norm, denoted by $\mathcal{H}_2$-norm, is defined as the restriction of the $\mathcal{H}_2$-norm over the interval $\Omega = [0,\omega]$ with $\omega \in \mathbb{R}_+$, where $\mathbb{R}_+$ denotes the set of positive real numbers. Given an asymptotically stable LTI model realization $\mathbf{H}$ with transfer function $H(s)$, $\|H\|_{\mathcal{H}_{2,\Omega}} := (\frac{1}{\pi}\int_\Omega \|H(j\nu)\|_F^2\, d\nu)^{\frac{1}{2}}$ [19, 27].

Main result: Stability guarantee of a set of large-scale models subjec t to input saturations

With reference to Figure 1, the proposed contribution, in three steps, are summarized in Algorithm 1. More specifically, an optimal frequency-limited approximation algorithm is first applied, followed by the creation of a frequency-dependent mismatch bound (Step *(i)*, Section "Multi-LTI model approximation and error bound"), then the interpolation and transformation into a Linear Fractional Representation (LFR) structure is achieved (Step *(ii)*, Section "Bounded-error reduced-order LFR model generation"), and finally, the stability of the overall uncertain, parameter-dependent model is firstly assessed thanks to a μ analysis, and then, when subject to control input saturation, through a novel IQC technique (Step *(iii)*, Section "Stability assessment").

Multi-LTI model approximation and error bound

Generally speaking, the main objective of the approximation step is to capture, with a stable low order model, the initial large-scale model most relevant dynamics. Various approaches exist for the approximation of large-scale LTI models (see [2] for a general overview of model reduction and refer to Box 1 for an overview of the tool used here to perform the model approximation step) and one of them consists in formalizing the model approximation problem as an optimization one. The problem then consists in finding a reduced-order model that minimizes a given norm of the approximation error.

In the literature, the $\mathcal{H}_2$-norm has often been considered and several methods are now available to address the corresponding optimal $\mathcal{H}_2$ model approximation problem (see e.g., [8, 10]). However, in many cases, considering a limited frequency interval only is more relevant since *(i)* the system dynamics might not be perfectly known over the whole frequency domain, meaning that the model is inaccurate in some frequency intervals. Discarding these areas enables the approximation accuracy to be increased, where the initial model is accurate. Besides *(ii),* controllers are usually designed to act over a limited frequency interval (due to actuator bandwidth or to prevent them from disturbing non-modeled dynamics), which means that a precise knowledge of the dynamics over the entire frequency domain is not necessarily useful. From the authors' point of view, the optimal approximation over a bounded frequency interval enables these practical considerations to be translated elegantly and is therefore preferred here. It is addressed through the use of the *frequency-limited $\mathcal{H}_2$-norm* in Section "Optimal frequency-limited $\mathcal{H}_2$ model approximation". However, it is worth noticing that the overall methodology summarized in Algorithm 1

more

model reduction toolbox

Box 1 - The MORE toolbox

The more toolbox gathers a set of tools aimed at alleviating the numerical burden induced by the complexity of dynamical models (e.g. for simulation, control, optimization, etc.).

More specifically, it contains several model approximation techniques designed to cope with several large-scale problems as depicted below.

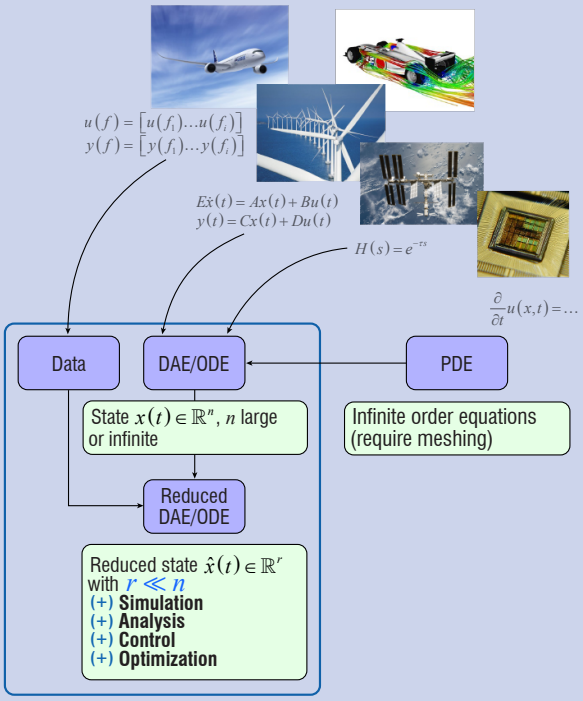

Figure B1-1 – Overview of the MORE toolbox

More formally, the problems that can be adressed are the following:

- **Reduction from state-space**: considering a LTI dynamical model $\mathbf{H}$ represented by a large-scale differential equation,

$$\begin{cases}\dot{x}(t)=Ax(t)+Bu(t)\\ y(t)=Cx(t)+Du(t)\end{cases} \quad \text{(B1-1)}$$

where $x(t)\in\mathbb{R}$, $u(t)\in\mathbb{R}^{n_u}$ and $y(t)\in\mathbb{R}^{n_y}$ are the state, command inputs and outputs of the model, respectively. The objective is to find a smaller model $\hat{\mathbf{H}}$ represented by

$$\begin{cases}\dot{\hat{x}}(t)=\hat{A}\hat{x}(t)+\hat{B}u(t)\\ \hat{y}(t)=\hat{C}\hat{x}(t)+\hat{D}u(t)\end{cases} \quad \text{(B1-2)}$$

with $\hat{x}(t)\in\mathbb{R}^r (r\ll n)$ and $\hat{y}(t)\in\mathbb{R}^{n_y}$ such that the input-output behaviors of $\mathbf{H}$ and $\hat{\mathbf{H}}$ are close.

In the toolbox, this closeness is generally considered through optimality considerations based on the H_2-norm of the approximation error or its restriction to a bounded frequency interval (as used in this paper).

- **Reduction from data**: the initial model is only known through a set of frequency data $\{s_i, H(s_i)\}_{i=1,\ldots,n}$ with $s_i\in\mathbb{C}$. The objective is then to find a low-complexity model such as $\hat{\mathbf{H}}$ in equation (B1-2) that matches the frequency data.

- **Reduction of infinite dimensional models**: the initial model is known through its irrational transfer function $H(s)\in\mathbb{C}^{n_y\times n_u}$ obtained for instance from a partial differential equation (PDE), from a delayed differential equation, etc. Again, the objective is to build a low-complexity model $\hat{\mathbf{H}}$ as in (B1-2) such that the input-output behavior of H is well reproduced (for instance in the $\mathcal{H}_2$ sense).

For further information, interested readers should refer to the site of the toolbox : www.onera.fr/more.

does not depend on the approximation strategy, since the approximation error is bounded in Section "Bound on the approximation error".

Optimal frequency-limited model approximation

Using the $\mathcal{H}_{2,\Omega}$-norm, one can formulate the approximation over a bounded frequency interval as an optimization problem. More specifically, given an asymptotically stable n^{th} order large-scale model $\mathbf{G}$ and a frequency interval Ω, the *optimal $\mathcal{H}_{2,\Omega}$ model approximation problem* consists in finding a reduced-order model $\hat{\mathbf{G}}$ of order $r \ll n$ that minimizes the $\mathcal{H}_{2,\Omega}$-norm of the approximation error $\mathbf{G}-\hat{\mathbf{G}}$, *i.e.*,

$$\hat{G} = \arg \min_{H \in H_\infty, \, \mathbf{rank}(H)=r} \|G-H\|_{\mathcal{H}_{2,\Omega}} \tag{9}$$

Here, Problem (9) is addressed using the method called *Descent Algorithm for Residue and Pole Optimization* (**DARPO**), proposed in [27]. It relies on the pole-residue formulation of the $\mathcal{H}_{2,\Omega}$-norm [28] and finds the poles and associated residues of the reduced-order model that satisfy the first-order optimality conditions associated with Problem (9). Note that, since this problem is not convex, the reduced-order model obtained this way is only a local minimum.

With reference to Algorithm 1 (Step *(i)*), the approximation algorithm is applied to each large-scale model $\mathbf{G}_i$, $i=1,\ldots,n_s$ resulting in n_s small-scale models $\hat{\mathbf{G}}_i$ minimizing the $\mathcal{H}_{2,\Omega}$-norm of the approximation error with $\mathbf{G}_i$, as stated in (2).

Note that both the approximation order r and the frequency-interval Ω are tuning parameters that depend on the considered application. However, as mentioned before, the frequency interval Ω can be chosen as the interval that contains the most relevant dynamics of the physical systems. Observing the decay of the eigenvalues of the product of the frequency-limited gramians $\mathcal{P}_\Omega \mathcal{Q}_\Omega$ (see e.g., [9, Chap. 4]), which can be viewed as the Hankel singular values in the frequency-limited case, can give an idea of the adequate approximation order r.

The stability analysis must take into account the error induced by the approximation step. For that purpose, a low-complexity model upper bounding the worst approximation error is built in the next section.

Bound on the approximation error

Let us denote by $F_i(s)=K(s)\,G_i(s)$ and $\hat{F}_i(s)=K(s)\,\hat{G}_i(s)$ the open-loops from the inputs of the large and small scale models to the output of the controller[3] $\mathbf{K}$. Let us denote the order of $\hat{F}_i(s)$ as $n=r+n_K$. The objective of this section is to model the approximation error $\Sigma_i(s)=F_i(s)-\hat{F}_i(s)$ $(i=1,\ldots,n_s)$ as a low-order additive output uncertainty. More specifically, a low-order filter $W(s)$ is sought, such that $\forall i=1,\ldots,n_s$, $\exists \Delta_{R_i} \in \mathcal{H}_\infty$ with $\|\Delta_{R_i}\|_{\mathcal{H}_\infty} \le 1$ and $F_i(s)=\hat{F}_i(s)+W(s)\Delta_{R_i}(s)$.

Then, the stability of the set of uncertain models $\{\hat{F}_i(s)+W(s)\Delta_R(s), \|\Delta_R\|_{\mathcal{H}_\infty} \le 1\}$ implies the stability of the finite set of models $\{F_i(s)\}_{i=1,\ldots,n_s}$. Note that any invertible filter $W(s)$, such that,

$$\max_{i=1,\ldots,n_s} \|W^{-1}\Sigma_i\|_{\mathcal{H}_\infty} \le 1 \tag{10}$$

can be used, since one can always exhibit $\Delta_{R_i}(s)=W^{-1}(s)\,\Sigma_i(s)$ such that $F_i(s)=\hat{F}_i(s)+W(s)\,\Delta_{R_i}(s)$.

[3] The controller is included here to be consistent with the interpolation step of Section "Bounded-error reduced-order LFR model generation".

The design of $W(s)$ then consists in a trade-off between complexity and conservatism. Indeed, one must find a $W(s)$ that is both an accurate modeling of the worst approximation error and whose complexity (order) is reasonable. For instance, $W=\max_{i=1,\ldots,n_s}\|\Sigma_i\|_{H_\infty}$ obviously satisfies (3). However, it does not offer an accurate model of the approximation error and might, therefore, be too conservative for stability analysis. A direct approach to design $W(s)$ satisfying (10) would consist in using non-smooth $\mathcal{H}_\infty$ optimization tools [3] to solve the following problem

$$\begin{array}{ll} \min & \|W\|_{\mathcal{H}_\infty} \\ s.t. & \left\|W^{-1}\Sigma_i\right\|_{\mathcal{H}_\infty} \le \quad i=1,\ldots,n_s \end{array} \tag{11}$$

However, depending on the application, the errors Σ_i might be too large for such an approach to be tractable. In those cases, a heuristic approach may then be preferable.

Bounded-error reduced-order LFR model generation

Consider the parametrically-dependent set $\{\hat{F}_i(s)\}_{i=1\ldots n_s}$ of reduced-order models obtained above; the objective is now to derive a limited-size LFR, such that μ and IQC-based analysis tools can then be applied. In the general case, involving **several parameters** ($\theta \in \mathbb{R}^p$), the n_s equations (4) must be solved for a parametric structure, e.g., $\Theta_i = diag(\theta_1 I_{n_{\theta_1}}, \ldots, \theta_{p_i} I_{n_{\theta_p}})$, whose size $n_\Theta = \sum_{k=1}^{p} n_{\theta_k}$ should be kept as small as possible. Efficient solutions, based on multivariate sparse polynomial or rational interpolation techniques, are detailed in [14, 5, 22].

In the case of a **scalar parameter** ($\theta \in \mathbb{R}$), a specific technique can be developed to compute low-order LFR models whose Δ-block will both include the parametric variations (Θ) and a normalized real-valued uncertain operator (Δ_p). The latter is introduced to "cover" the interpolation errors, as illustrated by Equation (4). The proposed technique, based on a polynomial state-space data interpolation approach, can be broken down into three steps, which are briefly presented next.

Step 1: model rewriting in a rescaled companion form

Reduced-size LFR models are easier to obtain when all varying data appear in a limited number of rows (or columns) of each state-space representation. A companion form is thus a good choice, but unfortunately leads to ill-conditioned matrices as the system order increases. As is also proposed in [7], a rescaled companion form will then be used. Using the notation $\hat{F}_i(s)=C_i(sI_n-A_i)^{-1}B_i+D_i$ the system is rewritten as:

$$\left(\begin{array}{c|c} A_i & B_i \\ \hline C_i & D_i \end{array}\right) = \left(\begin{array}{cccc|c} 0 & \lambda_1 & & 0 & 0 \\ \vdots & & \ddots & \vdots & \vdots \\ 0 & 0 & \ldots & \lambda_{n-1} & 0 \\ a_1^{(i)} & a_2^{(i)} & \ldots & a_n^{(i)} & b^{(i)} \\ \hline c_1^{(i)} & c_2^{(i)} & \ldots & c_n^{(i)} & d^{(i)} \end{array}\right) \tag{5}$$

where the scaling variables $\{\lambda_k\}_{k=1\ldots n-1}$, with the help of standard numerical balancing techniques, are tuned to optimize the average condition number of each matrix A_i. Note that the standard companion form is recovered for $\lambda_k=1$.

Remark 1

In the context of LFR modeling, the above description is of high interest since the varying state-space data all appear in the last two rows. Assuming that every coefficient is approximated by a p^{th} order polynomial, the size of $\Theta = \theta I_{n_\theta}$ will then be limited to $n_\Theta = 2p$.

Polynomial interpolation with guaranteed error bounds

Let us denote by Y_i the last two lines in Equation (12):

$$Y_i = \begin{pmatrix} a_1^{(i)} & a_2^{(i)} & \dots & a_n^{(i)} & b^{(i)} \\ c_1^{(i)} & c_2^{(i)} & \dots & c_n^{(i)} & d^{(i)} \end{pmatrix} \in \mathbb{R}^{2\times(n+1)} \quad (13)$$

and focus on the polynomial approximation of the finite set $\{Y_i\}_{i=1\dots n_s}$ with guaranteed and minimized error bounds. Given p, the order of the polynomial, the problem is reduced to the determination of an error matrix $E \in \mathbb{R}_+^{2\times(n+1)}$ and a set of matrices $\{X_q\}_{q=0\dots p}$, such that the non-negative entries of E are minimized under the following *linear* constraints (with $j = 1,2$ and $k = 1\dots n+1$):

$$\left| \left[X_0 + \sum_{q=1}^{p} \theta_i^q X_q - Y_i \right]_{j,k} \right| \le E_{j,k}, \; i = 1\dots n_s \quad (14)$$

The above optimization problem is easily solved by any standard linear programming solver. However, the order p of the polynomial should be carefully chosen. Low orders will indeed result in rough approximations yielding conservative models with large entries in E. Conversely, high order polynomials will improve the accuracy at the interpolation points. Moreover, critical oscillations are likely to appear between the interpolation points when the difference $n_s - p$ gets too small. This issue and possible remedies are further discussed in the applicative part.

LFR modeling

Proposition 1

From Inequalities (14), E-dependent "shaping" matrices $U(E)$ and $V(E)$ of appropriate dimensions and a bounded, real-valued, block-diagonal uncertain operator Δ_P:

$$\Delta_P = \mathbf{diag}\left(\delta_{p_1} I_{n\delta_{P_1}}, \dots, \delta_{p_r} I_{n\delta_{P_r}}\right) \quad (15)$$

can be easily defined, such that the function:

$$\mathcal{Y}(\theta, \Delta_P) = X_0 + \sum_{q=1}^{p} \theta^q X_q + U(E).\Delta_P.V(E) \quad (16)$$

satisfies the following statement:

$$\forall i = 1,\dots,n_s, \exists \Delta_P \,/\, |\delta_{p_k}| \le 1 \text{ and } \mathcal{Y}(\theta_i, \Delta_P) = Y_i \quad (17)$$

Proof

The above proposition is trivially satisfied with the following (non-minimal) choice:

$$\Delta_P = \mathbf{diag}\left(\delta_{p_1}, \dots, \delta_{p_{2n+2}}\right) \in \mathbb{R}^{(2n+2)\times(2n+2)}$$

$$U = \begin{pmatrix} 1\dots1 & 0\dots0 \\ 0\dots0 & 1\dots1 \end{pmatrix} \in \mathbb{R}^{2\times(2n+2)}$$

and $V(E) = \mathbf{diag}\left(E_{1,1}, \dots, E_{1,n+1}, E_{2,1}, \dots, E_{2,n+1}\right)$

Remarking that $\mathcal{Y}(\theta, \Delta_P)$ polynomially depends on θ and affinely depends on Δ_P, standard algorithms (see [15] for further details) can be applied to compute the interconnection matrix $\mathcal{X}$, such that:

$$\mathcal{Y}(\theta, \Delta_P) = \mathcal{F}_u(\mathcal{X}, \Theta, \Delta_P) = \mathcal{F}_u\left(\mathcal{X}, \mathbf{diag}\left(\theta I_{2p}, \Delta_P\right)\right) \quad (18)$$

Next, standard LFR object manipulations implemented in the LFR toolbox [15] yield the required open-loop LFR models depicted in (4) and (5). Once again, standard manipulations are used to "construct" the closed-loop $M(s) - \Delta$ standard forms that will include or not the saturation-type nonlinearity and will be used to check the stability.

Stability assessment

At this point, a low-order uncertain LFR model $\mathcal{F}_u(P(s), \Delta)$ covering the initial set $\{F_i(s)\}_{i=1\dots n_s}$ is available. The objective of this section is to prove the stability of the closed-loop LFR model $P(s)$, both with and without input saturation. As summarized in Algorithm 1, the proposed analysis method consists of two steps. No saturation is considered in the first, which can be viewed as a LFR model validation test. In a second step, an input saturation is introduced and the IQC-based analysis is considered.

Stability analysis without saturation using μ tools

Without saturation, the uncertain closed-loop model under consideration assumes an LTI standard form $M(s) - \mathbf{\Delta}$, where $\mathbf{\Delta} = \mathbf{diag}(\Theta, \Delta_P, \Delta_R(s))$ is a normalized LTI structured uncertainty block. As a result, the stability of the **continuum** (covering the initial set of full-order plants) of closed-loop models obtained for any admissible uncertainty inside the unit ball is guaranteed if and only if:

$$\forall \omega \ge 0, \mu_{\mathbf{\Delta}}\left(M(j\omega)\right) \le 1 \quad (19)$$

where $\mu_{\mathbf{\Delta}}(M)$, for any complex-valued matrix M, denotes the structured singular value with respect to $\mathbf{\Delta}$ and provides the inverse of the size of the critical uncertainty beyond which stability is no longer guaranteed (see [17] for further details). Testing (19) raises two difficulties. The computation of μ is an NP-hard optimization problem, which, in addition, must be solved for an infinite set of frequencies. However, as is emphasized in [23], recent implementations (used in this paper) of this μ test in [4, 24] provide quite efficient tools even for high-order plants with numerous and repeated uncertainties (see also [13]).

Remark 2

The proposed μ test is clearly a necessary stability condition. If there exists $\omega^* \ge 0$ such that $\mu_\Delta(M(j\omega^*)) > 1$, then the accuracy of the model should be improved in order to minimize the effects of Δ_P and $\Delta_R(s)$.

Stability analysis with saturation using IQC

IQC-based analysis techniques enable a wide range of problems to be studied, namely the robust stability and performance properties of the interconnection $M(s) - \mathbf{\Delta}$ of an LTI operator $M(s)$ with a structured model uncertainty $\mathbf{\Delta}$ containing nonlinearities, LTI and/or linear time-varying (LTV) parameters, neglected dynamics, delays, specific nonlinearities such as friction, hysteresis, etc. (see, e.g., [20]).

Here, standard IQC descriptions are used for both *LTI uncertainties, Δ and sector nonlinearities, denoted by φ*. The originality of our approach resides in the specific algorithm that has been developed to reduce the computational burden. Indeed, standard IQC-oriented analysis methods consist in solving KYP (Kalman-Yakubovitch-Popov)-based LMI conditions [16]. Theses standard approaches are however intractable for high-order models, since the number of scalar optimization variables quadratically increases with the closed-loop order [6]. Moreover, this approach is not compatible with the use of irrational multipliers[4].

IQC generalities

An IQC describes a relation between the input and output signals of an operator. Since these two formulations are completely equivalent, these constraints can be defined either in the time or the frequency domain. Nevertheless, frequency domain constraints are often preferred, since they lead to simpler stability conditions. The definition of an IQC is given in the frequency domain:

Definition 1

Two signals, respectively of dimension m and p, square integrable on $[0,\infty)$, i.e. : $v \in L_2^m[0,\infty)$, $w \in L_2^p[0,\infty)$, satisfy the IQC defined by $\Pi : j\mathbb{R} \to C^{(m+p)\times(m+p)}$, and Hermitian-valued function, iff:

$$\int_{-\infty}^{\infty} \begin{bmatrix} \tilde{v}(j\omega) \\ \tilde{w}(j\omega) \end{bmatrix}^* \Pi(j\omega) \begin{bmatrix} \tilde{v}(j\omega) \\ \tilde{w}(j\omega) \end{bmatrix} d\omega \geq 0 \qquad (20)$$

where $\tilde{v}(j\omega)$ and $\tilde{w}(j\omega)$ respectively correspond to Fourier transforms of v and w, such as $w = \Delta v$.

The problem consists in analyzing the closed-loop that corresponds to the interconnection by a positive feedback of $M(s)$ with Δ, where Δ can be nonlinear and non-stationary. Let us suppose that input and output signals of Δ satisfy the IQC defined by Π. The following result gives the stability criterion [16].

Theorem 1

Let us suppose that $M(s)$ is stable and that Δ is a causal and bounded operator, if

- *interconnection $M - \tau\Delta$ is well posed for any $\tau \in [0,1]$,*
- *$\tau\Delta$ satisfies the IQCs defined by Π, $\forall \tau \in [0,1]$,*
- *there exists $\varepsilon > 0$ such as:*

$$\forall \omega \in \mathbb{R} \quad \underbrace{\begin{bmatrix} M(j\omega) \\ I \end{bmatrix}^* \Pi(j\omega) \begin{bmatrix} M(j\omega) \\ I \end{bmatrix}}_{Z(j\omega)} \leq -\varepsilon I \qquad (21)$$

then, the closed-loop system is stable.

Let us consider a stable $M(s)$, forming the constant block of the LFR and an augmented block $\Delta \leftarrow \mathbf{diag}(\varphi, \Delta)$[5], where φ represents one sector slope-restricted nonlinearity (0,1). The global multiplier Π corresponding to Δ is built as follows (see [12, 16, 18] for additional details):

$$\Pi(j\omega) = \begin{bmatrix} 0 & 0 & x + j\omega\lambda + \omega^2\gamma & 0 \\ 0 & X(j\omega) & 0 & Y(j\omega) \\ x - j\omega\lambda + \omega^2\gamma & 0 & -2x - 2\omega^2\gamma & 0 \\ 0 & Y^*(j\omega) & 0 & -X(j\omega) \end{bmatrix} \qquad (22)$$

$$X(j\omega) = \mathbf{diag}\left(X_\Theta(j\omega), X_P(j\omega), x_{\Delta_R}\right)$$

$$Y(j\omega) = \mathbf{diag}\left(Y_\Theta(j\omega), Y_P(j\omega), 0\right)$$

where $X_\Theta(j\omega) = X_\Theta^*(j\omega) \geq 0 \in C^{n_\Theta \times n_\Theta}$, $X_P(j\omega) = X_P^*(j\omega) \geq 0 \in C^{(2n+2)\times(2n+2)}$, $Y_\Theta(j\omega) = -Y_\Theta^*(j\omega) \in C^{n_\Theta \times n_\Theta}$, $Y_P(j\omega) = -Y_P^*(j\omega) \in C^{(2n+2)\times(2n+2)}$, $x \geq 0$, $x_{\Delta_R} \geq 0$, $\gamma \geq 0$ and $\lambda \in \mathbb{R}$. Closed-loop stability is ensured if a solution of the following LMI can be found, $\forall \omega \in \mathbb{R}_+$:

$$\begin{bmatrix} M(j\omega) \\ I \end{bmatrix}^* \Pi\left(x, \lambda, \gamma, X(j\omega), Y(j\omega)\right) \begin{bmatrix} M(j\omega) \\ I \end{bmatrix} < 0 \qquad (23)$$

Proposed innovative method

In this paper, the optimization problem is solved directly from frequency domain inequalities through a grid-based approach. A similar approach is used in [1], but without guarantee of the solution validity over the entire frequency domain. Here, in order to guarantee that the solution is valid over the entire frequency domain, a specific technique based on [25, 4] is adapted to our problem [6]. In addition, another advantage is to limit the number of LMI constraints, since only active constraints are added in the LMI optimization problem. Here, the main result is presented.

Let $\Xi = (A_\Xi, B_\Xi, C_\Xi, D_\Xi)$ be the realization of $\Xi(s)$ (of order m), with $\Xi(j\omega) = (I - Z(j\omega))(I + Z(j\omega))^{-1}$ ($(I+Z)$ is invertible) where $Z(j\omega) = Z^*(j\omega)$ is the stability criterion (21), and $\Xi(j(\omega_0 + \delta\omega)) = \mathcal{F}_l(S(\omega_0), \delta\omega I_m)$, with $\forall\, \delta\omega \geq -\omega_0$, *i.e.*, $S(\omega_0)$ is interconnected to $\delta\omega$ as a lower LFT, where $\delta\omega$ is a real parameter. $S(\omega_0)$ is written as

$$S(\omega_0) = \begin{pmatrix} D_\Xi & \frac{C_\Xi}{\sqrt{j}} \\ \frac{B_\Xi}{\sqrt{j}} & -jA_\Xi \end{pmatrix} \star \left(\frac{1}{\omega_0} \begin{pmatrix} I & I \\ -I & -I \end{pmatrix} \right) \qquad (24)$$

Proposition 2

If $\bar{\sigma}(\Xi(\omega_0)) < 1$ then $\bar{\sigma}(\mathcal{F}_l(S(\omega_0), \delta\omega I_m)) < 1$ holds true for $\omega_0 + \delta\omega \in [\underline{\omega}, \bar{\omega}]$, where $\underline{\omega}$ and $\bar{\omega}$ are computed as $\underline{\omega} = \omega_0 + \frac{1}{\eta_n}$ and $\bar{\omega} = \omega_0 + \frac{1}{\eta_p}$, where η_n and η_p are the maximal magnitude real negative and positive eigenvalues of T, respectively, defined as

$$T = \begin{bmatrix} S_{22} & 0 \\ 0 & S_{22}^* \end{bmatrix} - \begin{bmatrix} 0 & S_{21} \\ S_{12}^* & 0 \end{bmatrix} X^{-1} \begin{bmatrix} S_{12} & 0 \\ 0 & S_{21}^* \end{bmatrix} \qquad (25)$$

where,

$$S(\omega_0) = \begin{bmatrix} S_{11} & S_{12} \\ S_{21} & S_{22} \end{bmatrix} \text{ and } X = \begin{bmatrix} I & S_{11} \\ S_{11}^* & I \end{bmatrix} \qquad (26)$$

Remark 3

When $\bar{\sigma}(\Xi(+\infty)) = 1$, $\bar{\omega} = +\infty \Leftrightarrow \eta_p = 0$, a null eigenvalue is obtained, which means that $\bar{\sigma}(\Xi(\omega))$ crosses the 0 dB axis for $\omega = +\infty$. However, the intersection of the stability criterion with the 0 dB axis has no physical meaning.

---

[4] This constraint renders it necessary to fix the poles of the multipliers a priori (via a time-consuming trial-and-error process), without any guarantee on the optimality of the selected poles.

[5] Note that Δ is the same uncertain block as in Section "Bounded-error reduced-order LFR model generation" (containing the neglected model reduction dynamics $\Delta_R(s)s$, parametric variations Θ and interpolation errors Δ_P), augmented with φ, the saturation nonlinearity.

Remark 4

The bilinear transformation $\Xi(j\omega) = (I - Z(j\omega))(I + Z(j\omega))^{-1}$ *with* $(I + Z)$ *invertible allows a positivity condition to be transformed into a weak gain condition:*

$$\bar{\sigma}(\Xi) \leq 1 \Leftrightarrow Z + Z^* \geq 0 \tag{27}$$

In the iterative approach, proposed in Algorithm 2, the validation step is performed *a priori* and during the LMI optimization problem resolution. The choice of the initial grid has no influence on the feasibility problem. It is possible to choose a singleton at the first iteration. However, in order to limit the number of iterations, and consequently the calculation time, without any *a priori* knowledge, it is recommended to take some frequencies roughly spread throughout the frequency domain. It is possible, when first solutions are obtained, to tune this initial frequency grid to decrease the number of iterations.

Algorithm 2 – Iterative IQC resolution

Data: $M(j\omega)$ the stable fixed block of the LFR, multiplier $\Pi(\omega_i)$ and $\omega_i \in \mathbb{R}_+$, $i = 1, \ldots n_f$.
Result: A stability proof of the LFR model, including nonlinear sector saturations.
while *stability not checked* **do**
For $i = 1, \ldots n_f$, check the stability criterion

$$\begin{bmatrix} M(j\omega_i) \\ I \end{bmatrix}^* \Pi(\omega_i) \begin{bmatrix} M(j\omega_i) \\ I \end{bmatrix} < 0 \tag{28}$$

if *(28) has solutions* **then**
- Set $\Pi_i \leftarrow \Pi(\omega_i)$ be the solution obtained at ω_i.
- Set $\omega_0 \leftarrow w_i$ and apply Proposition 2.
- For each solution Π_i, a frequency-domain $\Omega_i = [\underline{\omega}_i, \overline{\omega}_i]$ is obtained. $\Omega_{valid} = \bigcup_{i=1,\ldots,n_f} \Omega_i$.

if $\Omega_{valid} = [0 + \infty)$ **then**
The solution composed by the set of Π_i is validated on the whole frequency domain.
Stability is proved, **stop**.
else
- Determine the complementary set $\Omega_{novalid} = \mathbf{C}_{[0,+\infty)} \Omega_{valid}$.
- Select one or several frequencies in $\Omega_{novalid}$ and update the grid.

else
Stability cannot be proved, **stop**.

This approach allows the frequency domain irrational multipliers $X(j\omega)$ to be piecewise continuous. More specifically, between each Ω_i, these multipliers are discontinuous, consequently no state-space representation for these multipliers can exist. Involving a state-space representation in order to parameterize multipliers would necessarily lead to constraining the solution and increasing the conservatism. Of course, it is also possible to use rational multipliers with a frequency domain resolution, by using the factorized form of $X(s)$ presented previously [6]. The auxiliary matrix P is still avoided, but without the advantage of using irrational multipliers.

Application to an aeroelastic aircraft system

The methodology described in Section "Main result: Stability guarantee of a set of large-scale models subject to input saturations" and summarized in Algorithm 2 is now applied to check the stability of a set of $n_s = 3$ large-scale models ($n_i \approx 600$) representing the local behavior of an industrial aircraft for different Mach numbers, looped with $\mathbf{K}$, an anti-vibration controller ($n_K = 6$) [22].

Step 1: LTI approximation and error bound (II-B)

Approximation

The $n_s = 3$ large-scale models $\mathbf{G}_i$ of order $n_i \approx 600$, are approximated by $\hat{\mathbf{G}}_i$ of order $r = 16$ over $\Omega = [0, \omega_r]$. The frequency interval Ω is chosen to keep the low frequency behavior of the large-scale models, since it is known to be accurate, whereas the dynamics above ω_r are less accurately known and are therefore discarded. The approximation order r is then chosen experimentally to achieve a low approximation error over Ω. The relative approximation errors, *i.e.*, $e_i = \| G_i - \hat{G}_i \|_{\mathcal{H}_{2,\Omega}} / \| G_i \|_{\mathcal{H}_{2,\Omega}}$, $i = 1, 2, 3$, are respectively equal to 2.86 %, 2.39 % and 2.49 %. Figure 2 illustrates these low errors through the largest singular value of $\mathbf{G}_1$ and of $\hat{\mathbf{G}}_1$.

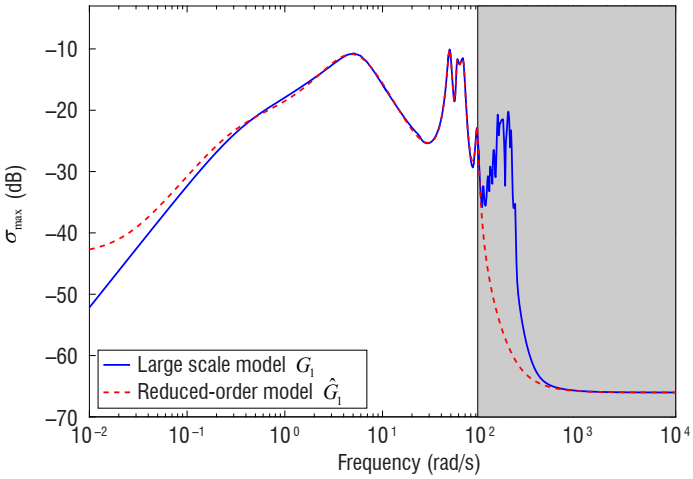

Figure 2 – The largest singular value of $\mathbf{G}_1$ and of the 16th order reduced-order model $\hat{\mathbf{G}}_1$ obtained with **DARPO**, with $\Omega = [0, \omega_r]$. The gray area represents the discarded frequencies (*i.e.*, above ω_r)

Figure 2 illustrates that the dynamics occurring at higher frequencies than ω_r (gray zone) are indeed discarded during the approximation step. By doing so, one can obtain very accurate reduced-order models over $\Omega = [0, \omega_r]$, as shown by the relative errors, which are all below 3 %.

The high-frequency dynamics require a complex model to be accurately captured, while the low-frequency ones, which contain the rigid behavior and the first flexible modes of the aircraft, can be captured more easily. This point is particularly obvious when comparing the relative errors obtained here to that obtained by optimal $\mathcal{H}_2$ approximation of the same aircraft model in [22]. In the latter case, with an approximation order $r = 16$, the $\mathcal{H}_2$ approximation error is above 30 %.

An alternative illustration of the relevance of the frequency-limited approach in comparison to the standard $\mathcal{H}_2$ approach is presented in Figure 4. The time responses of the approximation errors between the first input-output transfers of $\mathbf{H}_1$ and $\hat{\mathbf{G}}_1$ and an optimal $\mathcal{H}_2$ reduced-order model of order 16 for a sinusoidal input of frequency below and above ω_r are shown. One can see that the frequency-limited approach leads to a significantly lower error when the input signal acts below ω_r (left plot in Figure 4), while the $\mathcal{H}_2$ approach is more efficient outside of the frequency interval (right plot).

Approximation error modeling

The order of the approximation errors $\Sigma_i(s) = F_i(s) - \hat{F}_i(s) = K(G_i(s) - \hat{G}_i(s))$ prevents optimization tools from being used to design the filter $W(s)$ efficiently. That is why it is built here in a heuristic manner. More specifically, $W(s)$ is designed as a product of simple first-order filters $W(s) = k\Pi_{i=1}^{n_W} \frac{s-z_i}{s-p_i}$, where the poles p_i, zeros z_i and gain k are adjusted for $W(s)$ to be as close as possible to the approximation errors, while still ensuring that $\max_{i=1,\ldots,n_s} \| W^{-1}\Sigma_i \|_{\mathcal{H}_\infty} \leq 1$. The filter $W(s)$ obtained here has an order $n_w = 25$ and is plotted in Figure 3. One can observe that its singular value upper bounds the worst approximation error. In particular, with this filter, $\max_{i=1,\ldots,n_s} \| W^{-1}\Sigma_i \|_{\mathcal{H}_\infty} = 0.99 < 1$ is obtained.

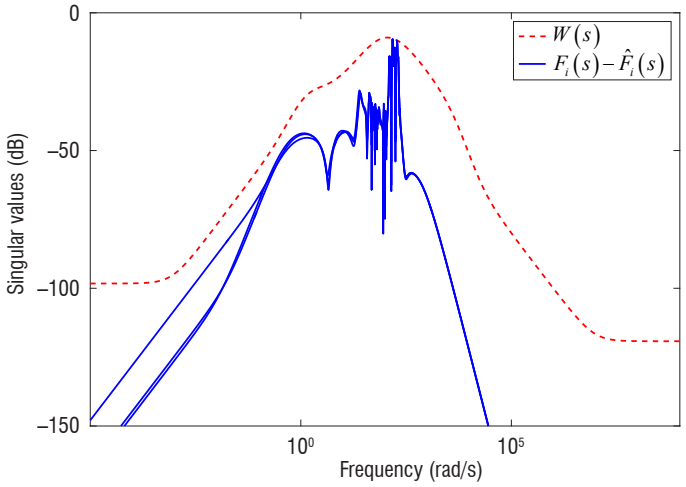

Figure 3 – Singular values of $W(s)$ and $F_i(s) - \hat{F}_i(s)$ $(i = 1, \ldots, n_s)$

Step 2: Interpolation and LFR modeling (II-C)

At this stage, a Mach-dependent family $\{\hat{F}_i(s)\}_{i=1\ldots3}$ of 22nd order LTI models is available, together with a common weighting function $W(s)$ shaping the worst-case approximation errors induced by the reduction process.

Polynomial approximation with guaranteed bounds

The interpolation technique summarized by the linear constraints (14) is initially applied with $p = 2$ and $n_s = 3$. The scalar parameter θ is normalized in such a way that $\theta = -1$ corresponds to the lowest Mach number of interest, while $\theta = 1$ corresponds to the highest value. Since $n_s - p = 1$, this first trial yields an exact approximation at each of the three interpolation points, but a poor behavior is observed elsewhere. Reducing the order p to 1 would yield a rough and unacceptable approximation. The only remaining option then consists in adding fictitious models for intermediate Mach numbers. This is achieved here by generating additional coefficients in (12), with a standard linear interpolation technique. Two models are then generated for Mach 0.825 and 0.875, and a new interpolation is thus realized with $n_s = 5$ for each of the 46 coefficients contained in the matrices Y_i of (6). A result of this interpolation is plotted in Figure 5 for one of the most varying coefficient, namely $\mathcal{Y}_{2,19}(\theta)$. The solid blue line corresponds to the nominal

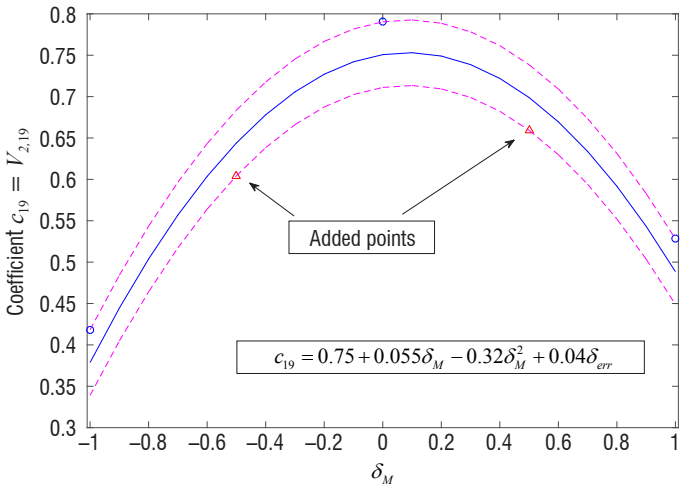

Figure 5 – Illustration of a 2nd order polynomial interpolation result with minimized guaranteed error bound for the coefficient $c_{19} = \mathcal{Y}_{2,19}$

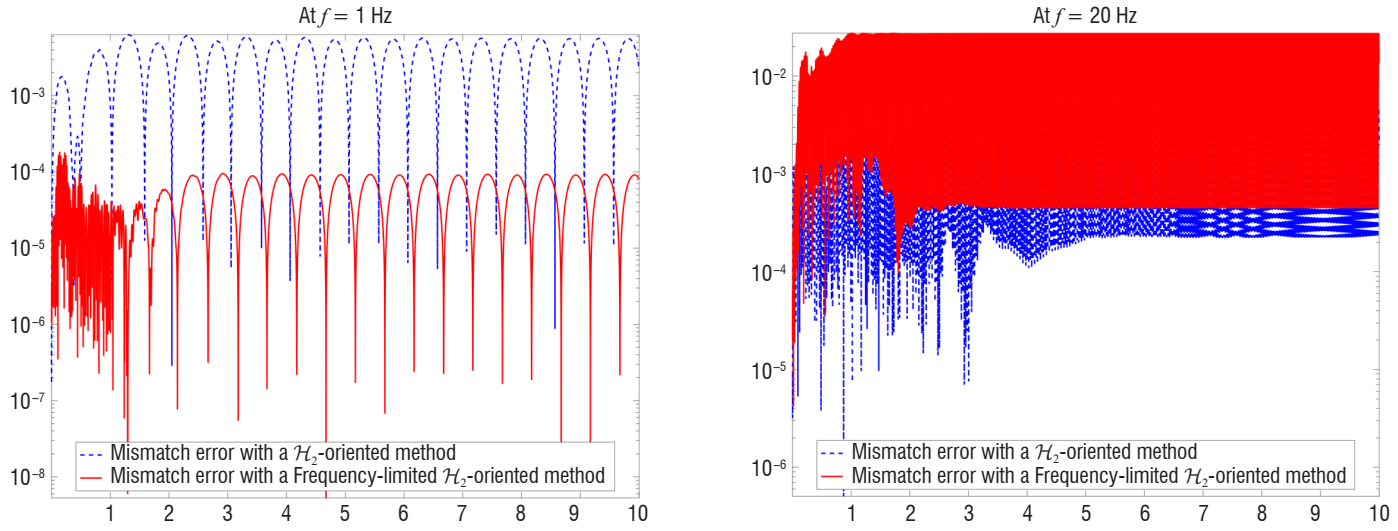

Figure 4 – Time responses of the approximation errors between the large-scale model $\mathbf{G}_1$ and the frequency-limited reduced-order model $\hat{\mathbf{G}}_1$ (solid red) and an $\mathcal{H}_2$ optimal reduced-order model of order 16 (dashed blue) for a sinusoidal input of frequency below ω_r (left) and above ω_r (right)

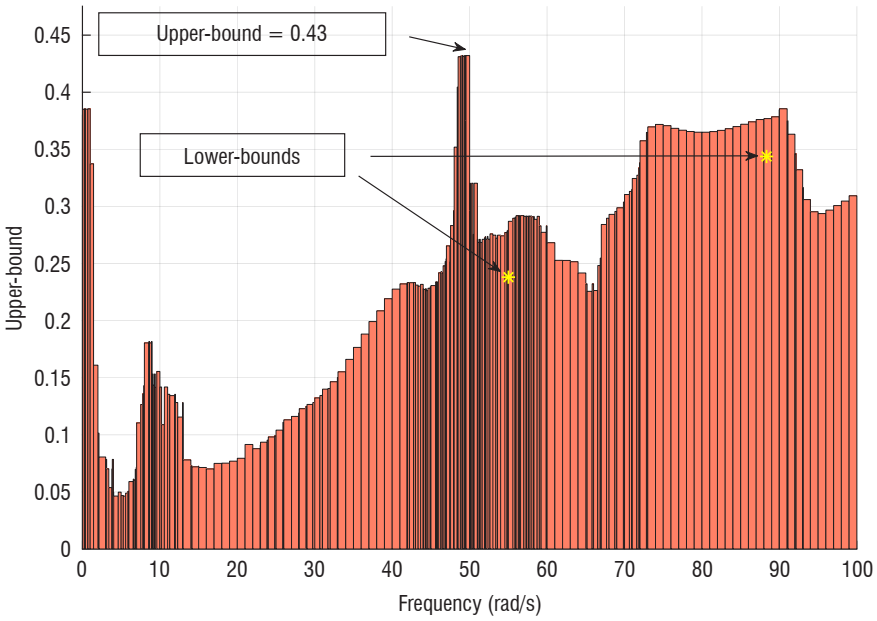

Figure 6 – Visualization of μ upper and lower bounds for the evaluation of robust stability margins: stability proved for $\| \Delta \|_\infty \leq 0.43^{-1} = 2.32$

plot, while the dashed red lines represent lower and upper bounds, including the five interpolation points. Note that the three coefficients from the initial set of models are all located on the same bound (the upper-bound for this coefficient). Quite interestingly, this property holds true for the 46 ($= 2 \times (r + n_K + 1) = 2 \times (n+1)$) coefficients, which permits the size of Δ_P to be reduced drastically in (15). Here, one obtains $\Delta_P = \delta_P I_2$ and (16) boils down to:

$$\mathcal{Y}(\theta, \Delta_P) = X_0 + \theta X_1 + \theta^2 X_2 + diag(\delta_P, \delta_P).V(E) \qquad (29)$$

LFR modeling

As has already been clarified in Section "Main result: Stability guarantee of a set of large-scale models subject to input saturations", $\mathcal{Y}(\theta, \Delta_P)$ is readily rewritten in a LFR format with the help of existing software [15]. Next, exposed in Equation (2), a global 47th-order ($= r + n_W + n_K$) dynamic LFR model encompassing the whole initial set of full-order open-loop plants is obtained. The structure of its 7 x 7 Δ-block is written as:

$$\mathbf{\Delta} = \mathbf{diag}\left(\theta I_4, \delta_P I_2, \Delta_R(s)\right) \qquad (30)$$

and has a **minimal** size that remains largely compatible with the specific μ and IQC based analysis tools to be applied next.

Step 3: Stability analysis (II-D)

Preliminary tests via μ analysis

As mentioned in Subsection "Stability assessment", the validity of the global LFR model is preliminarily checked without saturation. An uncertain LTI closed-loop model is then built and the μ analysis test (19) is performed. Since the complexity of our algorithm is not directly affected by the number of states, but mainly depends on the size and structure of $\mathbf{\Delta}$, the results are obtained in a few seconds on any standard computer. A **guaranteed** upper-bound of μ as a function of frequency is displayed in Figure 6. The yellow stars corresponding to lower-bounds reveal a rather low conservatism of our test, which can be summarized by:

$$\sup_{\omega \geq 0} \mu_{\mathbf{\Delta}}\left(M(j\omega)\right) = 0.43 \ll 1 \qquad (31)$$

The continuum of closed-loop models, for any admissible uncertainty, then clearly remains stable, which concludes the preliminary validation phase.

Stability assessment via IQC-based analysis

An input saturation – converted to a deadzone operator φ, is now inserted in the uncertain closed-loop whose $\mathbf{\Delta}$-block is then augmented: $\mathbf{\Delta} \leftarrow \mathbf{diag}(\varphi, \mathbf{\Delta})$. The initial frequency grid is $\omega_i = \{1, 5, 10, 20, 100\}$ rad/s with $i = 1, ..., 5$. To limit the number of decision variables and then the computation time, $X_\Theta(j\omega)$ and $Y_\Theta(j\omega)$ are chosen to be diagonal, which leads to 17 scalar decision variables for each frequency, even though it is possible to use the general form if no solution was obtained. In addition, 3 decision variables x, λ, γ come from the multiplier, which corresponds to the static nonlinearity φ. A solution has been obtained in 8 iterations and 104 frequencies. The total number of decision variables is $17 \times 104 + 3 = 1771$. The following remarks can be made:

- The solution $X(j\omega)$ is a positive, complex, constant and piecewise continuous 6×6 matrix. For example, at iteration 8, for $\omega_3 = 10$ rad/s, the solution $\Pi_3(j\omega)$ is valid over the frequency domain $\Omega_3 = [9.72, 32.82]$ rad/s. Finally, after 8 iterations $\Omega_{valid} = \bigcup_{i=1,...,104} \Omega_i = [0 + \infty)$, consequently the solution is validated on the whole frequency domain.

- An *a priori* trial and error approach to determine the parameterization for multipliers is not required here. Furthermore, with rational multipliers, if no solution is obtained with a specific parameterization, it is still impossible to conclude on the feasibility problem, since a different or more complex parameterization may have enabled a solution to be found. Both points highlight the methodological superiority of irrational multipliers, which can only be considered from a frequency domain point of view.

- Finally, the stability of the uncertain and nonlinear closed-loop is proved on the large-scale dynamical model.

Conclusion and perspectives

In this paper, a methodology enabling the stability of a set of controlled SIMO large-scale LTI dynamical models subject to input saturation to be assessed has been presented. Firstly, the large-scale models are reduced, interpolated and the associated errors are bounded. This leads to a small-scale LFR, which represents both the parametric variation of the initial set of models and the errors induced during the reduction and interpolation steps. The stability analysis is then achieved with an innovative algorithmic approach based on IQC techniques. Unlike standard methods that require a possibly conservative parameterization of the multiplier, here, no parameterization is required. This decrease in the conservatism enables the approach to be drastically improved. The methodology is successfully validated on an industrial set of controlled large-scale aircraft models subject to saturation limitations. The extension of the methodology to MIMO models is conditioned by the use of an interpolation technique with guaranteed error bounds. The development of such a technique is still under investigation. Similarly, determining whether the methodology can easily be extended to a broader class of models (e.g., descriptor models) requires further studies ■

References

[1] M. S. ANDERSEN, S. K. PAKAZAD, A. HANSSON, A. RANTZER - *Robust Stability Analysis of Sparsely Interconnected Uncertain Systems*. IEEE Transactions on Automatic Control, 59(8):2151–2156, 2014.

[2] A. C. ANTOULAS - *Approximation of Large-Scale Dynamical Systems*. Advances in Design and Control. SIAM, 2005.

[3] P. APKARIAN, D. NOLL - *Nonsmooth H_∞ Synthesis.* IEEE Transaction on Automatic Control, 51(1):71-86, 2006.

[4] J.-M. BIANNIC, G. FERRERES - *Efficient Computation of a Guaranteed Robustness Margin.* Proceedings of the IFAC World Congress, 2005.

[5] J. DE CAIGNY, R. PINTELON, J. F. CAMINO, J. SWEVERS - *Interpolated Modeling of lpv Systems.* IEEE Transactions on Control Systems Technology, 22(6):2232-2246, 2014.

[6] F. DEMOURANT - *New Algorithmic Approach Based on Integral Quadratic Constraints for Stability Analysis of High Order Models*. Proceedings of the European Control Conference, pp. 359-364, 2013.

[7] G. FERRERES - *Computation of a Flexible Aircraft LPV/LFT Model Using Interpolation.* IEEE transactions on Control Systems Technology, 19(1):132-139, 2011.

[8] P. FULCHERI, M. OLIVI - *Matrix Rational H_2 Approximation: A Gradient Algorithm Based on Schur Analysis.* SIAM Journal on Control and Optimization, 36(6):2103-2127, 1998.

[9] W. GAWRONSKI - *Advanced Structural Dynamics and Active Control of Structures*. Springer, 2004.

[10] S. GUGERCIN, A. C. ANTOULAS, C. A. BEATTIE - *H_2 Model Reduction for Large Scale Linear Dynamical Systems.* SIAM Journal on Matrix Analysis and Applications, 30(2):609-638, 2008.

[11] R. IONUTIU, J. ROMMES, W. H. A. SCHILDERS - *SparseRC: Sparsity Preserving Model Reduction for RC Circuits with Many Terminals*. IEEE Transactions on Computer-Aided Design of Integrated Circuits and Systems, 30(12):1828-1841, 2011.

[12] U. JONSSON, A. RANTZER - *A Unifying Format for Multiplier Optimization.* Proceedings of the American Control Conference, vol. 5, pp. 3859-3860, 1995.

[13] C. T. LAWRENCE, A. M. TITS, P. VAN DOOREN - *A Fast Algorithm for the Computation of an Upper Bound on the μ-Norm.* Automatica, 36(3):449-456, 2000.

[14] M. LOVERA, C. NOVARA, P. LOPES DOS SANTOS, D. E. RIVERA - *Guest Editorial Special Issue on Applied LPV Modeling and Identification.* IEEE Transactions on Control Systems Technology, 19(1):1-4, 2011.

[15] J-F. MAGNI - *Linear Fractional Representation Toolbox for Use with Matlab.* Technical report, ONERA, The French Aerospace Lab, 2006. Updated 2014 version available at http://w3.onera.fr/smac/.

[16] A. MEGRETSKI, A. RANTZER - *System Analysis via Integral Quadratic Constraints.* IEEE Transactions on Automatic Control, 42(6):819-830, 1997.

[17] A. PACKARD, J. C. DOYLE - *The Complex Structured Singular Value.* Automatica, 29(1):71-109, 1993.

[18] P. PARK - *Stability Criteria of Sector- and Slope-Restricted Lur'e systems.* IEEE Transactions on Automatic Control, 47(2):308-313, 2002.

[19] D. PETERSSON, J. LÖFBERG - *Model Reduction using a Frequency-Limited H_2-cost.* Systems & Control Letters, 67:32-39, 2014.

[20] H. PFIFER, P. SEILER - *Robustness Analysis of Linear Parameter Varying Systems Using Integral Quadratic Constraints.* International Journal of Robust and Nonlinear Control, 25(15):2843-2864, 2015.

[21] C. POUSSOT-VASSAL, T. LOQUEN, P. VUILLEMIN, O. CANTINAUD, AND J-P. LACOSTE - *Business Jet Large-Scale Model Approximation and Vibration Control.* Proceedings of the 11th IFAC ALCOSP, pp. 199-204, Caen, France, July 2013.

[22] C. POUSSOT-VASSAL, C. ROOS, T. LOQUEN, P. VUILLEMIN, O. CANTINAUD, J-P. LACOSTE - *Control-Oriented Modelling and Identification: Theory and Practice*. Chapter 11 - Control-oriented Aeroelastic BizJet Low-order LFT modeling, pp. 241-268. The Institution of Engineering and Technology (M. Lovera eds.), 2014.

[23] C. ROOS, J.-M. BIANNIC - *A Detailed Comparative Analysis of all Practical Algorithms to Compute Lower Bounds on the Structured Singular Value.* Control Engineering Practice, 44:219-230, 2015.

[24] C. ROOS, F. LESCHER, J.-M. BIANNIC, C. DOLL, G. FERRERES. *A Set of μ-Analysis Based Tools to Evaluate the Robustness Properties of High-dimensional Uncertain Systems.* Proceedings of the IEEE Multiconference on Systems and Control, pp. 644-649, 2011.

[25] A. SIDERIS, R. S. SANCHEZ PENA - *Robustness Margin Calculation with Dynamic and Real Parametric Uncertainty.* IEEE Transactions on Automatic Control, 35(8):970-974, 1990.

[26] P. VUILLEMIN, F. DEMOURANT, J-M. BIANNIC, C. POUSSOT-VASSAL - *Global Stability Validation of an Uncertain Large-Scale Aircraft Model.* Proceedings of the IEEE Multi-conference on Systems and Control, pages 152-157, 2014.

[27] P. VUILLEMIN, C. POUSSOT-VASSAL, D. ALAZARD - *Poles Residues Descent Algorithm for Optimal Frequency-Limited H_2 model approximation.* Proceedings of the European Control Conference, pp. 1080-1085, 2014.

[28] P. VUILLEMIN, C. POUSSOT-VASSAL, D. ALAZARD - *Spectral Expression for the Frequency-Limited H_2-Norm of LTI Dynamical Systems with High Order Poles.* Proceedings of the European Control Conference, pp. 55-60, 2014.

Pierre Vuillemin was graduated with an engineering degree from ENSEM (Nancy, France) and with a a M.Sc. degree in complex systems engineering from the University of Lorraine (Nancy, France) in 2011. He then pursued a Ph.D. in control systems theory within the Systems Control and Flight Dynamics Department at ONERA (Toulouse, France) and was graduated in 2014 from the University of Toulouse. After occupying a post-doctoral position in Nantes, he joined ONERA as a research scientist in 2016. His main interests concern optimization and its application in Control Systems Theory.

Fabrice Demourant was born in Istres, France, in 1975. He received the Engineering Degree and M.Sc. degree in control and signal processing from ENSICAEN, Caen, France, and the Ph.D. degree in control systems theory, System Control and Flight Dynamics Department, ONERA, Toulouse, France,in 2002. In 2003, he was an Engineer with AIRBUS,Toulouse, in the load control domain. Since 2005, he has been a Researcher with ONERA, where he is in charge of the methods and tools activities. He has a consolidated experience in control law design and analysis, modeling, and load/vibration control.

Charles Poussot-Vassal was born in Grenoble, France, in 1982. In 2005, he completed his Engineering degree and M.Sc. in Control and Embedded Systems from Grenoble INP-ESISAR (Valence, France) and Lund University of Technology (Lund, Sweden), respectively. In 2008, he completed his Ph.D. degree in Control Systems Theory, within the GIPSA-lab's control systems department (Grenoble, France). At the beginning of 2009, he worked as a Research Assistant with the Politecnico di Milano (Milan, Italy). From mid-2009, he has been Researcher with ONERA, the French aerospace lab (Toulouse, France). His main interests concern the (structured and parametric) large-scale and infinite dynamical model approximation techniques, linear and parametric control design and performance analysis, with application in aircraft systems, rivers, fluid flow and experimental tests.